



TESE DE DOUTORAMENTO

POROUS NANOSYSTEMS FOR BIOLOGICAL APPLICATIONS

María Fernanda Navarro Poupard

**ESCOLA DE DOUTORAMENTO INTERNACIONAL
PROGRAMA DE DOUTORAMENTO EN CIENCIA DE MATERIAIS**

SANTIAGO DE COMPOSTELA

ANO 2020





DECLARACIÓN DA AUTORA DA TESE

Dna. María Fernanda Navarro Poupard

Presento a miña tese, seguindo o procedemento axeitado ao Regulamento, e declaro que:

- 1) A tese abarca os resultados da elaboración do meu traballo.
- 2) De ser o caso, na tese faise referencia ás colaboracións que tivo este traballo.
- 3) A tese é a versión definitiva presentada para a súa defensa e coincide coa versión enviada en formato electrónico.
- 4) Confirmo que a tese non incorre en ningún tipo de plaxio doutros autores nin de traballos presentados por min para a obtención doutros títulos.

En Santiago de Compostela, 4 de Decembro de 2020

Asdo. María Fernanda Navarro Poupard





AUTORIZACIÓN DO DIRECTOR/TITOR DA TESE

D. Pablo Taboada Antelo

D. Pablo Alfonso del Pino González de la Higuera

INFORMAN:

Que a presente tese, correspóndese co traballo realizado por Dna. María Fernanda Navarro Poupard, baixo a nosa dirección, e autorizamos a súa presentación, considerando que reúne os requisitos esixidos no Regulamento de Estudos de Doutoramento da USC, e que como directores desta non incorre nas causas de abstención establecidas na Lei 40/2015.

En Santiago de Compostela, 4 de Decembro de 2020

Asdo. Pablo Taboada Antelo

Asdo. Pablo Alfonso del Pino
González de la Higuera



TABLE OF CONTENTS

TABLE OF CONTENTS.....	9
LIST OF FIGURES	11
LIST OF TABLES	25
LIST OF ACRONYMS AND ABBREVIATIONS.....	28
AGRADECIMIENTOS	33
RESUMO	36
RESUMEN.....	44
ABSTRACT	48
1. INTRODUCTION.....	52
1.1. NANOTECHNOLOGY, NANOMATERIALS, AND NANOPARTICLES: GENERAL CONCEPTS	52
1.1.1. <i>Classification of Nanoparticles</i>	53
1.1.2. <i>Synthesis of Nanoparticles</i>	53
1.1.3. <i>Growth Control of Nanoparticles in Solution</i>	54
1.1.4. <i>Functionalization of Nanoparticles Surface</i>	55
1.1.5. <i>Techniques for Nanoparticles Characterization</i>	57
1.1.6. <i>Applications of Nanoparticles</i>	58
1.2. PLASMONIC NANOPARTICLES.....	62
1.2.1. <i>General Concepts</i>	62
1.3. POROUS NANOPARTICLES	65
1.3.1. <i>General Concepts</i>	67
1.4. APPLICATIONS OF POROUS NANOPARTICLES IN CATALYSIS AND DRUG DELIVERY: A GENERAL OVERVIEW	69
1.5. OBJECTIVES.....	72
2. MATERIALS & METHODS.....	76
2.1. CHEMICALS	76
2.1.1. <i>Chapter 3</i>	76
2.1.2. <i>Chapter 4</i>	76
2.1.3. <i>Chapter 5</i>	77
2.2. CHARACTERIZATION TECHNIQUES	77
2.2.1. <i>Chapter 3</i>	77
2.2.2. <i>Chapter 4</i>	78
2.2.3. <i>Chapter 5</i>	78
2.3. METHODS	79
2.3.1. <i>Chapter 3</i>	79
2.3.2. <i>Chapter 4</i>	80
2.3.3. <i>Chapter 5</i>	82
3. COPPER BASED COORDINATION POLYMER NANOPARTICLES FOR CATALYTIC REDUCTION: METHYLENE BLUE INTO LEUCOMETHYLENE BLUE	88

3.1.	INTRODUCTION	88
3.2.	RESULTS AND DISCUSSIONS	91
3.2.1.	<i>The Influence of the Synthesis Parameters: Molar Ratio of the Reactants</i>	91
3.2.2.	<i>The Influence of the Synthesis Parameters: Reaction Time and Solvent (1st Part)</i> ...	93
3.2.3.	<i>The Influence of the Synthesis Parameters: Solvent (2nd Part)</i>	97
3.2.4.	<i>Selected Nanoparticles</i>	99
3.2.5.	<i>Structural Characterization</i>	100
3.2.6.	<i>Thermal Characterization</i>	106
3.2.7.	<i>Surface Area Characterization</i>	109
3.2.8.	<i>Physicochemical Characterization</i>	110
3.2.9.	<i>Catalytic Reduction on Methylene Blue</i>	113
3.3.	CONCLUSIONS	115
4.	GOLD NANOSTARS@ZEOLITIC IMIDAZOLATE FRAMEWORK 8 CORE-SHELL NANOSTRUCTURES FOR LIGHT TRIGGERED RELEASE: IN VITRO	119
4.1.	INTRODUCTION	119
4.2.	RESULTS AND DISCUSSIONS	123
4.2.1.	<i>The Influence of the Synthesis Parameters: CTAB as a Size-Directing Surfactant</i>	123
4.2.2.	<i>Colloidal Stability of Zeolitic Imidazolate Frameworks (ZIF-8 and -67)</i>	126
4.2.3.	<i>Encapsulation of Gold Nanostars (NSs) into Zeolitic Imidazolate Frameworks (ZIF-8) to form Core-Shell Nanocomposites</i>	127
4.2.4.	<i>Encapsulation of Dye Molecules in AuNS/ZIF-8 Nanocomposite (NC-HOE)</i>	130
4.2.5.	<i>Surface Functionalization in AuNS/ZIF-8 Nanocomposite (NC-HOE-PMA)</i>	132
4.2.6.	<i>Selected Nanoparticles</i>	136
4.2.7.	<i>Colloidal Stability of the Nanocomposites</i>	137
4.2.8.	<i>Structural Characterization</i>	140
4.2.9.	<i>Thermal Characterization</i>	142
4.2.10.	<i>Surface Characterization</i>	144
4.2.11.	<i>Thermoplasmonic Behavior Studies in Aqueous Solution and Inside Living Cells</i>	148
4.3.	CONCLUSIONS	150
5.	CACO ₃ SUB-MICROMETRIC CAPSULES FOR ULTRASOUND TRIGGERED RELEASE: IN VITRO AND IN VIVO.....	153
5.1.	INTRODUCTION	153
5.2.	RESULTS AND DISCUSSIONS	157
5.2.1.	<i>The Influence of the Synthesis Parameters: PVSA to control growth formation of CaCO₃ particles</i>	157
5.2.2.	<i>Structural Characterization: CaCO₃ particles</i>	159
5.2.3.	<i>CaCO₃ Macromolecule-Loaded Particles</i>	162
5.2.4.	<i>Multifunctional Sub-Micrometric Capsules (NCs)</i>	166
5.2.5.	<i>Optimization of Capsule Shell</i>	170
5.2.6.	<i>Characterization of the Multifunctional Sub-Micrometric Capsules (NCs)</i>	174
5.2.7.	<i>Bioactivity of Encapsulated and Ultrasound-Loading Released</i>	178
5.2.8.	<i>NCs Dispersion and Fluorescence Analysis after US Treatment</i>	185
5.2.9.	<i>Ultrasound-Triggered in vivo Delivery of rtPA</i>	186
5.3.	CONCLUSIONS	188
6.	APPENDIX	191
6.1.	CHAPTER 4 APPENDIX	191

6.1.1. <i>Cell Studies</i>	191
6.2. CHAPTER 5 APPENDIX	198
6.2.1. <i>In Vivo Studies</i>	198
7. GENERAL CONCLUSIONS.....	208
REFERENCES	211
APPENDIX- FIGURES RIGHTS & PERMISSIONS.....	233





LIST OF FIGURES

Figure	Page
Figure 1.1. Schematic illustration showing that material breaks down into smaller particles and this leads to surface area increase.....	52
Figure 1.2. Schematic illustration of the two general approaches for the synthesis of nanomaterials.....	54
Figure 1.3. Schematic illustration of nanoparticles modified with an amphiphilic polymer.....	55
Figure 1.4. Schematic illustrations of different LbL assembly methods with benefits (+) and limitations (-): a) the centrifugation method involves centrifugation (Cf) steps; b) Microfluidics method; c) “Electrophoretic polymer assembly”.....	56
Figure 1.5. Schematic illustration of a) homogeneous catalysis and b) heterogeneous catalysis.....	58
Figure 1.6. Schematic illustrations of a) in vitro vs. b) in vivo studies.....	59
Figure 1.7. Biophysico-chemical properties of nanoparticles for drug delivery.....	60
Scheme 1. Internal and external triggers for drug delivery systems.....	62
Figure 1.8. Scheme of the interaction of light and plasmonic NPs, resulting in scattering (far- and near-field), absorption, and energy transfer phenomena that have application in biotechnology.....	63
Figure 1.9. a) Energy and LSPR position for the plasmonic response of different NPs as a function of composition, size, and shape; b) Position of LSPR in Au NPs of different sizes; c) Position of LSPR in Au NPs of different shape (and size); d) Plasmonic response (LSPR position and extinction cross-section) of two gold spherical NPs interacting as a function of their interparticle distance.....	65
Figure 1.10. Schematic illustration of classes of porous materials.....	66
Figure 1.11. Schematic illustration of the difference between absorption and adsorption.....	67
Figure 1.12. a) Pore filling stages at different pressures (BET adsorption multi-layer). b) Different types of adsorption isotherms.....	69

Figure 3.1. a1) Self-assembly of metal ions and organic ligands; a2) Porous frameworks with different structures and dimensionality. b) Classification of porous coordination polymers into three categories. c) Structure of the cubic metal-organic framework HKUST-1.....	89
Figure 3.2. Schematic illustration of the synthesis of the Cu-based nanoparticles, and images of the resulting solutions at different $\text{CuCl}_2 \cdot 2\text{H}_2\text{O}$ concentrations and molar ratios shown in Table 1.....	92
Figure 3.3. SEM micrographs of different Cu-based nanoparticles: a, b) $2\text{MI}:\text{Cu}^{2+} = 5$; c, d) $2\text{MI}:\text{Cu}^{2+} = 10$; e, f) $2\text{MI}:\text{Cu}^{2+} = 15$; g, h) $2\text{MI}:\text{Cu}^{2+} = 20$ (NP1); i, j) $2\text{MI}:\text{Cu}^{2+} = 40$	93
Figure 3.4. Schematic illustration of synthesis for the analysis of the influence of the reaction time and solvent.....	94
Figure 3.5. SEM micrographs of different species of Cu-imidazole nanocomposites after drop-casting onto Si substrates: a,b) NP1 with an average diameter of 330 ± 27 (0.5%) nm; d,e) NP2 with an average edge length of 334 ± 111 (33%) nm. c,f) Size histograms (d_{NP1} : mean diameter of NP1 and L_{NP2} : mean length of NP2) obtained after measuring the diameter of over 300 NP1 (solvent: acetone, reaction time: 45 min) and NP2 (solvent: acetone, reaction time: 72 h), using ImageJ.....	95
Figure 3.6. Colloidal integrity of NP3 redispersed in H_2O : c1) Color evolution from 0 to 72 h; SEM micrographs after redispersion in H_2O and drop-casting on a Si substrate: c2) 30 min, c3) 24 h and c4) 72 h after mixing of the reactants.....	95
Figure 3.7. SEM micrographs of different species of Cu-imidazole nanocomposites after drop-casting onto Si substrates: a,b) NP1 with an average diameter of 330 ± 27 (0.5%) nm; d,e) NP3 with an average tip-to-tip length of 447 ± 65 (15%) nm. c,f) Size histograms (d_{NP1} : mean diameter of NP1 and L_{NP3} : mean length of NP3) obtained after measuring the diameter of over 300 NP1 (solvent: acetone, reaction time: 45 min) and NP3 (solvent: water, reaction time: 72 h), using ImageJ.....	96
Figure 3.8. TEM micrographs of a-d) NP1, e-f) NP2, and g-i) NP3 after drop-casting on TEM grids. The morphology of NP3 nanoparticles resembles that of recently reported for CuO NPs (0.5 mL of $\text{NH}_3 \cdot \text{H}_2\text{O}$, 30 min reaction). j) Image shows the SAED (selected area electron diffraction) of NP3 of image i).....	97
Figure 3.9. Schematic illustration of the synthesis of NP1 sample redispersed in different solvents, and SEM micrographs of the precipitate NP1 redispersed in solvents of increasing polarity: ethyl acetate (a,b), N,N-dimethylformamide (DMF; c,d), acetonitrile (e, f), methanol (g, h). Insets	98

show color images of the corresponding solutions. Colloidal integrity of NP1 redispersed in MeOH: i1) Color evolution from 0 (brownish) to 72 h (violetish); SEM micrographs after redispersion in MeOH and drop-casting on a Si substrate at: i2) 12 h, i3) 24 h and i4) 72 h after mixing of the reactants.....	
Figure 3.10. Schematic illustration and SEM images of the nanoparticles selected for this study.....	99
Figure 3.11. PXRD patterns of NP1 (grey), NP2 (red), and NP3 (blue), and a simulation of the tenorite form of copper (II) oxide (magenta) based on previous work.....	100
Figure 3.12. Frozen solution (120 K) EPR spectra of species: a) NP1 (grey; acetone); b) NP2 (red; acetone); c) NP3 (blue; water); d) Hyperfine transitions in the perpendicular region of the three species having “extra absorption” features towards the high-field end of the spectra, <i>i.e.</i> , superhyperfine splitting due to the interaction of the unpaired electron of Cu^{2+} with nitrogen ligands. Nine discontinued lines homogeneously spaced (1.5 mT) point at this superhyperfine splitting.....	102
Figure 3.13. a, b) Powder (RT) EPR spectra of NP1.....	103
Figure 3.14. a, b) Powder (RT) EPR spectra of NP2.....	104
Figure 3.15. a, b) Powder (RT) EPR spectra of NP3.....	105
Figure 3.16. FTIR spectra of the starting reactants and the three types of NPs obtained. Asterisks point at 2MI bands (pink) that are observed in NP1 (grey), NP2 (red), and NP3 (blue). Blue arrows point at metal-oxygen vibrations in NP3.....	106
Figure 3.17. TGA of the NPs: (a) NP1 in N_2 (grey); (b) NP1 in air (grey); (c) NP2 in N_2 (red); and (d) NP3 in N_2 (blue). Violet lines correspond to the first derivative of the TGA curves (a,c,d), and the orange line corresponds to the DSC of sample NP1 (air) (b), indicating the rate of temperature degradation.....	107
Figure 3.18. Temperature-dependent PXRD experiment carried out with NP1.....	108
Figure 3.19. TGA of reactants: Cu_2Cl , 2MI, and CTAB.....	109
Figure 3.20. N_2 sorption isotherms (a) and HK pore volume distribution (b) of NP1 (grey), NP2 (red) and NP3 (blue).....	110
Figure 3.21. a) UV-Vis spectra of NP1 (grey; in acetone), NP2 (red; in acetone) and NP3 (blue; in MilliQ water). b) UV-Vis spectra of the reactants: CuCl_2 , 2MI, and CTAB in water. c) Fluorescence spectra of reactants, NP1, and NP2 in acetone. d) Fluorescence spectra of reactants. e) Mean average hydrodynamic diameter obtained from DLS number-weighted size distribution of NP1 (grey; in acetone), NP2 (red; in acetone)	111

and NP3 (blue; in MilliQ water). Colored values above the hollow squares correspond to PDI values.....	
Figure 3.22. DLS histograms for NP1 (a), NP2 (b) and NP3 (c) (left: Intensity; middle: Volume; right: Number-weighted size distributions)	112
Figure 3.23. Absorbance at 664 nm (A) versus time for an equal mass of copper in, <i>i.e.</i> , NP1 (grey), NP2 (red) and NP3 (blue), and control sample (ctrl, black). A_0 is the absorption at 664 nm at time 0 s. Data considered for the kinetic fitting (first-order) are colored (initial 22 s). Insets show zoom areas of the fitting regions for selected samples and control.....	115
Figure 4.1. Single-crystal XRD structure of ZIFs. Left row: stick diagram; the large cage in ZIFs is represented with ZnN_4 tetrahedral sites in blue and CoN_4 ones in pink; ball and stick diagram representing IM (imidazole) and IM-type linkers (C: black, N: green, O: red, Cl: pink, H atoms are omitted. Left: zoomed images of porous cage of ZIF-8 (upper) and crystal structure of ZIF-8 with sodalite topology (bottom).....	121
Figure 4.2. A) Scheme of different post-synthetic surface functionalization processes for ZIF-8 crystals: inorganic nanoparticles; metal coating, and polymers, and their corresponding SEM images (scale bars: left: 20 nm,, middle and right: 500 nm, below a schematic representation of a Janus particle (center) is also shown.....	122
Figure 4.3. Schematic illustration of the synthesis of ZIF-8 or ZIF-67 nanoparticles and mean $d_{h(N)}$ of ZIF-8 and ZIF-67 <i>versus</i> concentration of added CTAB. The corresponding polydispersity index (PDI) is specified on top of each bar.....	125
Figure 4.4. a) Schematic illustration of the synthesis of ZIF-8 or ZIF-67 nanoparticles, and Mean $d_{h(N)}$ for one week for b) ZIF-67 particles in methanol and water, and c) ZIF-8 particles in methanol, water, and cell medium.....	126
Figure 4.5. Step-by-step formation of nanocomposites: seeds, stars and core-shells structure.....	128
Figure 4.6. Optical characterization of the as-prepared NPs seeds: a) UV/Vis absorption spectrum showing their Surface Plasmon Resonance (SPR) peak at $\lambda = 517$ nm; b) representative TEM image (scale bar corresponds to 50 nm); and c) the corresponding histogram of the number-weighted size distribution N of the core diameter d_c of NPs as determined from TEM images, $d_c = (11.4 \pm 0.9)$ nm. Optical characterization of the as-prepared NSs: d) UV/Vis absorption spectrum A showing their SPR peak at	129

$\lambda = 768$ nm; e) representative SEM image (scale bar corresponds to 200 nm); and f) the corresponding histogram of the number-weighted size distribution N of the tip-to-tip length L_{NS} of the NSs as determined from SEM images, $L_{NS} = (82.6 \pm 4.9)$ nm.....

Figure 4.7. SEM micrographs of core-shell AuNRs/ZIF-8 structures with different concentrations of AuNRs: a) 1nM (average size ≈ 150 nM), b) 2nM (average size ≈ 120 nM) and c) 4nM (average size ≈ 90 nM)..... **130**

Figure 4.8. a-b) Low and high magnification SEM micrographs of ZIF-8 nanoparticles (SE2: type II secondary electrons, 3kV). c) Histogram of the number-weighted distribution N of the particle diameter (*i.e.*, vertex-to-vertex distance) d_C of ZIF-8 particles, as determined from SEM images using ImageJ; $d_{ZIF-8} = 169 \pm 27$ nm. d-e) Low and high magnification SEM micrographs of NCs (SE2: type II secondary electrons, 3kV), scale bars correspond to 200 nm. f) Histogram of the number-weighted distribution N of the diameter (*i.e.*, vertex-to-vertex distance) d_{NC} of NCs, as determined from SEM images using ImageJ; $d_{ZIF-8} = 218 \pm 24$ nm..... **131**

Figure 4.9. Calibration curves of HOE in (a) MeOH and (b) water were obtained from fluorescence measurements under excitation at 350 nm (I). Fluorescence intensity (I) at the maximum emission peak as a function of HOE concentration c is plotted, and the calibration equation is obtained by fitting a linear regression line to the collected data; R^2 is the coefficient of determination..... **132**

Figure 4.10. Synthesis of poly (isobutylene–alt–maleic anhydride)–graft–dodecyl. a) Poly (isobutylene-alt-maleic anhydride) is used as hydrophilic backbone (pink box is showing one monomer unit). b) Dodecylamine is used as hydrophobic side chain. The amphiphilic polymer was obtained by reaction of the hydrophilic backbone with hydrophobic side chains. c) Structure of the amphiphilic polymer (PMA-g-dodecyl). The pink box in c shows a monomer unit with attached side chain (final molar mass of one polymer unit M_P). The hydrophobic and hydrophilic parts are drawn in red and blue, respectively..... **133**

Figure 4.11. Scheme of the PMA–functionalization procedure of NC. PMA polymer (the red box shows one monomer unit) and NCs are mixed in a round flask (3:1 MeOH:CHCl₃) in a ratio of 150 monomers per nm² of NC, the solvent is then evaporated using a rotary evaporator, and the final dried product is redispersed in sodium borate buffer (SBB pH=9) by mild sonication. Purification of the resulting NC-PMA is carried out by centrifugation and washing with water..... **134**

Figure 4.12. Representative SEM images of NC-PMA particles taken at different magnifications, with several detectors as well as voltages to get different information. a) Images collected with Everhart-Thornley detector **135**

(SE2, secondary electrons) at 3 kV; b) InLens detector (SE1, secondary electrons) at 20 kV; and c) AsB detector (backscattered electrons) at 20 kV. Scale bars correspond to 200 nm. d) Normalized UV/Vis absorption spectrum A_{norm} of NC particles showing their SPR peak at $\lambda = 790$ nm. Note that the UV/Vis spectrum of bare gold nanostars (NS) is also shown for comparison. e) Normalized fluorescence spectra I_{norm} of HOE before (free dye molecules) and after encapsulation into the nanocomposite (NC-HOE), as well as after PMA-functionalization (NC-HOE-PMA), respectively.....

Figure 4.13. DLS intensity- (I), volume- (V), and number-weighted (N) size distributions, d_h , of NC-HOE a) before b) and after PMA-functionalization (NC-HOE-PMA). The NC-HOE sample was dispersed in MeOH whereas the NC-HOE-PMA one was dispersed in water..... **136**

Figure 4.14. Schematic illustration of the different nanoparticles in this study..... **137**

Figure 4.15. DLS intensity-, volume-, and number-weighted size distributions, d_h , of NC a) before b) and after PMA-functionalization, NC-PMA as dispersed in water at different time points. c) Mean d_h for one week for NC (red) and NC-PMA (blue) in water (squares) and cell medium (circles), respectively..... **138**

Figure 4.16. a) Assay to check the lack of stability of bare NC (without PMA coating) in aqueous solution. NC particles initially stable in MeOH were centrifuged, MeOH (supernatant) was removed, and NC particles (precipitate) were redispersed in water, resulting in the dissolution of the ZIF-8 shell around the NSs. b-c) SEM micrographs of NCs with PMA coating (after exposure to aqueous solution, without centrifugation/purification) after drop casting on Si substrates. d-f) SEM micrographs of NCs acquired with different detectors: d) SE2, 3kV, e) InLens, 20kV, and f) AsB, 20kV..... **139**

Figure 4.17. PXRD spectra of ZIF-8 (grey), NC (orange) and NC-PMA (blue). For comparison, simulations of ZIF-8 [black, COD (Crystallography Open Database): 7111970] and Au-fcc (wine; COD: 9008463) are added. I_{norm} is the normalized intensity..... **140**

Figure 4.18. SERS spectra of free HOE and nanocomposites (NCs) with or without HOE trapped..... **142**

Figure 4.19. TGA of the different nanoparticles..... **143**

Figure 4.20. PXRD spectra of TGA residues. For comparison, simulations of ZnO (violet; COD: 2300112) and Au (wine; COD: 9008463) are added. **145**

I_{norm} is the normalized intensity.....	
Figure 4.21. a) N_2 sorption isotherms at 77 K of the different nanocomposites (NCs). b) HK pore volume distribution of selected samples.....	146
Figure 4.22. a) HOE release in methanol by fluorescence (I) after NIR illumination of the NC-HOE system (pink) at different concentrations (c); as controls, NC-HOE was heated in a thermostatic batch (50 °C, 1 min, yellow) or non-heated (red). b) Equivalent HOE release (I) in water for the NC-HOE-PMA system (blue); control samples at $c=0.05$ nM did not show any significant HOE release (*below the detection limit). c) SERS spectra of NCs after incubation with cells. Spectra were acquired in the presence and absence of NIR illumination (785 nm); solid and dashed lines represent the time points 0 h and 8 h, respectively. d-f) Confocal microscopy image of cells incubated with NC-HOE (d), NC-HOE-PMA(e) and NC-HOE-PMA after NIR treatment (f). In d-f), blue and orange color represent HOE and cell membrane staining (CellMask TM Deep Red), respectively; scale bar is 40 μm	149
Figure 5.1. Scanning electron microscope (SEM) images of different vaterite particle shape: a) CaCO_3 vaterite crystals. b) Core particle surface. c) Core particle interior. d) Schematic illustration of the formation process of a vaterite microsphere.....	154
Figure 5.2. a) Flower-like shaped vaterite. b) Rosette-shaped vaterite. c) Hexagonal shaped vaterite. d) Lens-shaped vaterite. e) Plate-shaped vaterite.....	155
Figure 5.3. Schematic representation of the experimental setup for the synthesis of CaCO_3 particles at different PVSA concentrations and DLS data of the number-weighted average size peak for particles at different PVSA concentrations; the number on top of each square corresponds to the polydispersity index (PDI).....	158
Figure 5.4. Low and high magnification SEM micrographs of different species of CaCO_3 particles from <i>Table 1</i> after drop casting on Si substrates: a-b) CC_0, d-e) CC_0.1, g-h) CC_0.2 and j-k) CC_1 (SE2, 3kV). c) Size histogram (d_{CC_0} : mean diameter of CC_0) obtained after measuring the diameter of over 100 CC_0 particles using ImageJ; $d_{\text{CC}_0} = 3163 \pm 709$ nm. f-l) Size histogram ($d_{\text{CC}_0.1}$, $d_{\text{CC}_0.2}$, d_{CC_1} : mean diameter of CC_0.1, CC_0.2 and CC_1, respectively) obtained after measuring the diameter of over 300 CC_0.1, CC_0.2 and CC_1 particles using ImageJ; $d_{\text{CC}_0.1} = 693 \pm 124$ nm, $d_{\text{CC}_0.2} = 541 \pm 83$ and $d_{\text{CC}_1} = 518 \pm 108$ nm.....	160

Figure 5.5. PXRD of samples 0 h (red line), 6h (black line) and 1 month (blue line). For comparison we added simulations of calcite (pink line, ICDD PDF: 98-007-9674) and vaterite (green line; ICDD PDF: 98-002-7827). Pink, green and red asterisks sit at characteristic peaks of calcite, vaterite and “unknown” phases, respectively.....	161
Figure 5.6. FTIR spectra of the a) CaCl_2 , Na_2CO_3 , PVSA precursors, and the calcium carbonate particles (CaCO_3 cores) in the presence of PVSA (50 μM). b) Zoomed area of FTIR spectra of the CaCO_3 cores at $\approx 600\text{-}1200\text{ cm}^{-1}$, showing characteristics carbonate vibrational bands of vaterite.....	162
Figure 5.7. Examples of correlation between concentration c_M (as determined by the Bradford assay in case of dye-labeled proteins, or as prepared in the case of dextran-RBITC) and fluorescence counts $I (\times 10^4)$. Linear fits (LF) in each case were used to calculate unknown concentrations c_M of rtPA-FITC, BSA-FITC, or dextran-RBITC, from fluorescence readings.....	163
Figure 5.8. Schematic representation of the synthesis of the macromolecule loaded CaCO_3 particles.....	164
Figure 5.9. a) SEM micrograph of core@BSA particles (scale bar is 1000 nm) (SE2, 10kV). b) Size histogram ($d_{\text{C@BSA}}$: mean diameter of core@BSA) obtained after measuring the diameter of 300 core@BSA particles using ImageJ; $d_{\text{C@BSA}} = 617 \pm 80\text{ nm}$. c) SEM micrograph of core@rtPA particles (scale bar is 2000 nm) (SE2, 3kV). b) Size histogram ($d_{\text{C@rtPA}}$: mean diameter of core@rtPA) obtained after measuring the diameter of over 300 core@rtPA particles using ImageJ; $d_{\text{C@rtPA}} = 651 \pm 76\text{ nm}$. In a,b) samples after drop casting on Si substrates are shown.....	165
Figure 5.10. Schematic illustration of the description of the layers in the NCs used in this work.....	166
Figure 5.11. a) TEM micrograph of ioNPs; b) Size histogram obtained with ImageJ software after measuring the core diameter of 300 ioNPs. Scale bar corresponds to 50 nm.....	167
Figure 5.12. Schematic representation of the LbL process starting with A) CaCO_3 cores loaded with macromolecules (core@cargo), which after coating with 2 bL of PSS/PDADMAC, ioNPs and an outermost gelatin-based bL (gelatin), and “EDTA-dissolution” of the CaCO_3 matrix, yield NCs loaded with macromolecules (NC@cargo). Arrows and numbers represent the different synthetic steps, including purification of the colloids by centrifugation. b) Schematic representation of LbL steps (layers of PSS or PDADMAC or ioNPs or gelatin): from cores to NCs.....	169

Figure 5.13. Low and high magnification SEM micrographs of LbL assembled polymer hollow capsules generated from CaCO ₃ template: a-f) hollow capsules containing 6 layers (poly-L-arginine/dextran sulfate/poly-L-arginine/AuNRs/poly-L-arginine/miRNA) (0.5M NaCl, poly-L-arginine at 1mg/mL, dextran sulfate at 2mg/mL) (a, b, c: InLens, 3kV, d: SE2, 3kV, e, f: InLens, 3kV).....	170
Figure 5.14. BSA encapsulation stability after LbL in CaCO ₃ cores (without “dissolving” the CaCO ₃ core matrix) or NCs (that is, the core dissolved), both nanosystems with increasing bL configurations: a) 2 bL, b) 4 bL and c) 6 bL for one week in PBS; Core or NC refer to the precipitated sample, and SN refers to the supernatant. All data represent mean \pm s.d. (three independent measurements). In all data, statistical significance was assessed by the <i>t</i> -test: each sample was compared with the basal level at 0 h (ns, not significant; * <i>P</i> < 0.05; ** <i>P</i> < 0.01; *** <i>P</i> < 0.001). d) Shell composition information: PS: PSS, PD: PDADMAC and ioNPs: iron nanoparticles; for example, 2bL: PSS/PDADMAC/ioNPs/PDADMAC/PSS.....	172
Figure 5.15. a) rtPA encapsulation stability in cores (without “dissolving” the CaCO ₃ matrix) or NCs (that’s is, with dissolved cores) for one week in PBS. Core or NC refer to the precipitated sample, and SN refers to the supernatant. All data represent mean \pm s.d. (three independent measurements). In all data, statistical significance was assessed by the <i>t</i> -test: each sample was compared with the basal level at 0 h (ns, not significant; * <i>P</i> < 0.05; ** <i>P</i> < 0.01; *** <i>P</i> < 0.001). b) Shell composition information: PS: PSS, PD: PDADMAC, ioNPs: iron nanoparticles and G: gelatin.....	173
Figure 5.16. Mean values of ζ -potential (blue colored square symbols) and hydrodynamic diameter (green colored square symbols) evolution after each layer deposition of rtPA-loaded NCs.....	174
Figure 5.17. a) SEM micrograph of NC@BSA particles (scale bar is 1000 nm) (InLens, 10kV). b) Size histogram ($d_{\text{NC@BSA}}$: mean diameter of NC@BSA) obtained after measuring the diameter of over 300 NC@BSA particles using ImageJ; $d_{\text{NC@BSA}} = 735 \pm 130$ nm. c) SEM micrograph of NC@rtPA particles without the outermost gelatin layer (scale bar is 1000 nm) (SE2, 3kV). d) Size histogram ($d_{\text{NC@rtPA}}$: mean diameter of NC@rtPA without the gelatin layer) obtained after measuring the diameter of over 150 NC@rtPA particles (no gelatin) using ImageJ; $d_{\text{NC@rtPA}} = 549 \pm 88$ nm. e) SEM micrographs of NC@rtPA particles with the outermost gelatin layer (SE2, 3kV). f) Size histogram ($d_{\text{NC@rg}}$: mean diameter of NC@rtPA+gelatin with the outermost gelatin layer) obtained after measuring the diameter of over 100 NC@rtPA+gelatin particles using ImageJ; $d_{\text{NC@rg}} = 780 \pm 210$ nm. g-h) High magnification SEM micrographs of NC@rtPA+gelatin particles with the outermost gelatin layer, ioNPs are distinguishable as bright dots in	176

the polymer shell of collapsed NCs (SE2, 3kV).....

Figure 5.18. NCs dispersion analysis by flow cytometry. The variation of the flow cytometry SSC and the fluorescence signal as a function of the fluorescently-labeled encapsulated molecules are shown. a) Scatter density plots of SSC signal versus FSC signal for different NCs with diverse cargos: rtPA (red) and BSA (blue). b) Scatter density plots of SSC signal versus fluorescence signal (from the corresponding channel, 512/18 nm for FITC for the NCs with the different cargos: rtPA (red), and BSA (blue). c) Scatter density plots of SSC signal versus fluorescence signal (from the corresponding channel, 512/18 nm for FITC for the non-fluorescent NCs. d) Representative histograms of side scattering distributions of different loaded-NCs samples (rtPA and BSA). e) Representative histograms of MFI from the different channels (512/18 nm for FITC) associated with the encapsulated cargo.....

Figure 5.19. a) Scheme of the bioactivity assay (upon binding of the chromogenic substrate, rtPA releases p-nitroalanine - pNA) to determine the rtPA amidolytic activity upon set-up: US were applied to the NCs in Eppendorf tubes.....

Figure 5.20. PAI-1 inhibition assay results of selected samples of free rtPA (rtPA-FITC) and encapsulated rtPA (NC@rtPA). All data represent mean \pm s.d. (three independent measurements). In all data statistical significance was assessed by the t-test: each sample was compared with Alteplase.....

Figure 5.21. a) NC@BSA with two, four and six bL (2bL, 4bL and 6bL), and exposed to US for 120 min (720 mW/cm², 2 MHz, 120-min). b) Fluorescence-quantified (Intensity, %) US-triggered delivery into the supernatant of BSA or rtPA for NC with different number of bL after 15 min of US application (720 mW/cm², 2 MHz). In all data, statistical significance was assessed by the *t*-test: each sample was compared with the corresponding sample without US (ns, not significant; **P* < 0.05; ***P* < 0.01; ****P* < 0.001).....

Figure 5.22. Enzymatic activity of rtPA released from NC@rtPA particles quantified in the supernatant by the fluorogenic assay SensoLyte® upon US application. In all data, statistical significance was assessed by the *t*-test: each sample was compared with the corresponding sample without US (ns, not significant; **P* < 0.05; ***P* < 0.01; ****P* < 0.001).....

Figure 5.23. Clots assay: a) Calibration curve of clot dissolution using increasing free rtPA concentrations. b) Absorption at 520 nm, A₅₂₀, after addition to the clots of: saline, free rtPA (1 µg/mL), NC@rtPA particles

with encapsulated rtPA (1 $\mu\text{g/mL}$) in the presence and absence of US, and non-loaded NC in the presence and absence of US (absorbance A_{520} measurements illustrate the ability of the different samples to dissolve the clots). All data represent mean \pm s.d. (three independent measurements). In all data, statistical significance was assessed by the *t*-test: each sample was compared with the saline group (ns, not significant; * $P < 0.05$; ** $P < 0.01$; *** $P < 0.001$).....

Figure 5.24. Schematic Illustration of the characterization of NCs before and after US treatment. US were applied to the NCs in Eppendorf tubes... **185**

Figure 5.25. NCs dispersion analysis after US treatment by flow cytometry. The variation of the FCS and the SSC signals of the NC and SN as a function of the US application are shown. a) Scatter density plots of FSC signal versus SSC signal, and SSC signal versus fluorescence signal (corresponding to the 512/18 nm channel for control NCs with rtPA in the supernatant. b) Scatter density plots of FSC signal versus SSC signal, and SSC signal fluorescence signal (corresponding to the 512/18 nm channel for control NCs with rtPA in the supernatant after US treatment. This assay confirms the US-triggered release of rtPA by fluorescence increases in the supernatant of NC after US treatment..... **186**

Figure 5.26. a) *In vivo* scheme to evaluate the rtPA encapsulation and the US drug release. b) Blood rtPA activity was determined in the 5 groups tested ($n = 3$), before treatment administration (blood rtPA basal levels), and 5, 15 and 40 min later on. All data represent mean \pm s.d. Statistical significance was assessed by two-way analysis of variance followed by Dunnett's multiple comparisons test. In b), each treatment time (5, 15 or 40 min) was compared with rtPA levels in the saline group; in c) each treatment was compared with the corresponding rtPA basal levels (ns, not significant; * $P < 0.05$; ** $P < 0.01$; *** $P < 0.001$; **** $P < 0.0001$)..... **187**

Figure 6.1. Cell viability using the resazurin assay of HeLa cells (A) and A549 cells (B) under exposure to increasing concentrations of the particles before (NC-HOE) and after PMA-functionalization (NC-HOE-PMA), and evaluated at two incubation times: 4 h (1) and 24 h (2). Half-maximal responses (EC_{50} values) were calculated by fitting (logistic function in OriginLab, fixing minimum viability to 0 %)...... **192**

Figure 6.2. Left: Schematic representation of the NIR irradiation set-up used to activate HOE-release from the NC-HOE-PMA particles inside living cells; middle: beam diameter; right: actual image of the collimation/zoom system..... **193**

Figure 6.3. Collage of confocal microscopy images (top-left: blue channel; top-right: bright field; bottom-left: orange channel; bottom-right: merged blue + orange) at different magnifications (A,B: 20X; C,D: 60X; E,F: 100X) **195**

for the NC-HOE nanosystem.....	
Figure 6.4. Collage of confocal microscopy images (top-left: blue channel; top-right: bright field; bottom-left: orange channel; bottom-right: merged blue + orange) at different magnifications (A,B: 20X; C,D: 60X; E,F: 100X) for the NC-HOE-PMA nanosystem.....	196
Figure 6.5. Collage of confocal microscopy images (top-left: blue channel; top-right: bright field; bottom-left: orange channel; bottom-right: merged blue + orange) at 60X magnification for the NC-HOE-PMA nanosystem after NIR treatment.....	197
Figure 6.6. GOT and GPT levels in mice. In all data statistical significance was assessed by the <i>t</i> -test; each sample was compared with the corresponding basal level (ns, not significant; * <i>P</i> < 0.05; ** <i>P</i> < 0.01).....	199
Figure 6.7. ICP-MS NCs Fe organ biodistribution in a) animals sacrificed 40 min after treatments or b) animals sacrificed 7 d after the treatments. ICP-MS data expressed as percentage of the injected dose (%ID) per organ in c) animals sacrificed 40 min after treatments or d) animals sacrificed 7 d after the treatments. Please, note that in c) and d) even for the animals not treated with Fe-containing samples data has been corrected considering the injected Fe (Fe _i) dose (128 µg) in order to show the endogenous Fe content. All data represent mean ± s.d. (three independent measurements). In all data statistical significance was assessed by the <i>t</i> -test, each sample was compared with the corresponding saline control (ns, not significant; * <i>P</i> < 0.05; ** <i>P</i> < 0.01).....	201
Figure 6.8. MRI image of a mouse's brain after NCs@rtPA i.v. injection at different times, left panel shows T2 MRI signal and right panel, T2* signal.....	202
Figure 6.9. MRI image of a mouse brain after NCs@rtPA and saline intraparenchymal injection. a,c) The MRI signal in T2 decreased 65.87 % in the right hemisphere, where the NCs@rtPA particles had been injected, in comparison with the left hemisphere, where the control (saline) was injected. b, d) In T2* the NCs MRI signal decreased 79.33 % compared with control signal. In all data statistical significance was assessed by the <i>t</i> -test, each sample was compared with the corresponding saline control (* <i>P</i> < 0.05; *** <i>P</i> < 0.001).....	203
Figure 6.10. a) <i>In vivo</i> scheme to evaluate the rtPA encapsulation and the US drug release. Treatments were administered through the femoral vein, and blood samples were further obtained from the carotid artery. This approach allowed to analyze the <i>in vivo</i> stability of the rtPA-encapsulation	205

and to evaluate the US-induced drug release. b, c) Blood rtPA activity was determined in the 5 groups tested ($n = 3$), before treatment administration (blood rtPA basal levels), and 5, 15 and 40 min later. All data represent mean \pm s.d. Statistical significance was assessed by two-way analysis of variance followed by Dunnett's multiple comparisons test. In b), each treatment time (5, 15 or 40 min) was compared with rtPA levels in the saline group; in c) each treatment was compared with the corresponding rtPA basal levels (ns, not significant; $*P < 0.05$; $**P < 0.01$; $***P < 0.001$; $****P < 0.0001$).....





LIST OF TABLES

Table	Page
Table 1.1. Type of nanomaterials.....	53
Table 1.2. Properties/characteristics to be determined for nanoparticles, and some of the corresponding characterization techniques.....	57
Table 3.1. $\text{CuCl}_2 \cdot 2\text{H}_2\text{O}$ concentrations and molar ratios used to produce different nanocomposites.....	92
Table 3.2. Peaks identified in NP1, NP2 and NP3 diffractograms, respectively.....	101
Table 3.3. EPR parameters of the X-band spectra of frozen solutions (120 K) of the three types of particles.....	103
Table 3.4. Comparison of copper concentration determination by two methods: colorimetric and ICP-MS.....	114
Table 3.5. Summary of the kinetic constant values k [s^{-1}] for the selected samples (equal Cu mass – 1.9 ng) and control (without Cu). A first-order catalytic behavior was considered, <i>i.e.</i> , $\text{Ln}(A/A_0) = -k \cdot t$, for the initial 22 s of the reaction.....	114
Table 4.1. Composition, structure, and network parameters of some ZIF series of compounds (ZIF-1 to 10 and ZIF-60 to 75).....	120
Table 4.2. Hydrodynamic diameters d_h (mean value \pm standard deviation SD) as derived from DLS measurements of ZIF-8 and ZIF-67 particles using different CTAB concentrations.....	125
Table 4.3. Hydrodynamic diameters d_h (mean value \pm standard deviation SD) as derived from DLS measurements for ZIF-8 particles dispersed in methanol, water, or in cell medium at different time points, and for ZIF-67 particles dispersed in methanol or water at different time points.....	127
Table 4.4. Hydrodynamic diameters, d_h , (mean value \pm standard deviation SD) as derived from DLS measurements of NC-HOE and NC-HOE-PMA. The polydispersity index (PDI) for each sample is also given. Data correspond to the raw ones shown in <i>Figure 4.13</i>	136
Table 4.5. Hydrodynamic diameters, d_h , (mean value \pm SD) as derived from DLS of nanocomposite particles before (NC) and after PMA-functionalization (NC-PMA), and dispersed in water or in cell culture medium at different time points. SD values correspond to the standard deviation of the diameter mean value as obtained from several repeats (n=3).....	139

Table 4.6. Major peaks: (relative intensity > 6%) identified in the ZIF-8 diffractogram, (relative intensity > 6%) identified in the NC diffractogram, and (relative intensity > 9%) identified in the NC-PMA diffractogram, respectively.....	141
Table 4.7. Organic and inorganic weight percentage (wt %) derived from TGA measurements in selected samples, and estimated % wt of Au, HOE and PMA.....	144
Table 4.8. Data extracted from the N ₂ isotherms analysis.....	148
Table 5.1. PVSA concentrations to produce different particles.....	158
Table 5.2. Mean average hydrodynamic diameters and ζ -potential values of CaCO ₃ particles at different PVSA concentrations.....	159
Table 5.3. Assignment of FTIR absorption bands of vaterite, calcite and aragonite.....	161
Table 5.4. Mean average hydrodynamic diameters and ζ -potential of nanocores.....	166
Table 5.5. Fluorescence data expressed in % corresponding to loading/leakage of macromolecules encapsulated in NCs.....	171
Table 5.6. Fluorescence data expressed in % corresponding to loading/leakage of macromolecules encapsulated in NCs.....	173
Table 5.7. Mean average hydrodynamic diameters and ζ -potential of nanocores and NCs.....	175
Table 5.8. Number of macromolecules encapsulated per NCs for different NC@rtPA batches.....	178
Table 5.9. Raw absorbance data and corresponding % values obtained for the chromogenic rtPA substrate. Free Alteplase was used as reference (100 %)......	180
Table 5.10. Raw absorbance data and the corresponding % values obtained for the chromogenic rtPA substrate and PAI-1.....	181
Table 5.11. Fluorescence quantification of US-induced cargo release from NC@BSA (2-, 4- and 6-bL) and NC@rtPA particles (three independent experiments using different NC@rtPA concentrations).....	182
Table 5.12. Sensolyte activity assay performed in NC@rtPA particles in the supernatant (SN) and precipitate (cargo) after 15 min of US.....	183
Table 5.13. Clots assay data.....	184
Table 6.1. Hepatotoxicity and nephrotoxicity markers: GOT, GPT, and creatinine levels.....	199



LIST OF ACRONYMS AND ABBREVIATIONS

Au	Gold	kDa	kilodaltons
°C	Celsius	M	Molar concentration
Ca²⁺	Calcium ions	μL	microliter
CaCl₂	Calcium chloride	μM	micromolar
CaCl₂·2H₂O	Calcium chloride dihydrate	min	minutes
CaCO₃	calcium carbonate	MeOH	methanol
cf.	confer/compare	mg / mL	milligram per milliliter
cm	centimeter	mL	milliliter
cm²	square centimeter	mM	milimolar
Co	Cobalt	Na₂CO₃	Sodium carbonate
Co(NO₃)₂ · 6H₂O	Cobaltous nitrate hexahydrate	NaHCO₃	Sodium bicarbonate
Cu	Copper	NIR	Near InfraRed
Da	Dalton	nM	nanomolar
e.g.	for example	rcf	relative centrifugal force
FITC	Fluorescein isothiocyanate	rpm	revolutions per minute
g / mol	gram per mol	UV	Ultraviolet
g	gram	XRD	X-ray powder diffraction
H₂O	water	ζ	Zeta
hrs	hours	Zn	Zinc
i.e.	that is	Zn(NO₃)₂ · 6H₂O	Zinc nitrate hexahydrate
K	Kelvin	ZnO	Zinc oxide



LIST OF PUBLICATIONS

This thesis work has led to the following publications:

1. **María F. Navarro Poupard**, Ester Polo, Pablo Taboada, Ana Arenas-Vivo, Patricia Horcajada, Beatriz Pelaz, and Pablo del Pino. *Aqueous Synthesis of Copper (II)-Imidazolate Nanoparticles*. Inorganic Chemistry, 57(19): p. 12056-12065 (2018).

Author's thesis main contributions to this study are explicitly indicated below:

Experimental: synthesis and characterization of the nanoparticles

Manuscript: preparation of the paper, specifically writing the initial draft (results and methods)

Note: porosity characterization was performed by collaborators (IMDEA Energy)

2. Ester Polo, **María. F. Navarro Poupard**, Luca Guerrini, Pablo Taboada, Beatriz Pelaz, Ramón A. Alvarez-Puebla and Pablo del Pino. *Colloidal bioplasmonics*. Nano Today, 20: p. 58-73 (2018).

Author's thesis main contributions to this review article are explicitly indicated below:

Manuscript: preparation of the review paper, specifically writing the initial draft (methods) and literature overview.

3. Carolina Carrillo-Carrión, Raquel Martínez, **María F. Navarro Poupard**, Beatriz Pelaz, Ester Polo, Ana Arenas-Vivo, Alessandro Olgiati, Pablo Taboada, Mahmoud G. Soliman, Úrsula Catalán, Sara Fernández-Castillejo, Rosa Solà, Wolfgang J. Parak, Patricia Horcajada, Ramon A. Alvarez-Puebla, and Pablo del Pino. *Aqueous Stable Gold Nanostar/ZIF-8 Nanocomposites for Light Triggered Release of Active Cargo Inside Living Cells*. Angewandte Chemie International Edition, 58(21): p. 7078-7082 (2019).

Author's thesis main contributions to this study are explicitly indicated below:

Experimental: synthesis and characterization of the nanocomposites

Manuscript: preparation of the paper, specifically writing the initial draft (results and methods)

Note: The entire experimental work involving cells were part of the PhD thesis of Raquel Martínez González (Completed). Raman spectroscopy and porosity characterization were carried out by collaborators.

4. Clara Correa-Paz, **María F. Navarro Poupard**, Ester Polo, Manuel Rodríguez-Pérez, Pablo Taboada, Ramón Iglesias-Rey, Pablo Hervella, Tomás Sobrino, Denis Vivien, José Castillo, Pablo del Pino, Francisco Campos and Beatriz Pelaz. *In vivo ultrasound-activated delivery of recombinant tissue plasminogen activator from the cavity of sub-micrometric capsules*. Journal of Controlled Release, 308: p. 162-171 (2019).

Author's thesis main contributions to this study are explicitly indicated below:

Experimental: synthesis and characterization of the nanocomposites

Manuscript: preparation of the paper, specifically writing the initial draft (results and methods)

Note: Ultrasound triggered release characterization and the entire experimental work in vitro and in vivo were part of the PhD thesis of Clara Correa Paz (Completed).

5. Raquel Martínez, **María. F. Navarro Poupard**, Aitor Álvarez, Enrica Soprano, Martina Migliavacca, Carolina Carrillo-Carrión, Ester Polo, Beatriz Pelaz and Pablo del Pino. *Nanoparticle behavior and stability in biological environments (Chapter 2)*. Nanoparticles for Biomedical Applications (Micro and Nano Technologies, Elsevier), ISBN 9780128166628: p. 5-18 (2020).

Author's thesis main contributions to this study are explicitly indicated below:

Manuscript: preparation of the book chapter, specifically writing the initial draft (methods) and literature overview.



AGRADECIMIENTOS

Agradezco a mis directores de Tesis, los doctores Pablo Taboada y Pablo del Pino, por haberme dado la oportunidad de realizar mi doctorado en el grupo de investigación y así como también por sus consejos, sabiduría y correcciones durante las diferentes etapas de este trabajo.

De manera muy especial y sincera quiero agradecer a la Dra. Beatriz Pelaz (Bea) quien con su apoyo, experiencia, conocimiento, paciencia y motivación a lo largo de este proceso permitió el desarrollo con éxito de este trabajo de investigación. Muchas veces gracias.

También me gustaría agradecer a la Dra. Ester Polo (Madame Ester) por la paciencia infinita que tiene al compartir su conocimiento en cualquier momento.

Mis agradecimientos también para las doctoras Raquel Martínez por los experimentos en células y Clara Correa del LINC (Laboratorio de Investigación en Neurociencias Clínicas) por los experimentos in vivo, así como para todos los colaboradores que hicieron posible el desarrollo de este proyecto de investigación.

Quiero también agradecer a todo el personal de la Unidad de Microscopia de RIAIDT por el análisis microscópico de las muestras que aparecen a lo largo de este trabajo.

De igual manera, gracias a la Universidad de Santiago de Compostela y al CIQUS (Centro Singular de Investigación en Química Biológica y Materiales Moleculares) por haberme brindado un espacio adecuado para el desarrollo de esta investigación, y por ende la culminación exitosa de mis estudios doctorales.

También quisiera agradecer a los miembros del Lab. de Física de Coloides y Polímeros (GFCP) y del Departamento de Física por su colaboración y apoyo: la Dra. Silvia, el Dr. Gerardo, el Dr. Alberto, Javier (Joven Clásico), Brenda (la Perdida), Valeria, Lilia y Victoria.

Así como también me gustaría agradecer en estas líneas, las risas, el apoyo y el tiempo que amigos y colegas del Lab. Bionanotools me han brindado de manera desinteresada durante el proceso de aprendizaje a lo largo del desarrollo de mi tesis doctoral: Aitor (o Juez Aitor), Dra. Clari (Team Nanocapsules), Enrica (Beetch No. 3), Dra. Polo (Beetch No.1 y Running partner), Manuel (o Manolito), Manuela (o Manu, Team Polymer Coating y Pesce), Marta (Tiramisú para tres), Marti (Fiesta loca), Raqui (Chica Quidditch), Mario y Alonso (Generación Alfa), Heidi (Umpa o La Marquesa), el Señor Nano (Amigo de todos) y Lala (La Duquesa), así como

a los que se han integrado recientemente, Manuel (el Chico de los dulces) y Antía (Thank you, next).

Y, por supuesto, mi más profundo agradecimiento, va para mi familia, mi abuelita, mis hermanos Jorge, Lalo e Ivonne, Sommer, Vale, y en especial a mi Mamá, a todos ellos gracias por su inspiración, ejemplo, motivación y apoyo a lo largo de todo este proceso.

Finalmente, quiero agradecer al Consejo Nacional de Ciencia y Tecnología (Conacyt) del Gobierno de México por hacer posible que realizará mis estudios doctorales en la Universidad de Santiago de Compostela con la financiación en toda mi etapa de doctorado mediante la concesión de la beca “Becas Conacyt Al Extranjero 2016-2020, Convocatoria 291060, CVU. 544612





RESUMO

O interese nas “cousas” nano expandiuse a unha grande variedade de diferentes ámbitos tales como a enerxía, tecnoloxía espacial, tecnoloxía informática, seguridade de alimentos, industria e biomedicina xa que cando a materia está organizada a nivel nanoscópico as propiedades do (nano)material difiren das da súa contraparte masiva. Istos sucede pois os efectos do tamaño e as interfaces inflúen fortemente no comportamento e as propiedades daquel. Nestas pequenas dimensións, na escala de nanómetros e onde o comportamento cuántico dos átomos vólvese importante, os materiais adquiren novas propiedades físicas e permiten así, o xurdimento dunha nova ciencia e potenciais novas aplicacións, que actualmente se coñece como a Nanotecnoloxía. Por isto, as propiedades física e químicas únicas dos materiais que ocorren naturalmente na nanoescala ofrecen aos científicos un camiño para utilizar eficazmente as devanditas propiedades para en novas aplicacións potenciais en todos os campos da ciencia.

Os materiais porosos con poros abertos ofrecen propiedades atractivas como unha rede de poros de baixa densidade, uniforme e modificable, e unha gran superficie e alta porosidad. Deste xeito, a fabricación de materiais nanoestructurados porosos está a atraer un interese crecente nunha ampla gama de aplicacións potenciais como, por exemplo, en catálise química, separación selectiva de proteínas por sorción, procesos de arrefriado, ou no eido da encapsulación e liberación controlada de fármacos, entre outros.

Esta tese doutoral está organizada en seis diferentes capítulos. O Capítulo 1 está dividido en cinco partes. As primeiras catro tentan proporcionar ao lector unha imaxe detallada dos conceptos básicos sobre os nanomateriais e as nanopartículas; a súa clasificación e organización; as metodoloxías para a súa síntese (“bottom- up” e “top- down”); o control do seu crecemento durante o proceso de síntese; potenciais métodos de funcionalización de nanomateriais/nanopartículas, en particular, empregando un polímero anfifílico para revestir e estabilizar nanopartículas orixinalmente hidrófobas en disolucións acuosas, ou unha metodoloxía de ensamblaxe de capa por capa (LbL “layer-by-layer”, das súas siglas en inglés). Tamén se comentarán as diferentes propiedades que se poden determinar e analizar a partir de diferentes técnicas experimentais de caracterización de nanomateriais e nanopartículas, o cal representa un paso importante para entender o comportamento do nanomaterial/nanopartícula e, así, poder explorar a súa potencial aplicación no mundo real.

Este traballo centrarase en varias clases de nanopartículas: nanopartículas plasmónicas, nanopartículas inorgánicas, nanopartículas inorgánicas-orgánicas porosas, así como tamén a combinación delas para deseñar as chamadas nanoestructuras porosas corazón@corona. O interese nas nanopartículas plasmónicas reside nas súas extraordinarias propiedades ópticas, xa que son capaces de absorber e dispersar a luz en rexións altamente específicas do espectro electromagnético (EM) con altos coeficientes de extinción molar (é dicir, varias ordes de magnitude máis altas que os fluoróforos orgánicos), polo que poder ser empregadas como axentes terapéuticos, de diagnóstico ou teragnósticos. Doutra banda, estudaríanse as nanopartículas porosas, xa que a súa porosidade dota á nanopartícula cun increment extraordinario na súa relación superficie-volume comparada con nanopartículas non-porosas de

similares dimensións. As nanopartículas porosas considéranse sumamente relevantes nos eidos da cromatografía, catálise, procesos de separación selectiva, administración de medicamento, etc.

Unha das potenciais aplicacións destes tipos de nanopartículas que abordaremos será a catálise química, a cal está moi presente en diversos procesos industriais, enerxéticos, medioambientais, e biolóxicos. Ademais, e xa como se mencionou anteriormente, as nanopartículas e nanomateriais teñen un grande abano de aplicacións no campo biomédico, e en especial, no eido da liberación controlada de fármacos. A este respecto, e de grande interese a posibilidade de que a carga bioactiva farmacolóxica poda ser liberada mediante estímulos internos (é dicir, endóxenos) ou externos (é dicir, exógenos). Neste traballo enfocáremos en dous estímulos en concreto: liberación dunha molécula por interacción dunha nanopartícula plasmónica con luz no infravermello cercano, e a liberación por medio de ultrasóns. Nembargantes, debe de terse en conta que o comportamento e a estabilidade das nanopartículas e nanomateriais na contorna biolóxica, e polo tanto, a súa capacidade de liberación das substancias bioactivas encapsuladas e de localización/direccionamento para exercer a súa actividade farmacolóxica vense influenciadas por diferentes factores tales como a coroa de proteínas que se pode formar ao redor da nanopartícula ou nanomaterial, a súa funcionalización, e as biointeraccións da superficie das nanopartículas co medio biolóxico que as rodea.

Finalmente, a quinta parte do Capítulo 1 constitúe a descrición dos obxectivos da presente tese de doutoramento, tendo como finalidade indicar os desafíos abordados no presente traballo na manipulación controlada e aplicación dirixida de materiais porosos na nanoescala. En particular, os intereses de investigación deste traballo céntranse na síntese coloidal controlada e a funcionalización de dous materiais porosos específicos baseados en polímeros de coordinación porosos (PCP, siglas en inglés) e nanopartículas poliméricas de carbonato de calcio (CCPN, das súas siglas en inglés), respectivamente, como nanotransportadores destinados a aplicacións biolóxicas e catalíticas.

Os enfoques de optimización de síntese para cada tipo de nanomaterial seguiron un esquema básico común como a introdución de aditivos ou axentes bloqueadores do crecemento durante a síntese química como estratexia elixida para controlar o proceso de nucleación e crecemento co obxectivo de lograr a morfoloxía e o tamaño de nanopartícula desexado. Este enfoque veu acompañado da adecuada caracterización e funcionalización destes nanopartículas para asegurar a súa estabilidade coloidal e finalmente demostrar as súas propiedades física e químicas de utilidade e dirixidas á aplicación en cuestión.

Para lograr o control preciso tanto do tamaño como da morfoloxía dos nanopolímeros coordinados (nanopartículas) porosos propuxéronse moitas estratexias sintéticas químicas e de microfabricación que inclúen roteiros solvotermales modificados (por exemplo, axentes moduladores, modificación de ligandos), métodos asistidos por microondas e ultrasóns, microemulsións, mecano-química ou fluídica. Con todo, moitos destes enfoques adoecen dun control deficiente da distribución do tamaño de partícula e da súa morfoloxía, así como de baixos rendementos de reacción.

Como consecuencia, os enfoques presentados nos Capítulos 2, 3, 4 e 5 deste traballo documentan métodos sinxelos que permiten controlar a morfoloxía e funcionalización dos nanomateriais desexados (é dicir, polímeros coordinados de Cu, ZIF-8 (Zn), e CCNP) con alta monodispersidade, dando lugar a nanopartículas porosas de morfoloxía e tamaño adecuados para aplicacións potenciais como a redución catalítica de azul de metileno, e para o control e entrega controlada e dirixida de compostos bioactivos, respectivamente.

Así, o Capítulo 2 describe os materiais e as metodoloxías utilizadas nos Capítulos 3, 4 e 5 para obter, caracterizar e testar as nanopartículas obtidas.

O Capítulo 3 mostra a fabricación de novas nanopartículas de polímeros de coordinación porosos compostas de Cu^{2+} e imidazolato utilizando un sinxelo enfoque sintético ascendente “bottom-up”. Os polímeros de coordinación (CP, siglas en inglés) son compostos poliméricos unidimensionais, bidimensionais ou tridimensionais (1D, 2D ou 3D) formados por entidades de coordinación repetidas (é dicir, inorgánicas, orgánicas ou híbridas inorgánico-orgánicas). Existen varias subclases de CP, incluídas as CP amorfas, os polímeros de coordinación porosos (PCP), os materiais órgano-metálicos (MOM, das súas siglas en inglés), as estruturas órgano-metálicas (MOF, das súas siglas en inglés), as redes de coordinación, etc.

Os PCP están formados por centros de catións, ou grupos, interconectados por ligandos orgánicos polidentados a través de fortes ligazóns iónico-covalentes, sendo xeralmente moi porosos e con densidades moi baixas. Unha característica interesante dos PCP é que mediante a combinación de ións e ligandos metálicos pódense producir estruturas con forma, tamaño de poro específico, funcionalidade de superficie, e propiedades de complexo metálico. Deste xeito, ata hoxe en día reportáronse máis de 20.000 estruturas de PCP con diversas características (tamaño de cristal, porosidade, xeometría e funcionalidade) que xorden como consecuencia das múltiples combinacións posibles de centros metálicos e ligandos orgánicos existentes.

Por outra banda, están os nanoPCP (que se denominan tamén como cristais de PCP), que teñen todas as súas dimensións laterais dentro do rango de tamaños de 1 a 500 nm, aínda que calquera PCP pode considerarse nanoestruturado debido á rede de baleiros nanométricos que posúen na súa estrutura. De cara a súa obtención, existen moi poucos protocolos para preparar nanoPCP monodispersos en comparación con aqueles para fabricar a súa contraparte masiva, a pesares de que se propuxeron moitas estratexias sintéticas químicas e de microfabricación para o lograr o control preciso tanto do seu tamaño como da súa morfoloxía, os cales carecen dun control eficiente da distribución do tamaño de partícula e da morfoloxía, así como de baixos rendementos de reacción. Neste traballo verificouse que o uso de surfactantes durante a síntese deste tipo de nanopartículas pode modificar o tamaño e morfoloxía destas.

Por tanto, como primeira aproximación neste Capítulo 3, e por medio do método sintético “bottom-up”, optimizáronse as concentracións e relacións molares dos elementos precursores dun nanoPCP baseado en cobre [é dicir, CuCl_2 , 2- metilimidazol (2MI) e bromuro de hexadeciltrimetilamonio (CTAB, siglas en inglés)] para producir nanopartículas porosas monodispersas. Estes nanoPCP baseados en Cu^{2+} teñen especial interese debido á súa abundancia natural, baixo custo e propiedades catalíticas e condutoras. Os datos experimentais indicaron que a adición do CTAB, o tempo de reacción e o disolvente final determinaron o

tamaño, morfoloxía e estrutura das distintas nanopartículas obtidas. Ademais, analizouse a estabilidade coloidal das mesmas, e os cambios morfolóxicos e a súa integridade estrutural e química en varios disolventes con diferentes polaridades. Como resultado, seleccionáronse tres tipos de nanopartículas para a súa caracterizacións, determinándose as propiedades fisicoquímicas básicas, como o tamaño, a actividade óptica e magnética, a porosidade, a estabilidade térmica, a estrutura, o envellecemento e, finalmente, a súa actividade catalítica na redución do azul de metileno.

No Capítulo 4, preséntase a preparación dun nanotransportador sensible á temperatura composto por nanopartículas plasmónicas sensibles á luz no infravermello próximo (NIR, das súas siglas en inglés) recubertas con estruturas órgano-metálicas (MOF), especificamente ZIF-8 (das súas siglas en inglés, zeolitic imidazolate framework-8), que é unha subclase de MOF que está composto por ións de zinc e aneis de imidazolato coordinados nunha estrutura de marco que dá como resultado unha topoloxía de sodalita (SOD). Como se mencionou anteriormente, os MOFs son unha subclase de CPs, que grazas a súa área de superficie alta, tamaño de poro axustable e amplas posibilidades de modificacións superficiais gañaron grande interese en aplicacións biomédicas, en especial os MOF sensibles a estímulos únicos ou múltiples para lograr unha liberación controlada do fármaco. A fabricación de nanoestruturas porosas corazón@corona mostran ser unha boa estratexia para promover e controlar a liberación dun fármaco baixo un estímulo externo específico.

Grazas a porosidade uniforme do ZIF e ás súas excelentes estabilidades químicas e térmicas, o ZIF-8 é un dos MOFs máis investigados para o seu uso como vehículo para a administración controlada de medicamentos. Isto permite xa ter un importante coñecemento sobre cómo controlar a súa xeración e crecemento, o que permite encapsular diferentes clases de materiais dentro del durante o proceso sintético, ou ben, posicionar moléculas na súa superficie para producir nanopartículas máis estables en disolucións acuosas. Así, o primeiro paso neste traballo foi o uso do surfactante CTAB para controlar a morfoloxía e o tamaño das nanopartículas de ZIF-8, demostrándose a súa influencia clave. Ademais, tamén se prepararon nanopartículas de ZIF-67 debido a que teñen similitudes co ZIF-8 na súa estrutura (sodalita) e ligandos orgánicos, permitindo unha comparación co ZIF-8 comparación nalgúñas análises tales como a influencia do surfactante no tamaño da nanopartícula ou a estabilidade coloidal en disolucións acuosas. Neste senso, observouse que as nanopartículas de ZIF-8 e ZIF-67 foron estables durante unha semana en metanol; nembargantes, as nanopartículas expostas a disolucións acuosas mostraron cambios nos seus tamaños, indicando a súa inestabilidade coloidal.

O seguinte paso neste capítulo foi a selección dunha nanoestrela de ouro como núcleo das nanopartículas porosas grazas á súa característica banda plasmónica centrada a ~ 770 nm, que é axeitada para a excitación dentro da xanela biolóxica terapéutica NIR-I. En canto á morfoloxía, as novas nanoestruturas porosas corazón@corona formadas mostraron unha morfoloxía poliédrica en comparación coas partículas de ZIF-8, as cales presentan unha morfoloxía cúbica.

Posteriormente, as nanoestruturas porosas corazón@corona desenvolvidas “cargáronse” con moléculas de bisbenzimidaz como elemento biofuncional. Como consecuencia da rápida diminución do tamaño dos MOFs de ZIF-8 tanto en auga como no medio celular, as nanoestruturas porosas corazón@corona desenvolvidas recubríronse cun copolímero anfifílico de poli (isobutileno-alt-anhídrido maleico) inxertado con-dodecilamina (PMA). Este polímero anfifílico protexe ao ZIF-8 da hidrólise acuosa e evita que o fármaco se filtre de forma non desexada no medio e/ou dentro das células vivas. Por último, a funcionalidade das nanopartículas foi probada en cultivos celulares, comprobándose que o mecanismo de liberación inducida do elemento bioactivo dependía de se a luz no infravermello próximo estaba axustada á absorción plasmónica do núcleo de nanostrela de ouro da nanopartícula. Como consecuencia, demostrouse que unha irradiación lumínica optimizada permitiu a creación de gradientes de temperatura locais para activar a termodifusión do fármaco, neste caso, as moléculas de bisbenzimidaz.

No Capítulo 5 mostrouse a fabricación de cápsulas submicrométricas sonosensibles, empregando como plantillas partículas de CaCO_3 , para a administración controlada de macromoléculas in vivo mediante a metodoloxía de ensamblaxe de capa por capa (LbL, das súas siglas en inglés) baixo a acción de ultrasóns aplicados. O método de ensamblaxe capa por capa permite encapsular diferentes tipos de moléculas, realizar o ensamblaxe con diferentes tipos de polímeros, así como tamén incorporar nanopartículas inorgánicas nas capas para proporcionar funcionalidades adicionais como, por exemplo capacidade de diagnóstico por imaxe mono/multimodal e/ou sensibilidade de resposta a estímulos internos e/ou externos.

Os estudos farmacolóxicos e biolóxicos realizados empregando cápsulas poliméricas derivadas de partículas de CaCO_3 ata hoxe en día como potenciais nanotransportadores de medicamentos inxectables in vivo utilizaron xeralmente partículas con tamaño micrométrico (tipicamente, con diámetros de 3 a 10 μm), o cal ten como consecuencia limitacións importantes como resultado do seu gran tamaño como, por exemplo, o seren opsonizadas e/ou secuestradas rapidamente dentro dos capilares dos pulmóns.

Por isto, neste traballo explorouse un enfoque orixinal para lograr a produción de nanocápsulas poliméricas (NC, das súas siglas en inglés) submicrométricas a partir de núcleos de partículas de CaCO_3 de aproximadamente 600 nm (ou mesmo menos) de diámetro. Para a obtención destas nanopartículas porosas, a metodoloxía de coprecipitación é o método máis común para a súa síntese mesturando, para iso, disolucións acuosas equimolares de CaCl_2 e Na_2CO_3 a temperatura ambiente. O carbonato cálcico ten tres polimorfos cristalinos anhidros, que inclúen a calcita, a aragonita e a vaterita. Neste caso, elixiuse a vaterita para a preparación de nanotransportadores para a administración controlada de fármacos grazas a súa grande porosidade e ampla área superficial, pero tamén debido a unha estabilidade moi baixa o que dá como resultado unha rápida desintegración en condicións relativamente suaves.

Por tanto, seleccionáronse partículas de vaterita de CaCO_3 (núcleos) como plantilla de núcleo de sacrificio temporal. Durante o seu crecemento, é dicir, durante a síntese, empregouse o polímero poli (ácido vinil sulfónico, PVSA, das súas siglas en inglés) como axente controlador da formación, crecemento e estabilizante dos núcleos de vaterita formados

inicialmente, atrasando a súa transformación no polimorfo calcita. Así, tamén se avaliou o efecto da concentración do PVSA no tamaño e estrutura das partículas de CaCO_3 , observándose que cando a concentración de PVSA engadida durante a síntese vai incrementándose o tamaño das nanopartículas de CaCO_3 decrece. En ausencia de PVSA, as partículas mostraron unha morfoloxía cúbica asociada coa calcita.

A continuación procedeuse a realizar a encapsulación de tres macromoléculas marcadas fluorescentemente: dextrano (peso molecular de 70 kDa), albúmina de suero bovino (BSA das súas siglas en inglés, con peso molecular de 66.5 kDa) e o activador de plasminóxeno tisular recombinante (rtPA, das súas siglas en inglés, peso molecular de 70 kDa), coa finalidade de estudar a eficiencia de encapsulación destas biomoléculas nas partículas de CaCO_3 . O rtPA é unha serina proteasa implicada na degradación dos coágulos sanguíneos, sendo a súa administración sistémica un dos principais tratamentos eficaces para o tratamento na fase aguda do ictus isquémico, así como nos infartos agudos de miocardio, tromboembolismo pulmonar, trombose arterial periférica, e trombose das veas das pernas. A eficiencia de encapsulación alcanzada para cada biomolécula foi distinta, sendo as nanopartículas cargadas con rtPA as de maior porcentaxe de encapsulamento.

Posteriormente, abordouse un proceso de ensamblaxe LbL mediante a adición de capas de polielectrólito non biodegradables con carga eléctrica alterna sobre os núcleos de CaCO_3 con biomacromoléculas encapsuladas previamente no seu interior. Para iso, só se empregaron partículas de CaCO_3 cargadas coas rtPA e BSA, sendo estas últimas utilizadas como sistema modelo de referencia. Cabe mencionar que a estratexia da técnica de ensamblaxe de capa por capa para a fabricación de cápsulas multicapa presentada neste Capítulo pódese aplicar de maneira sinxela para ensamblar cápsulas a partir de partículas de CaCO_3 e tamén alternar capas con outros tipos de polielectrólitos, partículas ou moléculas metálicas, para preparar materiais funcionais.

As partículas multicapa construíronse con capas de polielectrólitos de poli (4- estireno sulfonato de sodio, PSS, das súas siglas en inglés) e poli (cloruro de dialildimetilamonio, PDADMAC, das súas siglas en inglés), con nanopartículas de óxido de ferro dopadas con Mn/Zn (ioNP, das súas siglas en inglés) como capa alterna, e unha capa final externa formada por xelatina. Os ioNPs agregáronse para exercer como axente de contraste de imaxe por resonancia magnética (MRI, das súas siglas en inglés) e poder rastrexar as partículas tras a súa administración in vivo. Para formar a capa externa de xelatina empregouse xelatina básica, a cal se une de forma específica ao factor von Willebrand (vWF, das súas siglas en inglés), xa que se considera que as estratexias de direccionamento activo hacia ao vWF son mecanismos moi útiles para restaurar o fluxo sanguíneo cerebral sen aumentar as complicacións hemorráxicas intracerebrales.

Asemade, realizouse unha optimización do proceso de encapsulación utilizando as cápsulas cargadas con BSA para obter unha relación entre o número de capas e a estabilidade do fármaco ou biomolécula cargada na partícula despois de realizar o proceso de LbL, antes e despois de disolver os núcleos de CaCO_3 . A partir dos resultados obtidos, seleccionouse unha nanopartícula formada por dúas bicapas e avaliaouse a súa estabilidade cando se “carga” con

rtPA. A cuantificación desta biomolécula por nanocapsula foi avaliada polo método analítico de citometría de fluxo. Esta técnica tamén se usou para avaliar as alteracións que estivesen elacionadas con cambios da morfoloxía das partículas e da súa fluorescencia antes e despois de aplicarllas ultrasóns. Os resultados mostraronn que a aplicación de ultrasóns ás nanocápsulas desenvolvidas produce grandes alteracións na morfoloxía destas, así como tamén un sinal de fluorescencia máis brillante en comparación coas nanocápsulas ás cales non se lles aplicoaron os ultrasóns.

Finalmente, leváronse a cabo diferentes ensaios para avaliar a actividade encimática do rtPA, tanto dentro das nanocápsulas como unha vez liberado delas mediante a aplicación de ultrasóns. A liberación activada por ultrasóns do rtPA desde as nanocápsulas desenvolvidas realizouse tamén in vivo, observándose que o axente bioactivo foi completamente funcional e que posuía unha importante actividade terapéutica.





RESUMEN

La presente tesis tiene como objetivo proporcionar información adecuada acerca de los fundamentos sobre la manipulación controlada y aplicación dirigida de materiales porosos en la nanoescala. Los intereses de investigación de este trabajo se centran en la síntesis coloidal controlada y la funcionalización de dos materiales porosos específicos basados en polímeros de coordinación porosos (PCP, siglas en inglés) y nanopartículas poliméricas de carbonato de calcio (CCPN, siglas en inglés), respectivamente, como nanoportadores destinadas a aplicaciones biológicas y catalíticas.

Cuando la materia está organizada a nivel nanoscópico, las propiedades del (nano) material difieren de las de su contraparte masivo, pues los efectos del tamaño y las interfaces influyen fuertemente en el comportamiento y las propiedades del primero. Las propiedades físicas, químicas, mecánicas y ópticas únicas de los materiales que ocurren naturalmente en la nanoescala ofrecen a los científicos un camino para utilizar eficazmente estas propiedades para desarrollar materiales con aplicaciones potenciales en todos los campos de la ciencia.

Los materiales porosos con poros abiertos ofrecen propiedades atractivas como una red de poros de baja densidad, uniforme y sintonizable, una gran superficie y una alta porosidad. La fabricación de materiales nanoestructurados porosos está atrayendo un interés creciente para una amplia gama de aplicaciones potenciales en catálisis química, separaciones de proteínas selectivas por sorción, procesos de enfriamiento, administración controlada de fármacos, entre otros.

Esta tesis está organizada en seis capítulos. El capítulo 1 está dividido en cinco partes. Las primeras cuatro partes intentan proporcionar al lector una imagen detallada de los conceptos básicos sobre nanomateriales, incluidas las nanopartículas metálicas y porosas, y cómo sus propiedades y funcionalización permiten su uso como catalizadores y sistemas de administración de fármacos controlados. La quinta parte constituye la descripción de los objetivos que se persiguen en la presente tesis doctoral y mi contribución al trabajo desarrollado en los Capítulos 3, 4 y 5. Los enfoques presentados en estos capítulos documentan métodos sencillos que permiten controlar la morfología y funcionalización de los nanomateriales deseados (es decir, polímeros coordinados a base de Cu, ZIF-8, CCNP) a nanoescala con alta monodispersidad, dando lugar a nanopartículas porosas de morfología y tamaño adecuados para aplicaciones potenciales como la reducción catalítica de azul de metileno, y para el control y entrega dirigida de compuestos bioactivos respectivamente. Por último, el Capítulo 2 describe los materiales y la metodología utilizados en los Capítulos 3, 4 y 5.

Los polímeros de coordinación (CP, siglas en inglés) son compuestos poliméricos unidimensionales, bidimensionales o tridimensionales (1D, 2D o 3D) formados por entidades de coordinación repetidas (es decir, inorgánicas, orgánicas o híbridas inorgánico-orgánicas). Los polímeros coordinados porosos y las estructuras organometálicas (MOF, siglas en inglés) son subclases de CP. En el Capítulo 3, se fabricaron nuevas nanopartículas de polímero de coordinación poroso compuestas de Cu^{2+} e imidazolato utilizando un sencillo enfoque sintético ascendente. Los nanoPCP basados en Cu^{2+} han despertado interés debido a su abundancia

natural, bajo costo y propiedades catalíticas y conductoras. Las concentraciones y relaciones molares de los precursores [es decir, CuCl_2 , 2-metilimidazol (2MI) y bromuro de hexadeciltrimetilamonio (CTAB, siglas en inglés)] se optimizaron para producir nanopartículas monodispersas. Los datos experimentales indican que la adición del tensioactivo bromuro de hexadeciltrimetilamonio (CTAB), el tiempo de reacción y el disolvente final determinan el tamaño, morfología y estructura de las distintas NP obtenidas. Se investigó la estabilidad coloidal, los cambios morfológicos y la integridad estructural y química de las nanopartículas desarrolladas en varios disolventes con diferentes polaridades. Se determinaron las propiedades fisicoquímicas básicas de las nanopartículas seleccionadas, como el tamaño, la actividad óptica y magnética, la porosidad, la estabilidad térmica, la estructura, el envejecimiento y la actividad catalítica sobre la reducción del azul de metileno.

En el Capítulo 4, se presenta la preparación de un nanotransportador sensible a la temperatura que comprende nanopartículas plasmónicas sensibles a la luz en el IR cercano (NIR, siglas en inglés) recubiertas con estructuras organometálicas (MOF), específicamente ZIF-8, que es una subclase de MOF. Se seleccionó una nanoestrella de oro como núcleo de las partículas gracias a su característica banda plasmónica centrada a ~ 770 nm, que es adecuada para la excitación dentro de la ventana biológica terapéutica NIR-I. Las nanoestructuras porosas corazón@corona desarrolladas se cargaron con moléculas de bisbenzimidazoles como elemento funcional y se recubrieron con el polímero anfifílico poli [isobutileno-alt-anhídrido maleico] - injerto-dodecilo (PMA). Este polímero anfifílico protege al ZIF-8 de la degradación y evita que el fármaco se filtre de forma no deseada en medios acuosos o dentro de las células vivas. El mecanismo de liberación inducida del elemento bioactivo depende del si la luz infrarroja cercana está acoplada a la absorción plasmónica del núcleo de nanoestrella de oro, lo que permite la creación de gradientes de temperatura locales para activar la termodifusión del fármaco.

En el capítulo 5, se fabricaron cápsulas submicrométricas sonosensibles empleando como plantilla partículas de CaCO_3 para la administración controlada de macromoléculas in vivo mediante un ensamblaje capa por capa (LbL, siglas en inglés) bajo la acción de ultrasonidos. Los estudios biológicos actuales que utilizan generalmente cápsulas poliméricas derivadas de CaCO_3 con tamaño micrométrico (típicamente, con diámetros de 3 a 10 μm) presentan limitaciones importantes como potenciales nanotransportadores de medicamentos inyectables in vivo. Como resultado de su gran tamaño, es probable que estas cápsulas de LbL se secuestran rápidamente dentro de los capilares de los pulmones. Aquí, exploramos un enfoque original para producir cápsulas poliméricas (NC, siglas en inglés) submicrométricas a partir de núcleos de CaCO_3 de aproximadamente 600 nm (o incluso menos) de diámetro. Se seleccionaron, para ello, partículas de vaterita de CaCO_3 (núcleos) como plantilla de núcleo de sacrificio temporal y, a continuación, se encapsularon tres macromoléculas marcadas fluorescentemente: dextrano (70 kDa), albúmina de suero bovino (BSA siglas en inglés, 66,5 kDa) y activador de plasminógeno tisular recombinante (rtPA, siglas en inglés) (70 kDa). El ensamblaje de LbL se realizó mediante la adición de capas de polielectrolito con carga eléctrica alterna sobre los núcleos de CaCO_3 previamente con macromoléculas encapsuladas en su interior. Las partículas multicapa se construyeron con capas de polielectrolitos de poli (4-estireno sulfonato de sodio)

(PSS) y poli (cloruro de dialildimetilamonio) (PDADMAC), con nanopartículas de óxido de hierro dopadas con Mn / Zn (ioNP, siglas en inglés) como capa alterna, y una capa final más externa formada por gelatina. Los ioNP se agregaron como agente de contraste de imágenes por resonancia magnética (MRI, siglas en inglés) para poder rastrear las partículas tras su administración in vivo, mientras que la capa de gelatina se añadió. Para ello, se empleó gelatina básica, colágeno desnaturalizado por calor, que se une al factor von Willebrand (vWF, siglas en inglés). La liberación activada por ultrasonidos del activador tisular del plasminógeno recombinante (rtPA) desde las nanocápsulas desarrolladas se realizó in vitro e in vivo, observándose que el agente bioactivo fue completamente funcional y poseía una importante actividad terapéutica.





ABSTRACT

The present thesis aims to provide suitable information on the fundamentals about the controlled manipulation and targeted application of nanoscale porous materials. The research interests in this work are focused on the controlled colloidal synthesis and functionalization of two specific porous materials based on porous coordination polymers (PCPs) and calcium carbonate polymeric nanoparticles (CCPNs), as nanocarriers for intended biological and catalytic applications.

When matter is organized at the nanoscale, the properties of the (nano)material differ from those of its bulk counterpart, where size effects and interfaces strongly influence the behavior and properties of the former. The unique physical, chemical, mechanical, and optical properties of materials that naturally occur at the nanoscale offer scientists a path to effectively use these properties to develop materials with potential applications in all fields of science.

Porous materials with open pores offer attractive properties such as low-density, uniform, and tunable pore network, large surface area, and high porosity. The fabrication of porous nanostructured materials intended for the manipulation of the design, synthesis, functionalization, and characterization is attracting growing interest for a wide range of potential applications in chemical catalysis, sorption-selective protein separations, cooling processes, controlled drug delivery, among others.

This thesis is organized into six chapters. Chapter 1 is organized into five parts. The first four parts attempt to provide the reader with a detailed picture of the basic concepts on nanomaterials, including metal and porous nanoparticles, and how their properties and functionalization allow their use as controlled drug delivery systems and catalysts. The fifth part constitutes the description of the prospective objectives of the present PhD thesis and my contribution to the work developed in Chapters 3, 4, and 5. The approaches presented in these chapters document straightforward methods that allow for controlling the morphology and functionalization of the desired nanomaterials (*i.e.*, Cu-based coordinated polymers, ZIF-8, CCNPs) at the nanoscale with high monodispersity, giving rise to porous nanoparticles of adequate morphology and size for potential applications as the catalytic reduction of methylene blue, and to the controlled and targeted delivery of bioactive compounds respectively. Finally, Chapter 2 describes the materials and methodology used along Chapters 3, 4, and 5.

Coordination polymers (CPs) are one-, two-, or three-dimensional (1D, 2D, or 3D) polymeric compounds formed by repeating coordination entities (*i.e.*, inorganic, organic, or hybrid inorganic–organic). Porous coordinated polymers (PCPs) and metal-organic frameworks (MOFs) are sub-classes of CPs. In Chapter 3, novel porous coordination polymer nanoparticles composed of Cu²⁺ and imidazolate were fabricated using a facile bottom-up synthetic approach. Cu²⁺-based nanoPCPs have been raising interest due to their natural abundance, low cost, and catalytic and conductive properties. The concentrations and molar ratios of the precursors [*i.e.*, CuCl₂, 2-methylimidazole (2MI), and hexadecyltrimethylammonium bromide (CTAB)] were optimized to produce monodisperse nanoparticles. The experimental data indicate that the addition of the surfactant

hexadecyltrimethylammonium bromide (CTAB), the reaction time, and the final solvent determine the size, morphology, and structure of the different obtained NPs. The colloidal stability, morphological changes, and structural and chemical integrity of the developed nanoparticles in several solvents having different polarities were investigated. Basics physicochemical properties of selected nanoparticles (NPs), such as size, optical and magnetic activity, porosity, thermal stability, structure, aging, and catalytic activity on the reduction of methylene blue were determined.

In Chapter 4, the preparation of a thermoresponsive carrier comprising near-IR (NIR) plasmonic nanoparticles coated with metal-organic frameworks (MOFs), -specifically ZIF-8, which is a subclass of MOFs, is presented. A gold nanostar was selected as the particle core thanks to its characteristic plasmonic band centered at ~ 770 nm, which is suitable for excitation within the NIR-I therapeutic biological window. The developed porous core@shell nanostructures were loaded with bisbenzimidazole molecules as a functional cargo and coated with the amphiphilic polymer poly [isobutylene-*alt*-maleic anhydride]-graft-dodecyl (PMA). This amphiphilic polymer protects ZIF-8 from degradation and prevents the drug from undesired leakage in aqueous media or inside living cells. The induced release mechanism of the cargo depends on the use of near-IR-light coupled to the plasmonic absorption of the gold nanostar core, which creates local temperature gradients to trigger the drug thermo-diffusion.

In Chapter 5, a sonosensitive, sub-micrometric CaCO_3 -templated capsules for ultrasound-controlled delivery of macromolecules *in vivo* were fabricated via layer-by-layer (LbL) assembly. Current biological studies generally using micrometric size of CaCO_3 -derived capsules (typically, having diameters from 3 to 10 μm) present important limitations as potential *in vivo* i.v. injectable medicinal products. As a result of their large size, LbL capsules are likely to be rapidly sequestered within the capillaries in the lungs. Here, we explore an original approach to produced sub-micrometric CaCO_3 -templated polymer capsules (NCs) of approximately 600 nm (or even less) in diameter. CaCO_3 vaterite particles (cores) were selected as the temporal sacrificial core template. Three fluorescently labeled macromolecules were encapsulated: dextran (70 kDa), bovine serum albumin (BSA, 66.5 kDa), and recombinant tissue plasminogen activator (rtPA) (70 kDa). LbL assembly was performed by the addition of alternating charged polyelectrolyte layers onto the sacrificial macromolecule loaded CaCO_3 cores. The multilayer films were constructed with layers of poly(sodium 4-styrene sulfonate) (PSS) and poly(diallyl dimethylammonium chloride) (PDADMAC) polyelectrolytes, with Mn/Zn doped iron oxide nanoparticles (ioNPs) as an alternating layer, and an outermost layer of gelatin. The ioNPs were added as a magnetic resonance imaging (MRI) contrast agent to track the particles upon *in vivo* administration, and the layer of gelatin aiming to provide these nanocarriers with targeting capabilities. We adopted basic gelatin, heat-denatured collagen, which binds to von Willebrand factor (vWF). Ultrasound-triggered release of fully functional recombinant tissue plasminogen activator (rtPA) from the developed nanocapsules was done *in vitro* and *in vivo*, denoting an important therapeutic activity.





Chapter 1

1. Introduction

1.1. Nanotechnology, Nanomaterials, and Nanoparticles: General Concepts

Nanotechnology is described as the science and engineering that controls materials at nanoscale levels. In 1959, Richard Feynman was the first to discuss the concept of nanotechnology at the American Physical Society meeting with a talk entitled “There is plenty of room at the bottom”. A few years later, in 1974, Tokyo Science University Professor Norio Taniguchi defined the term “nanotechnology” as “processing of, separation, consolidation, and deformation of materials by an atom or by one molecule”. The nanometer (nm) scale refers to a billionth of a meter or factor of 10^{-9} . To be classified as nanostructured material at least one dimension of the material must be laying within the 1-100 nanometer range, including nanoparticles (NPs), nanowires, nanorods, nanocapsules, nanofibers, nanotubes, nanocomposites, nanostructured surfaces, and thin solids films with nanoscale thickness.^[1]

The interest on nano “things” has expanded into a variety of different areas such as energy, space technology, computing technology, industry, and biomedical applications, mainly because small particles have an enormous surface-to-volume ratio resulting in a high reactivity surface. In principle, by definition, the surface area of a three-dimensional solid is a measure of the total area occupied by the surface of the object. The surface area of a solid will increase if it is subdivided into smaller particles, and thus, new surfaces will be produced.

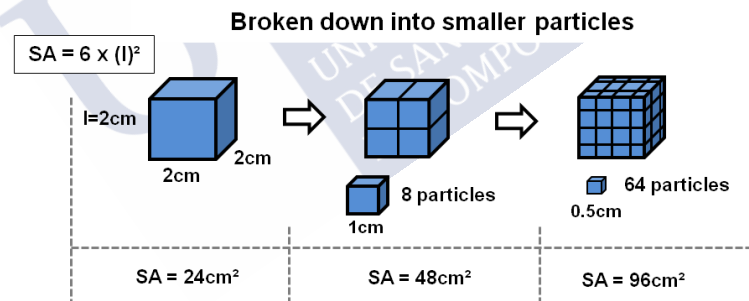


Figure 1.1. Schematic illustration showing that material breaks down into smaller particles and this leads to surface area increase.

For example, when a cube of 2 cm edge length with a surface area (SA) of 24 cm^2 is subdivided into 8 smaller cubes of 1 cm of length, the surface area will be 48 cm^2 ; now if we continuing cutting into 64 smaller cubes of 0.5 cm of length, the surface area will be 96 cm^2 (see *Figure 1.1*). At the naked eye, all cubes will have properties similar as the principal one ($l = 2\text{cm}$); however, at the nanoscale level, materials behave differently compared to larger scales, thus, the physical and chemical properties will change as a function of size due to the movement of atoms and molecules around and between each other within the material. Materials at nanometer-levels reveal new properties due to the increased surface-to-volume ratio compared to their bulk.^[2] Thus, specialized instruments will be required to investigate and to compare

changes in the physical and chemical properties in the nanosized material from those of the bulk one.^[3]

1.1.1. Classification of Nanoparticles

Nanomaterials can be classified based on their origin either natural or synthetic. In the case of natural nanomaterials, there are naturally occurring nanoparticles, that is, which are present in the environment regardless of human intervention, nanoparticles of natural products, and naturally produced nanoparticles of natural products.^[4] Meanwhile, synthetic nanomaterials or engineered nanoparticles are synthesized from bulk materials by humans through physical, chemical, biological, or hybrid methods for desired applications.^[5, 6] Furthermore, Jeevanandam *et al.* reported that nanomaterials can also be organized into four material-based categories summarized in *Table 1.1*.^[5] Other classifications for nanomaterials have been made by researchers based on their dimensions, crystalline form, and chemical composition.^[7-9] Chapters 3, 4, and 5 of this PhD thesis will focus on composite- and inorganic-based nanoparticles, respectively.

Table 1.1. Type of nanomaterials (adapted from ref.[5]).

Type-based nanomaterial	Features and examples
Carbon-based	fullerenes, carbon nanotubes, carbon nanofibers, graphene
Inorganic-based	metal and metal oxide NPs: Au, Ag, TiO ₂ , ZnO NPs, semiconductors: silicon, ceramics
Organic-based	NPs made principally from organic matter, dendrimers, micelles, polymeric NPs
Composite-based	Combination of NPs (carbon, organic and inorganic) with other NPs or bulk materials (ceramic, metal or polymer), hybrid nanofibers, metal-organic framework

NPs: nanoparticles

1.1.2. Synthesis of Nanoparticles

There are two general approaches for the synthesis of nanomaterials *i.e.*, i) bottom-up approach (*e.g.*, wet chemistry) and ii) top-down approach (*e.g.*, mechanical grinding) (see *Figure 1.2*).

Bottom-Up Approaches

Bottom-up approaches start with atoms and/or molecules as blocks in order to build up to nanostructures; these approaches involve the use of minituarized materials' components (*i.e.*,

up to atomic level) and their clever combination by means of self-assembly processes, where physical forces operating at the nanoscale are used to combine basic units that leads to the formation of stable structures.^[10-12] Most of the nanoscale materials are preparing through this route, which covers physical and chemical methods such as molecular self-assembly, physical/chemical vapor deposition, epitaxial growth, colloidal dispersion, sol-gel, ion beam techniques, solvothermal routes, microemulsions, and precipitation processes.^[10]

Top-Down Approaches

Top-down approaches start with a pattern generated on a large scale, which is reduced to the nanoscale afterworks; this kind of approaches involves the use of larger initial structures (*i.e.*, macroscopic), which breaks into smaller units that lead to the formation of uniform structures. Top-down methods include mechanical alloying, chemical etching, lithography, or micromachining methods, which are more expensive than self-assembly methods.^[1, 10, 11]

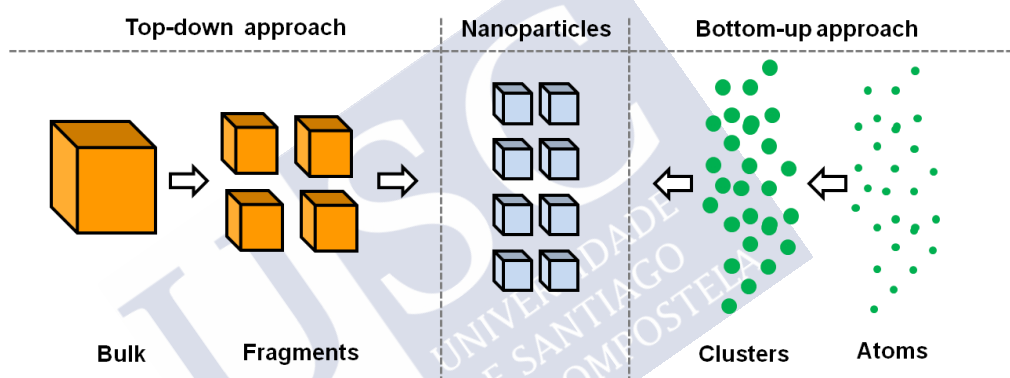


Figure 1.2. Schematic illustration of the two general approaches for the synthesis of nanomaterials.

1.1.3. Growth Control of Nanoparticles in Solution

Colloidal nanoparticles are nanoscale objects that are dispersed in water-based solvents in the case of hydrophilic particles, or organic solvents in the case of hydrophobic particles. Amphiphilic nanoparticles can be dispersed either in water-based or organic solvents.^[13]

Nowadays, the development of colloidal nanoparticles of different composition, size, shape (*e.g.*, planar, spherical, rod-like, etc.), and physical or chemical properties^[13] has been received enormous attention due to their potential applications in different fields such as medicine, and catalysis.^[14] Colloidal nanoparticles reveal unique and new magnetic, optical, electronic, and catalytic properties, which are related to their size, shape, composition, and/or crystalline structure and are different compared to their bulk counterparts.^[2, 14]

The growth of the NPs depends on the surface reactivity and the monomer's diffusion to the surface,^[2, 15] and in terms of rate, final size, and geometric shape, this growth can be controlled by the use of capping agents (*e.g.*, surfactant molecules, polymers, etc.) during the nanoparticle

formation process; these capping agents, that typically adsorb on the nanoparticles surface, stabilize the nuclei against aggregation by a repulsive force, resulting in a thermodynamically stable configuration of nanoparticles.^[13, 14]

1.1.4. Functionalization of Nanoparticles Surface

Modification of nanoparticle surfaces may provide several benefits such as colloidal stability, interaction with the particle environment, especially in biological systems, self-organization, incorporation of organic groups for a particular interaction, and possible controlled targeting.^[13, 16] In Chapters 4 and 5 of this PhD thesis, nanoparticles functionalized with an amphiphilic polymer to provide stability in aqueous solutions and preventing the cargo from release, and nanoparticles functionalized by rapid layer-by-layer assembly of polyelectrolytes (*i.e.*, the centrifugation method) for targeting delivery, will be presented, respectively. Therefore, a brief overview of the two aforementioned surface coating strategies will be discussed below.

Coating the Nanoparticles with an Amphiphilic Polymer

Amphiphilic polymers have been used for coating hydrophobic inorganic NPs, where these amphiphilic polymer coatings can stabilize originally hydrophobic nanoparticles in aqueous solutions.^[17, 18] Basically, hydrophobic nanoparticles are encapsulated inside the hydrophobic side chains of the polymer micelle resulting in a hydrophilic nanoparticle surface as shown in *Figure 1.3*.^[17]

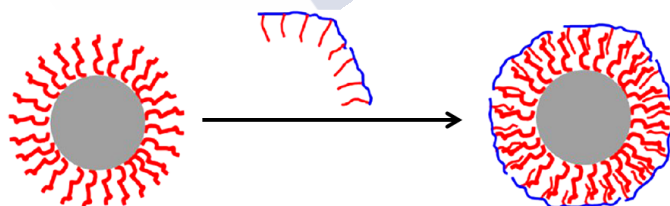


Figure 1.3. Schematic illustration of nanoparticles modified with an amphiphilic polymer. The nanoparticles cores (gray spheres) that are capped with hydrophobic ligands (drawn in red) are modified with an amphiphilic polymer (hydrophilic backbone drawn in blue and hydrophobic side chains drawn in red, respectively). The nanoparticles cores are embedded in the resulting polymer micelle, resulting in a hydrophilic nanoparticle surface. (Adapted with permission from ref. [17]. Copyright 2016, American Chemical Society).

Layer-by-Layer Assembly Methods

In 1996, Iler^[19] introduced a technique to fabricate multilayer films based on alternated layers of positively and negatively charged colloidal particles. Based on this work, Decher et al.^[20, 21] introduced a layer by layer (LbL) method to coat charged surfaces based on electrostatic attraction between polyelectrolytes layers of opposite charge.^[22] More recently, the design of

nanostuctured materials employing sacrificial templates by the simplicity and versatility of the layer-by-layer (LbL) assembly method has received increasing interest for biological applications because of the possibility of controlling of the shell thickness, surface charge, size, and permeability.^[23] Basically, LbL nanoparticles are formed by depositing consecutive layers of oppositely charged polyelectrolytes onto templates thorough electrostatic or covalent interactions, hydrogen bonding, or single polymer assembly, resulting in a multilayered film structure.^[23, 24] The templates can be a sacrificial particle that will dissolve to form a hollow-shell structure (*i.e.*, capsules) or remain a part of the multilayer structure (*i.e.*, core-shell particles).^[25] Moreover, the templates can be porous (*e.g.*, mesoporous silica, calcium carbonate, etc.) or non-porous (*e.g.*, gold NPs, quantum dots, etc.) particles,^[26] where porous ones have been used to encapsulate compounds.^[25, 27] Different methods for the assembly of multilayered particles have been reported being the centrifugation method the most conventional one.^[22, 25, 28-33]

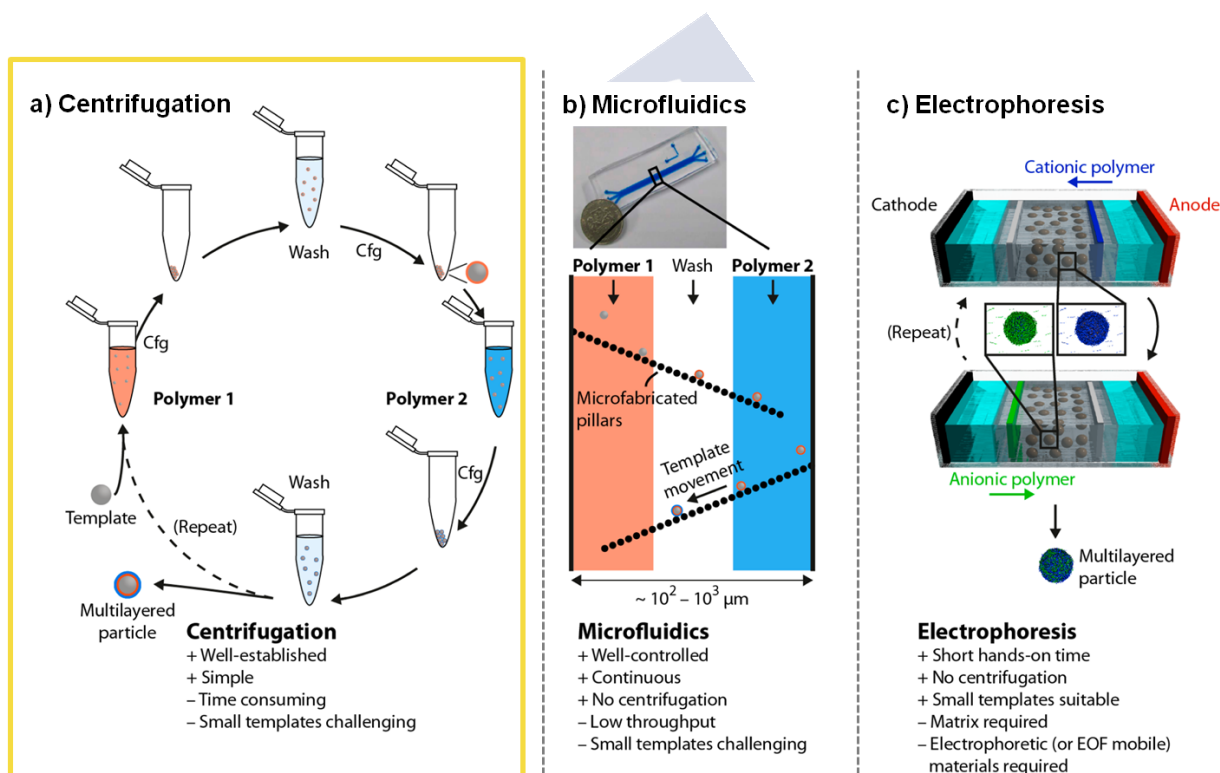


Figure 1.4. Schematic illustrations of different LbL assembly methods with benefits (+) and limitations (-): a) the centrifugation method involves centrifugation (Cfg) steps (adapted with permission from ref. [25]. Copyright 2013, American Chemical Society); b) Microfluidics method (adapted with permission from ref. [34]. Copyright 2011, The Royal Society of Chemistry); c) “Electrophoretic polymer assembly” (adapted with permission from ref. [35]. Copyright 2013, Wiley-VCH Verlag GmbH & Co. KGaA, Weinheim). (Adapted with permission from ref. [25]. Copyright 2013, American Chemical Society).

In the centrifugation method, particles can be collected by centrifugal sedimentation to separate adsorbed and free polymer for each layer (see Figure 1.4a). Although is a facile method, the unwanted aggregation of particles becomes stronger with dropping particles ‘size down (*i.e.*, sub-100 nm).^[25] Another method to fabricate multilayered capsules is the

microfluidic method; *Figure 1.4b* shows the “microfluidic pinball” developed by Kantak et al. where microfabricated templates can be moved back and forth to achieve layering in a confined laminar flow of a polymer solution.^[34] Scaling-up and the achievement of small templates are limitations of this method. Recently, Richardson et al. developed a method called “electrophoretic polymer assembly” in which templates are immobilized inside an agarose gel and layering can be achieved by electrophoresis by injecting the polyelectrolytes and allow them to pass through the matrix (see *Figure 1.4c*).^[35]

1.1.5. Techniques for Nanoparticles Characterization

Different characterization techniques have been used to study and characterize nanoparticles; usually, the combination of several ones provides comprehensive information about the nanomaterial structure and properties; however, sometimes the use of one or two is sufficient for the analysis of a particular property. *Table 1.2* summarizes a selection of experimental techniques for the analysis of various physicochemical properties of nanoparticles.

Table 1.2. Properties/characteristics to be determined for nanoparticles, and some of the corresponding characterization techniques (adapted from ref. [36]).

Parameter to determine	Corresponding technique*
Size (structural properties)	DLS, NTA, ICP-MS, UV-Vis, PXRD, SEM, TEM
Morphology	SEM, TEM
Elemental-chemical composition	SERS, PXRD, ICP-MS, EPR, SEM-EDX
Crystalline structure	SERS, PXRD, STEM
Size distribution	DLS, NTA, ICP-MS, SEM
Pore structure	TEM
Ligand binding/composition/mass, surface composition	FTIR, TGA, EPR
Surface area, specific surface area, pore size	BET
Surface charge	ζ -potential
Concentration	NTA, ICP-MS, UV-Vis
Agglomeration state	DLS, Zeta potential, SEM, TEM, UV-Vis

DLS: Dynamic light scattering, NTA: Nanoparticle tracking analysis, ICP-MS: Coupled plasma mass spectrometry, UV-Vis: UV-Vis spectroscopy, PXRD: Powder X-Ray diffraction, SERS: Surface-enhanced Raman spectroscopy, EPR: Electron paramagnetic resonance, SEM: Scanning electron microscopy, TEM: Transmission electron microscopy, STEM: Scanning transmission electron microscopy, SEM-EDX: Scanning electron microscopy-Energy Dispersive X-ray spectroscopy, FTIR: Fourier transform infrared spectroscopy, TGA: Thermal gravimetric analysis, BET: Brunauer-Emmet-Teller adsorption isotherm, ζ -potential: Zeta potential.

1.1.6. Applications of Nanoparticles

The material, the surface, and the surface modification of the particles have a very important role in the potential targeted application of a nanoparticle. According to R. A. Sperling and W. J. Parak,^[13] the application of colloidal nanoparticles can be divided into three classes:

- i) Labeling, tracing, and imaging.
- ii) Sensing and detection.
- iii) Active elements such as heat mediation, optical sensitizing, or delivery vehicles.

However, here, we will briefly discuss the use of nanoparticles specifically in catalysis and drug delivery, respectively, since the materials presented in the following chapters were fabricated to have the potential for application in the aforementioned areas.

Nanoparticles in Catalysis: General Concepts

Catalysis is a molecular phenomenon in which the chemical transformation of molecules into other molecules occurs^[37] through the use of chemical compounds, known as catalysts, that reduce the amount of energy and speed up the chemical reaction rate.

Catalysis is present in the industry, energy, environment, and life science, and can be divided into homogenous and heterogeneous. In homogeneous catalysis, catalysts and reaction mixture occupies the same phase (see *Figure 1.5a*), whereas in heterogeneous catalysis, catalysts occupy a different phase than the reaction mixture (see *Figure 1.5b*).^[38] Homogeneous catalysis can be said to be connected to molecular organometallic chemistry, while heterogeneous catalysis to surface science and solid-state chemistry.^[37, 39]

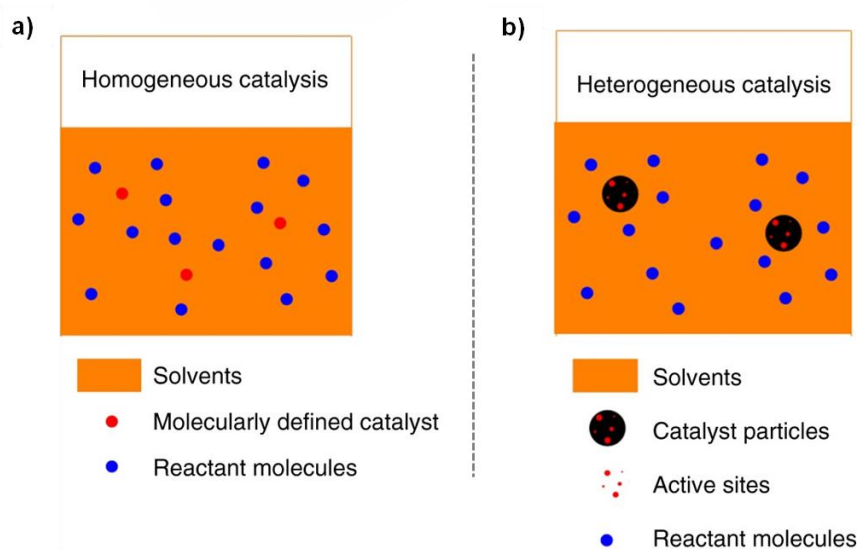


Figure 1.5. Schematic illustration of a) homogeneous catalysis and b) heterogeneous catalysis, respectively (adapted with permission from ref. [38]. Copyright 2018, Nature Communications).

The use of nanoparticles (NPs) in catalysis dates back to the 19th century with the emergence of photography (*i.e.*, Ag NPs) and the decomposition of hydrogen peroxide (*i.e.*, Pt NPs).^[40] Nanoparticles can interact with substrates and reagents and, hence, catalyze reactions; this is due to the large percentage of unsaturated coordination atoms that are located at the surface, edge, and corners of the nanoparticles compared to the total number of atoms.^[41]

Nanoparticles in Drug Delivery (in Vitro and in Vivo): General Concepts

To begin with, the first question to be answered might be: What do the terms “in vivo” and “in vitro” really mean? The terms are closely related but they are not the same: In vitro (*i.e.*, “within the glass”) studies are cell culture experiments performed outside a living cell or organism but inside a glass such as a test tube or Petri dishes (see *Figure 1.6a*) under artificial conditions and controlled environment settled down by the researchers. Most of the preliminary biological experiments are carried out in this manner. On the other hand, in vivo (*i.e.*, “within the living”) studies are experiments performed in living organisms, such as non-human and human animals, and plants (see *Figure 1.6b*), being crucial for the diagnostic and medical treatment.

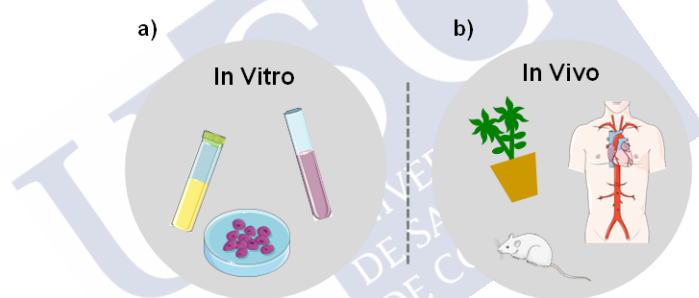


Figure 1.6. Schematic illustrations of a) in vitro vs. b) in vivo studies.

Researchers have developed nanoparticles to be used as nanocarriers for therapeutic compounds such as drugs or contrast agents for imaging.^[42, 43] The nanoparticles for drug delivery can be produced from soft (*i.e.*, organic and polymeric) or hard (*i.e.*, inorganic) materials with different sizes, chemical compositions, shapes, structures, morphologies, surfaces properties, and loaded with drugs (see *Figure 1.7*).^[44] The behavior and stability of nanoparticles in the biological environment are governed by different properties, such as protein corona, functionalization, and nanoparticle surface interactions with the surrounding medium.^[45]

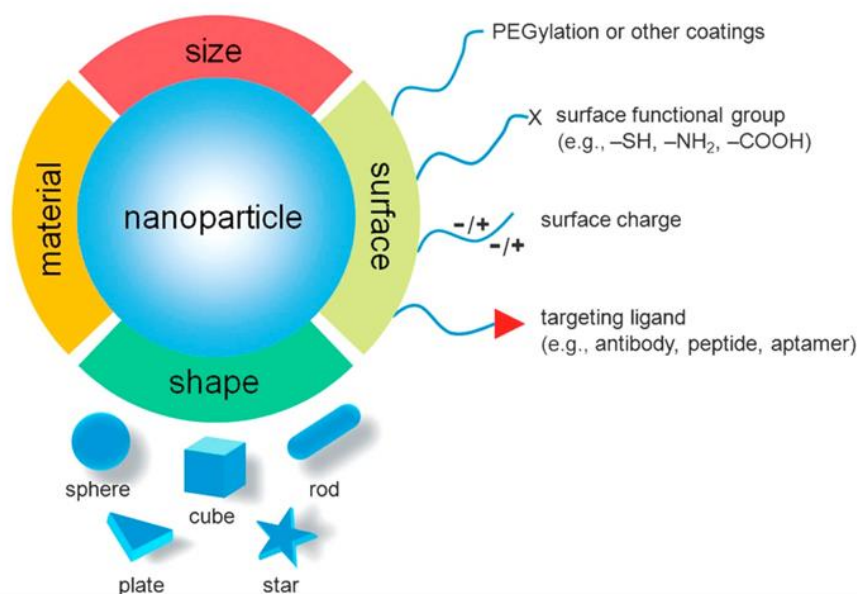


Figure 1.7. Biophysico-chemical properties of nanoparticles for drug delivery (adapted with permission from ref. [44]. Copyright 2014, Wiley - VCH Verlag GmbH & Co. KGaA).

In Vitro Nanoparticles Behavior

Nanoparticles not only use different mechanisms to enter cells but can also induce their uptake if they become associated with the cellular membrane. Most of the nanoparticles carrying drugs needs to be taken into the cell (*i.e.*, eukaryotic cells), in most cases through endocytic mechanisms.^[46, 47] The size, shape, and chemistry surface are factors affecting the nanoparticle endocytosis.^[46, 48, 49]

There are four types of endocytosis mechanisms: clathrin-mediated endocytosis, caveolae-mediated endocytosis, macropinocytosis, and phagocytosis.^[48, 49] Clathrin- (*i.e.*, a protein whose main function is to coat intracellular vesicles) and caveolae- (*i.e.*, a subtype of lipid raft that is identified in the plasma surface) mediated endocytosis pathways (*i.e.*, the energy-dependent activity by which cells internalize biomolecules) indicate receptor-mediated endocytosis, and typically are observed during the cellular uptake of nanoscale materials such as viruses and ligand-coated nanoparticles.^[48-50] In these endocytosis pathways, the nanoparticles are directly covered by plasma proteins when exposed to physiological environments.^[49]

Phagocytosis is the uptake of foreign materials as large as 0.5 μm and occurs in professional phagocytes such as macrophages, neutrophils, monocytes, and dendritic cells.^[46]

Whereas, macropinocytosis is a non-specific process that involves the internalization of fluids and particles together into the cell, in which the uptake of small particles dominates (*i.e.*, <0.15 μm).^[46, 49]

The majority of the internalized particles are mainly located inside vesicle structures; when the nanoparticles are attached to the outer cell membrane or already inside the cell, different cellular responses can occur, such as cytotoxicity, oxidative stress, pro-inflammatory responses,

and/or DNA damage.^[51] Furthermore, researchers have reported that the mechanical properties and cellular behavior can be affected by internal and external forces acting through the cytoskeleton upon particle uptake; the cytoskeleton is a system of protein filaments present in the cytoplasm of eukaryotic cells and helps cells to maintain their shape, internal organization, transports intracellular cargo, and provides mechanical support.^[52, 53]

In Vivo Nanoparticles Behavior

Multiple studies of nanoparticles for biomedical applications have been published; however, their use in clinical practice is far from being properly established, especially due to the lack of understanding concerning the interactions between nanoparticles and blood and interstitial fluids.^[54] This is because immediately after injection, nanoparticles undergo different physiological behaviors before reaching the desired targets.^[42] Upon intravenous administrations, nanoparticles establish their initial interactions with blood components, being formed layers of adsorbed proteins around them; this process is known as opsonization (or biofouling). The protein-nanoparticle binding affinity and the protein-protein interactions control the adsorption of proteins on the nanoparticle's surfaces, therefore, conferring a different "biological identity" to the nanoparticle. Before reaching the desired target (*i.e.*, binding to receptors at diseased cells) and subsequent internalization, sequestration of nanoparticles can occur by the liver and/or spleen (reticuloendothelial organs).^[42, 55]

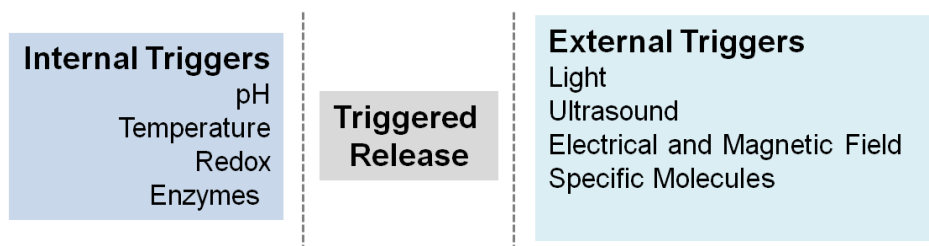
The elimination of nanoparticles from the blood by renal excretion is also a biological obstacle to be considered in order to achieve a safe use of nanoparticles in therapeutic applications. Choi et al. found that nanoparticles (*i.e.*, quantum dots) smaller than 6 nm in diameter resulted in a rapid excretion by kidneys and, therefore, being cleared out from the body.^[56] On the other hand, when nanomaterials are larger than 200 nm they accumulate in the liver and spleen,^[47] unless they are made of degradable materials.^[57]

Biological Identity of Nanoparticles

Nanoparticles can enter the human body through different routes: via inhalation or oral ingestion, bloodstream, through the lungs and skin.^[58] Besides the "synthetic identity" of the nanoparticle (*i.e.*, size, shape, chemistry surface), the cellular uptake of nanoparticles will also depend on the protein corona formed after being exposed to the biological environment.^[54] The protein corona provides the biological identity of the nanoparticles and is a dynamic coating of biomolecules that forms around the nanoparticle in physiological environments affecting its physiological and therapeutic responses.^[54, 58]

Stimuli-Responsive Drug Delivery Systems: Internal and External Triggers

The controlled release of a drug from a carrier can be triggered by single or multiple internal (*i.e.*, endogenous) or external (*i.e.*, exogenous) stimuli (see *Scheme 1*) at the desired time, location and/or amount of dose, where the carrier system directed binds to a target.^[59, 60]



Scheme 1. Internal and external triggers for drug delivery systems.

A stimulus-drug release event is what is known as *triggering*, whereas the use of a stimulus to send a drug delivery carrier to a specific location is known as *targeting*.^[60]

Triggering can be active or passive. In a passive process the property of the target tissue is the one that takes control over the process (*i.e.*, pH, size exclusion or the local concentration of an enzyme); one example of passive triggering is when a carrier is fabricated with pH-sensitive materials; this carrier may disintegrate when entering the acidic interior of the cell and, thus, allowing the release of the cargo.^[60-62] On the other hand, active triggering systems may release their cargo by the application of an external energy source.^[60, 63, 64]

Externally triggered drug delivery systems have been considered as promising to enhance the safety and efficacy of the treatment process.^[60, 65] In Chapters 4 and 5 two actively external trigger systems will be presented: light-triggered and ultrasound-triggered, respectively.

1.2. Plasmonic Nanoparticles

Plasmonic nanoparticles can be found in a variety of applications serving as therapeutic, diagnostic, or theranostic agents. The production of finely-tailored plasmonic nanomaterials and the development of their surface functionalization tools are the keys to provide them with colloidal stability and/or specificity in complex biological media.^[66]

1.2.1. General Concepts

Surface plasmon resonances result from the coupling between an external electric field, usually of light, \vec{E}_0 , and the plasma oscillations of free electrons, for instance, at the interface between a metal and a dielectric material (*e.g.*, air, aqueous solution, etc.).^[66]

Typically, this coupling occurs within the electromagnetic spectrum from ultraviolet (UV) to near-infrared (NIR). In the case of metallic NPs,^[67] carbon nanomaterials^[68] or some doped semiconductors and metal oxides,^[69] with sizes equal or less than the wavelength of the excitation light (UV-to-NIR), surface plasmon resonances are localized and referred to as localized surface plasmons resonances (LSPRs).

LSPRs are responsible for the large, wavelength-selective increment in absorption, scattering, and electric field (EF) enhancement at the NP surface.^[70, 71] Thus, plasmonic NPs are capable of absorbing and scattering light at highly specific regions of the electromagnetic

(EM) spectrum with high molar extinction coefficients (*i.e.*, several orders of magnitude higher than organic fluorophores).^[66]

Optical Properties of Plasmonic Nanoparticles

The optical properties of plasmonic NPs are determined by their extinction cross-section (*i.e.*, σ_{ext}), that is, the sum of the absorption and the scattering cross-sections (*i.e.*, σ_{abs} and σ_{sc} , respectively).^[72] LSPRs give rise to three physical phenomena indicated below:^[66]

- Resonance absorption of light centered at the LSPRs' energy (*i.e.*, localized surface plasmon resonance, or LSPR), which is determined by the σ_{abs} .^[73]
- Far-field scattering of light (*e.g.*, colors of colloidal solutions of noble metal NPs), which is determined by the nanomaterial σ_{sc} at distances, d , larger than the NP dimensions (for instance, the NPs radius r_{NP}), *i.e.*, $d > r_{\text{NP}}$.^[74]
- Near-field scattering of light, resulting in enhancement of the optical near-field (*i.e.*, the concentration of light within extremely small volumes in the close surrounding of the NPs), *i.e.*, $d < r_{\text{NP}}$.^[75]

These plasmonic responses have led to numerous applications in diverse fields, such as sensing and biosensing,^[76] photothermal therapy (PTT),^[77] optoacoustic imaging (OI),^[78] two-photon luminescence (TPL) imaging,^[79] photovoltaics,^[80] or optical communications,^[81] among others (see *Figure 1.8*).

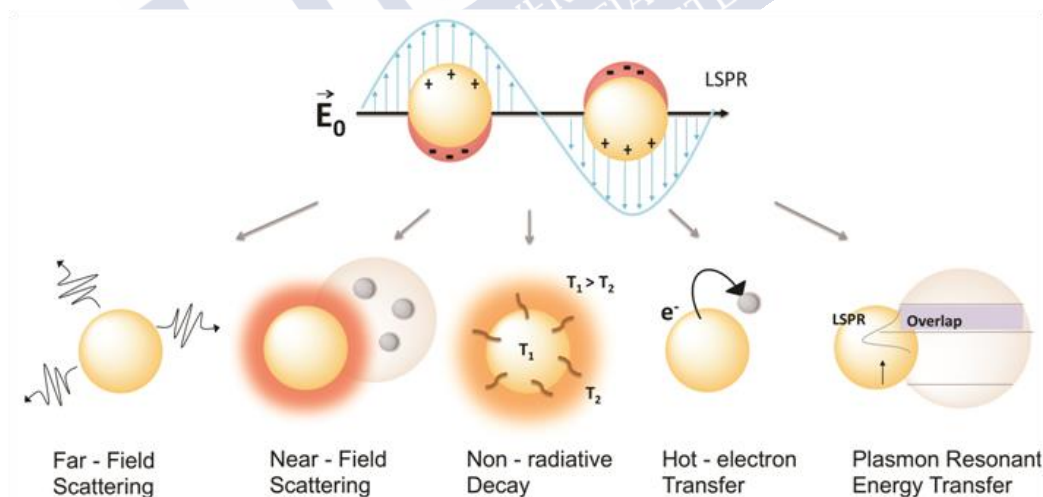


Figure 1.8. Scheme of the interaction of light and plasmonic NPs, resulting in scattering (far- and near-field), absorption, and energy transfer phenomena that have application in biotechnology (adapted with permission from ref.[66] . Copyright 2018, Elsevier Ltd).

Development of Plasmonic Nanoparticles: Biological Purpose

The application of plasmonics in biology and medicine is known as bioplasmonics (*i.e.*, also termed nanobiotechnology or nanobiology). The pioneering work by Mirkin's Group about

colorimetric biosensing based on the distance-dependent optical properties of Au NPs may be considered as one of the initial triggers to the rapid development of nanotechnology in general, and bioplasmonics in particular.^[82, 83]

A variety of plasmonic probes have typically been used in bioapplications, including sensing, light-based therapies, or imaging. Not only synthetic methodologies for fabricating plasmonic nanomaterials but methods for their coating (*i.e.*, organic coatings mostly) and functionalization have been a subject of intense research. These surface characteristics are crucial to providing NPs with colloidal stability in physiological environments, as well as to provide NPs with different functionalities (*e.g.*, specificity towards bioanalytical targets, antifouling, self-assembly, *etc.*).^[84]

Thus, bioplasmonics makes use of plasmonic NPs as nanoantennas or nanotransducers, which can be photoactivated and, then, enable different responses, including nanoheating, reporting reactions (*e.g.*, binding, aggregation, *etc.*), or surface-enhanced signals (surface-enhanced Raman, fluorescence and IR absorption spectroscopies).

Depending on the specifically addressed bioapplication, the excitation wavelength and NP's properties (scattering/absorption, coating) need to be properly matched to obtain the desired optimized plasmonic response (*e.g.*, nanoheating, field enhancement, colorimetric change, *etc.*).^[85]

Researchers have been developing synthetic methods to fabricate plasmonic NPs with controlled and tunable LSPRs responses through the fine manipulation of parameters such as composition, size, shape, and aggregation (see *Figure 1.9a*).^[67, 73]

When designing a plasmonic material for bioapplications, the first thing to consider is that the adjustment of the LSPR response of the final colloids can be made by varying the NP composition thanks to the amount of available plasmonic materials (*i.e.* Au, Ag, Cu and its chalcogenides, Al, Rh, Ru, In, Li or Na, among others). However, the specific characteristics of the plasmonic response (in the UV for Rh, Ru, In),^[86, 87] low stability to oxidation in biological media (Al, Na, Li), or intrinsic toxicity for *in vivo* applications (Cu, Ag, chalcogenides) reduce dramatically the number of choices available for a given application.

Moreover, size is another important parameter that can be modified to tune the plasmonic response as it affects both the LSPR position and the extinction cross-section of the NPs. Regarding the LSPR position, for the same composition and geometry LSPR shifts to the red as the NP size increases (see *Figure 1.9b*). Nevertheless, the variation of the NP size has two other implications: i) the larger the NP is, the more the classical surface plasmon dominates the quantum core plasmon and becomes more concentrated near the surface of the NP, resulting usually in the generation of a larger electric field at the surface.^[88] ii) for, *in vivo* applications, larger NPs are less efficiently excreted by the organism.^[56]

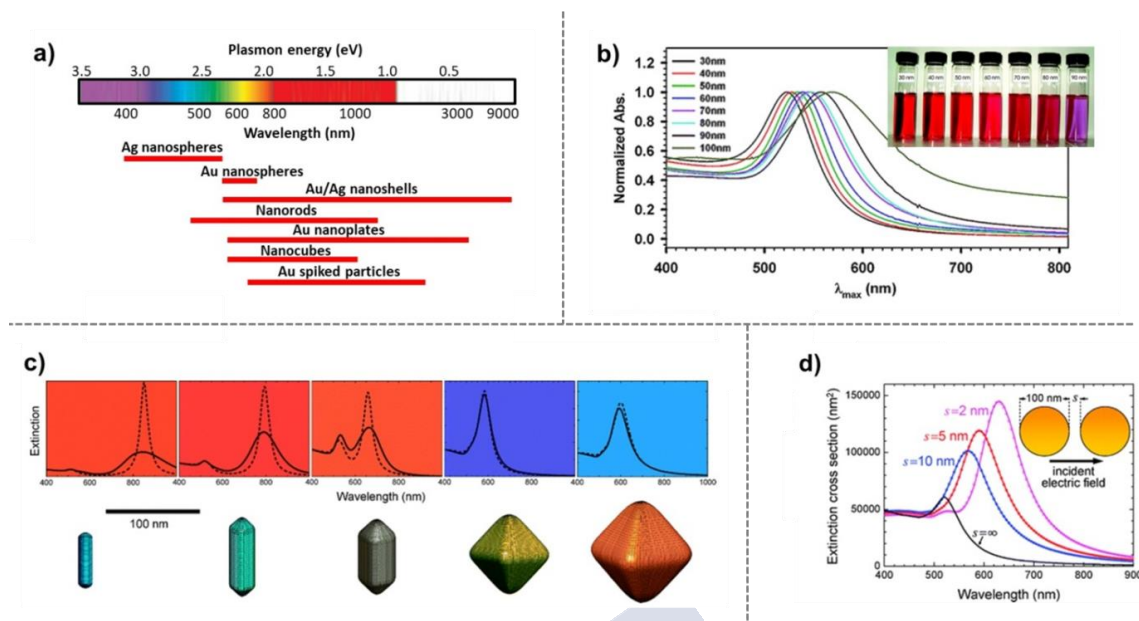


Figure 1.9. a) Energy and LSPR position for the plasmonic response of different NPs as a function of composition, size, and shape; b) Position of LSPR in Au NPs of different sizes (adapted with permission from ref.[89]. Copyright 2007, American Chemical Society). c) Position of LSPR in Au NPs of different shape (and size); d) Plasmonic response (LSPR position and extinction cross-section) of two gold spherical NPs interacting as a function of their interparticle distance (adapted with permission from ref.[90]. Copyright 2008, Royal Society of Chemistry). (Adapted with permission from ref.[66]. Copyright 2018, Elsevier Ltd).

In this regard, the shape is by far the parameter that more extensively modifies the LSPR both in its position and distribution on the NP surface. For example, by controlling the shape of Au NPs (see *Figure 1.9c*), LSPR can be easily tuned from the visible to the NIR. Furthermore, the generation of apexes, spikes, or sharped ends (*e.g.*, triangles, rods, or stars) concentrates the surface electromagnetic fields on those regions generating intra-NP hot spots that can be efficiently exploited in sensing applications.^[91] The reverse side of this tuning, however, resides in the fact that most of the protocols which drive NP shape control requires the use of specific surfactants that strongly bind to the surface of the NPs. However, these residual surface elements often enable further NP functionalization steps or even their interaction with desired species in the biological media. Finally, the last essential factor that can be used for plasmonic tuning is based on the plasmon coupling between neighboring NPs. Typically, NP aggregation shifts the plasmon to the red (see *Figure 1.9d*).^[66]

1.3. Porous Nanoparticles

Porous materials are made of solid phases that form the porous frame and the pores throughout the solid. Some materials may have holes as a result of defects that will negatively influence the performance of the material; therefore, these materials are not considered as porous materials.

It was until the mid 1990s that porous materials were classified as inorganic and carbon-based materials depending on their composition.^[92, 93] However, coordination polymers have positioned themselves as a new category within porous materials (see *Figure 1.10*).^[93]

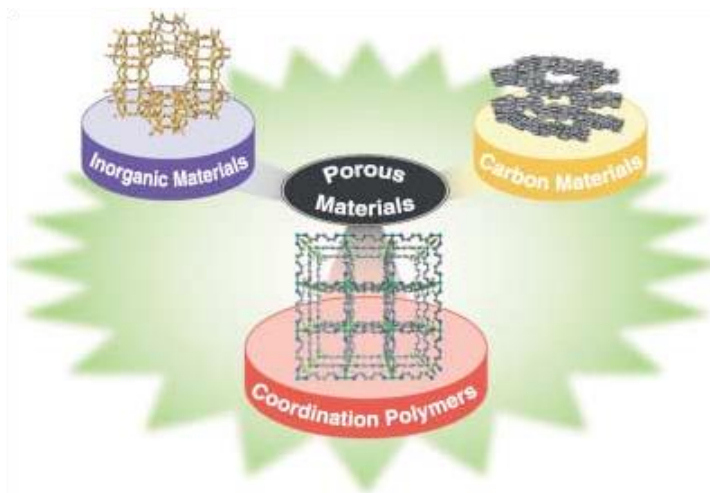


Figure 1.10. Schematic illustration of classes of porous materials (adapted with permission from ref. [93] . Copyright 2004, Wiley - VCH Verlag GmbH & Co. KGaA).

Moreover, porous materials are low-density solids with a uniform and tunable pore network, large surface area, and high porosity.^[94] The ratio of the total pore volume to the volume of the particles or agglomerate is known as porosity.^[95] According to the International Union of Pure and Applied Chemistry (IUPAC),^[96] the pore size and structure have been classified, as follows:^[97, 98]

- *Micropores* (internal pore width < 2 nm)
 - *Ultramicropores* (< 0.7 nm)
 - *Supermicropores* (from 0.7 to 2 nm)
- *Mesopores* (internal pore width from 2 to 50 nm)
- *Macroporous* (internal pore width > 50 nm)

The surface of porous adsorbents or materials is divided into two categories: external and internal surface: The internal surface is the surface corresponding to all the pore walls, while the external one is that outside the pores.^[95] We will find that, generally, in the literature micropores and mesopores are denoted as nanopores. Porous materials are part of a growing research interest thanks to their large surface area, control over porosity and functionality for specific applications, and when sized down to the nanoscale with good controllable dimensions they are considered to be very relevant for chromatography, catalysis, sorption-selective protein separations, and cooling processes, but also for drug delivery due to their versatility for loading different types of cargos such as drugs.^[99-101] Besides, porous materials from natural

biopolymers (*e.g.*, chitosan, collagen, cellulose) and synthetic biopolymers [*e.g.*, poly(lactic acid), poly(lactic-co-glycolic acid)] have also increasing interest in the biomedical field and food packaging applications, among other areas.^[102] Average pore size, average particle diameter, specific surface area, mean effective porosity, particle shape are important parameters on porous materials that will determine their application.^[103]

There are different types of porous nanomaterials such as porous coordination polymers, metal-organic frameworks, silica, calcium carbonate, calcium phosphate, calcium silicate, porous starch, porous polymers, among others.^[27, 101, 104]

Chapters 3, 4, and 5 will look at two specific porous materials based on porous coordination polymers (PCPs) and calcium carbonate polymeric nanoparticles (CCPNs), respectively, as nanocarriers for intended biological and catalytic applications. Comprehensive information on each material will be provided in the corresponding chapter.

1.3.1. General Concepts

Adsorption Process

The surface of porous and finely dispersed solids can be characterized by gas adsorption methods. Adsorption should not be confused with absorption (see *Figure 1.11*). Adsorption can be defined as a surface phenomenon characterized by the accumulation of molecules from the vapor phase or any solution onto the surface or pores of a solid.^[105, 106]

Generally, an adsorption process can be classified as of physical (*physisorption*) or chemical (*chemisorption*) origin. *Physisorption* occurs when an adsorbable gas comes into contact with the surface of a solid and is related to van der Waals forces. In the case of *chemisorption*, chemical bonds are formed as a consequence of chemical reactions between the solid and the adsorbate (gas). Desorption is the reverse process where a decrease in the amount of adsorbate can be observed. Conversely, in the *absorption process*, atoms, molecules, or ions diffuse into the bulk solid. *Sorption* is a wider term that includes both, adsorption and absorption.^[106]

At a constant temperature (*i.e.*, typically at liquid N₂ one, 77 K) the relationship between the adsorbed solid per unit mass (Q) and the gas pressure (p) is generally described through *adsorption isotherms*, where Q is presented as a function of the relative pressure p/p_0 , (p_0 is the saturation vapor pressure).^[107, 108]

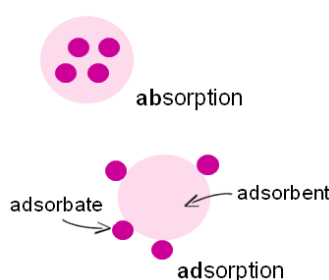


Figure 1.11. Schematic illustration of the difference between absorption and adsorption.

Overview of BET Theory and Determination of Surface Area: The Brunauer-Emmet-Teller (BET) Adsorption Method

The BET method has become the preferred one to determine the surface area of solids based on the adsorption of a gas onto a surface. In 1940, Stephen Brunauer, Paul Emmett, and Edward Teller developed the BET theory, which is closely related to Langmuir's one developed by Irving Langmuir in 1916. Langmuir's theory assumes that gas molecules on the surface of a sample form an adsorbed monolayer; in this case, all the adsorbed molecules are in contact with the surface of the adsorbent material. On the other hand, BET theory assumes that multilayers of gas molecules are able to form onto the adsorbent, and all layers are in thermodynamic equilibrium.^[109]

The type of adsorbate and adsorbent, the adsorbent surface area, and the experimental conditions are factors that affect the adsorption rate. *Figure 1.12a* represents the BET adsorption multilayer model^[110] with the different stages is composed of, as explained below:

S1: Isolated sites on the sample surface begin to adsorb gas molecules at low pressure.

S2: As gas pressure increases, coverage of adsorbed molecules increases to form a monolayer onto the solid surface.

S3: Further increases of gas pressure will cause the beginning of multi-layer coverage; smaller pores in the sample will fill in firstly.

S4: Further increases of the gas pressure will cause a complete coverage of the sample and all the pores will be filled in. When the solid area is fully covered by each adsorbed gas molecule, then the surface area can be calculated. Data collected will be displayed in the form of BET isotherms. The BET equation,^[95] uses the adsorption isotherm information to determine the amount of gas needed in creating the monomolecular layer onto the sample surface:

$$\frac{p/p_0}{n(1-p/p_0)} = -\frac{1}{n_m C} + \frac{C-1}{n_m C} (p/p_0) \quad (1.1)$$

where p is the pressure, p_0 is the saturation pressure, n is the specific amount of the adsorbed gas at the relative pressure p/p_0 , and n_m is the specific monolayer capacity. C is the BET constant, which is exponentially related to the energy of monolayer adsorption.

Types of Adsorption Isotherms

Brunauer *et al.* identified five different types of physisorption isotherms (Type I-V).^[111] Later on, IUPAC (International Union of Pure and Applied Chemistry) proposed a more complete classification^[96] (see *Figure 1.12b*):^[112]

Type I isotherm is concave to the relative pressure axis (p/p^0) and is obtained for microporous solids having relatively small external surfaces such as some activated carbons, molecular sieve zeolites, and some porous oxides, where the adsorbate uptake rate will depend on the accessible micropore volume instead of the total internal surface area.

Type II isotherm is given by non-porous or macroporous adsorbents with unrestricted monolayer-multilayer adsorption. *Type II* and *Type IV* isotherms have a *point M* at the beginning of the middle, almost linear section (see *Figure 1.12b*), which indicates that the monolayer coverage is completed, and multilayer adsorption is ready to begin. *Type IV* isotherm is obtained for mesoporous industrial adsorbents.

Type III isotherm is convex to the relative pressure axis (p/p^0) and does not display an observable monolayer formation implying that the adsorbate-adsorbent interactions are relatively weak.

Type V isotherms are given by water adsorption on hydrophobic microporous and mesoporous adsorbents, and at low p/p^0 , they display a shape similar as *Type III* ones.

Type VI isotherm represents the layer-by-layer adsorption given by a highly uniform non-porous surface.^[95, 110, 112]

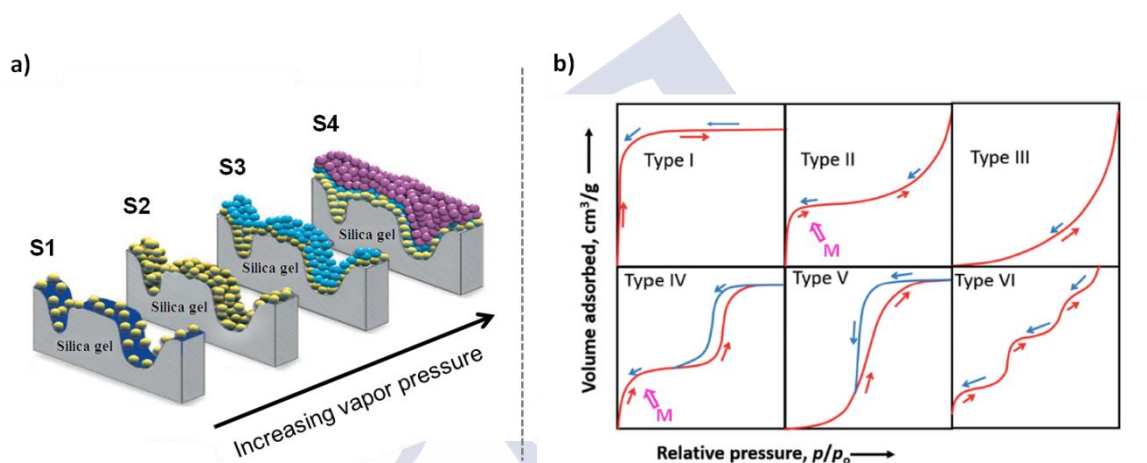


Figure 1.12. a) Pore filling stages at different pressures (BET adsorption multi-layer) (adapted with permission from ref. [110]. Copyright 2012, John White). b) Different types of adsorption isotherms (adapted with permission from ref. [112]. Copyright 2019, The Royal Society of Chemistry).

1.4. Applications of Porous Nanoparticles in Catalysis and Drug Delivery: A General Overview

Catalysis

Nanoparticles' catalytic activity plays a significant role in chemical processes in both industry and academia, where the shape and the surface atom orientation of the nanoparticle will affect the activity and stability of the catalytic reaction.^[39, 113]

Functionalized nanoparticles have gained interest in catalysis, such as coordination polymers, metal-based, graphene-based, carbon nanotubes, core-shell structures, quantum dots, and porous polymers.^[39, 113-120] Moreover, nanomaterials prepared from earth-abundant and inexpensive metals have been proposed as alternative choices to the rare and expensive noble-

metals used as catalysts in chemical processes.^[121] In the case of porous materials, the surface holes can also allow the transit of host molecules through the guest materials.^[122]

Thus, in our case, we are interested in nanostructures based on metal ions and inorganic/organic ligands linked by coordination bonds, know them as coordination polymers (CPs),^[93, 122, 123] these network materials have been used as potential catalysts in heterogeneous catalysis^[93, 119] because they can be porous, they can have catalytically active transition metals centers, and can be designed by changing the metal ions, ligands, anions, coordinated modes, etc. resulting in a large variety of molecular structures.^[122-124]

Therefore, in Chapter 3, we will go through more details about the nanosystem that we selected for the study in question.

Drug Delivery: NIR Light-Triggered

NIR light can interact with plasmonic nanoparticles (i.e., commonly gold nanostructures) to produce what is known as the photothermal effect, where the plasmonic nanoparticle efficiently convert photon energy to heat, creating an increment of the local temperature and thus allowing the release of the entrapped drug.^[60]

The development of plasmonic nanoparticles with LSPR in the NIR (*i.e.*, first biological window, 700-950 nm), and techniques employing NIR sources, has occupied a large fraction of the bioplasmonics research. This is due to the need to avoid attenuation of incident light by most abundant biological components, such as blood, water, and fat, which delimit the biological windows.^[66]

Moreover, by designing the plasmonic NPs surrounded with a porous-selective material shell (*e.g.*, metal-organic frameworks MOFs), an extraordinary size-selectivity of small molecules can be achieved.^[125] In our case, we are interested in core-shell structures based on MOFs and plasmonic nanoparticles; therefore, in Chapter 4, we will go through more details about the nanosystem that we selected for the study in question.

Drug Delivery: Ultrasound-Triggered

In 1989, Kost et al. reported the first study on ultrasound-responsive delivery systems.^[126] Ultrasound consists of longitudinal pressure waves (i.e., sound waves) with frequencies higher than the audible limit of human hearing (i.e., > 20 kHz), and can be classified as low (*i.e.*, 20-100 kHz) or high frequency (> 1 MHz). In principle, ultrasounds at high frequencies can cause thermal damage to cells and tissue induced by heat.^[60] The use of ultrasound as a potential trigger for drug release from nanocarriers has gained increasing attention due to its safety and low cost.^[59, 127] Currently, microbubbles, liposomes, micelles, hydrogels, and polymeric multi-layered capsules are the most existing carriers' systems for ultrasound-triggered drug delivery.^[127]

In our case, we are interested in polymeric multi-layered capsules; therefore, in Chapter 5, we will go through more details about the nanosystem that we selected for the study in question.



1.5. Objectives

General Objectives

Inorganic porous materials have attracted increasing interest thanks to their unique properties such as low-density, uniform, and tunable pore network, large surface area, and high porosity. The properties of porous materials depend on intrinsic factors such as porosity, pore morphology pore size, and pore distribution, which are related to material's selection for a given application.

This Ph.D. thesis aims to demonstrate the importance to control the size, morphology, and functionalization at the nanoscale of the following porous materials: Cu-based coordination polymeric nanoparticles, zeolitic imidazolate framework 8, and calcium carbonate polymeric nanoparticles, respectively. Here, we then focused on exploring three nanoscale synthetic approaches to construct the particles mentioned above as potential candidates for the catalytic reduction of methylene blue and for the construction of external stimuli-responsive drug delivery nanocarriers, respectively. The synthesis optimization approaches for each study followed three basic points: i) Starting with the introduction of additives or growth-blocking agents during the synthesis as a strategy for controlling the nucleation and growth process in order to achieve the desired nanoparticle morphology and size; then, ii) the approaches were accompanied by the appropriate characterization and functionalization of these nanomaterials to assess their colloidal stability; to finally iii) demonstrating their application-targeted properties. My contribution to the work described in the following Chapters 3, 4, and 5, was mostly focused on the synthesis and physicochemical characterization of various porous nanomaterials: a novel Cu⁺²-based nanoPCPs, ZIF-based NPs, and LbL nanocapsules.

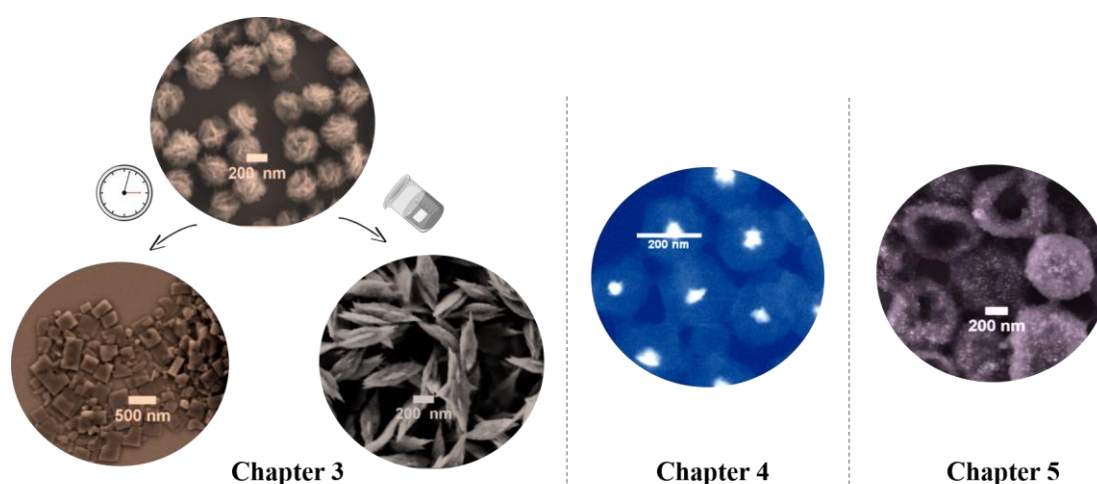
Specific Objectives

Chapter 3 The objectives here can be summarized in: i) To develop a straightforward aqueous synthetic route to fabricate novel Cu-based porous coordination polymer nanoparticles, ii) to optimize the concentration and molar ratios of the reactants including a growth-arresting surfactant (hexadecyltrimethylammonium bromide, CTAB), in order to demonstrate that the obtained nanoparticles can be produced with very high monodispersity, iii) to prove that the synthesis conditions do not lead to a decomposition of the organic linker in the nanoparticles, iv) to prove that the reaction time and the solvent influence on the properties and morphology of the resulting nanoparticles, and v) to evaluate the activity of the nanoparticles in the catalytic reduction of methylene blue.

Chapter 4 The objectives here can be summarized in: i) To demonstrate that zeolitic imidazolate framework-based particles can be produced with very high monodispersity and controlled size using surfactants, ii) to prove that having

control over the growth of ZIF-8 particles it is possible to encapsulate gold nanostars inside ZIF-8 during the synthesis, iii) to demonstrate the loading of the bisbenzimidazole compound Hoechst H 33258 (HOE) by soaking the porous nanocomposite inside the cargo solution, iv) to prove that a post-functionalization strategy based on poly-[isobutylene-alt-maleic anhydride]-graft-dodecyl (PMA) prevents the drug from being released in aqueous medium and inside living cells, and v) to evaluate the thermoplasmonic-responsive release behavior of encapsulated active molecules within the nanocomposite through illumination with near-IR (NIR) light inside living cells.

Chapter 5 The objectives here can be summarized in: i) To demonstrate that CaCO_3 particles can be produced with very high monodispersity and desired size and shape in the presence of poly(vinylsulfonic acid) (PVSA), ii) to demonstrate the encapsulation of three fluorescently labeled macromolecules: dextran (70 kDa), bovine serum albumin (BSA, 66.5 kDa) and recombinant tissue plasminogen activator (rtPA) (70 kDa) via core pre-loading by means of a co-precipitation method, iii) to exploit the layer-by-layer assembly technique to construct our nanosystem based on alternating layers of non-biodegradable poly(sodium 4-styrene sulfonate) (PSS) and poly(diallyl dimethylammonium chloride) (PDADMAC) polyelectrolytes, with Mn/Zn doped iron oxide nanoparticles (ioNPs) as a middle layer, and an outermost one of gelatin in order to provide our nanocarriers with targeting capabilities, iv) to prove that our nanosystem is robust enough to prevent rtPA cargo leakage and, at the same time, to allow US-triggered macromolecule release, and v) to evaluate the ultrasound-triggered release behavior of rtPA *in vitro* and *in vivo* as well as the enzymatic activity of rtPA after being released from the nanocapsules.







Chapter 2

2. Materials & Methods

2.1. Chemicals

General Considerations

All glassware was first cleaned with detergent followed by *aqua regia*, which oxidizes and dissolves residual organic and inorganic impurities, and then carefully rinsed with Milli-Q water and acetone to guarantee an extremely cleaned glass surface. *Aqua regia* solution is prepared by mixing 3 volume parts of hydrochloric acid (HCl) with 1 volume part of nitric acid (HNO₃) and should be used fresh. *Aqua regia* is a corrosive and strong oxidizing agent that should be prepared with care in a well-ventilated fume cupboard with protective clothing, goggles, and gloves.

Reagents were used as received without further purification or modification unless specifically specified. Reagents were purchased from Sigma-Aldrich (reference codes are provided in the following) unless otherwise specified.

2.1.1. Chapter 3

Copper(II) chloride dihydrate (CuCl₂·2H₂O 99.999%, molecular weight MW= 170.48 g·mol⁻¹) was purchased from Stream Chemicals; hexadecyltrimethylammonium bromide (CTAB, 98%, MW = 364.45 g·mol⁻¹) and 2-methylimidazole (2MI, 99%, MW = 82.10 g·mol⁻¹) were purchased from Sigma-Aldrich. All materials were used as received without further purification. Milli-Q water (18.2 MΩ cm) was used in all the experiments.

2.1.2. Chapter 4

Sodium citrate (3.5 mL, 60 mM; Sigma Aldrich #W302600); citric acid (1.5 mL, 60 mM; Acros #A0350656); milli-Q water (18.2 MΩ cm); ethylenediaminetetraacetic acid (EDTA, Sigma Aldrich #EDS); hydrogen tetrachloroaurate (III) (HAuCl₄, Alfa Aesar #12325); AgNO₃ (Sigma Aldrich #209139); cetyltrimethylammonium bromide aqueous solution (CTAB, Sigma Aldrich #H9151); zinc nitrate hexahydrate [Zn(NO₃)₂·6H₂O; Sigma Aldrich #96482]; cobalt (II) nitrate hexahydrate [Co (NO₃)₂·6H₂O, Sigma Aldrich #239267]; 2-methylimidazole (MeIm; Sigma Aldrich #M50850); Hoechst 33258; Sigma Aldrich #96482); Dulbecco's Modified Eagle Medium (DMEM 1X, Gibco, #41966-029); CellMask™ Deep Red (ThermoFisher, #C10046); Milli-Q water (18.2 MΩ cm).

2.1.3. Chapter 5

CaCl₂·2H₂O (147.01 g/mol, #223506); Milli-Q water (18.2 MΩ cm); poly(vinylsulfonic acid) (PVSA, 30 wt. % in H₂O, 5 g/mol, #278424); Na₂CO₃ (105.99 g/mol, #S7795); Pierce™ Coomassie Plus Assay Kit; ThermoFisher #23236; Dextran labeled with rhodamine B isothiocyanate (RBITC, Dextran-RBITC) was used as received (average MW = 70 kDa, #R9379); BSA (66 kDa, #A2153); rtPA (70 kDa, Alteplase, Actilyse™, Boehringer Ingelheim); fluorescein-5-isothiocyanate (FITC, #1245460250); size exclusion column (PD-10, MWCO = 5000 Da; #GE17-0851-01); poly(sodium 4-styrenesulfonate (PSS, MW = 70 kDa, #243051); poly(diallyldimethylammonium chloride (PDADMAC, MW = 250 – 300 kDa, #409022); gelatin (Sigma, #G9391); Fe(acac)₃ (5 mmol, Sigma, #517003); ZnCl₂ (1.1 mmol, Sigma, #229997); MnCl₂ (1.6 mmol, Sigma, #244589); oleic acid (31.5 mmol, Sigma, #364525); oleylamine (60.8 mmol, Sigma, #O7805); benzylether (34.2 mmol, Sigma, #108014); poly(isobutylene-alt-maleic anhydride) (Sigma, #531278); dodecylamine (Sigma, #D222208); ethylenediaminetetraacetic acid (EDTA, Sigma Aldrich #EDS); chromogenic substrate (MW = 658.9 g/mol, #T2943); fluorogenic-based assay SensoLyte® (SensoLyte® AMC tPA Activity Assay Kit from Anaspec, #AS-72160).

2.2. Characterization Techniques

2.2.1. Chapter 3

Optical characterization in solution was performed using a Biochrom Libra S60 UV–visible spectrophotometer. Fluorescence characterization in solution was performed using a Horiba FluoroMax-3 spectrometer. Thermogravimetric analysis (TGA) of powder samples was performed using a TA Instruments Inc. Q5000 operating in nitrogen with sample purge gas flow of 25 mL·min⁻¹, or air, and samples scanned at a heating rate of 10 °C·min⁻¹ from 30 to 800 °C. Elemental analysis was carried out in a Flash 2000 analyser from Thermo Scientific. Fourier-transform infrared spectroscopy (FTIR) of powder samples was performed using a Perkin-Elmer Two equipped with ATR; samples were scanned from 550–3500 cm⁻¹. A X-ray diffractometer Philips was used to studying the crystalline powder of samples; the samples were examined in the range of 2θ between 2° and 75°, with a passage of 0.02° and a time by step of 2s. X-ray thermodiffraction experiment was performed using a D8 Advance Bruker AXS θ-2θ diffractometer equipped with a LYNXEYE XE detector with a copper radiation source (Cu Kα, λ = 1.5406 Å), and an Anton Paar XRK 900 high-temperature chamber. Data were collected under synthetic air atmosphere (10 mL·min⁻¹) in the 2θ range 4-60° and the temperature range of 30-800°C at 10°C intervals. NP hydrodynamic size and polydispersity index (PDI) were determined by dynamic light scattering (DLS) using a Malvern Zetasizer Nano ZSP. TEM images were acquired with a HRTEM Libra 200 FE OMEGA operated at 200 kV. SEM images were acquired with a FESEM Zeiss Ultra Plus operated at 3 kV. Inductively coupled plasma mass spectrometry (ICP-MS) was performed using an ICP-MS quadrupolar Agilent 7700x. Electron paramagnetic resonance (EPR) spectroscopy was performed using a CW X-band EPR Bruker EMX spectrometer. N₂ sorption isotherms (77 K) were done in an AUTO-SORB system

(Quantachrome Instruments). Before the measurement, the sample was evacuated at 50 °C for 16 h. The specific surface was determined by applying the BET equation (Brunauer, Emmett & Teller) in the pressure interval $P/P_0 = 0.02-0.15$ (being P_0 the saturation pressure). Pore size distribution was calculated by the HK method (Horvath-Kawazoe).

2.2.2. Chapter 4

UV/Vis Spectroscopy: A Biochrom Libra S60 UV–visible spectrophotometer was used to record UV/Vis absorption spectrum of the nanocomposites (NCs) in water. **Fluorescence Spectroscopy:** The fluorescence spectrum of HOE before encapsulation (i.e. free dye) and after loading into NCs was determined by fluorescence characterization using a Horiba FluoroMax 3 spectrometer. **TEM images** were acquired with a HRTEM Libra 200 FE OMEGA operated at 200 kV. **SEM images** were acquired with a FESEM Zeiss Ultra Plus operated at 3 kV. **Dynamic Light Scattering (DLS) and Zeta-Potential (ζ):** The hydrodynamic diameter (d_h) and polydispersity index (PDI) of NCs were determined by DLS using a Malvern Zetasizer Nano ZSP equipped with a 10 mW He–Ne laser operating at a wavelength of 633 nm and fixed scattering angle of 173°. The zeta-potential of the particles after PMA functionalization and dispersed in MilliQ water was measured with laser Doppler anemometry (LDA) by using the same Malvern Zetasizer Nano ZSP instrument. **Powder x-ray diffraction (PXRD):** An X-ray diffractometer Phillips was used to study the crystalline powder of samples; the samples were examined in the range of 2θ between 2° and 75°, with a passage of 0.02° and a time by step of 2s. **Thermogravimetric Analysis (TGA):** Thermogravimetric analysis (TGA) of powder samples (freeze-dried) was performed using a TA Instruments Inc, SDT Q-600 thermobalance with a general heating profile from 30 to 600 °C with a heating rate of 5 °C·min⁻¹ under air using a flux of 100 mL min⁻¹. **N₂ sorption isotherms (77 K)** were done in an AUTO-SORB system (Quantachrome Instruments, Boynton Beach, FL, USA). Before measurement, samples were evacuated at 150 °C for 16 h. Specific surface area was determined by applying BET equation (Brunauer, Emmett & Teller) in the pressure interval $P/P_0 = 0.01-0.3$ (being P_0 the saturation pressure). Pore volume and pore size distribution were calculated by the NLDFT method (Non-Localized Density Functional Theory) and the HK (Horvath-Kawazoe) methods, respectively. **Confocal images** of living cells were captured on an Andor Dragonfly spinning disk confocal system mounted on a Nikon TiE microscope equipped with a Zyla 4.2 PLUS camera (Andor, Oxford Instruments). The intracellular monitoring of cargo delivery upon illumination with a NIR light (785 nm, 3 mW) was carried out by using Surface-enhanced Raman spectroscopy (SERS) imaging with a confocal microscope. The inelastic radiation was collected with a Renishaw Invia system, using a high-resolution grating of 1200 g cm⁻¹ and a NIR laser (785 nm).

2.2.3. Chapter 5

An X-ray diffractometer Philips was used to study the crystalline powder of samples; the samples were examined in the range of 2θ between 2° and 75°, with a passage of 0.02° and a

time by step of 2s. The morphology and size of NPs, cores and nanocapsules were characterized by electron microscopy (HRTEM Libra 200 FE OMEGA operated at 200 kV and FESEM Zeiss Ultra Plus operated at 3 kV); for the size histograms (*i.e.*, average diameters) 150-300 nanoparticles (*i.e.*, cores or nanocapsules), were analyzed using ImageJ. Hydrodynamic diameters of cores and nanocapsules, ζ -potential values and polydispersity index were determined by DLS using a Malvern Zetasizer Nano ZSP. Optical characterization in solution of cores, nanocapsules, supernatants and dye-labeled biomacromolecules was performed using a Biochrom Libra S60 UV–visible spectrophotometer, a Horiba FluoroMax-3 spectrometer, a Tecan Infinite F200 PRO microplate reader and/or a NanoDrop 3300 fluorospectrometer, respectively. Pierce TM Coomassie Plus Assay Kit; ThermoFisher was used to determine the protein concentrations. Macromolecule loading was evaluated by fluorescence quantification. Nanocapsules concentration and quantification of macromolecules per nanocapsule (*i.e.*, fluorescence per nanocapsule) were evaluated by flow cytometry using a Guava® easyCyte BG HT flow cytometer (Millipore®), at a constant flow rate of 0.12 $\mu\text{L/s}$, using a blue laser emitting at 488 nm and a green laser emitting at 532 nm as excitation. The signal of the NCs ($d > 500$ nm) from the background in fluorescence, forward and the side light scattering detector can be discerned. Background measurements in PBS buffer were performed before each measurement series. Quantification of the rtPA activity in different samples was performed by a chromogenic assay. US-triggered macromolecule release was quantified by fluorescence measurements. In the case of US-released rtPA from nanocapsules, rtPA was additionally quantified by a fluorogenic assay (Sensolyte) and a clot assay. A Reflotron system was used to analyze toxicity markers after administration of loaded nanocapsules. US experiments were carried out in polypropylene Eppendorf tubes and Transonic Gel@ was used to transmit the US waves. After US treatments, the samples were transferred to a 96-well plate in which the blood clots were formed. Inductively coupled plasma mass spectrometry (ICP-MS) was performed using an ICP-MS Agilent 7700x, which was used to quantify Fe content in different organs. Statistical significance was assayed by the t-test test using GraphPad Prism 6. Swiss male mice (25 to 30 g, Harlan Laboratories, Barcelona, Spain) were used as animal model to investigate the *in vivo* performance of the rtPA loaded nanocapsules particles for US-controlled release of rtPA. MRI studies were conducted on a 9.4 T horizontal bore magnet (BrukerBioSpin, Ettlingen, Germany) with 12 cm wide actively shielded gradient coils (440 mT/m).

2.3. Methods

2.3.1. Chapter 3

Synthesis of Nanocomposites

Typically, 1 mL of an aqueous solution of 2MI (1 M) and 1 mL of an aqueous solution of CTAB (1 mM) were added simultaneously to 1 mL of an aqueous solution of $\text{CuCl}_2 \cdot 2\text{H}_2\text{O}$ (at different concentrations). The reaction may be scaled at least up to 30 mL (*i.e.*, 10 mL instead of 1 mL of each reactant) with equivalent results.

The solution was gently stirred for 1 min in which the color of the solutions changed from bluish to brownish. Then, the solution was left undisturbed for 45 min at room temperature (RT). The resulting nanocomposites were purified by centrifugation (7192 rcf, 15 min), the supernatant was discarded, and the precipitate was redispersed either in 3 mL of water or 3 mL of acetone (other solvents such as methanol, acetonitrile, ethyl acetate, and dimethylformamide were also tested).

2.3.2. Chapter 4

Synthesis of Nanoparticles Seeds

First, 144 mL of Milli-Q water were placed in a 250 mL three-necked round-bottomed flask connected with a condenser and heated up until boiling (*ca.* 100 °C) with a heating mantle. Then, a mixture of sodium citrate (3.5 mL, 60 mM) and citric acid (1.5 mL, 60 mM) was added and kept under vigorous stirring (450 rpm) for 30 min. After that, 0.1 mL of 30 mM ethylenediaminetetraacetic acid (EDTA) was injected, followed by the quick addition of 1 mL aqueous solution of 25 mM hydrogen tetrachloroaurate (III) (HAuCl₄). After 60 s the color of the mixture changed from pale yellow to dull blue and then to wine-red, indicating the growth of spherical NPs. The heating was then switched off, while the solution was kept under magnetic stirring. When the temperature had dropped to 95 °C (*ca.* 5 min), the three-neck flask was immersed in a cold-ice water bath to arrest the NP growth. The concentration of the Au NPs was determined from absorption spectra,^[17]

$$A(\lambda) = \varepsilon_{NP}(\lambda) \cdot l_{sol} \cdot C_{NP} \quad (2.1)$$

the molar extinction coefficient $\varepsilon_{NP}(\lambda)$ and the absorption $A(\lambda)$ depend on the wavelength λ and the solvent. l_{sol} is the path length of the cuvette in which the absorbance has been measured (*i.e.*, the distance that the light passes in the nanoparticle suspension during measurements).

Synthesis of the Gold Nanostars (NSs)

In a glass flask, 20 mL of an aqueous HAuCl₄ solution (0.25 mM) were mixed with 0.03 mL of HCl (1 M) and 1.5 mL of the previously prepared NPs seeds, stirring the solution (350 rpm) at room temperature. To this mixture, 0.15 mL of 1 mM AgNO₃ and 0.15 mL of 66.67 mM ascorbic acid were added simultaneously. After 10 min, 5 mL of 0.2 M cetyltrimethylammonium bromide aqueous solution (CTAB) were added to arrest the NS growth. The solution was kept under stirring for 2 min, and the flask was then immersed in a cold-ice water bath for 10 min. Finally, the NSs were collected by centrifugation (4000 rcf, relative centrifugal force, 10 min), washed twice with diluted CTAB solution ($5 \cdot 10^{-4}$ M), and finally redispersed in CTAB solution ($5 \cdot 10^{-4}$ M) to ensure the stability of NSs during their storage.

Synthesis of ZIF-8 and ZIF-67

1 mL of 1.3 M 2-methylimidazole aqueous solution was placed in a glass vial under magnetic stirring at room temperature (RT). Then, 1 mL of 0.025 M zinc nitrate hexahydrate $[\text{Zn}(\text{NO}_3)_2 \cdot 6\text{H}_2\text{O}]$ (ZIF-8) or cobalt (II) nitrate hexahydrate $[\text{Co}(\text{NO}_3)_2 \cdot 6\text{H}_2\text{O}]$ (ZIF-67) aqueous solution was added, and immediately after, 1 mL of cetyltrimethylammonium bromide aqueous solution (CTAB) at different concentrations (0, 0.5, 1 and 2 nM) was added. The mixture was stirred for 2 min and left undisturbed for 3 h at RT. Finally, the particles were collected by centrifugation (7000 rcf, 5 min), washed twice with methanol (MeOH) and finally, redispersed in 3 mL of MeOH.

Synthesis of Pristine ZIF-8 particles

1 mL of 1.3 M MeIm aqueous solution was placed in a glass vial under magnetic stirring at room temperature (RT). Then, 1 mL of 0.025 M $\text{Zn}(\text{NO}_3)_2 \cdot 6\text{H}_2\text{O}$ aqueous solution was added, and immediately after, 1 mL of $5 \cdot 10^{-4}$ M CTAB aqueous solution was added. The mixture was stirred for 2 min and left undisturbed for 3 h at RT, observing during this time the gradually appearance of whitish turbidity, which indicated the formation of the ZIF-8 particles. Finally, the particles were collected by centrifugation (7000 rcf, 5 min), washed twice with methanol (MeOH) and finally, redispersed in 3 mL of MeOH.

Synthesis of Core-Shell AuNS/ZIF-8 Nanocomposite (NC)

The synthetic and purification protocol for the NCs was equivalent to the one previously described for pristine ZIF-8 particles, but a NP solution (NSs at a concentration of 2 nM in $5 \cdot 10^{-4}$ M CTAB aqueous solution) was added instead of the CTAB solution. The resulting NCs redispersed in 3 mL of methanol (MeOH).

Loading Procedure (Hoechst)

NC were loaded with Hoechst (HOE, a fluorescent dye widely used to stain the cell nucleus) just by mixing the NC as dispersed in MeOH (1 mL, 0.67 nM) with a solution of HOE in MeOH (100 μL , 1.87 mM), having, thus, $3 \cdot 10 \times 10^5$ HOE/NC during the incubation. The mixture was incubated overnight at RT to ensure that the maximum loading was reached regardless of the diffusion kinetics of the dye molecules through the NC pores. Then, the excess of the dye was removed by centrifugation and the NC-HOE was washed twice with MeOH to remove the HOE weakly adsorbed onto the ZIF-8 surface.

PMA-Based Amphiphilic Polymer (synthesis)

PMA was synthesized by mixing 20 mmol of poly (isobutylene-alt-maleic anhydride) and 15 mmol of dodecylamine in 40 mL of tetrahydrofuran. The solution was kept under magnetic stirring and reflux (70 °C) overnight. The day after, the solvent was evaporated under vacuum

and the dried polymer was redispersed with 40 mL of chloroform to obtain a final monomer (monomer molecular weight is 154 g/mol) concentration of 0.5 M.

PMA-Functionalization Procedure

NC or NC-HOE as dispersed in MeOH were mixed with PMA in chloroform solution (150 monomers per nm² surface area of NC, assuming a spherical particle of diameter 218 nm), and the solvent (3:1 MeOH:CHCl₃) was slowly evaporated in a rotary evaporator. Then, the dried product was resuspended by adding *ca.* 5 mL of sodium borate buffer (0.1 M, pH 9), aided by sonication (1 min). The resulting NCs (NC-PMA or NC-HOE-PMA) were collected by centrifugation (7000 rfc, 10 min), washed twice with water, and finally redispersed in water.

2.3.3. Chapter 5

Synthesis of CaCO₃ Cores with Different PVSA Concentrations

CaCO₃ sub-micrometric cores were prepared as follows: 1 mL of 20 mM CaCl₂·2H₂O (147.01 g/mol) solution and poly(vinylsulfonic acid) (PVSA) at different concentrations (0, 50, 100 and 500 µM) were mixed under continuous stirring (550 rpm) in a beaker with a magnetic stirrer. Then, 1 mL of 20 mM Na₂CO₃ (105.99 g/mol) solution was added rapidly, the beaker was covered (protected from light), and the solution was mixed (550 rpm) for 30 min at room temperature (RT) in a magnetic stirrer. The cores were obtained by precipitation at 3·10³ rcf (5 min). After centrifugation, the precipitate was washed with a sodium bicarbonate buffer solution (0.1 M NaHCO₃, pH 9) and washed/precipitated once more at 3·10³ rcf (5 min). Finally, the cores were resuspended in 1 mL of Milli-Q water.

Dye labeling (BSA and rtPA- FITC)

The dye-protein was collected according to the manufacturer's instructions (PD-10 Desalting columns):

- Equilibrate the column with approximately 25 mL elution buffer. Discard the flow-through (you can use the plastic tray to collect the flow-through) 4.
- Add sample of a total volume of 2.5 mL. If the sample is less than 2.5 ml, then add buffer until the total volume of 2.5 ml is achieved. Discard the flow-through. 5.
- Elute with 3.5 ml buffer and collect the flow-through.

To avoid the precipitation of rtPA-FITC, the column was equilibrated with 3.5 mg/mL arginine in PBS (10 mM, pH 7.4). The same buffer was used to collect the rtPA-FITC. Without this concentration of arginine, rtPA precipitation inside the PD-10 column occurred quickly, as could be observed simply by visual inspection.

Synthesis of Macromolecule-Loaded Cores

CaCO₃ sub-micrometric cores loaded with dye-labeled biomacromolecules (BSA-FITC, BSA-RBITC, rtPA-FITC, dextran-RBITC) were prepared as follows: 1 mL of 20 mM CaCl₂·2H₂O (147.01 g/mol) solution and poly(vinylsulfonic acid) (PVSA, 0.1 mM; 30 wt. % in H₂O, 5 g/mol) were mixed under continuous stirring (550 rpm) in a beaker with a magnetic stirrer. Then, 20 µL of dye-labeled biomacromolecule ($c_M = 1$ mg/mL) were added. After 5 min of stirring at room temperature (RT), 1 mL of 20 mM Na₂CO₃ (105.99 g/mol) solution was added rapidly, the beaker was covered (protected from light), and the solution was mixed (550 rpm) for 30 min at RT in a magnetic stirrer. The cores were obtained by precipitation at $3 \cdot 10^3$ rcf (5 min). After centrifugation, the precipitate was washed with a sodium bicarbonate buffer solution (0.1 M NaHCO₃, pH 9) and washed/precipitated one more time at $3 \cdot 10^3$ rcf (5 min). Finally, the cores were resuspended in 1 mL of the NaHCO₃ buffer and immediately used for LbL.

PMA-Based Amphiphilic Polymer (synthesis)

PMA was synthesized by mixing 20 mmol of poly (isobutylene-alt-maleic anhydride) and 15 mmol of dodecylamine in 40 mL of tetrahydrofuran. The solution was kept under magnetic stirring and reflux (70 °C) overnight. The day after, the solvent was evaporated under vacuum and the dried polymer was redispersed with 40 mL of chloroform to obtain a final monomer (monomer molecular weight is 154 g/mol) concentration of 0.5 M.

Synthesis of Mn/Zn-doped Fe Oxide NPs (ioNPs)

The inorganic precursors, Fe(acac)₃ (5 mmol), ZnCl₂ (1.1 mmol) and MnCl₂ (1.6 mmol) were placed in a three neck 50 mL round bottom flask. Then, the organic surfactants oleic acid (31.5 mmol), oleylamine (60.8 mmol) and the solvent benzylether (34.2 mmol) were added. The mixture was degassed at 90 °C for 30 min and then, heated to 200 °C (ca.5 °C/min) under N₂ atmosphere. Finally, the temperature was increased to 310 °C at a constant rate of 3.3 °C/min and held the temperature at ca. 310 °C for 1 h. After the solution reached room temperature (RT), methanol was added to the resultant mixture and the ioNPs were cleaned by centrifugation (1500 rcf, 5 min). Finally, after 3 centrifugation steps, the precipitate (ioNP) were redispersed in an organic solvent (chloroform) and stored in the refrigerator (4 °C). To make the oleic acid/oleylamine capped ioNPs stable in aqueous solution, NPs were coated with the amphiphilic polymer dodecyl grafted-poly (isobutylene-alt-maleic anhydride) (PMA). The coating procedure takes place by mixing the solution of ioNPs and PMA in chloroform. After this, the solvent was slowly evaporated under vacuum in a rotavapor system until the mixture was completely dried. Afterwards, the anhydride rings of the polymer chains were opened by the addition of sodium borate buffer (0.1 M, pH 12). The ioNPs were cleaned from the excess of PMA by centrifugation (3×10^4 rcf, 30 min). This process was repeated twice and the final ioNPs solution was kept in MilliQ water.

Preparation of the Gelatin Layer

0.6 g of basic gelatin were dissolved in 12 mL of milliQ water at 50 °C under stirring. When the gelatin was completely dissolved, 12 mL of acetone were rapidly added to the solution. After 10 s, part of the gelatin precipitated in the form of a dense solid. This purified gelatin was dried, and a solution of 7 mg/mL in water was prepared and used for the LbL process.

Layer-by-Layer Assembly (LbL)

• Nanocapsules of Non-Biodegradable Polymers

LbL deposition of polymers and ioNPs was carried out onto freshly prepared macromolecule-loaded cores. Solutions of poly(sodium 4-styrene) sulfonate (PSS, MW = 70 kDa) and poly(diallyldimethylammonium) chloride (PDADMAC, MW = 250 – 300 kDa) at 20 mg/mL and 0.5 M NaCl were prepared in NaHCO₃ buffer (0.1 M NaHCO₃, pH 9). Then, 0.5 mL of the cores (in buffer) were added dropwise into 0.5 mL of PSS solution. The solution was mixed in a vortex mixer for 5 min, and the cores@PSS were precipitated at 3×10^3 rcf (5 min) and washed/precipitated one more time with the buffer solution. Next, the PDADMAC solution was used (same conditions as the PSS deposition) to form the next layer (*i.e.*, cores@PSS/PDADMAC). The solution was mixed in a vortex mixer for 5 min, and the cores@PSS were precipitated at 3×10^3 rcf (5 min) and washed/precipitated one more time with the buffer solution. Then, after the first PSS/PDADMAC bilayer (bL), 0.5 mL of the cores (in buffer) were added dropwise into 0.5 mL of ioNPs solution (in milliQ water, 0.5 M NaCl) to form a layer of ioNPs (*i.e.*, cores@PSS/PDADMAC/ioNPs). Next, a second PDADMAC/PSS bL was formed as previously described (*i.e.*, cores@PSS/PDADMAC/ioNPs/PDADMAC/PSS).

Alternatively, an outermost layer based on basic gelatin was formed (*i.e.*, cores@(PSS/PDADMAC) – (ioNPs) –(PDADMAC/PSS) – gelatin) or additional PDADMAC/PSS bilayers were formed, that is, structures with 4 or 6 bilayers: cores@PSS/PDADMAC/ioNPs/(PDADMAC/PSS)×3 or ×5, respectively.

Finally, the CaCO₃ cores coated with the polyelectrolytes, ioNPs, and gelatin were exposed to ethylenediaminetetraacetic acid (EDTA, 0.02 M, pH 5.5) for 1 hour to produce the hollow NCs loaded with the selected biomacromolecules. Finally, the NCs were washed/precipitated twice at 5×10^3 rcf (5 min).

• Nanocapsules of Biodegradable Polymers

Biodegradable polyelectrolytes, dextran sulfate sodium salt (10 kDa, 2mg/mL, 0.5 M NaCl) (Sigma, #51227) and poly-L-arginine hydrochloride (m.w.70 kDa, 1mg/mL, 0.5 M NaCl) (Sigma, #P3892) as negative and positive respectively, were deposited on CaCO₃ nanoparticles (20 mM - CaCl₂·2H₂O, 20mM - Na₂CO₃, 100μM - PVSA), using layer-by-layer assembly, 0.5mL CaCO₃ nanoparticles (in water) were added to polyelectrolyte solution (0.5 mL). In addition, AuNRs (14.5nM, 0.5mL) and miRNA (50 nM, 0.5mL, Sigma) (30 min at 37 °C, 500

rpm before LbL) were added as a layer. Then, the solution was shaken with a vortex mixer for 5 min (in the case of miRNA 2 h at 37 °C, 500rpm) and precipitated at 5000 rfc for 5 min and washed two times with water. Finally, CaCO₃ NPs coated with the polyelectrolytes were exposed to EDTA (0.02M) to produce hollow nanocapsules.

Post-Loading Method

The hollow nanocapsules of biodegradable polymers were incubated for 2 h at 70°C in an Atorvastatin (ATV) (100µL, 1mg/mL) (Millipore, #189291) solution, and then washed twice with water. Finally, the product was stored at 4°C before characterization.







Chapter 3

3. Copper Based Coordination Polymer Nanoparticles for Catalytic Reduction: Methylene Blue into Leucomethylene Blue

3.1. Introduction

Coordination Polymers

Coordination polymers (CPs) are one-, two-, or three dimensional (1D, 2D, or 3D) polymeric compounds formed by repeating coordination entities (*i.e.*, inorganic, organic or hybrids inorganic-organic). There are several subclasses of CPs, including amorphous CPs, porous coordination polymers (PCPs), metal-organic materials (MOMs), metal-organic frameworks (MOFs), coordination networks (CNs), and so forth. Since the late 1990s, CP chemistry and related applications have greatly evolved from the pioneering contributions on reticular synthesis involving metal centers and organic linkers,^[128] mostly by the groups of O. M. Yagui,^[129, 130] G. Férey,^[131] R. Robson,^[132] and S. Kitagawa.^[133] The initial research interest of PCPs was mainly driven by their structure-dependent network of voids, which makes them ideal materials for storage and separation of different molecules and macromolecules, and for catalysis. PCPs are formed by cation centers, or clusters, interconnected by polydentate organic ligands through strong iono-covalent bonds,^[134-136] and usually highly porous, having very low densities (in the range of $0.2 \text{ g}\cdot\text{cm}^{-3}$). Porous frameworks of PCPs are built by the self-assembly of metal ions, acting as nodes, and organic ligands, acting as spacers (*see Figure 3.1a1*). One interesting feature of PCPs is that by combining metal ions and ligands, frameworks with specific pore size, shape, surface functionality, and metal-complex properties can be produced. The vast diversity of reported PCPs (over 20,000 structures) in terms of crystal size, porosity, geometry, and functionality arises from the multiple possible combinations of metallic centers and organic ligands.^[137, 138] Metal ions are usually those that determine the dimensionality of PCPs: in this manner, in one dimensional (1D) structures the metal ion is coordinated with two ligand molecules that results in a chain; for two dimensional (2D) structures, three or four ligand molecules are coordinated around the metal ion; and for obtaining three dimensional (3D) structures metal ions of higher coordination numbers such as tetrahedral or octahedral are used (*see Figure 3.1a2*).^[123]

The classification of PCPs into three categories based on the framework structure was carried out in 1998, which consists of first, second, and third-generations as shown in *Figure 3.1b*.^[139] When the adsorbed guests are removed from materials of the *first-generation* (*i.e.*, microporous framework compounds), the porosity of the framework collapses in an irreversible process. Whereas *second-generation* materials have stable and robust porous framework compounds that maintain their crystalline structure before and after guest sorption. *Third-generation* materials have flexible porosity framework compounds, which can be transformed when a

physical or chemical stimulus is applied.^[122, 139] Recently, nonporous high-density MOFs have been proposed as next-generation functional materials in diverse fields.^[140, 141]

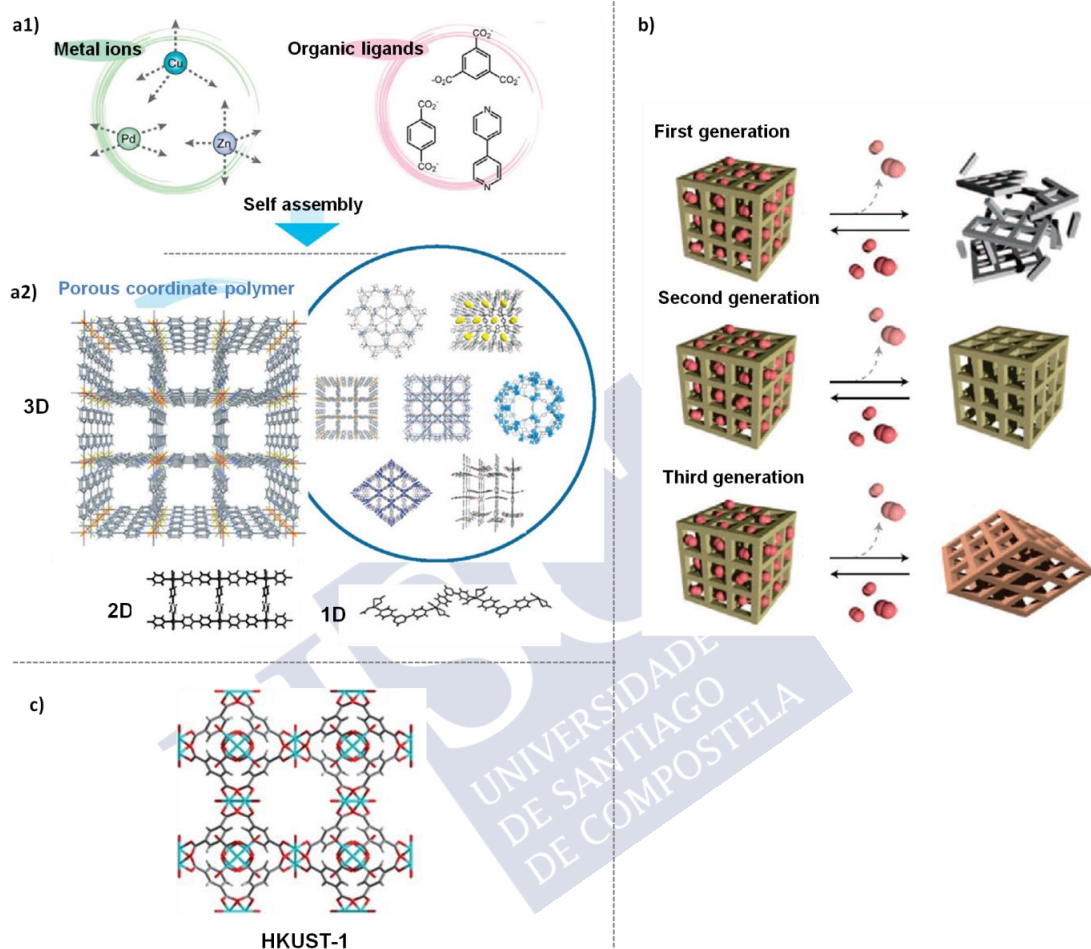


Figure 3.1. a1) Self-assembly of metal ions and organic ligands (adapted with permission from refs. [136]. Copyright 2017, Wiley - VCH Verlag GmbH & Co. KGaA); a2) Porous frameworks with different structures and dimensionality (adapted with permission from refs. [123, 136] Copyright 2017, Wiley - VCH Verlag GmbH & Co. KGaA; Copyright 2010, Wiley - VCH Verlag GmbH & Co. KGaA, respectively). b) Classification of porous coordination polymers into three categories (adapted with permission from ref. [139]. Copyright 2009, Macmillan Publishers Limited). c) Structure of the cubic metal-organic framework HKUST-1 (adapted with permission from ref. [142]. Copyright 2010, The Royal Society of Chemistry).

Initial efforts on PCP chemistry were put on building crystalline new porous bulk three-dimensional structures, in which synthetic control over crystal size, shape, and dispersity was not the key objective. This was so because large single crystals usually facilitate the faster structural resolution of new crystalline phases, as well as because pore size and physicochemical stability were the most useful characteristics in applications such as storage and catalysis. Besides this conventional research aim, recent efforts are also focused on the precise control and modulation of the crystal size and shape and their integration in applicable

devices. In contrast to pure inorganic materials, in which the nanoscale dimensions brings new, highly useful, physicochemical properties (*e.g.*, nanomagnetism, nanoplasmonics, quantum-dots), PCPs, independently of their size, porosity or structure, exhibit localized electronic states rather than delocalized ones.^[143] Conversely, nanoscale PCPs (*i.e.* nanoPCPs) offer a large surface area and ordered tunable porosity that is of great interest for relevant applications such as drug-delivery and device-material nanotechnology.^[144-146]

Composite nanomaterials composed of nanoPCPs and inorganic NPs have been proposed to produce multifunctional nanomaterials (*e.g.*, surface-enhanced Raman scattering nanoprobe,^[125] therapeutics,^[63] theranostic agents^[147, 148]) for bioapplications and enhanced catalysis.^[149, 150] Notice that here amorphous or 1D nanoscale colloids made of organic ligands and metal centers (as in crystalline MOFs) will be referred to as nanoscale CPs (*i.e.*, nanoCPs),^[151] whereas nanoPCPs will be here referred to as PCP crystals having all of their lateral dimensions within the size range of 1-500 nm, although any PCP may be considered nanostructured due to the network of nanometric voids.

Overall, rather few protocols exist to prepare monodisperse nanoPCPs compared with those to fabricate bulk PCPs; some exceptions are Zeolitic Imidazolate Framework 8 (ZIF-8),^[125, 152, 153] diverse MIL (MIL-53, MIL-88A, MIL-88Bt, MIL-89, MIL-100 and MIL-101-NH₂; MIL = Materials of Institut Lavoisier),^[154, 155] diverse UiO (UiO-66, UiO-66-NH₂, UiO-67, UiO-68-NH₂; UiO = Universiteteti Oslo),^[156-158] M-TCPP (M = Zn, Cu, Cd or Co, TCPP = tetrakis(4-carboxyphenyl)porphyrin) nanosheets,^[159] Prussian Blue,^[160] HKUST-1 (HKUST = Hong Kong University of Science and Technology),^[161, 162] porphyrinic-Zr MOF,^[163] NU-1000 (NU = Northwestern University),^[164] and others.^[144, 165]

To attain the fine control of both size and morphology of nanoPCPs, many chemical and microfabrication synthetic strategies have been proposed, including modified solvothermal routes (*e.g.* modulator agents, ligand modification), microwaves- and ultrasound-assisted methods, microemulsions, mechanochemistry or fluidics.^[166] However, many of these approaches suffer from poor control of the particle size distribution and morphology, as well as low reaction yields.

More recently, the use of surfactants under soft conditions (*i.e.*, water, low temperatures, atmospheric pressure) has revealed to be an asset compatible with large-scale production to control both the size and morphology of the zinc imidazolate ZIF-8.^[167] The use of surfactants during the synthesis alters the surface energy of the particles, lowering the surface tension, and thus modifying the shape. The interaction between the surfactant and the surface of the particle during the synthesis will depend on the characteristics of the surfactant head and tail groups and the molar ratio with respect to the precursors.^[168]

Motivation

With regards to Cu⁺²-based nanoPCPs, and despite their industrial interest (*e.g.* natural abundance, low cost, catalytic and conductive properties),^[121] only a few examples can be found

in the literature, being mostly based on the HKUST-1 structure^[169-171] (see Figure 3.1c). Importantly to say that, in these works, the use of surfactants has been also proposed as PCPs growth controlling additives.^[170, 171]

Keeping in mind everything above-mentioned, the development of straightforward high-yield bottom-up methods to fabricate nanosized Cu-based nanoPCPs is desired to better understand and explore their potential catalytic properties. Herein, a straightforward aqueous synthetic route to produce highly monodisperse Cu-based nanoPCPs with different shape is described. Morphology and size of the crystallites, structure, colloidal stability, optical and magnetic activity, and catalytic properties of the obtained NPs were deeply investigated.

3.2. Results and Discussions

3.2.1. The Influence of the Synthesis Parameters: Molar Ratio of the Reactants

Previous works have proposed a variety of chemical methods (bottom-up) for the fabrication of Cu-based CPs based on mixing Cu⁺² salts (mostly Cu(NO₃)₂) and organic ligands containing several carboxylates, such as 2,5-dihydroxyterephthalic acid,^[172] 2-hydroxyterephthalic acid,^[173] 3,3',5,5'-tetrakis(3,5-dicarboxyphenyl)-2,2',4,4',6,6'-hexamethylbiphenyl^[174] and 1,3,5-benzenetricarboxylate.^[175] Also, a few examples of Cu-based CPs built from imidazoles linkers have been also reported so far.^[176-178]

Herein, NPs were fabricated by simply mixing aqueous solutions of CuCl₂ and 2-methylimidazole (2MI), which is the linker used together with Zn²⁺ salts for the fabrication of the ZIF-8 solids.^[179] As a growth-arresting surfactant, CTAB was added using a molar ratio 2MI:CTAB of 10³, (see Table 3.1). The surfactant CTAB has been previously used to arrest ZIF-8 growth, thereby resulting in highly monodisperse ZIF-8 nanoMOFs and nanocomposites based on ZIF-8 and Au NPs.^[125, 180] Surfactants are amphiphilic organic compounds, having water-insoluble and water-soluble moieties. Therefore, a surfactant molecule contains hydrophobic (their tails) and hydrophilic groups (their heads). Most of the surfactants have a hydrocarbon chain as their tail, which can be branched, linear or aromatic. Surfactants are classified based on the polar head group into four types: i) *anionic surfactants* have anionic functional groups in their head, such as sulfate, sulphonate, and phosphate (e.g., sodium dodecyl sulfate, SDS), ii) *cationic surfactants*, having cationic functional groups at their head, such as quaternary ammonium cation (e.g., cetyltrimethylammonium bromide, CTAB), iii) *zwitterionic surfactants* have both cationic and anionic centers in the molecular structure, and the cationic part is based on primary, secondary, or tertiary amines or quaternary ammonium cations, and the anionic part can include sulfonate or carboxylate, and iv) *non-ionic surfactants* where their hydrophilic groups are of non-dissociable type (e.g., Triton X-100).^[181]

In the present work, concentration and molar ratios of the reactants were optimized to produce monodisperse NPs (i.e., sample Cu50 in Table 3.1). Figure 3.2 shows images taken after the reaction for the different particle solutions shown in Table 3.1, whereas their SEM images are shown in Figures 3.3a-j.

Briefly, in a typical synthesis an aqueous solution containing copper (1mL, different concentrations), 2MI (1mL, 1 M), and CTAB (1mL, 1 mM) was gently stirred for 1 min, in which the color of the solutions rapidly changed from bluish to brownish. We hypothesize that this change of color indicates the formation of the Cu^{2+} -imidazolate network, whose growth is arrested by the presence of CTAB to yield monodisperse NPs. Then, the solution was left undisturbed for 45 min at room temperature (RT). The resulting particles were then purified by centrifugation (7900 rpm, 15 min; unless otherwise specified), the colorless supernatant was discarded and the precipitate was redispersed and stored in 3 mL acetone. SEM inspection of the redispersed precipitate revealed the presence of NPs (in the following, referred to as NP1), which show spherical morphology (see *Figure 3.3g-h*) with an average diameter (d) of 330 ± 27 (0.5%) nm (see *Figure 3.5c* or *3.7c*).

Table 3.1. $\text{CuCl}_2 \cdot 2\text{H}_2\text{O}$ concentrations and molar ratios used to produce different nanocomposites.

Sample	$\text{CuCl}_2 \cdot 2\text{H}_2\text{O}$ [mM]	Cu^{2+} : 2MI: CTAB [mol]	2MI: Cu^{2+} [mol]	Cu^{2+} : CTAB [mol]
Cu25	25	1: 40: 0.040	40	25
Cu50 (NP1)	50	1: 20: 0.020	20	50
Cu67	67	1: 15: 0.015	15	67
Cu100	100	1: 10: 0.010	10	100
Cu200	200	1: 5: 0.005	5	200

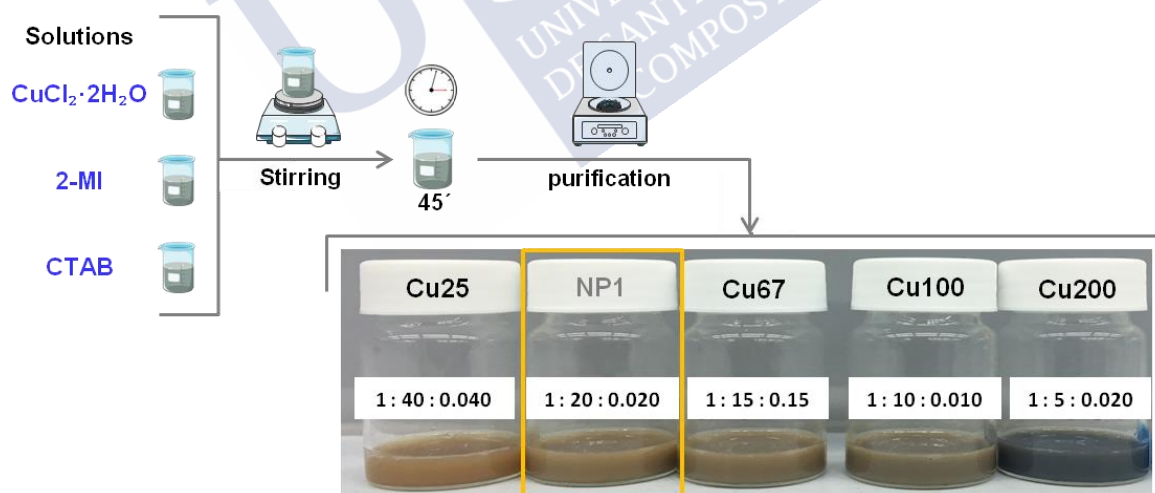


Figure 3.2. Schematic illustration of the synthesis of the Cu-based nanoparticles, and images of the resulting solutions at different $\text{CuCl}_2 \cdot 2\text{H}_2\text{O}$ concentrations and molar ratios shown in Table 1.

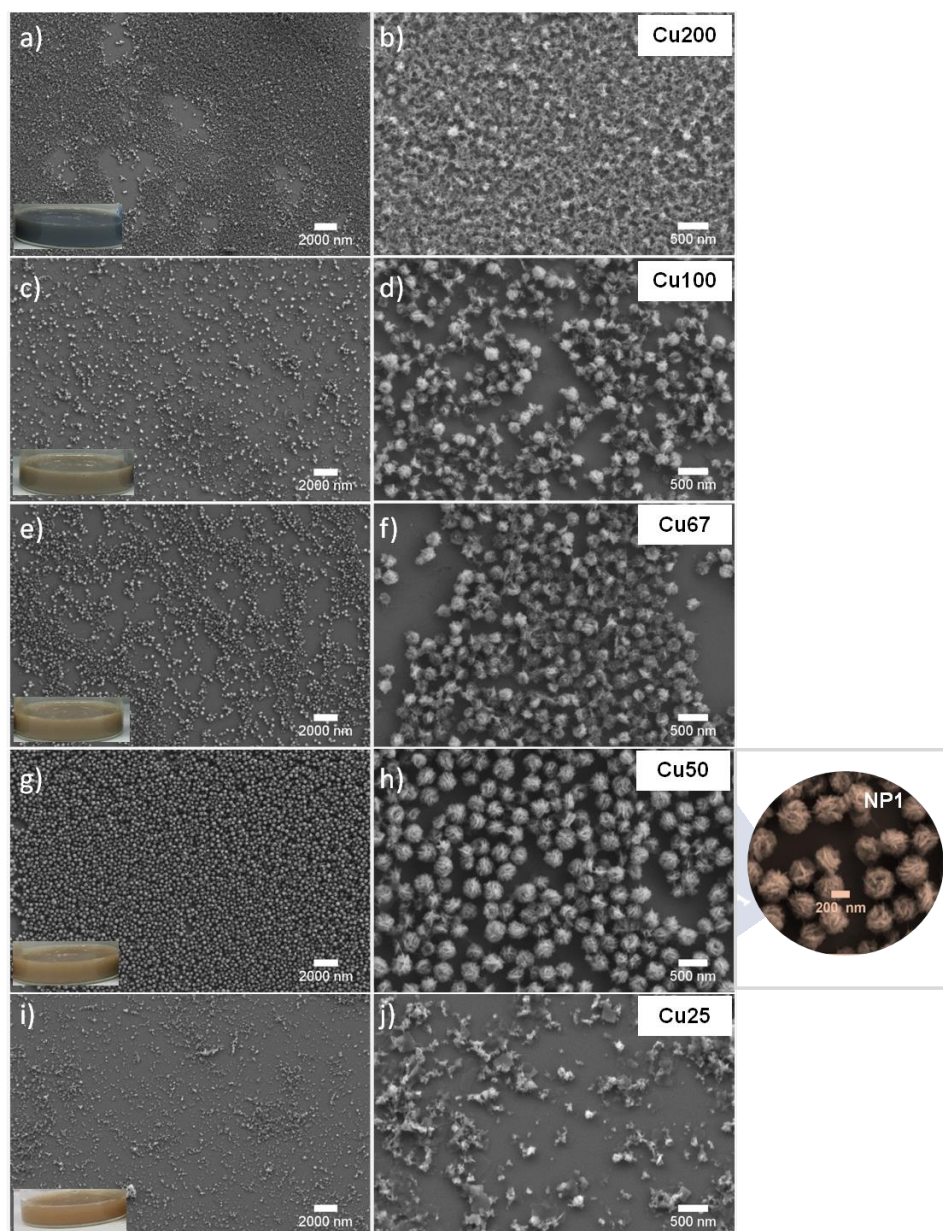


Figure 3.3. SEM micrographs of different Cu-based nanoparticles: a, b) 2MI:Cu²⁺ = 5; c, d) 2MI:Cu²⁺ = 10; e, f) 2MI:Cu²⁺ = 15; g, h) 2MI:Cu²⁺ = 20 (NP1); i, j) 2MI:Cu²⁺ = 40 (adapted with permission from ref. [182]. Copyright 2018, American Chemical Society).

3.2.2. The Influence of the Synthesis Parameters: Reaction Time and Solvent (1st Part)

Previous results have shown that sample labeled as Cu50 (*i.e.*, NP1) with molar ratio 2MI:Cu²⁺ of 20 (and 2MI:CTAB of 10³) showed the best monodispersity, thus, we will use NP1 sample for further experiments. *Figure 3.4* shows the pathways for the synthesis followed in this section.

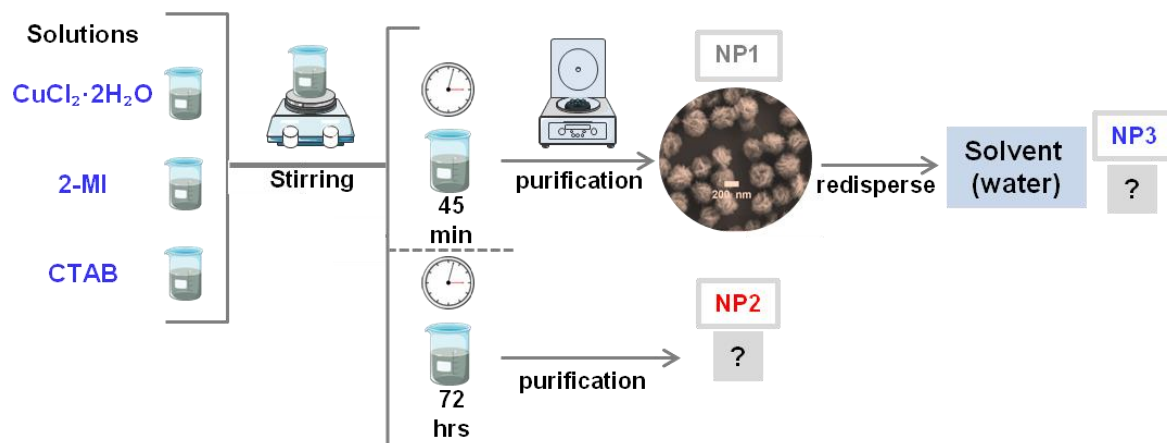


Figure 3.4. Schematic illustration of synthesis for the analysis of the influence of the reaction time and solvent.

i) **Reaction Time (NP2)**

The influence of reaction time was investigated by allowing the reaction to progress at RT, and left undisturbed for 72 h (or even longer: samples inspected even after 6 months did not show any visual difference and remain colloidally stable). The brownish solution appearance remained similar (45 min vs. 72 h, or months) without the presence of apparent precipitates. After 72 h, the nanocomposites were purified by centrifugation, the colorless supernatant was discarded, and the precipitate was redispersed and stored in 3 mL acetone. SEM images revealed the formation of thin nanosheets (see *Figures 3.5d-e*) having an edge length (L) of 334 ± 111 (33%) nm, cf. *Figure 3.5f*, which, in the following, will be referred to as NP2. We hypothesize that the thin entangled nanosheets spherically assembled (NP1, see *Figures 3.5a-b*) thermodynamically evolve to larger nanosheets (*i.e.*, NP2). Equivalent transmission electron microscopy (TEM) micrographs of NP1 and NP2 can be found in *Figures 3.8a-f*.

ii) **Solvent –water (NP3)**

On the other hand, the dispersion of NP1 (see *Figures 3.7a-b*) in MilliQ water also produced color (brownish to grayish) and morphology changes, which evolved over time. At this respect, initially MilliQ water-dispersed samples are composed of fibers (see *Figures 3.6a-b*) as observed from SEM images, but evolved with time and purification after 72 h of incubation (see *Figures 3.6c1-c4*).

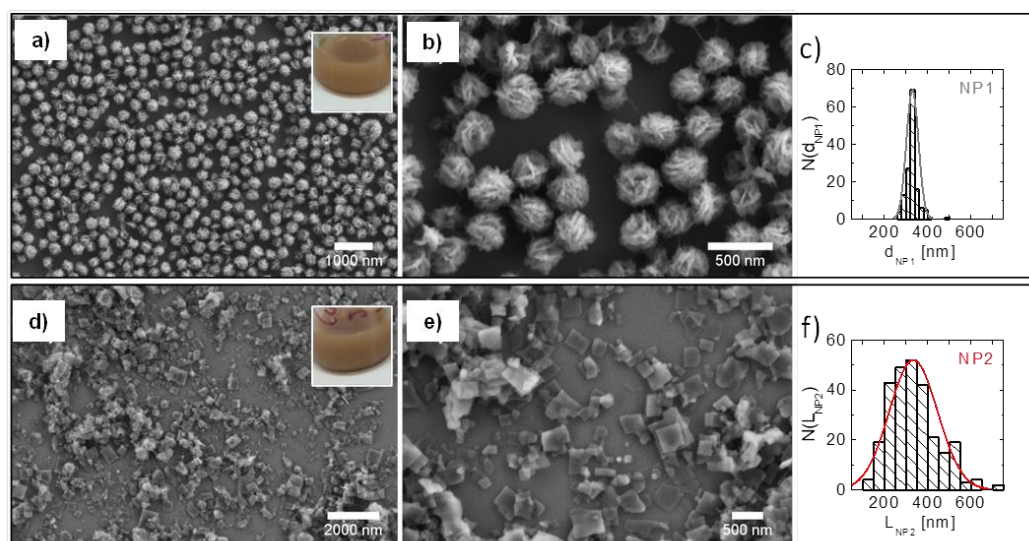


Figure 3.5. SEM micrographs of different species of Cu-imidazole nanocomposites after drop-casting onto Si substrates: a,b) NP1 with an average diameter of 330 ± 27 (0.5%) nm; d,e) NP2 with an average edge length of 334 ± 111 (33%) nm. c,f) Size histograms (d_{NP1} : mean diameter of NP1 and L_{NP2} : mean length of NP2) obtained after measuring the diameter of over 300 NP1 (solvent: acetone, reaction time: 45 min) and NP2 (solvent: acetone, reaction time: 72 h), using ImageJ (adapted with permission from ref. [182]. Copyright 2018, American Chemical Society).

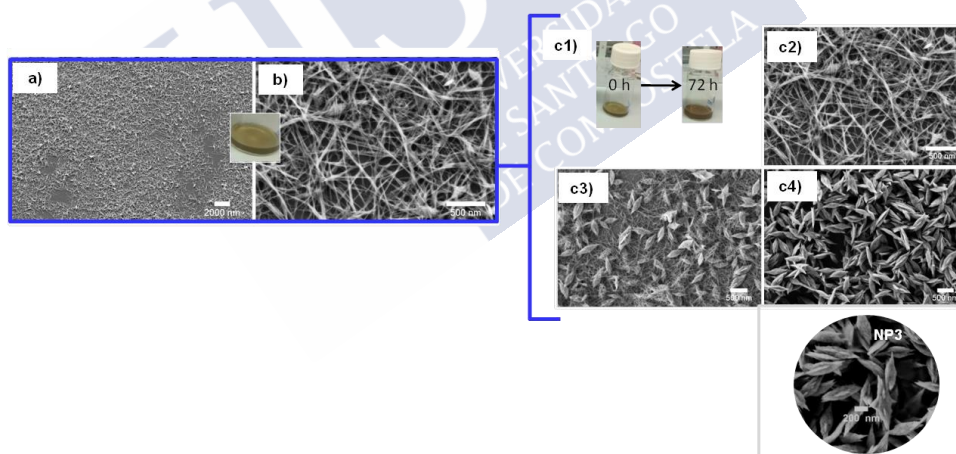


Figure 3.6. Colloidal integrity of NP3 redispersed in H₂O: c1) Color evolution from 0 to 72 h; SEM micrographs after redispersion in H₂O and drop-casting on a Si substrate: c2) 30 min, c3) 24 h and c4) 72 h after mixing of the reactants (adapted with permission from ref. [182]. Copyright 2018, American Chemical Society).

The morphology of the complexes resembles nanospikes (see *Figures 3.7d-e* for SEM and *Figure 3.8g* for TEM images, respectively, in the following referred to as NP3), with an average tip-to-tip length (L) of 447 ± 65 (15%) nm, *cf.* *Figure 3.7f*, and which remain colloiddally stable (with no apparent color or morphology change by SEM inspection) over much longer periods (so far, up to months). This morphological evolution is rather comparable with that observed for CuO nanowire/microflower recently reported.^[183]

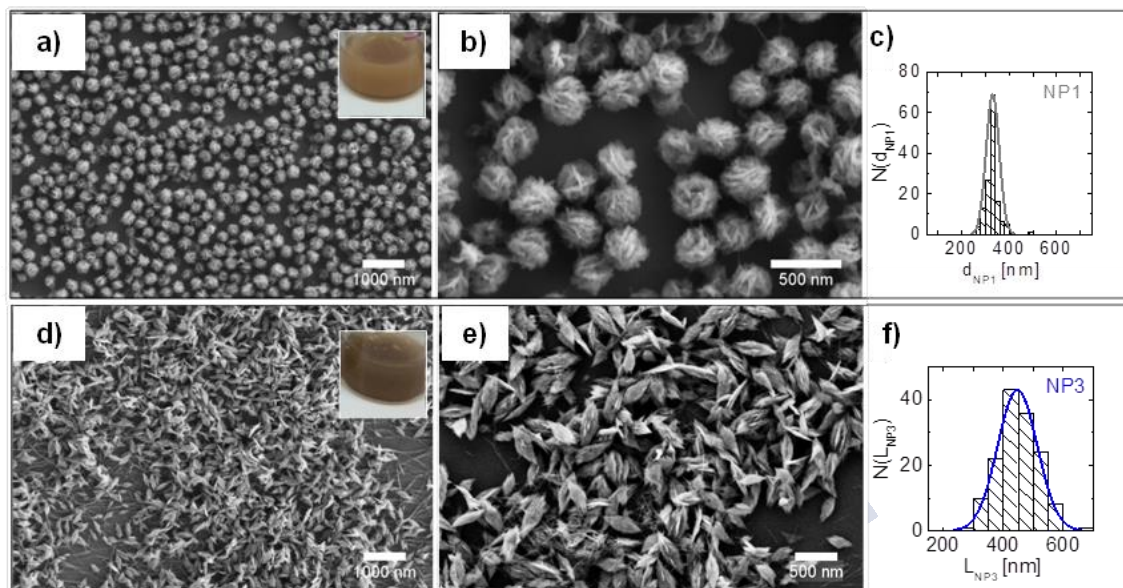


Figure 3.7. SEM micrographs of different species of Cu-imidazole nanocomposites after drop-casting onto Si substrates: a,b) NP1 with an average diameter of 330 ± 27 (0.5%) nm; d,e) NP3 with an average tip-to-tip length of 447 ± 65 (15%) nm. c,f) Size histograms (d_{NP1} : mean diameter of NP1 and L_{NP3} : mean length of NP3) obtained after measuring the diameter of over 300 NP1 (solvent: acetone, reaction time: 45 min) and NP3 (solvent: water, reaction time: 72 h), using ImageJ (adapted with permission from ref. [182]. Copyright 2018, American Chemical Society).

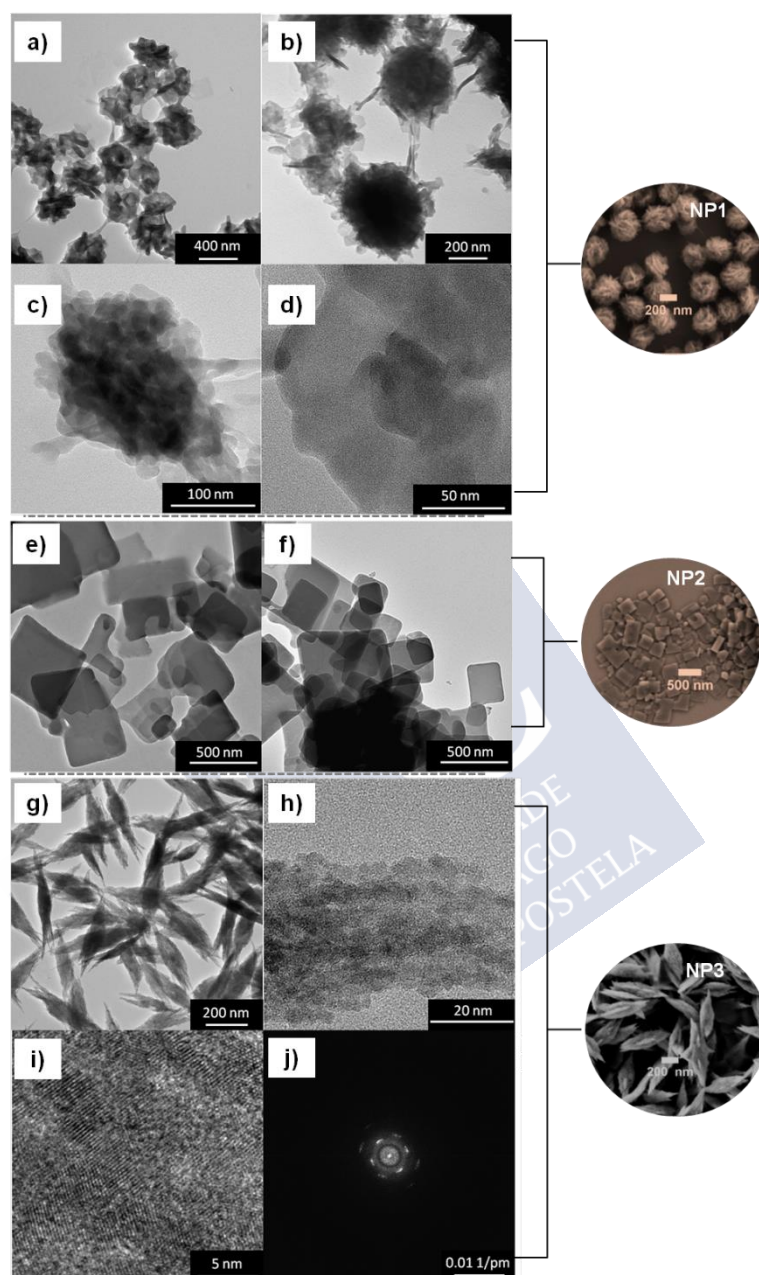


Figure 3.8. TEM micrographs of a-d) NP1, e-f) NP2, and g-i) NP3 after drop-casting on TEM grids. The morphology of NP3 nanoparticles resembles that of recently reported for CuO NPs (0.5 mL of $\text{NH}_3 \cdot \text{H}_2\text{O}$, 30 min reaction).^[183] j) Image shows the SAED (selected area electron diffraction) of NP3 of image i) (adapted with permission from ref. [182]. Copyright 2018, American Chemical Society).

3.2.3. The Influence of the Synthesis Parameters: Solvent (2nd Part)

Apart from water, the influence of different solvents in NP1 morphology was also evaluated. After 45 min of reaction and followed by purification as previously described, the precipitate formed by NP1 was redispersed in different solvents of increasing polarity, that is, ethyl acetate, N, N-dimethylformamide (DMF), acetonitrile, and methanol (see *Figures 3.9a-h*).

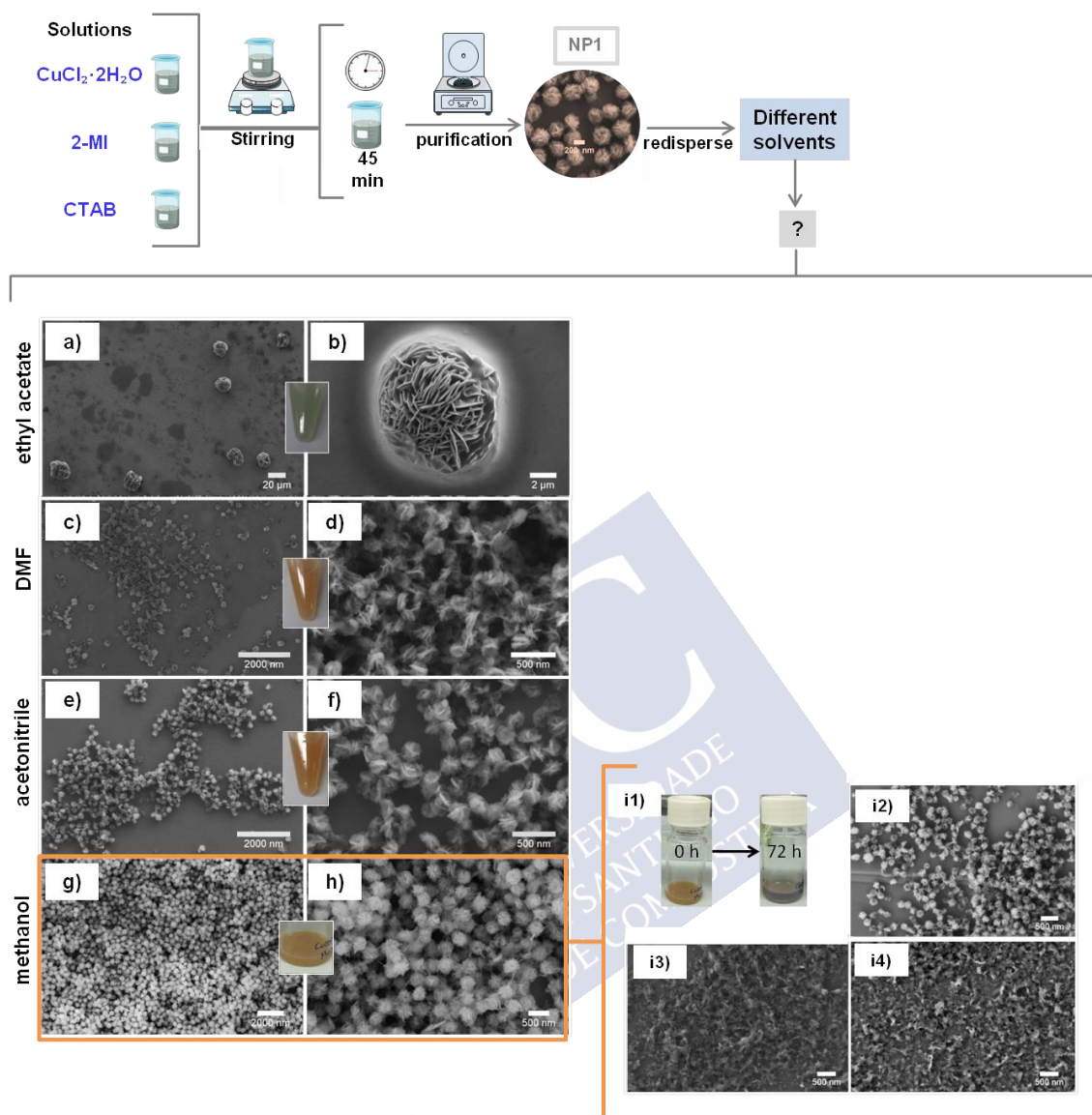


Figure 3.9. Schematic illustration of the synthesis of NP1 sample redispersed in different solvents, and SEM micrographs of the precipitate NP1 redispersed in solvents of increasing polarity: ethyl acetate (a,b), N,N-dimethylformamide (DMF; c,d), acetonitrile (e, f), methanol (g, h). Insets show color images of the corresponding solutions. Colloidal integrity of NP1 redispersed in MeOH: i1) Color evolution from 0 (brownish) to 72 h (violetish); SEM micrographs after redispersion in MeOH and drop-casting on a Si substrate at: i2) 12 h, i3) 24 h and i4) 72 h after mixing of the reactants (adapted with permission from ref. [182]. Copyright 2018, American Chemical Society).

After redispersion in DMF (see *Figures 3.9c-d*), acetonitrile (see *Figures 3.9e-f*) or methanol (see *Figures 3.9g-h*), followed by purification by centrifugation, the solution color (brownish) and the morphology of the resulting particles morphology resembled those of NP1 (*i.e.*, acetone), *cf.* *Figures 3.3g-h*, suggesting the stability of the obtained nanomaterial. In contrast, redispersion in ethyl acetate triggered an immediate color (brownish to greenish) and morphology changes (microstructures formation, see *Figures 3.9a-b*). Besides, samples

redispersed at the beginning in methanol, which retained color and morphology similar as NP1, underwent a change in color (brownish to violetish) and morphology over time, as shown by SEM inspection (see *cf.* evolution of the samples redispersed in methanol over 72 h, *Figures 3.9i1-i4*). Similarly, samples redispersed in DMF and acetonitrile underwent a change in color over time.

3.2.4. Selected Nanoparticles

To summarize the previous results, the sample labeled as Cu50 (*i.e.*, NP1) showed the best-defined nanosphere morphology after 45 minutes of reaction. Then, if the reaction time increased to 72 hours, the nanospheres NP1 resembled an entangled network of nanosheets (*i.e.*, NP2). Additionally, the influence of different solvents in NP1 morphology was also evaluated; however, the dispersion of NP1 in water tuned its shape from fibers to nanospikes (*i.e.*, NP3) after 72 hours.

NP1, NP2, and NP3 are particularly interesting samples due to its colloidal stability over time that was inspected visually by monitoring the sedimentation behavior of them. Therefore, the samples shown in *Figure 3.10* (*i.e.*, NP1, NP2, and NP3) will be used for further characterizations.

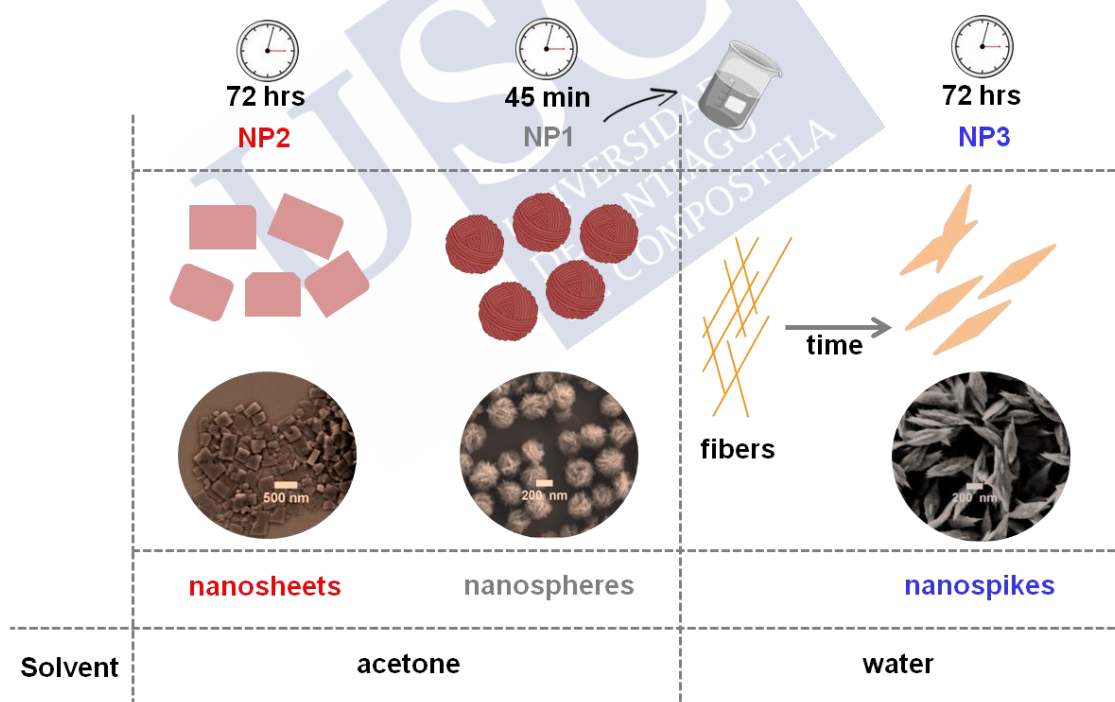


Figure 3.10. Schematic illustration and SEM images of the nanoparticles selected for this study.

3.2.5. Structural Characterization

i) Powder X-Ray Diffraction (PXRD)

NP1, NP2, and NP3 exhibit a crystalline state characterized by long-range order, with two types of Powder X-Ray Diffraction (PXRD) patterns, *cf.*, *Figure 3.11*. First, despite a slight difference in the full width at half maximum (FWHM), NP1 and NP2 share an identical new structure, having main diffraction peaks at *ca.* 14.1, 14.5, 29.5, 33.1 and 48°. The structural solving was, however, not possible due to the weak diffraction power as well as their small crystallite size. The different FWHM (see *Table 3.2*) might be related to the larger crystal size of NP2. The nanosheets of NP2 seem to be those detangled from the NP1 nanospheres as a result of thermodynamic crystallization.

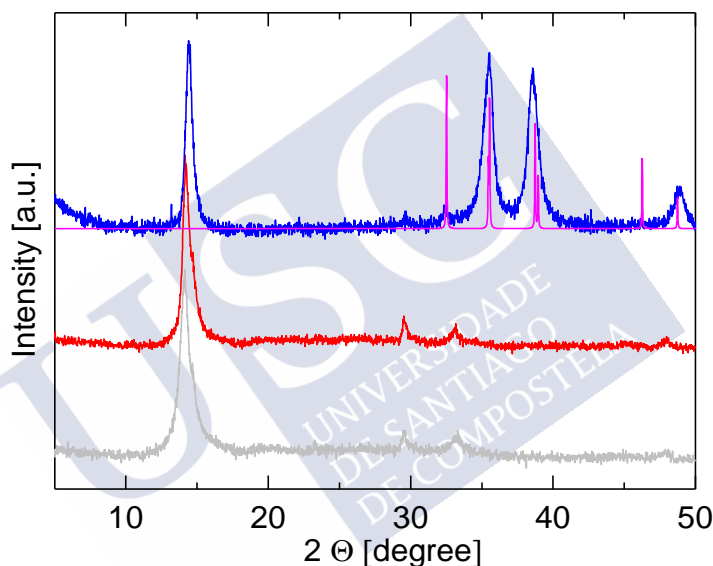


Figure 3.11. PXRD patterns of NP1 (grey), NP2 (red), and NP3 (blue), and a simulation of the tenorite form of copper (II) oxide (magenta) based on previous work (adapted with permission from ref. [182]. Copyright 2018, American Chemical Society).^[184]

In the second type of PXRD patterns, corresponding to NP3, two crystalline phases coexist: i) Bragg reflections at 14.4 and 29.7°, corresponding to the NP1/NP2 phase; and ii) diffraction peaks at 32.3, 35.5, 38.5 and 49° that can be assigned to the 110, 111, 200 and 202 Miller indices of the tenorite form of copper (II) oxide (see *Figure 3.11*),^[183] coming probably from the partial transformation of NP1 into CuO after redispersion in Milli-Q water. This result is in total agreement with the TEM observations shown in *Figure 3.8*. Several relevant peaks were identified by PXRD and summarized in *Table 3.2*.

Table 3.2. Peaks identified in NP1, NP2 and NP3 diffractograms, respectively.

Sample	Pos. [° 2 θ]	Height [cts]	FWHM Left [° 2 θ]	d - spacing [Å]	Rel. Int. [%]	Area [cps·° 2 θ]
NP1	14.179(3)	586(13)	0.40(1)	6.24142	100.00	102.14
	14.50(2)	378(12)	1.05(1)	6.10316	64.54	174.11
	29.576(9)	101(5)	0.36(2)	3.01793	17.31	16.12
	33.08(2)	56(4)	0.51(5)	2.70598	9.57	12.53
	34.2(3)	10(2)	3.5(5)	2.62169	1.75	15.55
	47.89(3)	32(3)	0.80(8)	1.89779	5.40	11.19
NP2	14.11(1)	727(7)	0.74(3)	6.27122	100.00	284.20
	14.70(4)	107(24)	0.16(8)	6.02139	14.73	19.80
	29.50(4)	83(6)	0.29(9)	3.02511	11.36	14.93
	33.13(8)	60(4)	0.8(2)	2.70212	8.22	29.50
	48.2(2)	32(2)	4.0(5)	1.88704	4.42	36.70
NP3	14.403(8)	668(7)	0.50(2)	6.14456	100.00	168.38
	29.68(2)	52(5)	0.3000	3.00715	7.72	6.27
	32.37(8)	48(6)	0.3(2)	2.76375	7.22	7.35
	35.53(1)	553(6)	0.97(3)	2.52495	82.83	183.02
	38.573(7)	530(5)	0.80(2)	2.33218	79.32	199.79
	48.95(5)	144(4)	1.1(1)	1.85936	21.49	69.57

ii) *Electron Paramagnetic Resonance (EPR)*

Electron paramagnetic resonance (EPR) spectroscopy is a powerful technique to characterize the electronic structure of paramagnetic metal centers, such as Cu²⁺ in metalloproteins,^[185] MOFs,^[186] and molecules.^[187] In an EPR experiment, the unpaired electron spin of the Cu²⁺ interacts with the magnetic field and the surrounding nuclear spins, thereby providing a spectrum with a characteristic pattern that provides information about the coordination ligands and the geometry of the Cu²⁺ complex. EPR spectroscopy is very sensitive to changes in the electronic configuration of a Cu²⁺ center and, thus, highly useful to inspect the Cu²⁺-2MI species investigated here. *Figures 3.12a-c* shows the EPR spectra of NP1, NP2, and NP3 in frozen solutions (120 K), which include all possible orientations of an analogous single crystal with respect to the magnetic field. The three solids show the typical features of Cu²⁺-imidazole complexes,^[188] therefore, demonstrating the formation of the Cu-N bond in the three NPs. Due to the interaction of the unpaired electron spin of the Cu²⁺ and its nuclear spin (3/2), the hyperfine pattern of each species exhibits three of the four hyperfine transitions in the parallel

region of the spectra (low-field range, *i.e.*, four-arrow pattern in *Figure 3.12*) while the fourth component is masked by an overlap with the hyperfine transitions in the perpendicular region and with “extra absorption” features towards the high-field end of the spectra,^[189] *cf.* *Figure 3.12*. In Cu^{2+} complexes, nitrogen ligands can interact with the unpaired electron of the Cu^{2+} and give rise to a further splitting of the hyperfine pattern, *cf.* *Figure 3.12d*, referred to as superhyperfine pattern, which accounts for the number of nitrogen ligands. Remarkably, the nine-line superhyperfine splitting (1.5 mT) is consistent with four strongly coordinating and largely equivalent nitrogen ligands in a square planar coordination, as previously reported in Cu(II)-metalloproteins and tetrakisimidazolecopper(II) sulfate.^[185, 189, 190] We speculatively associate a better resolution of the superhyperfine splitting of NP2/NP3 in comparison with NP1 as an indication of a more equivalent nitrogen-copper interaction (*i.e.*, similar bond distances and tetragonal distortion), resulting from the longer crystallization time and refinement of the structure after thermodynamic growth compared to the kinetic growth observed for NP1/NP3.

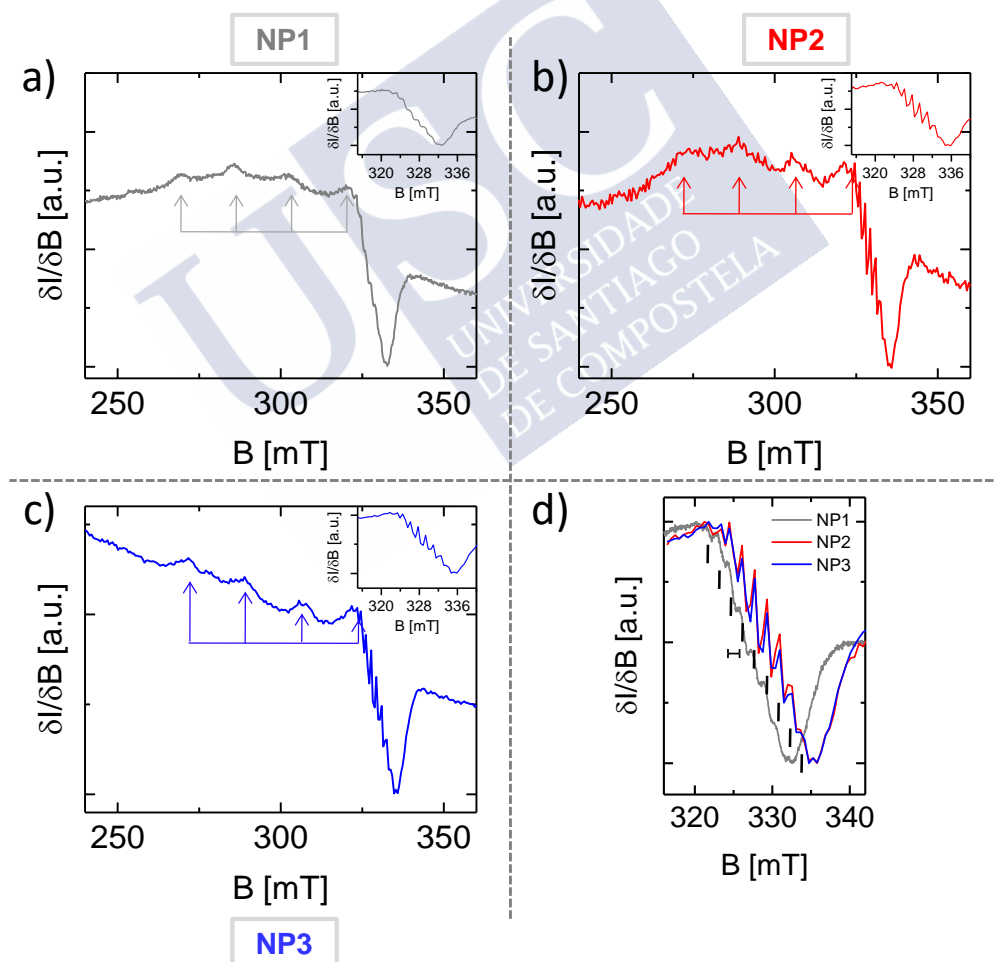


Figure 3.12. Frozen solution (120 K) EPR spectra of species: a) NP1 (grey; acetone); b) NP2 (red; acetone); c) NP3 (blue; water); d) Hyperfine transitions in the perpendicular region of the three species having “extra absorption” features towards the high-field end of the spectra, *i.e.*, superhyperfine splitting due to the interaction of the unpaired electron of Cu^{2+} with nitrogen ligands. Nine discontinued lines homogeneously

spaced (1.5 mT) point at this superhyperfine splitting (adapted with permission from ref. [182]. Copyright 2018, American Chemical Society).

Besides, these spectra present varying degrees of distortion due to $\text{Cu}^{+2}\text{-Cu}^{+2}$ dipolar coupling, particularly dominant in NP3, which is apparent in the EPR powder spectra (RT) of the three species, *cf.*, full-width spectra in *Figures 3.13-15*. *Table 3.3* gives numerical values of the four-arrow patterns depicted in *Figure 3.12*. EPR spectra of NP2 and NP3 are very similar, both providing parameters listed in *Table 3.3* and superhyperfine splitting (1.5 mT) towards the high-field end of the spectra. It is important to notice that copper (II) oxide, a major component of NP3 as determined by PXRD, is EPR-silent due to extensive spin-spin interactions among neighboring Cu(II) ions, which results in a diamagnetic ground state.^[191] Therefore, the EPR signal observed in NP3 is in agreement with the presence of Cu-N bonds related to Cu^{2+} complexes (likely as NP2), as previously discussed for PXRD data.

Table 3.3. EPR parameters of the X-band spectra of frozen solutions (120 K) of the three types of particles.

Sample	g_{\parallel}	A_{\parallel} (mT)
NP1	2.28	16.7
NP2	2.26	17.2
NP3	2.26	17.2

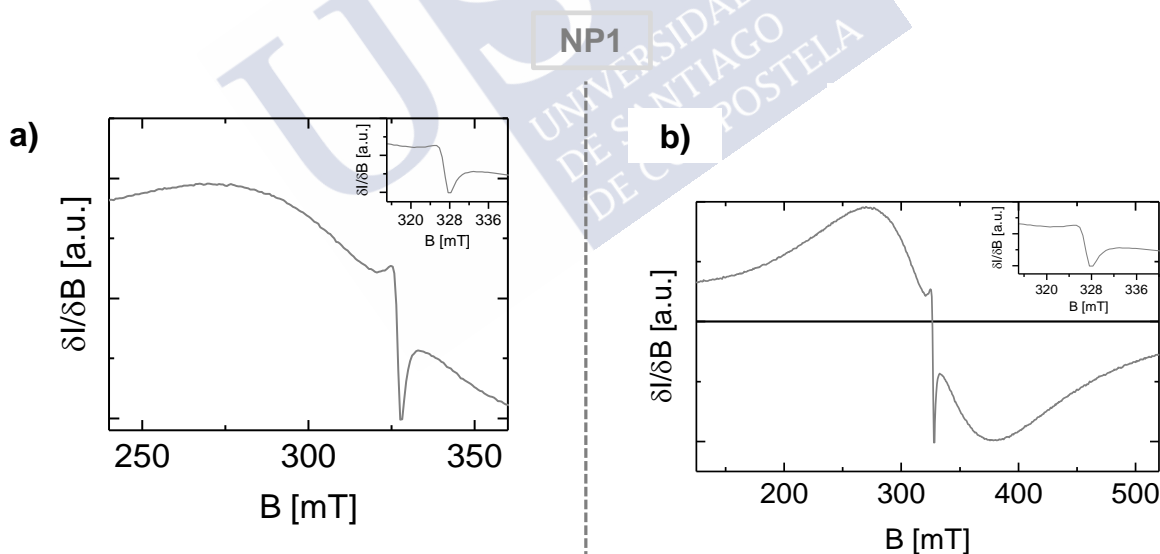


Figure 3.13. a, b) Powder (RT) EPR spectra of NP1 (adapted with permission from ref. [182]. Copyright 2018, American Chemical Society).

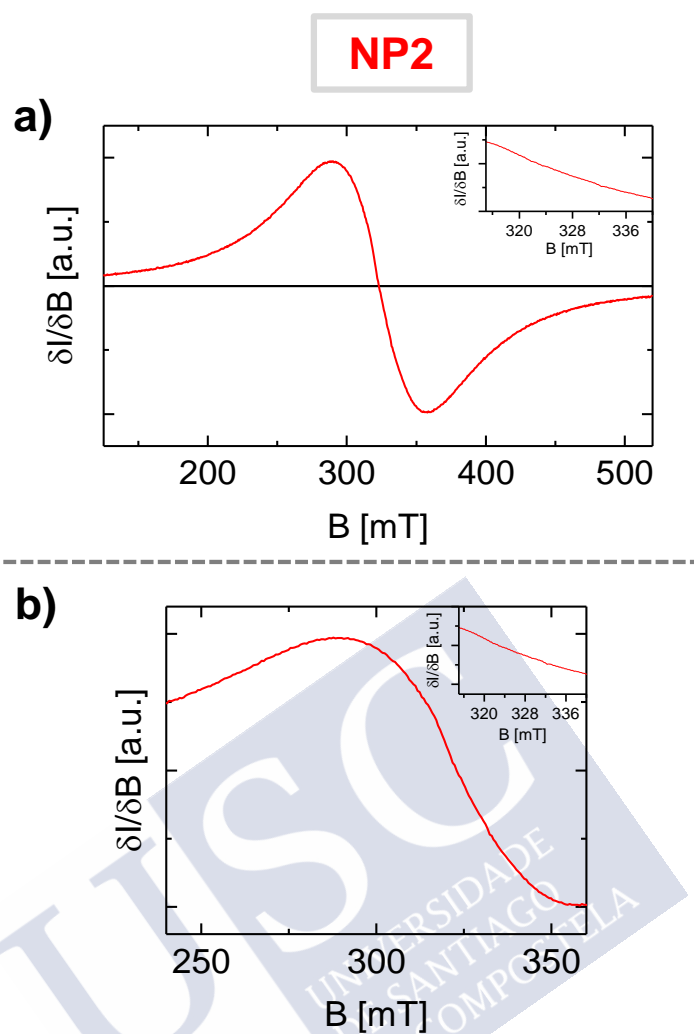


Figure 3.14. a, b) Powder (RT) EPR spectra of NP2 (adapted with permission from ref. [182]. Copyright 2018, American Chemical Society).

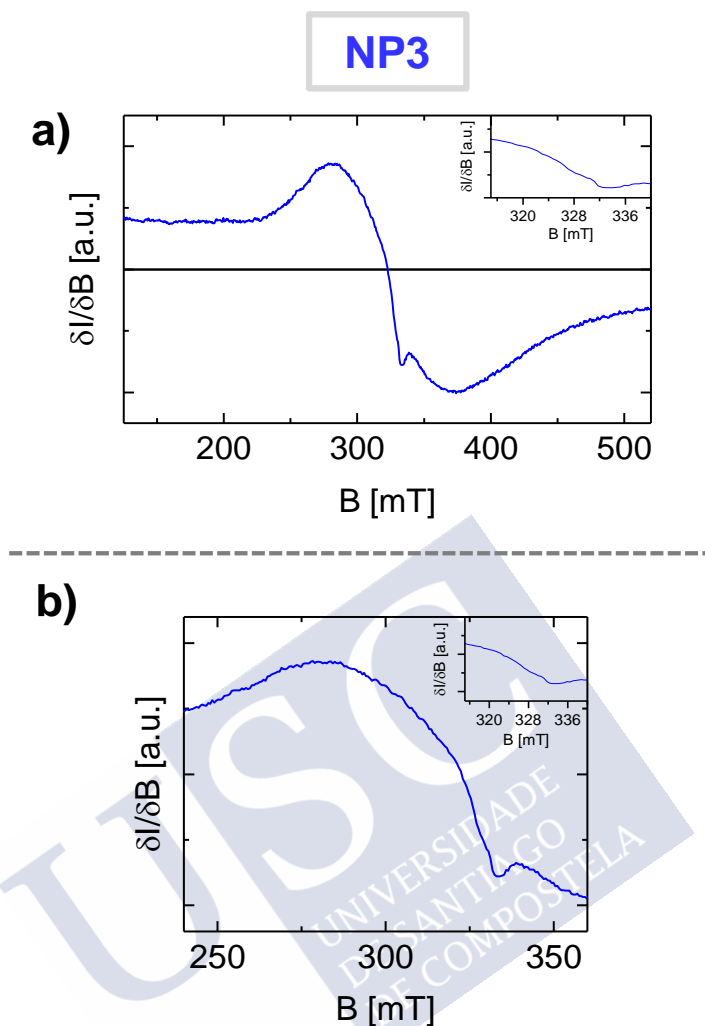


Figure 3.15. a, b) Powder (RT) EPR spectra of NP3 (adapted with permission from ref. [182]. Copyright 2018, American Chemical Society).

iii) *Fourier-Transform Infrared Spectroscopy (FTIR)*

Fourier-transform infrared spectroscopy (FTIR) is a useful technique for the determination of functional groups in the structure of compounds, thus, FTIR may provide information on the structure of the Cu-2MI coordination polymers. FTIR spectra corroborate the presence of 2MI in NP1, NP2, and NP3, as shown by the characteristic 2MI bands, *cf.* asterisks in *Figure 3.16*. Most notably, the three NPs share bands of the 2MI linker at 1438 cm^{-1} and 1296 cm^{-1} due to C-N stretching, and at 1115 cm^{-1} and between $900\text{--}700\text{ cm}^{-1}$ due to C-H stretching. FTIR spectrum of the 3 solids are almost identical, except for NP3, as it exhibits broad bands around 3300 cm^{-1} due to water absorption (-OH stretching), and at frequencies of 610 and 515 cm^{-1} , which are ascribable to metal-oxygen vibrations, thereby confirming the presence of copper(II) oxide. The FTIR features of these three compounds match that of ZIF-8,^[153] as expected due to the use of the same 2MI linker. In this regard, it is worth reminding that CTAB bands at 2915

and 2847 cm^{-1} are derived from the C–H stretching vibration of methyl and methylene groups; in the case of the three NPs, the band at 2847 cm^{-1} seems to vanish, while the band at 2915 cm^{-1} , characteristic of C–H stretching of methyl groups in ZIF-8 solids, still remains. Although we cannot rule out the presence of CTAB, it is unlikely its presence in the analyzed particles provided that the low CTAB concentration used during the synthesis (*i.e.*, below the critical micelle concentration; 2MI:CTAB molar ratio of 1000:1) and the centrifugal purifications with MilliQ water and acetone.

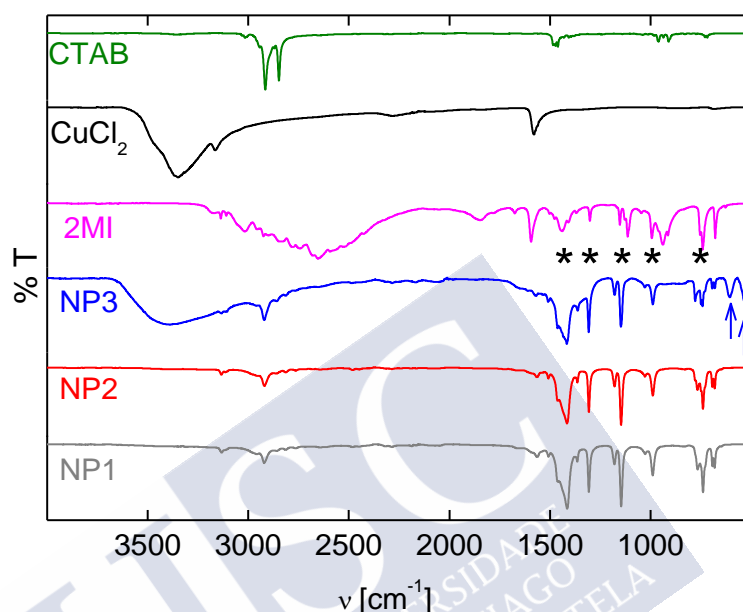


Figure 3.16. FTIR spectra of the starting reactants and the three types of NPs obtained. Asterisks point at 2MI bands (pink) that are observed in NP1 (grey), NP2 (red), and NP3 (blue). Blue arrows point at metal-oxygen vibrations in NP3 (adapted with permission from ref. [182]. Copyright 2018, American Chemical Society).

3.2.6. Thermal Characterization

To investigate the thermal behavior of NP1, both thermogravimetric analysis (TGA, under air and N_2 atmospheres) and temperature dependent PXRD (in air) experiments were performed. TGA curve of NP1 (see *Figures 3.17a-b*) shows two-weight losses: a first sharp mass loss ($\sim 20\text{ wt\%}$) at around $220\text{ }^\circ\text{C}$, and then, a progressive weight loss ($\sim 50\text{ wt\%}$) between 250 and $700\text{ }^\circ\text{C}$, associated with the total combustion of 2MI and the final formation of CuO ($\sim 30\text{ wt\%}$). Note here that the first weight loss is assigned to the departure of 2MI ligand from the particles considering that free ligand is removed from 150 to $200\text{ }^\circ\text{C}$ (see *Figure 3.19*). The higher departure temperature of the ligand within the solid is in agreement with the establishment of interactions with Cu (as previously proved by EPR), observing two types of ligand fractions (departure at 220 and $>250\text{ }^\circ\text{C}$), which might be interacting in a different manner. Also note that under an air atmosphere, degradation and formation of the CuO residue occurs faster than in the N_2 atmosphere. We used both atmospheres to qualitatively study the formation of the CuO residue.

TGA curves of NP2 show a similar behavior than NP1 but with a lower weight loss at 220 °C (20 vs. 25 wt%; cf., Figure 3.17c). From TGA and elemental analysis, the chemical formula $\text{Cu}(\text{C}_4\text{H}_5\text{N}_2)_2$ (theoretical: C=42.5, N=24.8, H=4.5 and Cu=28.2 %) is proposed for NP1 or NP2 (experimental: C = 41.5, N = 24.2, H = 4.4, Cu = 24 % for NP1, and C = 42.3, N = 25.53, H = 4.3, Cu=29 % for NP2, respectively). The better correlation with the proposed formula of NP2 might be a result of its better crystallization. Finally, TGA of NP3 sample exhibits a similar profile with a higher content of remaining CuO (see Figure 3.17d), in agreement with the presence of this oxide because of the partial degradation of NP1 in water.

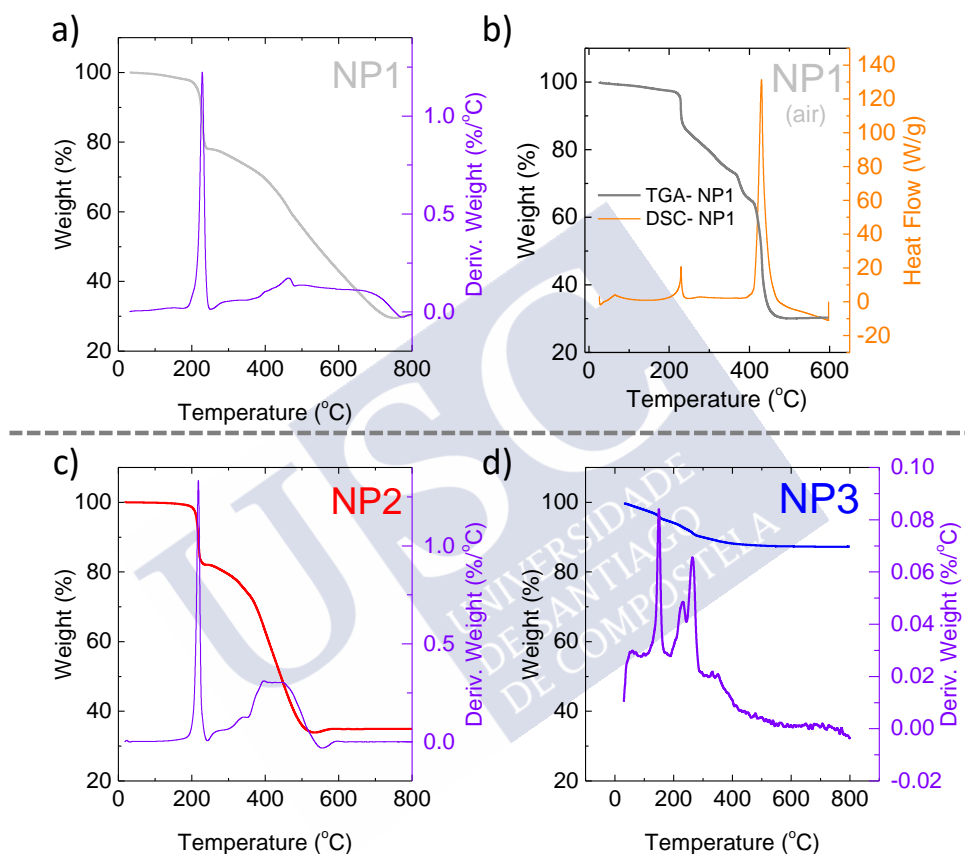


Figure 3.17. TGA of the NPs: (a) NP1 in N_2 (grey); (b) NP1 in air (grey); (c) NP2 in N_2 (red); and (d) NP3 in N_2 (blue). Violet lines correspond to the first derivative of the TGA curves (a,c,d), and the orange line corresponds to the DSC of sample NP1 (air) (b), indicating the rate of temperature degradation (adapted with permission from ref. [182]. Copyright 2018, American Chemical Society).

Furthermore, as observed by temperature dependent PXRD of NP1 (see Figure 3.18), the initial ligand departure leads to the collapse and amorphization of the crystalline framework, being the NP1 solid thermally stable up to around 200 °C. Previous thermo-diffraction analysis done to ZIF-8 under air reveal that its structure remains stable up to 300 °C, while NP1 only withstand 200 °C.^[192] Nevertheless, similar experiments carried out with HKUST-1 revealed a similar thermal stability compared to NP1, as the structure starts its degradation after 150 °C and becomes completely amorphous after 200 °C under air.^[193]

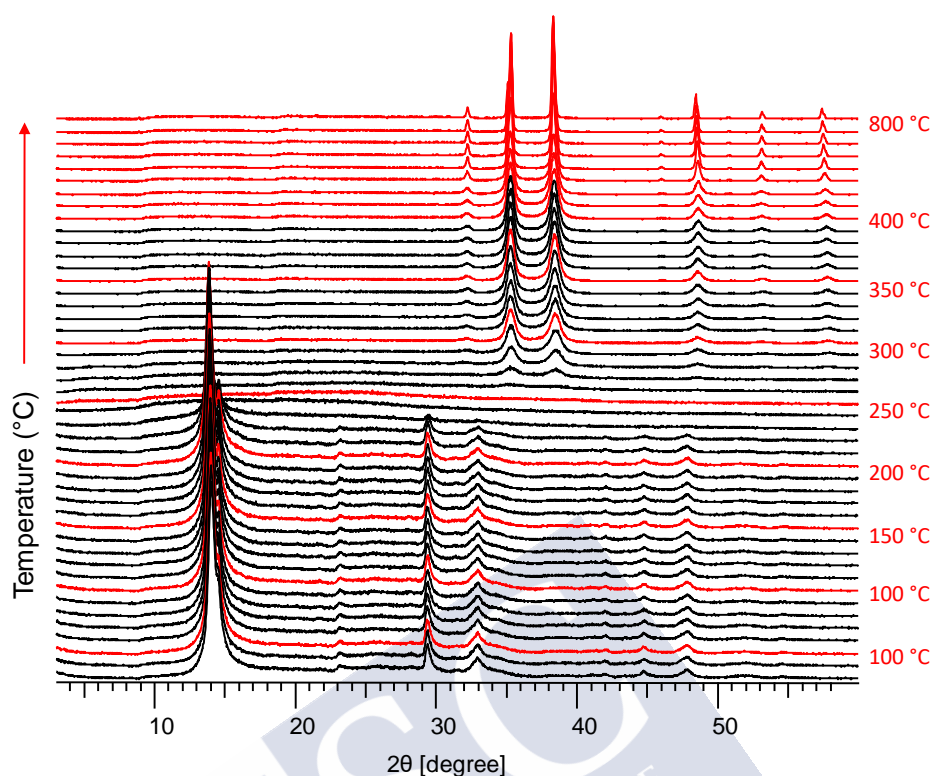


Figure 3.18. Temperature-dependent PXRD experiment carried out with NP1 (adapted with permission from ref. [182]. Copyright 2018, American Chemical Society).

TGA analysis of all the chemicals involved in the Cu-based CPs synthesis under N_2 atmosphere from room temperature to 800 °C was also done (see *Figure 3.19*). In all cases, including $CuCl_2$, no inorganic residues were found. 2-MI was completely decomposed at *ca.* 200 °C, CTAB at *ca.* 280 °C, and $CuCl_2$ presented three weight losses: one at *ca.* 120 °C, which is probably related to the loss of hydration water, and two others at *ca.* 500 °C and *ca.* 680 °C.

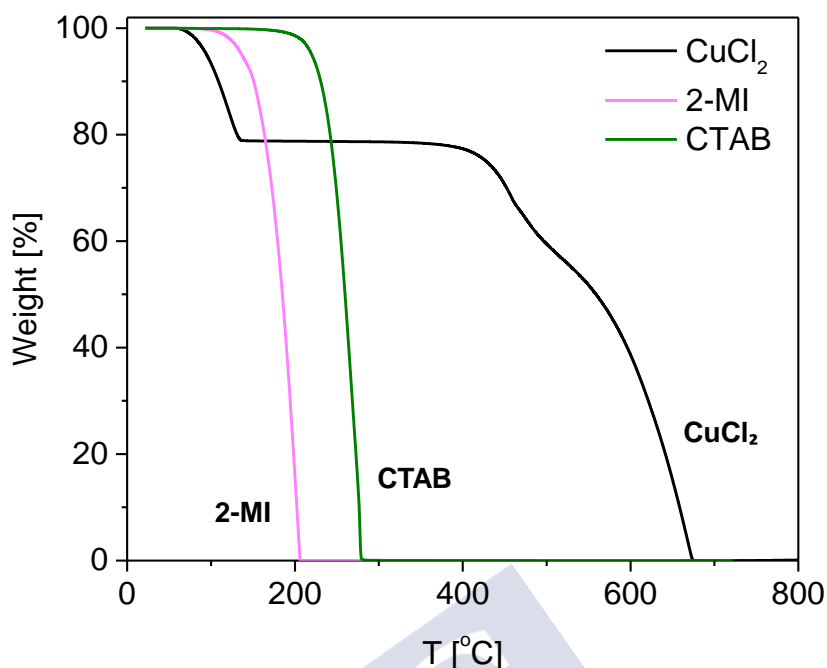


Figure 3.19. TGA of reactants: Cu_2Cl , 2MI, and CTAB (adapted with permission from ref. [182]. Copyright 2018, American Chemical Society).

3.2.7. Surface Area Characterization

Figure 3.20a shows the N_2 sorption isotherms of samples NP1, NP2 and NP3 at 77 K, with Brunauer, Emmett & Teller (BET; $P/P_0 < 0.15$) specific surface areas of 144, 86 and $53 \text{ m}^2 \cdot \text{g}^{-1}$, respectively. Although exhibiting a N_2 accessible microporosity, the BET surface is quite low regarding other imidazolate-based (ZIF-8(Zn): $S_{\text{BET}} = 1800 \text{ m}^2 \cdot \text{g}^{-1}$)^[179] or Cu-based MOFs (Cu trimesate HKUST-1: $S_{\text{BET}} = 1100 \text{ m}^2 \cdot \text{g}^{-1}$).^[175, 194] The higher surface of NP1 with respect to NP2 could be related to the presence of defects, in consonance with the better crystallization of the solid after 72 h of reaction, and agrees with the results of PXRD and EPR. Furthermore, the additional continuous N_2 adsorption at higher relative pressures ($P/P_0 > 0.2$) might correspond to adsorption on the outer surface of the NPs, being more important in the smaller entangled-nanosheets of NP1 than in NP2, with larger crystal size. In both samples, the porosity is associated with a pore size distribution of around 1 nm-diameter (estimated by the Horváth-Kawazoe -HK method) (see Figure 3.20b). Finally, NP3 possesses the lowest surface area, $S_{\text{BET}} = 53 \text{ m}^2 \cdot \text{g}^{-1}$, and this might be explained by the partial degradation of the NP1 to a dense CuO phase ($S_{\text{BET}} = 4 \text{ m}^2 \cdot \text{g}^{-1}$) after solvent exchange.^[195]

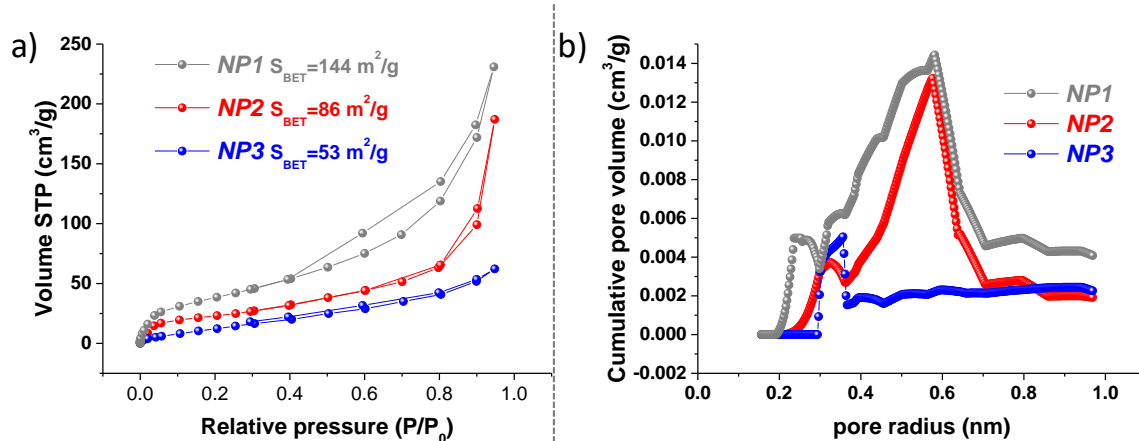


Figure 3.20. N₂ sorption isotherms (a) and HK pore volume distribution (b) of NP1 (grey), NP2 (red) and NP3 (blue) (adapted with permission from ref. [182]. Copyright 2018, American Chemical Society).

3.2.8. Physicochemical Characterization

Basic physicochemical properties of NP1 (acetone), NP2 (acetone) and NP3 (MilliQ water) in solution were investigated, including UV-Vis, fluorescence spectroscopy and dynamic light scattering (DLS). Upon storage at 4 °C, the NPs were colloiddally stable over long extended periods (months), with no apparent change of color or morphology. The UV-Vis-NIR spectrum of NP2 shows a narrow absorption band centered at 380 nm, which broadens in NP1 and even further in NP3, in which a broad absorption in the range 300 – 900 nm dominates, *cf.* Figure 3.21a. The spectra of NP1 and NP2 (*i.e.*, band at 380 nm) show no clear similarities with those of the used precursors (see Figure 3.21b) or other Cu-NMOFs, Cu₂O or CuO nanostructures,^[195, 196] or Cu(II)-histidine complexes.^[197] In contrast, the spectrum of NP3 resembles that of CuO nanosheets previously reported.^[198] Fluorescence spectroscopy of NP1, NP2, and NP3 shows no significant fluorescence emissions (see Figures 3.21c-d).

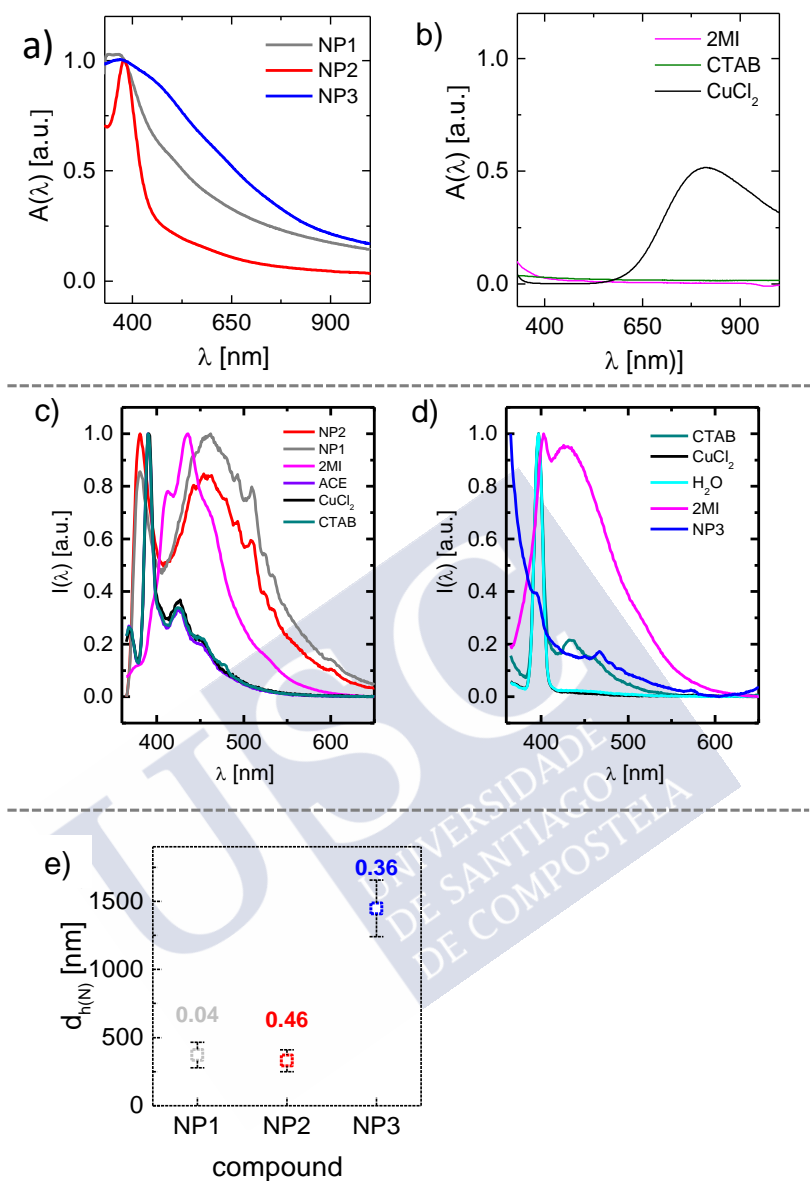


Figure 3.21. a) UV-Vis spectra of NP1 (grey; in acetone), NP2 (red; in acetone) and NP3 (blue; in MilliQ water). b) UV-Vis spectra of the reactants: CuCl_2 , 2MI, and CTAB in water. c) Fluorescence spectra of reactants, NP1, and NP2 in acetone. d) Fluorescence spectra of reactants. e) Mean average hydrodynamic diameter obtained from DLS number-weighted size distribution of NP1 (grey; in acetone), NP2 (red; in acetone) and NP3 (blue; in MilliQ water). Colored values above the hollow squares correspond to PDI values (adapted with permission from ref. [182]. Copyright 2018, American Chemical Society).

The hydrodynamic size of the NPs was also evaluated by DLS, which was rather similar as the size values observed from SEM inspection, *cf.* Figure 3.21e. DLS raw data are given in Figures 3.22a-c. Also, low polydispersity indexes (PDI) were found for NP1 (0.04), whereas

for NP2 and NP3 these were larger (0.46 and 0.36, respectively), *cf.* Figure 3.21e, as expected from SEM analysis.

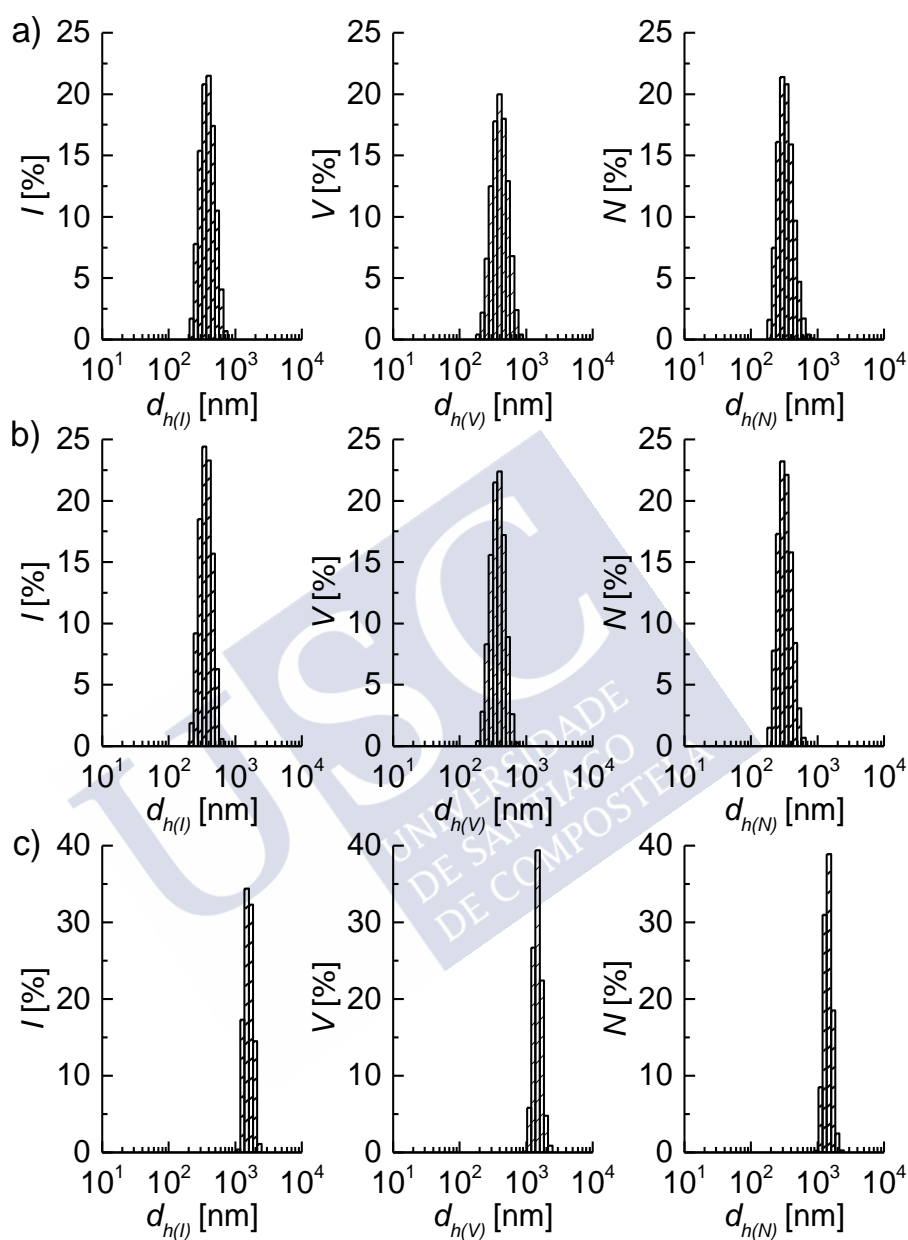


Figure 3.22. DLS histograms for NP1 (a), NP2 (b) and NP3 (c) (left: Intensity; middle: Volume; right: Number-weighted size distributions) (adapted with permission from ref. [182]. Copyright 2018, American Chemical Society).

In agreement with the results presented above, the main outcomes of this green bottom-up synthesis of the three NPs are briefed: i) a new crystalline structure of a copper imidazolate has been synthesized, ii) the formation of strong interactions between the Cu^{2+} inorganic building units and the 2-MI ligands has been demonstrated by EPR, iii) the synthesized NPs possess high

monodispersity and colloidal stability in acetone and water with a tuned morphology, iv) the NPs exhibit thermal stability up to 200 °C, and iv) they exhibit a moderate microporosity associated to 1 nm-diameter pore. Thus, one can conclude that these properties agree with those attributed to nanoPCPs.

3.2.9. Catalytic Reduction on Methylene Blue

Methylene blue (MB) (tetramethylthionine chloride, $C_{16}H_{18}ClN_3S$) is a cationic, blue-colored dye, which belongs to the thiazine dye class. This heterocyclic aromatic dye is dark blue in an oxidizing environment and will turn colorless as leucomethylene blue (LMB) if exposed to a reducing agent. The reduction reaction of methylene blue is generally monitored under the UV-VIS spectroscopy technique. The absorption spectrum of methylene blue exhibits a strong maximum peak at 664 nm at the start of the reaction and gradually will diminish in intensity over the time after adding a reductant (*e.g.*, $NaBH_4$, ascorbic acid, hydrazine, glucose, etc.)^[199-201] and a catalyst into the system, converting methylene blue in leucomethylene blue. Sodium borohydride ($NaBH_4$) is an inorganic compound widely used as a reducing agent in catalytic reduction of methylene blue.

Most of the studies frequently use the Langmuir-Hinshelwood model for the reduction of MB.^[199, 201] In this mechanism, the substrate (MB) and the reductant are absorbed onto the nanoparticle's (NP) surface, and both react each other on the active surface area of the catalyst (NP) until the formation of a product; this product formed will be desorbed from the surface of the NP. The catalyst (NP) acts as an electron-carrier surface, facilitating the electron transference between the reductant (*i.e.*, donor) and MB (*i.e.*, acceptor), which results in the reduction of MB into LMB. In the case of $NaBH_4$, acting as a reducing agent in aqueous solution, the release of hydrogen from its surface will also play an important role in binding the MB molecules to the surface of the catalyst (NP).^[201]

Thus, as a proof of concept, the catalytic activity of the three NPs was assayed towards their capability to trigger the reduction of methylene blue (MB, blue) into leucomethylene blue (LB, colorless) in MeOH in the presence of $NaBH_4$. To make a fair comparison among NPs, reactions were performed keeping the copper mass constant (*i.e.*, 1.9 ng).

i) Determination of Copper Concentration

To determine the copper concentration in the NP solutions, a classic colorimetric method was employed. This method is based on the complexation of Cu^{2+} with ammonium to produce the blue-colored compound $Cu(NH_3)_4^{2+}$.^[202] Thus, a calibration curve was prepared using a standard solution 0.1 M of $CuCl_2$ in water. In general, the copper solution was mixed with pure ammonium. The chemicals were left to react for 5 min and then, the absorbance was measured in a plate reader (Tecan Infinite 200 using a 570 nm filter). For sample preparation, 500 μ L of the sample (NP1, NP2 or NP3) or of Cu standards were mixed with 250 μ L of ammonium, 100 μ L of HCl concentrated, and 150 μ L of water were added to adjust the final volume to 1 mL. After the reaction was completed, 200 μ L of each solution were transferred to a 96-well plate

to perform the absorbance reading. To establish the precision of this colorimetric method, two control samples (NP1 and NP3) were measured in parallel using the colorimetric method and ICP-MS.

The results are summarized in *Table 3.4*, which indicates that the copper concentration obtained by the two methods were very similar. Therefore, we used the colorimetric method to measure the copper concentration of all the samples studied in this work. In general, stock samples of NP1, NP2, or NP3 with copper concentrations of 47.4, 60.0, and 60.7 μM , respectively, were stored in the refrigerator (4 °C).

Table 3.4. Comparison of copper concentration determination by two methods: colorimetric and ICP-MS.

Sample	$C_{\text{Cu, A}}[\text{mM}]$	$C_{\text{Cu, ICP}}[\text{mM}]$	Ratio A/ICP
NP1	2.17	2.25	0.97
NP3	1.59	1.65	0.96

ii) Reduction of Methylene Blue (MB, Blue) Into Leucomethylene Blue (LB, Colorless) in MeOH

The reduction of MB into LB was followed by collecting the absorbance at 664 nm (A) during 100 s (one measurement per s),^[203] cf. *Figure 3.23*. First, 970 μL of MeOH were mixed with 15 μL of MB from a stock solution ($9.37 \cdot 10^{-4}$ M, MeOH). Then, 5 μL of a freshly prepared solution of NaBH_4 (130 mM, MeOH) and 5 μL of the sample (1.9 ng Cu, MeOH) or MeOH (control) were added. The reaction progress was monitored by UV-Vis spectroscopy.

The catalytic properties of the three solids were calculated by analyzing the kinetics of the catalytic reaction (k , $\text{Ln}(A/A_0)$), taking into account the initial 22 s, cf. *Table 3.5*, that is, k [s^{-1}] is obtained from the slope of the curves $\text{Ln}(A/A_0)$ vs time. The blank absorption (control) was measured using the same parameters but in the presence of only MeOH instead of the sample (NP1, NP2, and NP3) solution.

Table 3.5. Summary of the kinetic constant values k [s^{-1}] for the selected samples (equal Cu mass - 1.9 ng) and control (without Cu). A first-order catalytic behavior was considered, i.e., $\text{Ln}(A/A_0) = -k \cdot t$, for the initial 22 s of the reaction.

Sample	k (s^{-1})
NP1	$53.7 \cdot 10^{-3} \pm 1.2 \cdot 10^{-3}$
NP2	$67.6 \cdot 10^{-3} \pm 0.3 \cdot 10^{-3}$
NP3	$2.6 \cdot 10^{-3} \pm 1.6 \cdot 10^{-5}$
Ctrl	$2.6 \cdot 10^{-3} \pm 1.7 \cdot 10^{-5}$

As expected, NP1 and NP2 present significantly higher catalytic properties (i.e., high k) than the low-porosity NP3 or the control sample. The obtained k values are in the order of previous reports using equivalent catalytic reactions.^[204, 205] However, these values are not fully

comparable due to different experimental conditions, including the solvent used (water or methanol), and the amount of NaBH_4 used, in our case *ca.* 12 times lower than previous reports.^[204, 205] Remarkably and despite those experimental differences, it is worth mentioning that, in our case, the amount of material used *per* experiment is in the ng order, while in previously discussed works it is in the mg range *i.e.*, 1 mg,^[204] and 0.05 mg^[205] of the nanocatalyst. This fact points out the high catalytic activity of our systems under the present conditions.

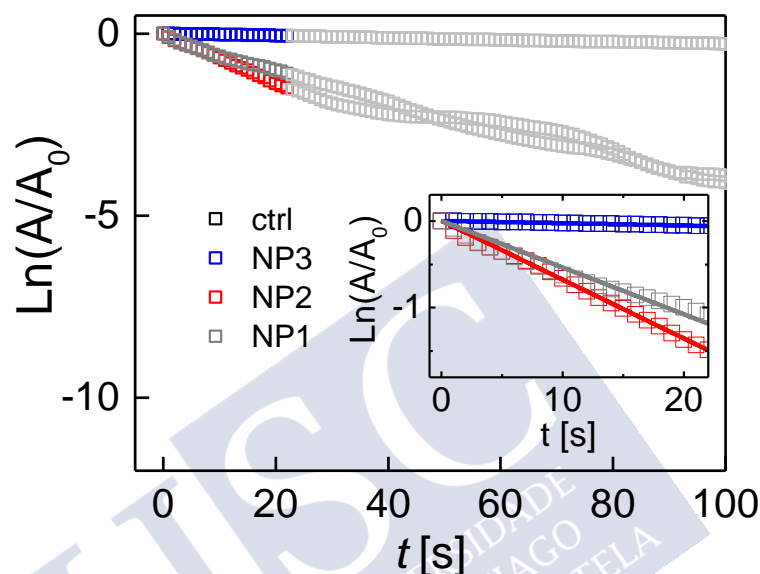


Figure 3.23. Absorbance at 664 nm (A) versus time for an equal mass of copper in, *i.e.*, NP1 (grey), NP2 (red) and NP3 (blue), and control sample (ctrl, black). A_0 is the absorption at 664 nm at time 0 s. Data considered for the kinetic fitting (first-order) are colored (initial 22 s). Insets show zoom areas of the fitting regions for selected samples and control (adapted with permission from ref. [182]. Copyright 2018, American Chemical Society).

3.3. Conclusions

In this chapter, we described a bottom-up green chemical method for the preparation of a new nanometric microporous coordination polymer (*i.e.*, NP1/NP2). Different concentrations and molar ratios of the reactants [*i.e.*, CuCl_2 , 2-methylimidazole (2MI), and hexadecyltrimethylammonium bromide (CTAB)] produce different nanocomposites, which can be optimized to achieve highly monodisperse nanoparticles. The addition of CTAB, the reaction time, and the effect of the solvent during the synthesis determine the size, morphology, and structure of the resulting nanoparticles. A molar ratio 2MI: Cu^{2+} of 20 (and 2MI: CTAB of 10^3) was found as optimum to produce highly monodisperse nanospheres. These nanospheres (NP1) with an average edge length of approx. 330 nm, evolve into nanosheets (NP2) with an average tip-to-tip length of approx. 334 nm if the reaction time is left to 72 h or even longer. NP1 and NP2 nanoparticles were found to be colloiddally stable in acetone over months. However, the presence of water in the nanospheres (NP1) solution leads to a change in particle morphology,

starting with the formation of nanofibers which evolve into nanospikes (NP3), with an average tip-to-tip length of approx. 447 nm, and which are mainly composed of copper oxide, in agreement with PXRD results. Then, these particles (NP3) appear to be a degradation product of NP1 nanospheres. Samples NP1 and NP2 exhibited a microporosity associated with 1 nm-diameter and a BET specific surface of 144, 86 m²·g⁻¹, respectively. On the other hand, NP3 particles presented the lowest BET specific surface of 53 m²·g⁻¹. This may agree considering NP3 as a degradation product of NP1, mainly composed of copper oxide, although it also contains a Cu²⁺-2MI porous phase. FTIR spectra corroborated that the synthesis conditions did not lead to a decomposition of the organic linker since all samples exhibited the characteristics bands of 2MI. The formation of strong interactions between the Cu²⁺ inorganic building units and the 2-MI ligands was also demonstrated by EPR. Finally, NP1 and NP2 displayed good activity towards the catalytic reduction of methylene blue.







Chapter 4

4. Gold Nanostars@Zeolitic Imidazolate Framework 8 Core-Shell Nanostructures for Light Triggered Release: in Vitro

4.1. Introduction

Metal-Organic Frameworks

Metal-organic frameworks are a subclass of CPs which has revolutionized the field of supramolecular chemistry and its applications. Here, we adopt the following definition of MOF: “a class of CPs comprising organic linkers wherein metal–ligand interaction/bonding leads to 2D or 3D crystalline network structures” as proposed by S. Seth and A. J. Matzger.^[206] Recently, MOFs have gained interest as next-generation functional materials in diverse fields,^[141, 207] especially in biomedical applications for achieving a controlled drug release^[208-210] due to their high surface area, tunable pore size, wide possibilities of surface modifications,^[153, 211-213] and good biodegradability and biocompatibility.^[214] Therefore, MOF-based single or multiple stimuli-responsive nanosystems have been attracted many researchers seeking to achieve a material with controllable drug release properties. These systems may undergo chemical or physical transformations when activated by internal [endogenous, *i.e.*, redox, pH, enzymes, adenosine triphosphate (ATP)] or external (exogenous, *i.e.*, light, magnetic field, temperature, ions, pressure) triggers. According to Yarza *et al.* the release of the molecular cargo depends on three points: “1) the biodegradability of the MOF under physiological conditions, 2) the drug diffusion through the pores, and 3) the matrix-drug-solvent interactions”.^[215]

Zeolitic Imidazolate Frameworks (ZIF)

Zeolites are crystalline porous materials of different structures, hydrated alkaline or alkaline-earth aluminosilicates, having a framework assembled from corner-sharing TO₄ tetrahedral sites (T=Al, Si), and ordered micropore networks along with large active surfaces.^[93, 216] There are more than 150 zeolites with different frameworks synthesized in laboratories or present in nature.^[217] ZIFs are a class of MOFs that are topologically isomorphic with zeolites; generally, they are formed by the coordination of metal ions (Zn²⁺, Co²⁺, etc) and imidazolate linkers. For example, Park *et al.* reported twelve zeolite-like MOFs (*i.e.*, ZIF-1 to 12) (see *Table 4.1*). Phenyl or methyl groups with IM linkers can be used to obtain some zeolitic imidazolate frameworks [*i.e.*, benzimidazolate and (PhIM), or 2-methylimidazolate (MeIM), respectively],^[179] among others groups. Zeolite minerals can be abbreviated in a 3-letter code that corresponds to the first 3 letters of the mineral name; however, for synthetic materials the code is more complex since it includes numbers to identify different products from a particular laboratory.^[217] In 2008, Banerjee *et al.* synthesized 25 ZIFs structures in which sixteen of them (*i.e.*, ZIF-60 to 77, see *Table 4.1*) had new compositions and a new structure.^[218] Some of the corresponding single crystal x-ray structures of the ZIF crystals which appear in *Table 4.1* are also illustrated in *Figure 4.1*.

Table 4.1. Composition, structure, and network parameters of some ZIF series of compounds (ZIF-1 to 10 and ZIF-60 to 75, adapted from refs. [179, 218], respectively).

ZIF- <i>n</i>	Composition	Net	Zeolite	<i>T/V</i> , nm ³	<i>d</i> , Å	<i>N</i>
ZIF-3	Zn (IM) ₂	dft	DFT	2.66	8.02	16
ZIF-8	Zn (MeIM)₂	sod	SOD	2.47	11.6	24
ZIF-10	Zn (IM) ₂	mer	MER	2.25	12.12	24
ZIF-60	Zn (IM) _{1.5} (MeIM) _{0.5}	mer	MER	2.24	9.4	24
ZIF-65	Co(nIM) ₂	sod	SOD	2.32	10.4	24
ZIF-67	Co (MeIM)₂	sod	SOD	2.46	11.6	24
ZIF-68	Zn (PhIM)(nIM)	gme	GME	2.12	10.3	24
ZIF-69	Zn(cbIM)(nIM)	gme	GME	2.09	7.8	24
ZIF-70	Zn (Im) _{1.13} (nIM) _{0.87}	gme	GME	2.10	15.9	24
ZIF-72	Zn(dclM) ₂	lcs	-	3.16	1.9	12
ZIF-74	Zn(nIM)(mbIM)	gis	GIS	2.66	2.6	20
ZIF-75	Co(nIM)(mbIM)	gis	GIS	2.66	2.62	20

Zeolite: DFT- DAF-2 (Davy Faraday Research Laboratory-two), SOD- sodalite, MER- merlinoite, GME-gmelinite, GIS- gismodine [Zeolite A (Linde Division, Union Carbide)]; *T/V*: density of metal atoms per unit volume; *d*: diameter of the largest sphere that fits into the framework; *N*: number of vertices of the largest cage; Net information: Reticular Chemistry Structure Resource (<http://rcsr.anu.edu.au/>).

Zeolitic imidazolate framework 8 (ZIF-8) is a subclass of metal-organic frameworks (MOFs), which is composed of zinc ions and imidazolate rings coordinated in a framework structure resulting in a sodalite (SOD) topology with a pore size of 11.6 Å and a pore opening of 3.4 Å.^[218] ZIF-8 crystals may present different morphologies: cubic, rhombic dodecahedral (RD), or truncated rhombic dodecahedral (TRD). Cravillon *et al.* demonstrated the solvothermal morphological evolution of ZIF-8 over time; the crystal growth formation starts with an all [100]-oriented cube, and then, transforms into TRD to finally, according to the authors, accomplish the stable equilibrium morphology of ZIF-8 (RD).^[219]

ZIF-8 is among the most frequently investigated ZIF thanks to its uniform porosity and excellent chemical and thermal stabilities make ZIF-8^[179] suitable for its use as a carrier for controlled drug delivery.^[101, 220, 221] Besides, the high degree of knowledge and control over the localization of nucleation and growth of ZIF-8 particles during synthesis allows a variety of materials that can be encapsulated within the ZIF-8 structures. High loading efficiency, unlimited cargo size, and low leakage are the advantages of this technique.^[222] This strategy is called *in situ* encapsulation; aside from biomolecules,^[220] inorganic particles with different shapes have been successfully encapsulated into ZIF-8 crystals (*e.g.*, nanorods stars, cubes, spheres).^[125, 153] Moreover, the possibility of incorporating functional guest molecules within colloidal ZIF-8 particles not only applies via encapsulation, but also researchers have positioned these guests along the outer surface of ZIF-8 crystals.^[211-213]

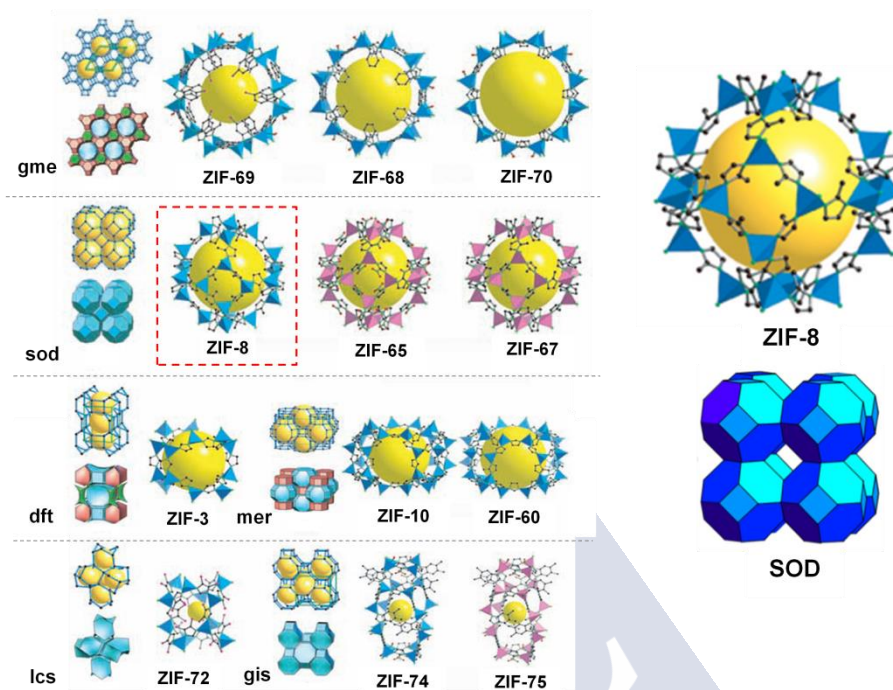


Figure 4.1. Single-crystal XRD structure of ZIFs. Left row: stick diagram; the large cage in ZIFs is represented with ZnN_4 tetrahedral sites in blue and CoN_4 ones in pink; ball and stick diagram representing IM (imidazole) and IM-type linkers (C: black, N: green, O: red, Cl: pink, H atoms are omitted; adapted with permission from ref. [218]. Copyright 2008, American Association for the Advancement of Science). Left: zoomed images of porous cage of ZIF-8 (upper) and crystal structure of ZIF-8 with sodalite topology (bottom) (adapted with permission from ref. [179, 223]. Copyright 2006, The National Academy of Sciences of the USA; Copyright 2017, Elsevier B.V, respectively).

At this respect, in biological applications a highly stable suspension of particles in an aqueous medium is set as a requirement to avoid embolism after in vivo injection (*i.e.*, there should be neither aggregation nor particles precipitation); therefore, the surface of nanoMOFs functionalized with different molecules has been envisaged to accomplish this requirement. This MOF surface modification can be made during the particle synthesis or post-synthetically. *Figure 4.2* shows different post-synthetic surface functionalizations of ZIF-8 crystals with different elements. To mention some examples, Zhu *et al.* proposed a strategy for the outer layer functionalization of different MOFs (*i.e.*, ZIF-8, ZIF-67, UiO-66, MIL-88A, HKUST-1, MIL-101(Cr), CPP-3, MIL-96 and Eu-MOF) through the coordination of a phenolic-inspired lipid molecule, DPGG (*i.e.*, 1,2-dipalmitoyl-sn-glycero-3-galloyl), with the metal surface nodes/sites of the different MOFs in non-polar solvents.^[212] Besides, Li and Zeng reported two different approaches (*i.e.*, *post-growth attachment* and *on-site reduction*) to incorporate inorganic nanoparticles onto the surface of ZIF-8 crystals (see *Figure 4.2*, left). This bonding is generated by the interaction between the stabilizing layer of surfactants surrounding the incorporated Au or Ag nanoparticles (with sizes of 1-3 nm) and the Zn^{2+} ions of the outer

surface of two ZIF-8 nanocrystals with different morphologies (*i.e.*, cubic hexahedron and rhombic dodecahedron).^[213] In 2016, Ayala *et al.* proposed a strategy to fabricate Janus particles (*i.e.*, multicompartamental, asymmetric particles with two chemically distinct regions on their surfaces)^[224, 225] that behave as molecular motors in sodium and H₂O₂ aqueous ethanol solutions (*i.e.*, Janus ZIF-8@Pt particles). Their method consisted in the evaporation of metals (*i.e.* Au, Co or Pt) on the surface of different MOFs (*i.e.*, ZIF-8, UiO-66 or UiO-66-SH) that leads to an asymmetric morphology with a controllable metal-film thickness^[211] (see *Figure 4.2 center*).

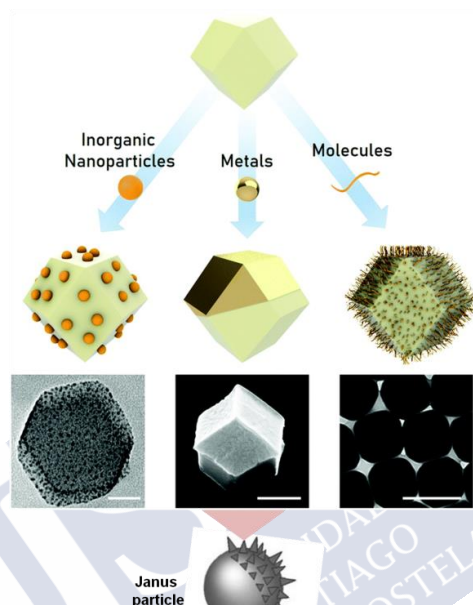


Figure 4.2. A) Scheme of different post-synthetic surface functionalization processes for ZIF-8 crystals: inorganic nanoparticles (left, adapted with permission from ref. [213] Copyright 2013, American Chemical Society); metal coating (center, adapted with permission from ref. [211] Copyright 2016, The Royal Society of Chemistry), and polymers (right, adapted with permission from ref. [212] Copyright 2018, WILEY-VCH Verlag GmbH & Co. KGaA), and their corresponding SEM images (scale bars: left: 20 nm, middle and right: 500 nm, (adapted with permission from ref. [222] Copyright 2019, The Royal Society of Chemistry); below a schematic representation of a Janus particle (center) is also shown (adapted with permission from ref. [224] Copyright 2015, The Royal Society of Chemistry).

Functionalized ZIF-8 frameworks have been also studied as stimulus-responsive systems for the sustained delivery of a wide variety of drugs.^[223, 226-228] In the case of internal stimuli, pH-responsive ZIF-8 systems have been frequently reported for drug delivery.^[221, 229-232] However, light-responsive drug delivery MOFs systems have increased recent attention due to the possibility to achieve spatiotemporal controlled release provided by irradiation with light of a specific wavelength.^[233] For example, Sharsheeva *et al.* proposed a nanocomposite based on titania nanotubes, ZIF-8 particles and the antitumor drug doxorubicin (*i.e.*, DOXO-ZIF-8-TNT). They demonstrated that this nanosystem was capable of releasing an appropriate amount of drug to effectively suppress the viability of IMR-32 neuroblastoma cells by locally applying UV radiation for 40 minutes.^[233] Controllable release of the drug from the DOXO-ZIF-8-TNT

nanocomposites is possible due to the photocatalytic activity of titania nanotubes that decomposes ZIF-8 particles in the aqueous medium. The release kinetics of doxorubicin in a PBS buffer solution (*i.e.*, pH=7.4) is significantly different in the presence and absence of UV irradiation, that is, in the absence of UV light, a scarce release of the drug was observed.

Motivation

The biocompatible microporous zeolitic imidazolate framework 8 (ZIF-8)^[179] has been widely proposed for the sustained delivery of a wide variety of drugs.^[223, 226-228] Although with a progressive release, most previous reports refer to that 80-90% of the encapsulated cargo is released within the first ~10 h in physiological environments. Hence, its clinical applications are several restricted as a result of the chemical instability of ZIF-8 in water,^[234] which largely degrades (depending on the ZIF-8 mass to water ratio and medium pH),^[227, 235] thus, releasing its cargo.

The development of core-shell nanostructures based on MOF and inorganic nanoparticles (NPs) seems a good strategy to promote and control drug delivery under a specific external stimulus (*e.g.*, light, magnetic fields, ultrasounds), as already demonstrated for other materials.^[236] These types of nanocomposites have been recently explored for optical sensing,^[125] therapeutics,^[63] theranostic,^[147] and heterogeneous catalysis with promising results.^[149] However, the precise (temporal and spatial) controlled delivery of the cargo inside cells upon stimuli has not been achieved, since the stability issues of MOFs in aqueous solution has not yet been addressed.

Therefore, here we present the design of a thermoresponsive carrier comprising gold nanostars (NSs) coated with ZIF-8 and stabilized with the amphiphilic polymer poly[isobutylene-*alt*-maleic anhydride]-graft-dodecyl (PMA). The newly developed core-shell nanostructures (we will refer to them as nanocomposites NCs) with a high drug loading efficiency (similar as the conventional ZIF-8) are stable in aqueous solution and can be activated to release the cargo upon illumination with near-IR (NIR) light in both aqueous solution and inside living cells.

4.2. Results and Discussions

4.2.1. The Influence of the Synthesis Parameters: CTAB as a Size-Directing Surfactant

Commonly, ZIFs have been synthesized by combining a hydrated metal salt and an imidazolate-type linker via solvothermal methods, at room temperature in organic solvents (*e.g.*, methanol, DMF, THF, and DEF), or in pure water. In the case of ZIF-8, which is composed of Zn (II) ions and imidazolate rings coordinated in a framework structure, different researchers have synthesized this type of MOF in aqueous solution at room temperature^[125, 223, 237] to avoid the use of toxic organic solvents, but also to decrease the economical cost of preparing ZIFs-based materials. Also, the use of surfactants in the synthesis has been used to

control the ZIF-8 crystal growth process, acting as growth inhibitors, capping agents, and aggregation inhibitors.^[238]

The use of cetyltrimethylammonium bromide (CTAB) as a capping agent to control the morphology and the size of ZIF-8 crystals have been previously reported.^[180, 238, 239] Additive agents can act as sites for nucleation and growth of ZIF-8 particles.^[239]

Thus, as a first step, we prepared ZIF-8 particles in the presence of CTAB at different concentrations (see *Table 4.2*). We also prepared ZIF-67 particles (see *Table 4.2*) for comparison and to validate our analysis. Zeolitic imidazolate framework 67 (ZIF-67) is a subclass of metal-organic frameworks (MOFs), which is composed of Co (II) ions and imidazolate rings (in the case of ZIF-8 and ZIF-67: 2-methylimidazole) coordinated in a framework structure. ZIF-8 and ZIF-67 have similarities in their structure and organic ligands, they have the same sodalite (SOD) topology, the same pore size of 11.6 Å, and pore opening of 3.4 Å (see *Figure 4.1* and *Table 4.1*), making their mechanism of formation very close to each other.^[218] Different researchers have done the *in vitro* evaluation of cobalt-based nanoparticles as drug carriers, and found to generate oxidative stress, inflammatory response, cell proliferation, and DNA damage.^[240, 241] Therefore, we will only here use ZIF-67 particles for comparative purposes, and to analyze in the near future other potential applications in the field of catalysis and energy production and storage.

Briefly, in a typical synthesis, an aqueous solution containing zinc or cobalt nitrate (1mL, 0.025 M), 2MI (1mL, 1.3 M), and CTAB (1mL, different concentrations) was gently stirred for 2 min. Then, the solution was left undisturbed for 3 hours at room temperature (RT). The resulting particles were then purified by centrifugation (7000 rcf, 5 min; unless otherwise specified), the colorless supernatant was discarded, and the precipitate was redispersed and stored in 3 mL MeOH.

Figure 4.3 shows the synthesis of ZIF-8 or ZIF-67 nanoparticles, and the mean $d_{h(N)}$ size of both ZIF-8 and ZIF-67, which is observed to decrease as the CTAB concentration increases.^[238, 242]

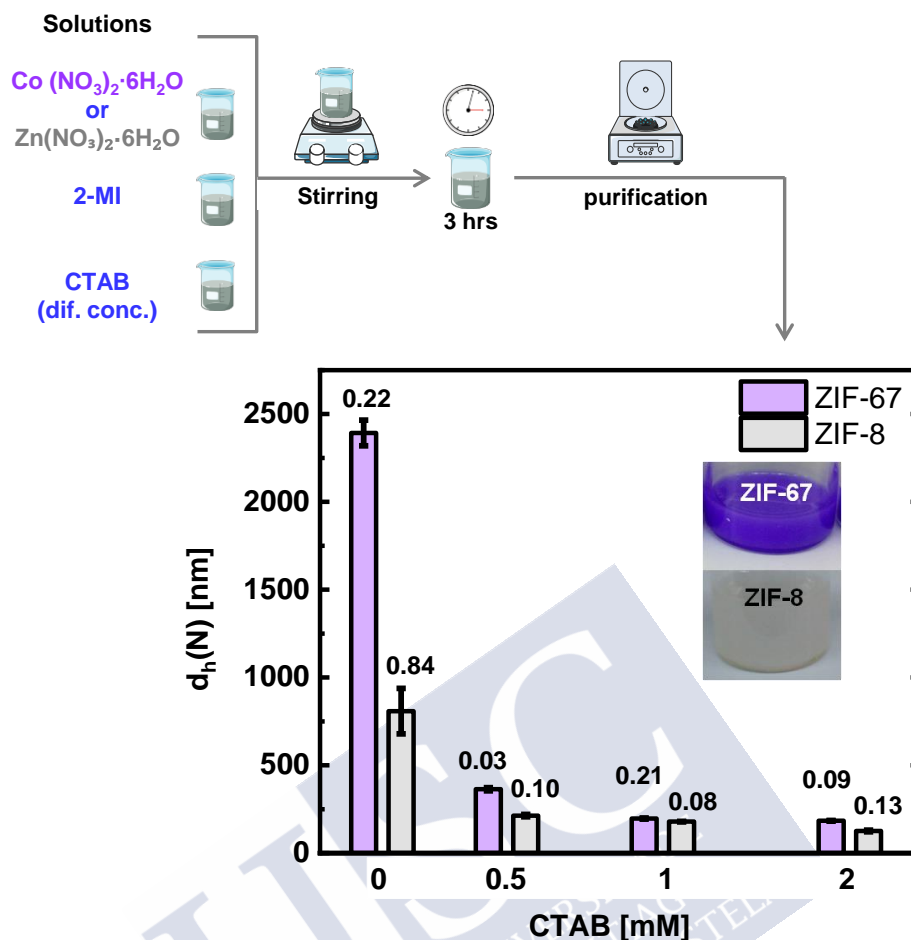


Figure 4.3. Schematic illustration of the synthesis of ZIF-8 or ZIF-67 nanoparticles and mean $d_{h(N)}$ of ZIF-8 and ZIF-67 versus concentration of added CTAB. The corresponding polydispersity index (PDI) is specified on top of each bar.

Table 4.2. Hydrodynamic diameters d_h (mean value \pm standard deviation SD) as derived from DLS measurements of ZIF-8 and ZIF-67 particles using different CTAB concentrations.

Sample	CTAB [mM]	$d_{h(I)}(\text{nm})$	$d_{h(N)}(\text{nm})$	PDI
ZIF-8	0	808.5 ± 130.6	808.4 ± 129.8	0.84 ± 0.06
	0.5	279.4 ± 3.5	213.4 ± 6.4	0.10 ± 0.01
	1	207.6 ± 0.9	179.3 ± 0.8	0.08 ± 0.10
	2	156.3 ± 3.6	126 ± 5	0.13 ± 0.06
ZIF-67	0	2604 ± 63	2392 ± 73	0.22 ± 0.07
	0.5	411.5 ± 12.15	363.7 ± 8.8	0.03 ± 0.05
	1	292.7 ± 38.8	197.1 ± 3.2	0.21 ± 0.01
	2	227.3 ± 2.2	184.1 ± 1.9	0.09 ± 0.02

$d_{h(I)}$ and $d_{h(N)}$ refer to the mean average hydrodynamic diameter from the intensity and number-weighted size distributions derived from DLS, respectively. PDI refers to the polydispersity index. Standard deviation values were calculated from three independent measurements.

4.2.2. Colloidal Stability of Zeolitic Imidazolate Frameworks (ZIF-8 and -67)

Colloidal stability of ZIF-8 and ZIF-67 was evaluated for one week by DLS in methanol and water, and for ZIF-8 in cell medium as well (see Table 4.3). Figure 4.4a shows the synthesis of ZIF-8 and ZIF-67 nanoparticles, *i.e.*, an aqueous solution containing zinc or cobalt (1mL, 0.025 M), 2MI (1mL, 1.3 M), and CTAB (1mL, $5 \cdot 10^{-4}$ M) was gently stirred for 2 min. Then, the solution was left undisturbed for 3 hours at room temperature (RT), followed by purification as described before. MeOH (supernatant) was removed and the resulting particles (precipitate) were redispersed in the different solvents and DLS measurements were performed at different time points.

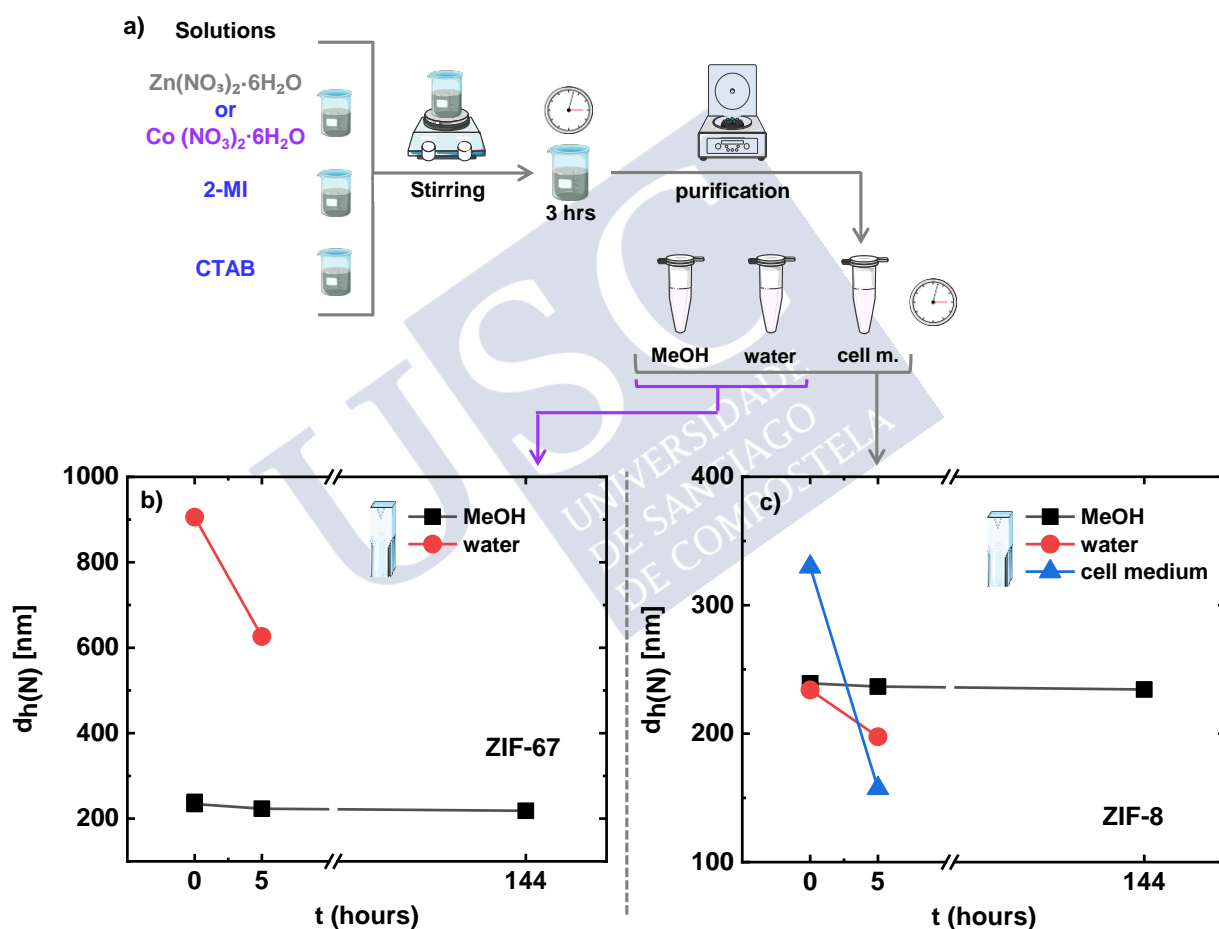


Figure 4.4. a) Schematic illustration of the synthesis of ZIF-8 or ZIF-67 nanoparticles, and Mean $d_h(N)$ for one week for b) ZIF-67 particles in methanol and water, and c) ZIF-8 particles in methanol, water, and cell medium.

The results showed that the d_h of ZIF-8 and ZIF-67 samples in methanol remained stable over one week, indicating that methanol did not affect their integrity and stability.

In contrast, the integrity of ZIF-67 samples was compromised in water as reflected by the rapid increase of d_h immediately after placed in aqueous solution (see *Figure 4.4b*). Similarly, the integrity of ZIF-8 samples was compromised in both water and cell medium as reflected by the rapid decrease of d_h after 5 h (see *Figure 4.4c*).

Table 4.3. Hydrodynamic diameters d_h (mean value \pm standard deviation SD) as derived from DLS measurements for ZIF-8 particles dispersed in methanol, water, or in cell medium at different time points, and for ZIF-67 particles dispersed in methanol or water at different time points.

Sample	Solvent	Time (h)	d _{h(I)} (nm)	d _{h(N)} (nm)	PDI
ZIF-8	MeOH	0	276.8 ± 2.2	239.1 ± 0.9	0.03 ± 0.02
		5	274.8 ± 3.7	236.7 ± 5.1	0.07 ± 0.04
		144	268 ± 5	234.4 ± 4.7	0.04 ± 0.04
	Water	0	267 ± 4	234 ± 2	0.04 ± 0.02
		5	361.9 ± 65.3	197.6 ± 4.1	0.19 ± 0.02
	Cell medium	0	337.1 ± 36.2	329.8 ± 35.9	0.8 ± 0.1
		5	158 ± 48	157.4 ± 48.8	1.0 ± 0.0
ZIF-67	MeOH	0	310.0 ± 6.6	234.3 ± 19.1	0.10 ± 0.02
		5	339.4 ± 6.5	223.2 ± 16.5	0.12 ± 0.06
		144	305.5 ± 5.6	218.4 ± 2.4	0.13 ± 0.02
	Water	0	950.9 ± 69.9	905.8 ± 54.6	0.08 ± 0.07
		5	777.2 ± 102.2	626.5 ± 18.4	0.22 ± 0.03

$d_{h(I)}$ and $d_{h(N)}$ refer to the mean average hydrodynamic diameter from the intensity and number weighted size distributions derived from DLS, respectively. PDI refers to the polydispersity index. Standard deviation values were calculated from three independent measurements.

4.2.3. Encapsulation of Gold Nanostars (NSs) into Zeolitic Imidazolate Frameworks (ZIF-8) to form Core-Shell Nanocomposites

Once confirmed that the ZIF-8 size can be tuned by the addition of CTAB during the synthesis,^[125, 238] our next step was to encapsulate a single gold nanostar within ZIF-8 particles. Gold nanostars (NSs) were selected as the core due to their characteristic plasmonic band centered at ~ 770 nm (see *Figure 4.6d*),^[17] which is suitable for excitation within the therapeutic window.^[66] Therefore, NSs were used as seeds to grow a ZIF-8 shell around.^[125, 152]

CTAB-coated gold nanostars (NSs) were synthesized according to a previously reported protocol,^[17] using spherical citrate-stabilized gold nanoparticles (NPs) with an average core diameter of *ca.* 11 nm as seeds, Ag^+ ions as blocking facet agents, and ascorbic acid as a reducing agent (see *Figure 4.5*).

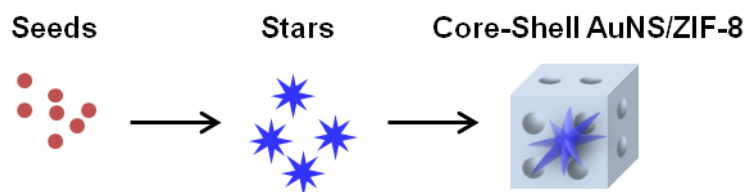


Figure 4.5. Step-by-step formation of nanocomposites: seeds, stars and core-shell structure.

i) Nanoparticles (NPs) Seeds

The seed NPs were synthesized following the citrate-reduction procedure reported by Schulz *et al.*^[243] (for more details see *section 2.3.2*).

ii) Optical Characterization

UV/Vis absorption spectra of the obtained NPs seeds and the NSs as recorded in aqueous solution are provided in *Figures 4.6 a* and *d* respectively. The concentration of the seed NPs was determined from the UV/Vis spectra by using the Lambert-Beer law.^[17] Hereby, an extinction coefficient at 450 nm of $\epsilon(450) = 8.27 \times 10^7 \text{ M}^{-1} \cdot \text{cm}^{-1}$ was assumed,^[244] taking into account that the average (\pm standard deviation) core diameter of the seed NPs was $d_C = (11.4 \pm 0.9) \text{ nm}$ as determined by Transmission Electron Microscopy (TEM) analysis (see *Figures 4.6 b-c*). In a typical synthesis of Au seed NPs as previously described in Chapter 2, without concentration or purification steps, the concentration of NPs was $c_{NP} = 3.7 \text{ nM}$.^[17] Since these NPs were used as seeds for NSs growth, the number of NSs is assumed to be the same as that of the added NP seeds. The purified NSs were finally diluted in CTAB solution ($5 \cdot 10^{-4} \text{ M}$) at a molar concentration of 2 nM (NPs concentration) for their storage and further use. Scanning Electron Microscopy (SEM) analysis of the as-prepared NSs (see *Figures 4.6 e-f*) presented the typical star-shaped morphology with an average (\pm standard deviation) tip-to-tip length of $L_{NS} = (82.6 \pm 4.9) \text{ nm}$.

iii) Core-Shell AuNS/ZIF-8 Nanocomposite (NC)

The synthetic and purification protocol for the NCs was equivalent to the one previously described for pristine ZIF-8 particles, but a NP solution (NSs at a concentration of 2 nM in $5 \times 10^{-4} \text{ M}$ CTAB aqueous solution) was added instead of the CTAB solution. In this case, the appearance of bluish turbidity was gradually observed during the formation of ZIF-8. The resulting NCs redispersed in 3 mL of methanol (MeOH) were assumed to have a particle concentration of 0.67 nM, since this is the final concentration of NSs in the solution and it is assumed that one NC was formed per NS (*i.e.*, NSs acted as seeds and under optimized conditions, almost all the ZIF-8 particles contained a NS in the center).

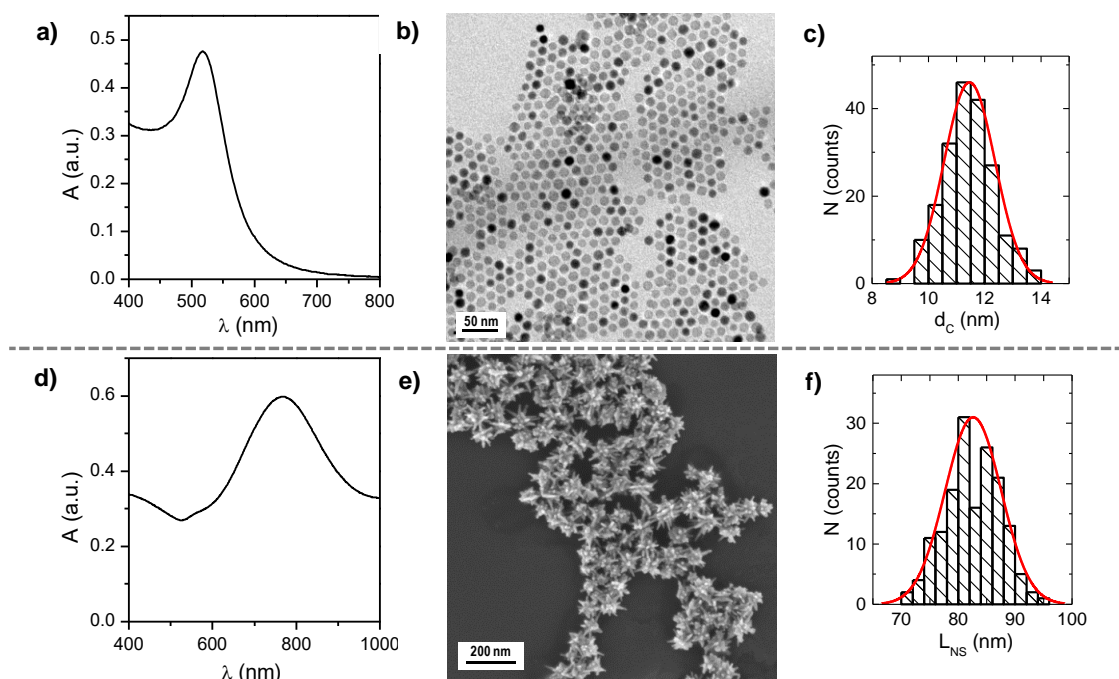


Figure 4.6. Optical characterization of the as-prepared NPs seeds: a) UV/Vis absorption spectrum showing their Surface Plasmon Resonance (SPR) peak at $\lambda = 517$ nm; b) representative TEM image (scale bar corresponds to 50 nm); and c) the corresponding histogram of the number-weighted size distribution N of the core diameter d_c of NPs as determined from TEM images, $d_c = (11.4 \pm 0.9)$ nm. Optical characterization of the as-prepared NSs: d) UV/Vis absorption spectrum A showing their SPR peak at $\lambda = 768$ nm; e) representative SEM image (scale bar corresponds to 200 nm); and f) the corresponding histogram of the number-weighted size distribution N of the tip-to-tip length L_{NS} of the NSs as determined from SEM images, $L_{NS} = (82.6 \pm 4.9)$ nm (adapted with permission from ref. [245]. Copyright 2019, Wiley-VCH Verlag GmbH & Co. KGaA).

The choice of the NSs at a concentration of 2 nM was influenced by prior optimization of core-shell Au nanorods (NRs)/ZIF-8 nanostructures by varying the Au nanorods concentration (*i.e.*, 1, 2 and 4 nM) in $5 \cdot 10^{-4}$ M CTAB aqueous solution in the synthesis. Scanning electron microscopy (SEM) revealed the resulting core-shell AuNRs/ZIF-8 nanostructures having a different concentration of AuNRs (see *Figure 4.7*). In the case of 1 nM, smaller ZIF-8 particles appear to be empty, and in the bigger ones, only a few AuNRs are observed to be located inside the framework structures (see *Figure 4.7a*). With 2 nM of AuNRs, SEM results confirmed that all AuNRs are confined within the ZIF-8 particles and with similar sizes and well-defined morphology (see *Figure 4.7b*). Finally, increasing the concentration of AuNRs up to 4 nM, it was noticed that, as when using 2 nM AuNRs, most of the ZIF-8 particles contained an AuNR in the center and only residual AuNRs are observed to be located outside the framework structures (see *Figure 4.7c*). This result indicated that CTAB-coated AuNRs act as seeds onto which the ZIF-8 grows.

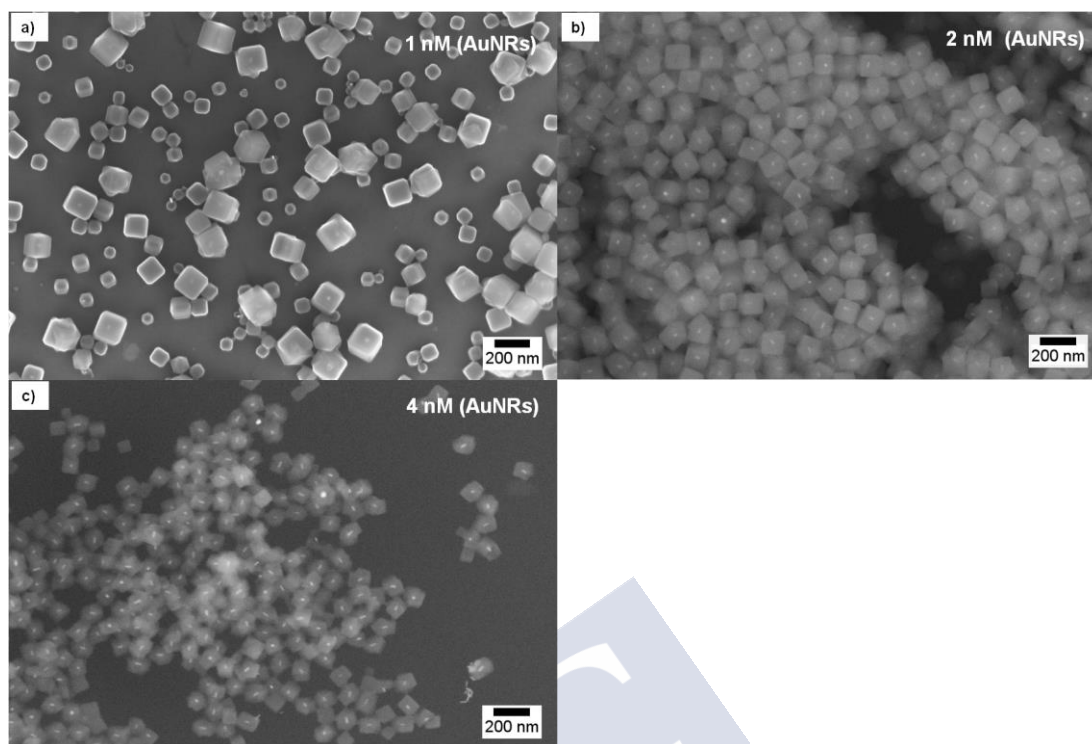


Figure 4.7. SEM micrographs of core-shell AuNRs/ZIF-8 structures with different concentrations of AuNRs: a) 1nM (average size ≈ 150 nM), b) 2nM (average size ≈ 120 nM) and c) 4nM (average size ≈ 90 nM).

Thus, the number of AuNSs seeds was chosen by the optimization process mentioned before to minimize by-products, in this case, such as non-coated NSs and/or pristine ZIF-8 nanoparticles. Scanning electron microscopy (SEM) revealed the resulting NCs having a polyhedral morphology with an average size of $\sim 218 \pm 24$ nm (see *Figures 4.8a-c*); *Figures 4.8d-f* shows bare ZIF-8 particles with cubic morphology^[180, 238] with an average size of 169 ± 27 nm, as control, when no NSs are added.

4.2.4. Encapsulation of Dye Molecules in AuNS/ZIF-8 Nanocomposite (NC-HOE)

The next step was the encapsulation of the bioactive cargo. We choose the bisbenzimidazole compound Hoechst H 33258 (HOE), a blue fluorescent dye typically used for DNA staining in molecular biology.^[246] The properties of HOE are particularly interesting for our purposes because DNA-unbound HOE is less fluorescent (ca. 1:30) than DNA-bound one, and free or released HOE will stain cell nuclei.^[246]

Then, NCs were loaded with HOE (NC-HOE) by soaking the NCs in a HOE solution (in methanol). After purification, an average of $\sim 2.9 \times 10^5$ HOE/NC was estimated by fluorescence measurements (using calibration curves, Figure 4.9) (see *section 2.3.2*).

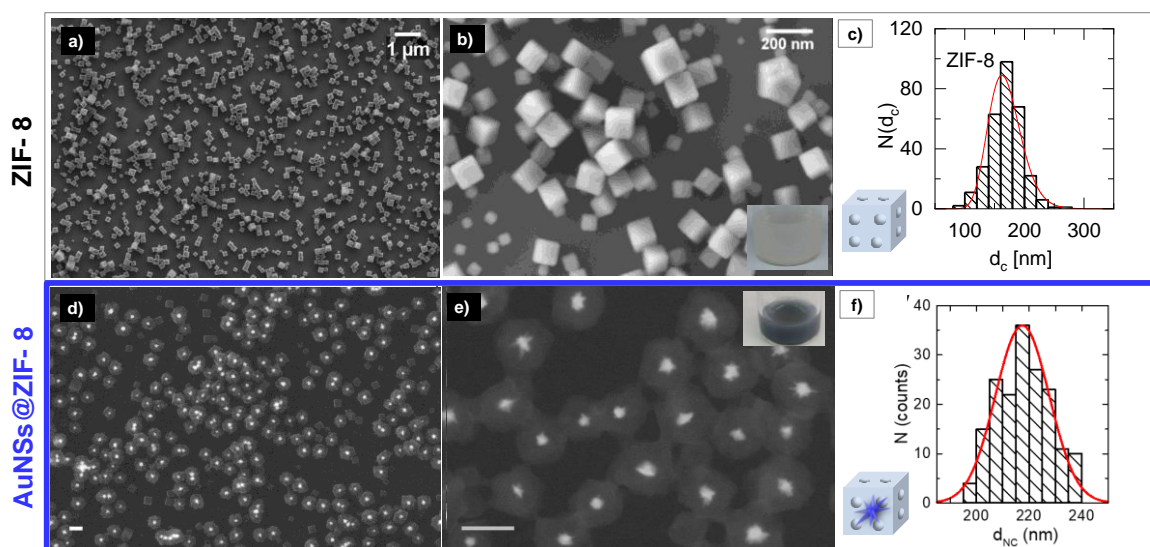


Figure 4.8. a-b) Low and high magnification SEM micrographs of ZIF-8 nanoparticles (SE2: type II secondary electrons, 3kV). c) Histogram of the number-weighted distribution N of the particle diameter (*i.e.*, vertex-to-vertex distance) d_c of ZIF-8 particles, as determined from SEM images using ImageJ; $d_{ZIF-8} = 169 \pm 27$ nm. d-e) Low and high magnification SEM micrographs of NCs (SE2: type II secondary electrons, 3kV), scale bars correspond to 200 nm. f) Histogram of the number-weighted distribution N of the diameter (*i.e.*, vertex-to-vertex distance) d_{NC} of NCs, as determined from SEM images using ImageJ; $d_{ZIF-8} = 218 \pm 24$ nm (adapted with permission from ref. [245]. Copyright 2019, Wiley-VCH Verlag GmbH & Co. KGaA).

i) Quantification by Fluorescence Measurements

The amount of HOE molecules loaded into the NCs as dispersed in MeOH was quantified by fluorescence ($\lambda_{exc}/\lambda_{em}=350/480$ nm) indirectly, by measuring the HOE remaining in the supernatants after centrifugation and washing steps of the particles. The HOE concentration in the supernatant was determined by interpolation of the measured fluorescence intensity (I) to a previously constructed analytical calibration curve (see *Figure 4.9a*). This led to a value (mean \pm standard deviation, $n=2$) of $2.94 \times 10^5 \pm 5.64 \times 10^2$ HOE per NC. It is worth noting that direct fluorescence measurements of the HOE molecules loaded into the NC led to an underestimation of the loaded amount, which is likely due to fluorescence quenching of HOE trapped in the ZIF-8 pores.

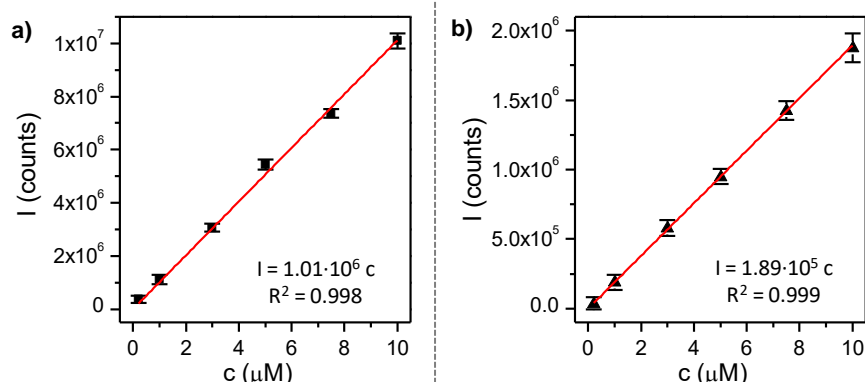


Figure 4.9. Calibration curves of HOE in (a) MeOH and (b) water were obtained from fluorescence measurements under excitation at 350 nm (I). Fluorescence intensity (I) at the maximum emission peak as a function of HOE concentration c is plotted, and the calibration equation is obtained by fitting a linear regression line to the collected data; R^2 is the coefficient of determination (adapted with permission from ref. [245]. Copyright 2019, Wiley-VCH Verlag GmbH & Co. KGaA).

4.2.5. Surface Functionalization in AuNS/ZIF-8 Nanocomposite (NC-HOE-PMA)

Next, a polymer grafting strategy was developed to “trap” the HOE inside the ZIF-8 voids and avoid its leakage. To that aim, we employed a post-functionalization strategy based on coating the NCs with PMA which has been extensively used for the functionalization of inorganic NPs.^[17]

i) *PMA-Based Amphiphilic Polymer*

NC and NC-HOE were functionalized with a PMA-based amphiphilic polymer (*i.e.*, poly [isobutylene–alt–maleic anhydride]–graft–dodecyl) in order to provide them with long-term colloidal stability in aqueous solution. The synthesis of the PMA (see *section 2.3.2*) as well as the protocol for the PMA-functionalization was performed as described previously (see *Figure 4.10*).^[17] The PMA optimization was based on achieving an optimum functionalization, that is, producing NC-PMA particles, which are colloidally stable in aqueous solution, while using the minimum amount of PMA for avoiding the formation of a large excess of free PMA micelles in solution. Anyhow, these free polymer micelles were removed by centrifugation. A scheme of the PMA–functionalization procedure of NC is shown in *Figure 4.11*.

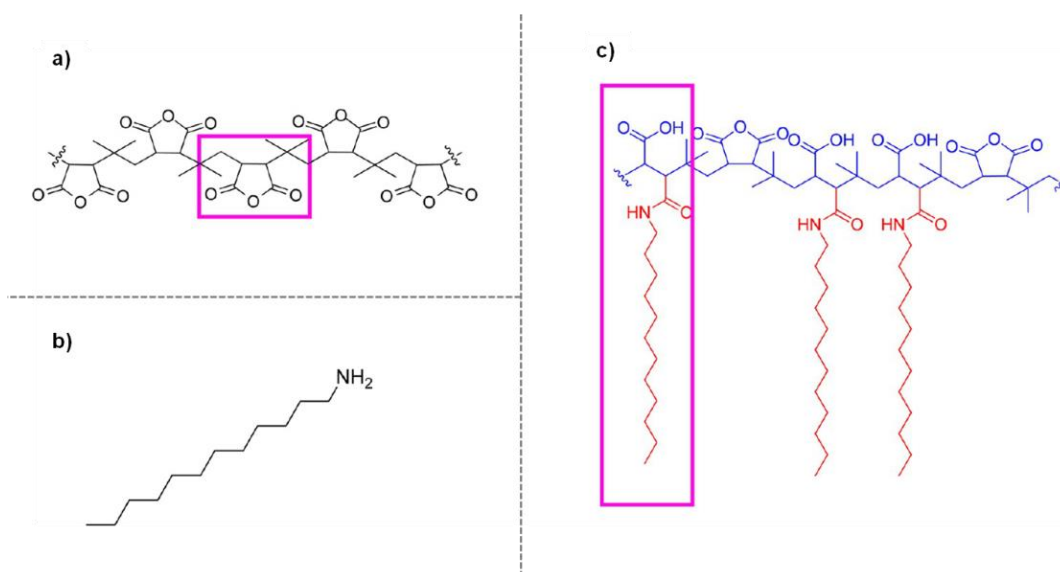


Figure 4.10. Synthesis of poly (isobutylene-alt-maleic anhydride)-graft-dodecyl. a) Poly (isobutylene-alt-maleic anhydride) is used as hydrophilic backbone (pink box is showing one monomer unit). b) Dodecylamine is used as hydrophobic side chain. The amphiphilic polymer was obtained by reaction of the hydrophilic backbone with hydrophobic side chains. c) Structure of the amphiphilic polymer (PMA-g-dodecyl). The pink box in c shows a monomer unit with attached side chain (final molar mass of one polymer unit M_p). The hydrophobic and hydrophilic parts are drawn in red and blue, respectively. (Adapted with permission from ref. [17]. Copyright 2016, American Chemical Society).

ii) *Quantification by Fluorescence Measurements*

A comparative analysis of TGA, N₂ isotherms and fluorescence HOE Quantification was further evaluated. The quantification of the HOE after the PMA-functionalization step was carried out by fluorescence measurements as described previously, here the measurements and calibration curve were performed in water, *cf.* Figure 4.9b. The amount of HOE after the PMA-functionalization decreased to $\sim 2/5$ ($1.25 \times 10^5 \pm 6.11 \times 10^2$ dyes molecules per NC) of the original HOE content in NC-HOE, which may indicate that there is some HOE-leakage during the PMA-functionalization process and/or PMA was encapsulated, partially occupying the ZIF-8 voids.

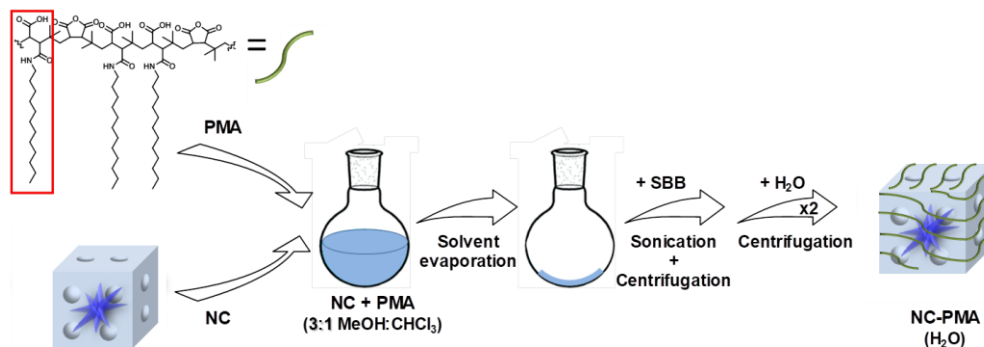


Figure 4.11. Scheme of the PMA-functionalization procedure of NC. PMA polymer (the red box shows one monomer unit) and NCs are mixed in a round flask (3:1 MeOH:CHCl₃) in a ratio of 150 monomers per nm² of NC, the solvent is then evaporated using a rotary evaporator, and the final dried product is redispersed in sodium borate buffer (SBB pH=9) by mild sonication. Purification of the resulting NC-PMA is carried out by centrifugation and washing with water (adapted with permission from ref. [245]. Copyright 2019, Wiley-VCH Verlag GmbH & Co. KGaA).

iii) Colloidal Characterization

After PMA functionalization and redispersion in water, the purified nanocomposites (NC-HOE-PMA) retained the polyhedral morphology, bluish aspect (see *Figures 4.12a-c*) and the hydrodynamic diameter of the original NCs (for comparison see *Table 4.4* and *Figure 4.13*), with ζ -potential from +34.2 to -27.5 mV before and after PMA functionalization, respectively, consistent with that obtained from other PMA-coated NPs.^[17] Additionally, UV-Vis spectroscopy was used to record the UV/Vis absorption spectrum of NCs in water, showing a SPR band centered at 790 nm (see *Figure 4.12d*). *Figure 4.12e* shows the fluorescence spectra of HOE before encapsulation (*i.e.* free dye) and after their loading into the NCs, in which a significant shift of the maximum emission peak was observed (from 472 nm to 480 nm), attributed to the interaction of HOE molecules with the ZIF-8 and/or the change of the surrounding medium inside the ZIF-8 pores. It is worth mentioning that PMA-functionalization of NCs led to a further redshift of the HOE emission from 480 nm to 492 nm.

After PMA-functionalization, the HOE loading dropped to ~40% of the original content (~1.2·10⁵ HOE/NC); this result suggests that some dye leakage may occur during PMA-functionalization and/or PMA partially replaced the dye within the porous ZIF-8 MOF structure, as mentioned previously.

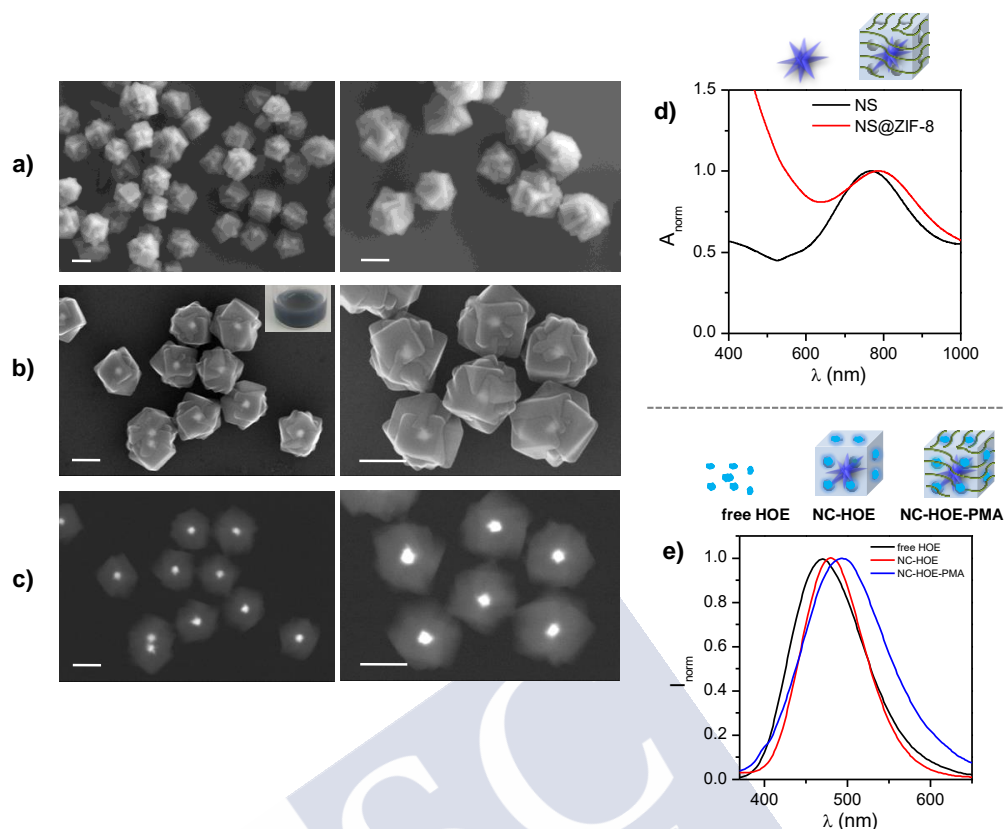


Figure 4.12. Representative SEM images of NC-PMA particles taken at different magnifications, with several detectors as well as voltages to get different information. a) Images collected with Everhart-Thornley detector (SE2, secondary electrons) at 3 kV; b) InLens detector (SE1, secondary electrons) at 20 kV; and c) AsB detector (backscattered electrons) at 20 kV. Scale bars correspond to 200 nm. d) Normalized UV/Vis absorption spectrum A_{norm} of NC particles showing their SPR peak at $\lambda = 790$ nm. Note that the UV/Vis spectrum of bare gold nanostars (NS) is also shown for comparison. e) Normalized fluorescence spectra I_{norm} of HOE before (free dye molecules) and after encapsulation into the nanocomposite (NC-HOE), as well as after PMA-functionalization (NC-HOE-PMA), respectively (adapted with permission from ref. [245]. Copyright 2019, Wiley-VCH Verlag GmbH & Co. KGaA).

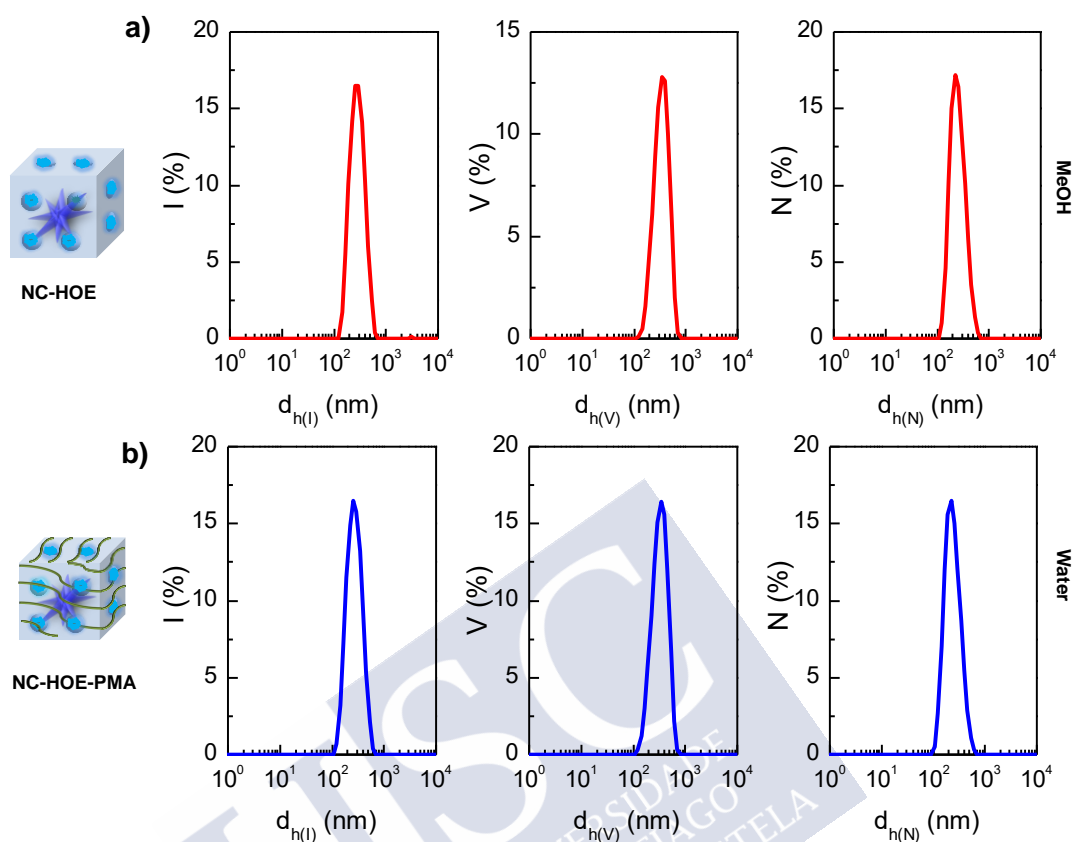


Figure 4.13. DLS intensity- (I), volume- (V), and number-weighted (N) size distributions, d_h , of NC-HOE a) before b) and after PMA-functionalization (NC-HOE-PMA). The NC-HOE sample was dispersed in MeOH whereas the NC-HOE-PMA one was dispersed in water (adapted with permission from ref. [245]. Copyright 2019, Wiley-VCH Verlag GmbH & Co. KGaA).

Table 4.4. Hydrodynamic diameters, d_h , (mean value \pm standard deviation SD) as derived from DLS measurements of NC-HOE and NC-HOE-PMA. The polydispersity index (PDI) for each sample is also given. Data correspond to the raw ones shown in Figure 4.13.

Sample	$d_{h(I)}(\text{nm})$	$d_{h(V)}(\text{nm})$	$d_{h(N)}(\text{nm})$	PDI
NC-HOE	289 ± 92	356 ± 106	244 ± 88	0.09
NC-HOE-PMA	273 ± 98	348 ± 103	235 ± 85	0.26

$d_{h(I)}$, $d_{h(V)}$ and $d_{h(N)}$ refer to the mean average hydrodynamic diameter from the intensity, volume and number-weighted size distributions derived from DLS, respectively. PDI refers to the polydispersity index. Standard deviation values were calculated from three independent measurements.

4.2.6. Selected Nanoparticles

To summarize the previous results, the addition of CTAB during the synthesis can be tuned the size of ZIF-8 particles. Then, the growth of a ZIF-8 particle on a single gold nanostar resulting in a core-shell structure was performed, followed by the encapsulation of the bioactive

cargo (*i.e.*, Hoechst). Finally, the samples were functionalized with a PMA-based amphiphilic polymer (*i.e.*, poly [isobutylene–alt–maleic anhydride]–graft–dodecyl). *Figure 4.14* shows the different nanoparticles in this chapter with their respective acronym.

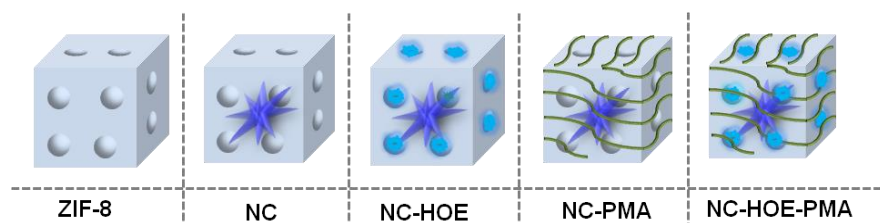


Figure 4.14. Schematic illustration of the different nanoparticles in this study.

4.2.7. Colloidal Stability of the Nanocomposites

Colloidal stability of PMA- and non-PMA (*i.e.*, NC-PMA and NC, respectively) functionalized systems was evaluated in water and cell medium for one week by DLS (see *Table 4.5*). The integrity of non-PMA (or NC) samples was compromised in both media as reflected by the rapid decrease of d_h (< 5 h), as shown in *Figures 4.15a* and *c*.

By simple visual inspection, one could also see how the characteristic turbidity of the NCs (*i.e.*, non-PMA) gradually disappears within few hours as observed from *Figure 4.16a*. Moreover, scanning electron microscopy (SEM) inspection of NCs redispersed in water illustrates their “disintegration” (see *Figures 4.16b-c*). On the other hand, d_h of samples with PMA remained stable, indicating that water or cell medium did not affect their integrity (see *Figures 4.15b-c*), which was also corroborated by SEM inspection of NC-PMA after dispersion for one week in water (see *Figures 4.16d-f*).

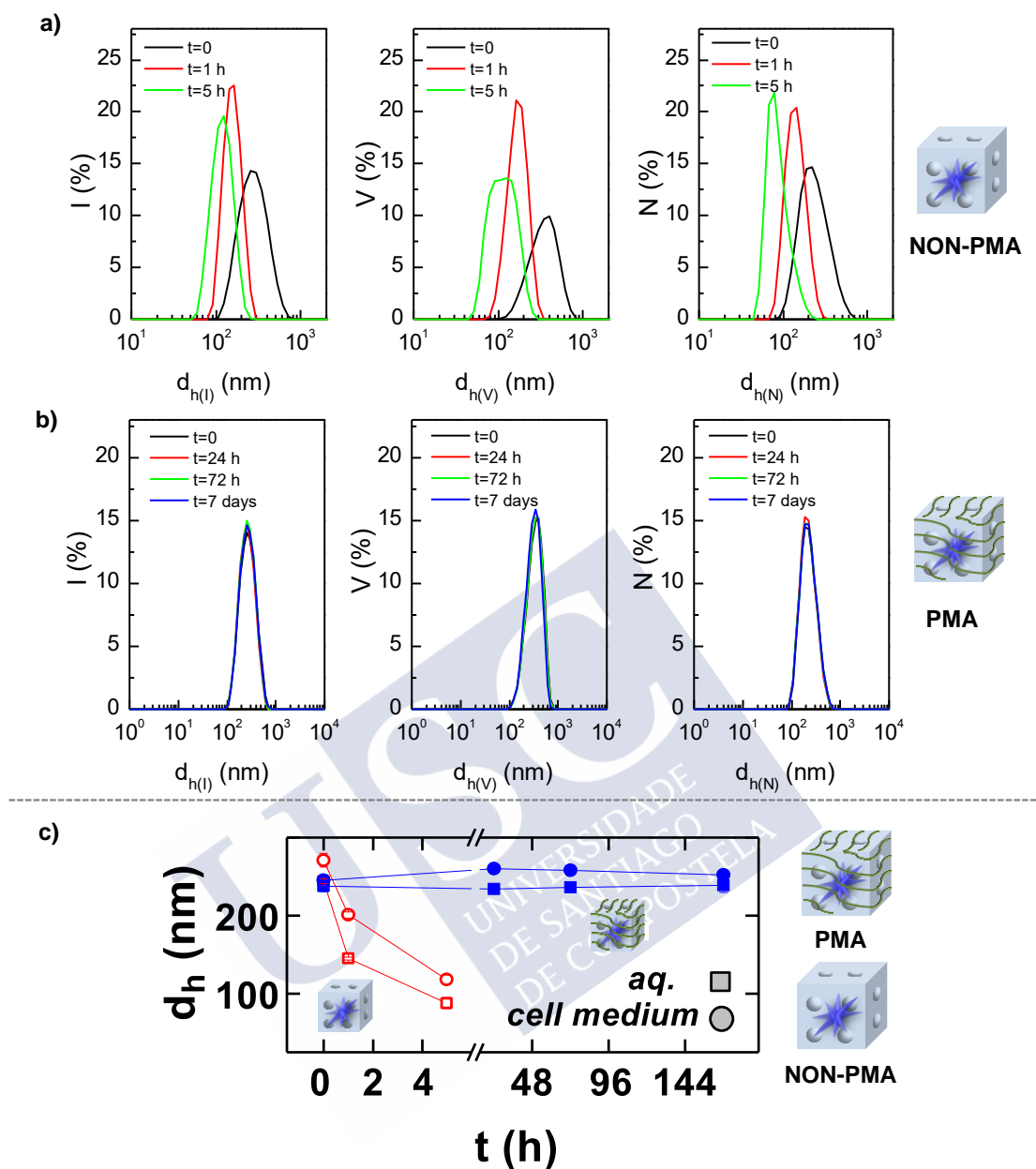


Figure 4.15. DLS intensity-, volume-, and number-weighted size distributions, d_h , of NC a) before b) and after PMA-functionalization, NC-PMA as dispersed in water at different time points. c) Mean d_h for one week for NC (red) and NC-PMA (blue) in water (squares) and cell medium (circles), respectively (adapted with permission from ref. [245]. Copyright 2019, Wiley-VCH Verlag GmbH & Co. KGaA).

Table 4.5. Hydrodynamic diameters, d_h , (mean value \pm SD) as derived from DLS of nanocomposite particles before (NC) and after PMA-functionalization (NC-PMA), and dispersed in water or in cell culture medium at different time points. SD values correspond to the standard deviation of the diameter mean value as obtained from several repeats ($n=3$).

NC								
Time	water				cell medium			
	$d_{h(I)}$ (nm)	$d_{h(V)}$ (nm)	$d_{h(N)}$ (nm)	PDI	$d_{h(I)}$ (nm)	$d_{h(V)}$ (nm)	$d_{h(N)}$ (nm)	PDI
0 h	289 \pm 7	356 \pm 4	244 \pm 3	0.09	297 \pm 10	378 \pm 12	271 \pm 9	0.22
1 h	159 \pm 4	172 \pm 3	145 \pm 2	0.17	219 \pm 4	232 \pm 5	201 \pm 4	0.36
5 h	122 \pm 4	119 \pm 6	88 \pm 7	0.25	154 \pm 6	142 \pm 7	118 \pm 6	0.30
NC-PMA								
Time	water				cell medium			
	$d_{h(I)}$ (nm)	$d_{h(V)}$ (nm)	$d_{h(N)}$ (nm)	PDI	$d_{h(I)}$ (nm)	$d_{h(V)}$ (nm)	$d_{h(N)}$ (nm)	PDI
0 h	283 \pm 5	359 \pm 8	238 \pm 7	0.21	292 \pm 9	362 \pm 12	245 \pm 7	0.23
24 h	273 \pm 8	349 \pm 7	234 \pm 5	0.26	315 \pm 9	375 \pm 15	260 \pm 5	0.22
72 h	277 \pm 6	346 \pm 9	236 \pm 5	0.24	321 \pm 8	371 \pm 13	258 \pm 6	0.27
7 days	281 \pm 5	345 \pm 7	239 \pm 9	0.24	318 \pm 9	369 \pm 13	252 \pm 7	0.32

$d_{h(I)}$, $d_{h(V)}$ and $d_{h(N)}$ refer to the mean average hydrodynamic diameter from the intensity, volume and number-weighted size distributions derived from DLS, respectively. PDI refers to the polydispersity index. Standard deviation values were calculated from three independent measurements.

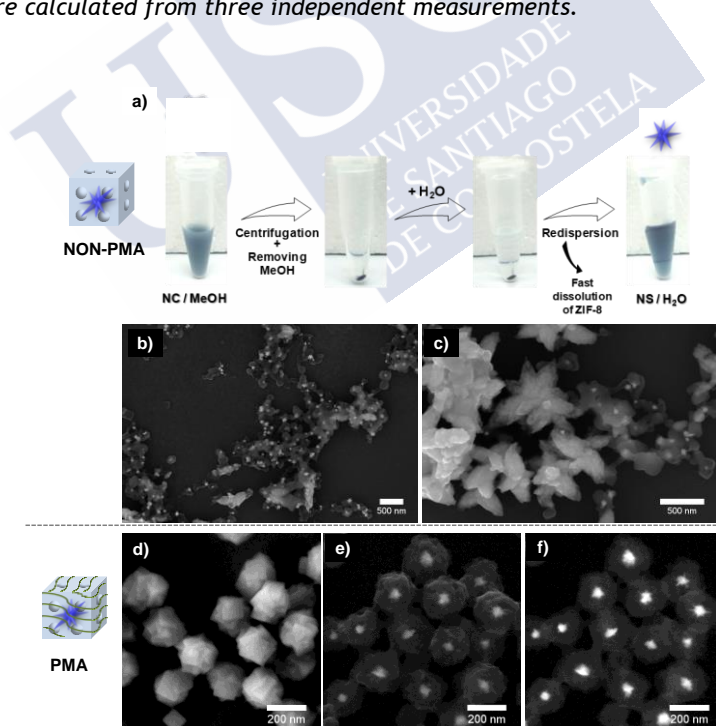


Figure 4.16. a) Assay to check the lack of stability of bare NC (without PMA coating) in aqueous solution. NC particles initially stable in MeOH were centrifuged, MeOH (supernatant) was removed, and NC particles (precipitate) were redispersed in water, resulting in the dissolution of the ZIF-8 shell around the NSs. b-c) SEM micrographs of NCs with PMA coating (after exposure to aqueous solution, without centrifugation/purification) after drop casting on Si substrates. d-f) SEM micrographs of NCs acquired with different detectors: d) SE2, 3kV, e) InLens, 20kV, and f) AsB, 20kV (adapted with permission from ref. [245]. Copyright 2019, Wiley-VCH Verlag GmbH & Co. KGaA).

Structural Characterization

i) Powder X-ray Diffraction (PXRD)

Powder X-ray diffraction (PXRD) analysis of both PMA and non-PMA coated samples exhibit the characteristic Bragg peaks of ZIF-8 and Au⁰, and confirms that PMA-functionalization does not affect the ZIF-8 shell crystallinity (see *Figure 4.17*). The relevant peaks identified by PXRD analysis for each sample are summarized in *Table 4.6*.

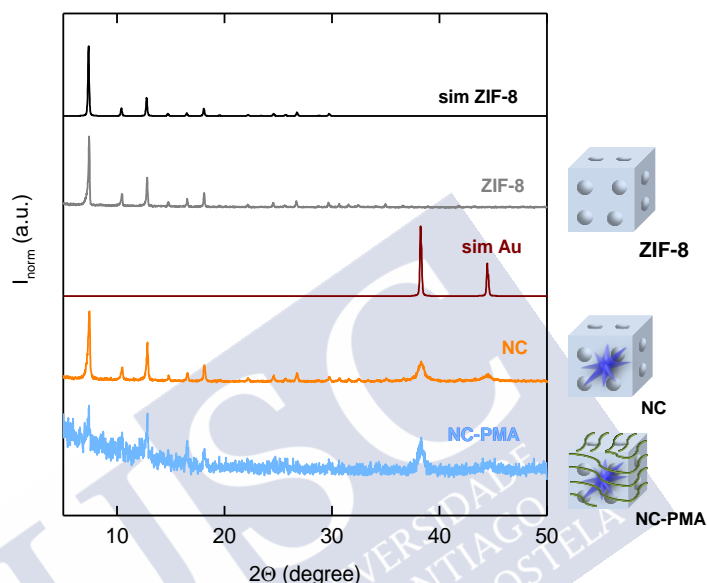


Figure 4.17. PXRD spectra of ZIF-8 (grey), NC (orange) and NC-PMA (blue). For comparison, simulations of ZIF-8 [black, COD (Crystallography Open Database): 7111970] and Au-fcc (wine; COD: 9008463) are added. I_{norm} is the normalized intensity (adapted with permission from ref. [245]. Copyright 2019, Wiley-VCH Verlag GmbH & Co. KGaA).

ii) Surface Enhanced Raman Spectroscopy (SERS)

Once we confirm that our NCs are stable in aqueous solution, the next step was to test the effective encapsulation of HOE into the MOF composites by surface enhanced Raman spectroscopy, SERS (with and without PMA and/or HOE). Free HOE was used as control (see *Figure 4.18*). The results indicated that SERS spectra of plasmonic NCs without HOE were dominated by the characteristic vibrational modes of ZIF-8 (the imidazole ring puckering, 685 cm⁻¹; the CN stretching, 1146 cm⁻¹ and the CH wagging, 1460 cm⁻¹).^[247] Nevertheless, when NCs were loaded with HOE, none of these vibrational features can be observed as a consequence of the strong signal promoted by the dye in close contact with the plasmonic surface (ring breathing, 980 cm⁻¹; CH deformation 1270 and 1455 cm⁻¹ and CC and CN stretchings, 1554 and 1575 cm⁻¹), *i.e.*, samples NC-HOE and NC-HOE-PMA showed the characteristics SERS peaks for Hoechst dye and the small characteristics vibration modes of ZIF-8.

Table 4.6. Major peaks: (relative intensity > 6%) identified in the ZIF-8 diffractogram, (relative intensity > 6%) identified in the NC diffractogram, and (relative intensity > 9%) identified in the NC-PMA diffractogram, respectively.

Sample	Pos. [$^{\circ}2\theta$]	Height [cts]	FWHM Left [$^{\circ}2\theta$]	d - spacing [\AA]	Rel. Int. [%]
ZIF-8	7.38	597	0.14	11.963	100.0
	12.79	270	0.12	6.914	45.2
	18.10	140	0.11	4.898	23.5
	10.44	116	0.13	8.468	19.5
	16.53	84	0.08	5.359	14.1
	26.68	57	0.13	3.338	9.6
	14.77	270	0.12	5.991	8.2
	24.52	44	0.12	3.628	7.5
	29.68	42	0.11	3.008	7.0
NC (non-PMA)	7.39	531	0.19	11.948	100.0
	12.81	264	0.16	6.904	49.6
	38.28	132	0.65	2.349	24.9
	18.13	127	0.17	4.891	23.9
	10.46	94	0.17	8.452	17.7
	26.73	65	0.10	3.332	12.2
	16.54	60	0.16	5.354	11.2
	14.81	43	0.12	5.977	8.2
	24.55	43	0.18	3.623	8.2
	29.73	37	0.10	3.002	6.9
	44.38	35	0.87	2.039	6.6
NC-PMA	7.36	24	0.17	12.001	100.0
	16.52	22	0.17	5.361	89.6
	12.78	21	0.25	6.923	88.5
	38.24	19	0.62	2.352	76.8
	18.13	13	0.26	4.889	52.2
	14.79	11	0.09	6.923	45.5
	8.44	11	0.09	10.463	45.0
	10.46	11	0.11	8.447	44.4
	29.70	5	0.20	3.005	22.5
	24.44	5	0.30	3.639	22.2
	44.54	5	1.30	2.033	19.7
	25.50	2	0.50	3.489	9.7

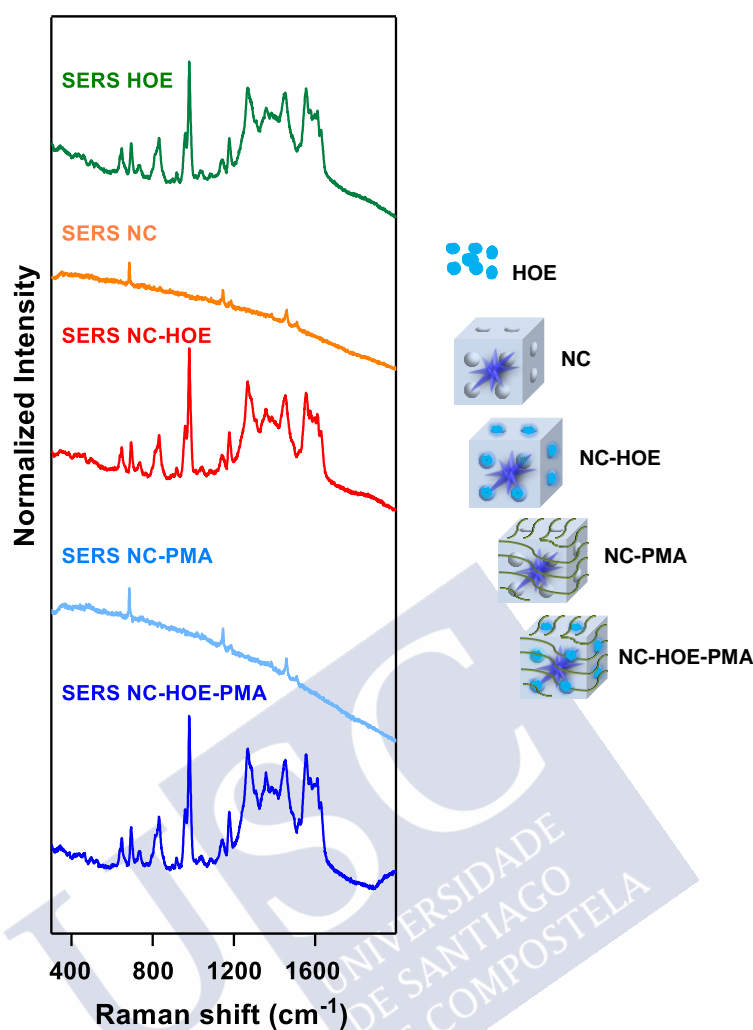


Figure 4.18. SERS spectra of free HOE and nanocomposites (NCs) with or without HOE trapped (adapted with permission from ref. [245]. Copyright 2019, Wiley-VCH Verlag GmbH & Co. KGaA).

4.2.8. Thermal Characterization

Furthermore, the thermodynamic characterization of the prepared NCs and pristine ZIF-8 were systematically investigated by thermogravimetric analysis (TGA) performed under air atmosphere (see *Figure 4.19*). The samples without PMA showed a sharp weight loss (50–60 wt%) at around 400 °C, associated with the total combustion of 2-methylimidazole and the formation of different inorganic residues: ZnO in case of ZIF-8, or ZnO and Au⁰ in case of NC and NC-HOE, as identified by XRPD of the residues (see *Figure 4.20*). PMA-modified samples showed an initial mass loss (~10 wt%) associated with the PMA glass transition (150–250 °C) and a final departure (~20 wt%) at around 250–350 °C,^[17] followed by the combustion of the 2-methylimidazole as observed in non-PMA samples (~400 °C). The different inorganic residues served us to estimate the relative content of Au, PMA, ZIF-8 and HOE among samples (see *Table 4.7*).

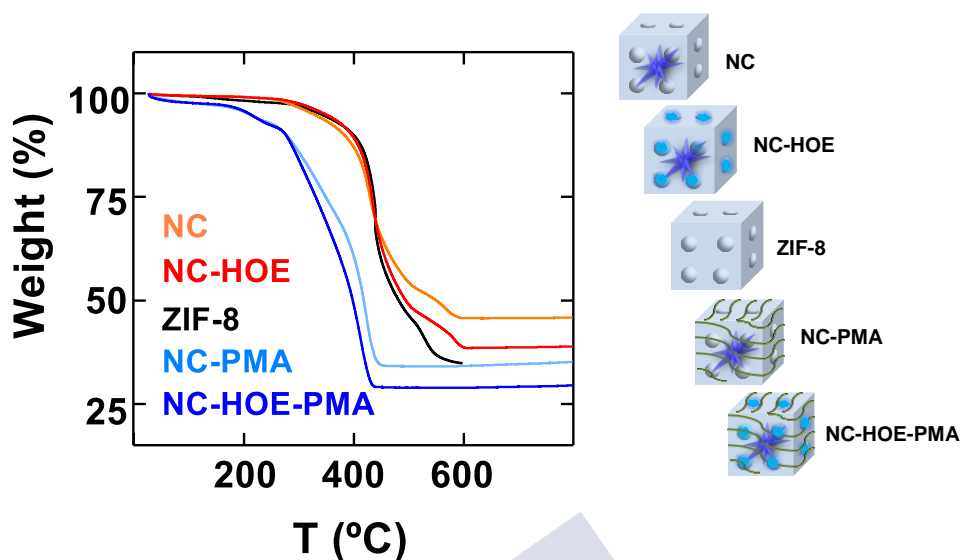


Figure 4.19. TGA of the different nanoparticles (adapted with permission from ref. [245]. Copyright 2019, Wiley-VCH Verlag GmbH & Co. KGaA).

i) Recalculation of the Inorganic and Organic Content

Taking into account the evaporation of water and remaining solvents within the porosity $T < 150\text{ }^{\circ}\text{C}$, the recalculation of the inorganic and organic content (% wt = weight percentage) of the samples (*i.e.*, ZIF-8, NC, NC-HOE, NC-PMA and NC-HOE-PMA), is described below (numerical values are provided in Table 12):

NS wt % in NCs: considering there is no loss of organic content of ZIF-8 (MeIm) during the synthesis:

$$\text{Inorganic wt \% NC}_{\text{equivalent}} = \frac{\text{Organic wt \% NC}}{\text{Organic wt \% ZIF-8}} \times \text{Inorganic wt \% ZIF-8} \quad (4.1)$$

$$\text{NS wt \%} = \text{Total Inorganic wt \% NC} - \text{Inorganic wt \% NC}_{\text{equivalent}} \quad (4.2)$$

HOE wt % in NC-HOE: considering the inorganic content (NS and Zn) remains constant:

$$\text{Organic wt \% NC-HOE}_{\text{equivalent}} = \frac{\text{Inorganic wt \% NC-HOE}}{\text{Inorganic wt \% NC}} \times \text{Organic wt \% NC} \quad (4.3)$$

$$\text{HOE wt \%} = \text{Total Organic wt \% NC-HOE} - \text{Organic wt \% NC-HOE}_{\text{equivalent}} \quad (4.4)$$

PMA wt % in NC-PMA: considering the inorganic content (NS and Zn) remains constant:

$$\text{Organic wt \% NC-PMA}_{\text{equivalent}} = \frac{\text{Inorganic wt \% NC-PMA}}{\text{Inorganic wt \% NC}} \times \text{Organic wt \% NC} \quad (4.5)$$

$$\text{PMA wt \%} = \text{Total Organic wt \% NC-PMA} - \text{Organic wt \% NC-PMA}_{\text{equivalent}} \quad (4.6)$$

HOE & PMA wt% in NC-HOE-PMA: considering the inorganic content (NS and Zn) remains constant and that 1/3 of HOE remains inside after PMA functionalization:

$$\text{Organic wt \% NC-HOE-PMA}_{\text{equivalent}} = \frac{\text{Inorganic wt \% NC-HOE-PMA}}{\text{Inorganic wt \% NC}} \times \text{Organic wt \% NC} \quad (4.7)$$

$$\text{(PMA+HOE) wt \%} = \text{Total Organic wt \% NC-HOE-PMA} - \text{Organic wt \% NC-HOE-PMA}_{\text{equivalent}} \quad (4.8)$$

$$\text{HOE wt \%} = \left(\frac{2}{5}\right) \frac{\text{Inorganic wt \% NC-HOE-PMA}}{\text{Inorganic wt \% NC-HOE}} \times \text{HOE wt \% in NC-HOE} \quad (4.9)$$

$$\text{PMA wt \%} = \text{(PMA+HOE) wt \%} - \text{HOE wt \%} \quad (4.10)$$

Table 4.7. Organic and inorganic weight percentage (wt %) derived from TGA measurements in selected samples, and estimated % wt of Au, HOE and PMA.

Sample	Organic wt %	Inorganic wt %	Au wt %	HOE wt %	PMA wt %
ZIF-8	63.92	36.08	n/a	n/a	n/a
NC	52.89	47.11	17.26	n/a	n/a
NC-HOE	60.57	39.43	14.44	16.30	n/a
NC-PMA	64.95	35.05	12.84	n/a	25.60
NC-HOE-PMA	70.10	29.90	10.95	4.94	31.59

4.2.9. Surface Characterization

i) *N₂ Isotherms Analysis*

The surface area and porosity properties of the different the types of particles were evaluated by nitrogen adsorption-desorption experiments. N₂ sorption measurements at 77 K of ZIF-8, NC, NC-HOE, NC-PMA and NC-HOE-PMA showed type I isotherms (see *Figure 4.21a*), characteristic of microporous materials, with a BET specific surface areas (S_{BET}) of 1800, 1570, 1260, 850 and 220 m²·g⁻¹, respectively. Specific surface area was determined by applying BET equation (Brunauer, Emmett & Teller) in the pressure interval P/P₀ =0.01-0.3 (being P₀ the saturation pressure).

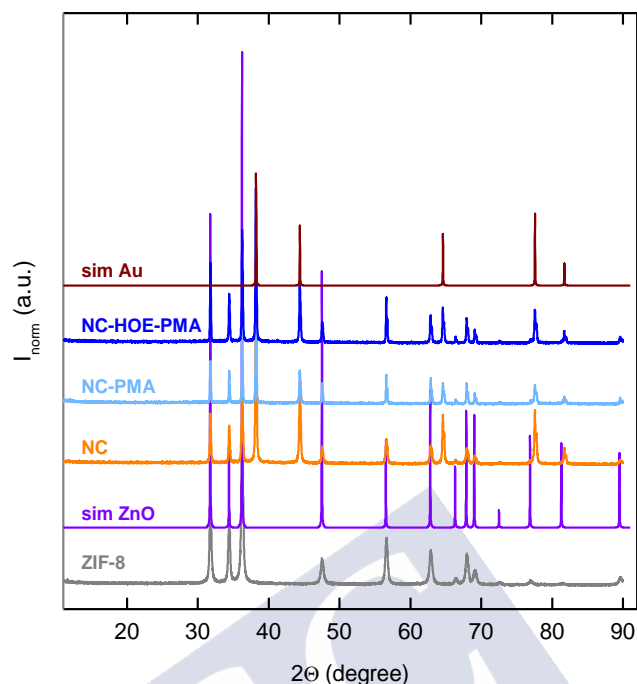


Figure 4.20. PXRD spectra of TGA residues. For comparison, simulations of ZnO (violet; COD: 2300112) and Au (wine; COD: 9008463) are added. I_{norm} is the normalized intensity (adapted with permission from ref. [245]. Copyright 2019, Wiley-VCH Verlag GmbH & Co. KGaA).

The normalization of the S_{BET} by the porous ZIF-8 weight shows no significant difference between the ZIF-8 and NCs, indicating that the ZIF-8 shell shares the same textural properties as the pristine ZIF-8 (see *Table 4.8*). The important reduction of the microporosity (normalized S_{BET} before and after HOE encapsulation ~ 1800 versus $1500 \text{ m}^2 \cdot \text{g}^{-1}$) confirms that the HOE is allocated within the ZIF-8 shell.

The corrected surfaces indicate that PMA not only provides an outer coating for the NCs, but also partially fills the NC-PMA ($S_{\text{BET}} \approx 1440 \text{ m}^2 \cdot \text{g}^{-1}$), which agrees with the results obtained by fluorescence ($\sim 60\%$ HOE loss after PMA, final corrected $S_{\text{BET}} \approx 470 \text{ m}^2 \cdot \text{g}^{-1}$). Furthermore, the additional and progressive N_2 sorption at higher pressures ($P/P_0 = 0.3-0.9$) in the PMA-coated samples suggests gas adsorption on the surface polymer branches ($0.25 \text{ cm}^3 \cdot \text{g}^{-1}$ in NC-PMA versus $0.06 \text{ cm}^3 \cdot \text{g}^{-1}$ in the pristine ZIF-8, respectively). Of note, the volume occupied by HOE in NCs (estimated from the total HOE content and N_2 sorption measurements: $V \sim 0.13 \text{ cm}^3 \cdot \text{g}^{-1}$, see *Table 4.8* and *Figure 4.21b*, and from fluorescence data: $V \sim 0.15 \text{ cm}^3 \cdot \text{g}^{-1}$, is within the range of its theoretical volume ($V \sim 0.24 \text{ cm}^3 \cdot \text{g}^{-1}$, estimated by taking into account the volume of a HOE molecule under vacuum and its loading in the solid. Pore volume and pore size distribution were calculated by the NLDT method (Non-Localized Density Functional Theory) and the HK (Horvath-Kawazoe) methods, respectively.

In fact, although the estimated HOE dimensions ($18.5 \times 4.1 \times 4.1 \text{ \AA}$) are slightly larger than the accessible windows of ZIF-8 ($\sim 3.6 \text{ \AA}$),^[248] the potential HOE rearrangement and the flexibility of ZIF-8^[249] support the HOE location within the porous particle structure in agreement with SERS data.

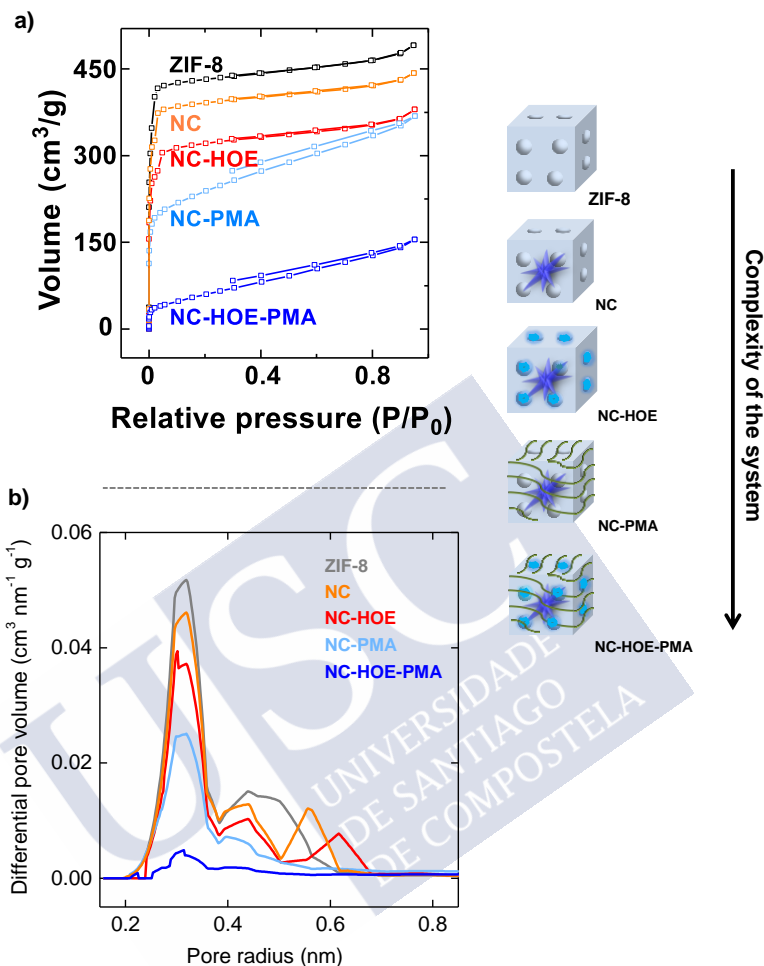


Figure 4.21. a) N_2 sorption isotherms at 77 K of the different nanocomposites (NCs). b) HK pore volume distribution of selected samples (adapted with permission from ref. [245]. Copyright 2019, Wiley-VCH Verlag GmbH & Co. KGaA).

ii) Comparative Analysis of TGA, N_2 Isotherms and Fluorescence HOE Quantification

HOE content in NC was estimated from different characterization data, providing values in the same order of magnitude. Notice that we had to take rough approximations such as the volume of one NC, the concentration of NC or the number of HOE per NC (from fluorescence data).

TGA:

Considering the % wt values in *Table 4.7*, the weight ratio HOE/ZIF-8 is:

$$R_{\text{ZIF-8}}^{\text{HOE}} = \frac{g_{\text{HOE}}}{g_{\text{ZIF-8}}} = \frac{\text{HOE wt \%}}{100 - \text{NS wt \%} - \text{HOE wt \%} - \text{NS wt \%}} = 0.24 \quad (4.11)$$

Then, taking the number of HOE molecules ($MW_{\text{HOE}} = 424 \text{ g/mol}$) corresponding to the HOE ratio above calculated, and the HOE volume ($V_{\text{HOE}} = 18.5 \times 4.1 \times 8.6 \text{ \AA} = 0.65 \times 10^{-21} \text{ cm}^3$, overestimated dimensions of HOE in vacuum) per g of ZIF-8, the pore volume occupied by the HOE load can be estimated as:

$$\text{Pore volume}_{\text{HOE}} = R_{\text{ZIF-8}}^{\text{HOE}} \times MW_{\text{HOE}}^{-1} \times N_A \times V_{\text{HOE}} = 0.22 \text{ cm}^3 \text{g}^{-1} \quad (4.12)$$

N₂ Isotherms:

Considering the data (corrected) from *Table 4.8*, the pore volume occupied by the HOE loaded is:

$$\text{Pore volume}_{\text{HOE}} = \text{Pore volume}_{\text{NC}} - \text{Pore volume}_{\text{NC-HOE}} = 0.13 \text{ cm}^3 \text{g}^{-1} \quad (4.13)$$

HOE Loading Estimated from Fluorescence Quantification:

From the HOE loading estimation based on fluorescence data (*i.e.*, $N_{\text{HOE}} = 2.93 \times 10^5 \pm 6.20 \times 10^2 \text{ HOE/NC-HOE}$), we can make an approximation of the pore volume occupied by the HOE loading as:

$$\text{Pore volume}_{\text{HOE}} = N_{\text{HOE}} \times V_{\text{HOE}} \times (V_{\text{NC-HOE}} - V_{\text{NS}})^{-1} \times \rho_{\text{eff,NC}} = 0.15 \text{ cm}^3 \text{g}^{-1} \quad (4.14)$$

where the volume of one NC-HOE was approximated to that of one cube of edge $L = 154 \text{ nm}$ (which corresponds to a square of edge 154 nm circumscribed in a circle of diameter 218 nm), and then

$$V_{\text{NC-HOE}} - V_{\text{NS}} = L^3 = 3.60 \times 10^{-15} \text{ cm}^3 \quad (4.15)$$

Also, we estimated the density of a NC as:

$$\rho_{\text{eff,NC}} = 0.012 \times \rho_{\text{Au}} + 0.988 \times \rho_{\text{ZIF-8}} = 0.50 \text{ g cm}^{-3} \quad (4.16)$$

where $\rho_{\text{Au}} = 19.3 \text{ g cm}^{-3}$, $\rho_{\text{ZIF-8}} = 0.35 \text{ g cm}^{-3}$, and we estimated from geometrical considerations and the TGA analysis (Au wt % in NC) that one NS occupies *ca.* 1.2 % of V_{NC} .

Table 4.8. Data extracted from the N₂ isotherms analysis.

Sample	S _{BET} (m ² g ⁻¹)	Micropore volume (P/P ₀ <0.3) (cm ³ g ⁻¹)	S _{BET} (m ² g ⁻¹) *	Micropore volume (P/P ₀ <0.3) (cm ³ g ⁻¹)*	Mesopore volume (P/P ₀ =0.3-0.9) (cm ³ g ⁻¹)*
ZIF-8	1800	0.68	-	-	0.06
NC	1570	0.61	1840	0.74	0.10
NC-HOE	1260	0.51	1510	0.61	0.12
NC-PMA	850	0.40	1440	0.67	0.25
NC-HOE-PMA	220	0.11	470	0.24	0.23

* corrected considering exclusively the ZIF-8 weight

4.2.10. Thermoplasmonic Behavior Studies in Aqueous Solution and Inside Living Cells

Photothermal characterization of the nanosystems and the entire experimental work involving cells were part of the Ph.D. thesis of Raquel Martínez González (Completed) (see *Chapter 6 Appendix 6.1*).

Results arising from the thermoplasmonic behavior studies of NCs in aqueous solution and inside living cells can be summarized as follows:

- 1) Bare (in methanol) and PMA-coated (in water) NCs were irradiated for 1 min (7 W/cm²) with a NIR optical system. It was found that the greater the concentration, the higher the temperature was achieved (~44 °–56 °C) (see *Figure 4.22a*).
- 2) After irradiation, NCs were precipitated and the HOE content (released) in the supernatant was quantified by fluorescence. The irradiated samples showed a much higher HOE release than the control ones, heated in a thermostatic bath (1 min, 50 °C), or than non-treated samples (RT) (see *Figure 4.22b*).
- 3) HOE-loaded, non-PMA- and PMA-coated NCs were added to adherent cells. The intracellular monitoring of cargo delivery upon illumination with a NIR light (785 nm, 3 mW) was carried out using SERS imaging with a confocal microscope.
 - 3.1) From SERS results (see *Figure 4.22c*); no signals belonging to HOE were detected for NC-HOE. This is consistent with the degradation of ZIF-8 in the water previously to cell uptake. In the case of NC-HOE-PMA, a clear HOE signal was recorded in certain regions of the cell (likely in lysosomes)^[250] previous to light illumination. In fact, after 8 h of irradiation no HOE signal could be discerned. However, the release kinetics clearly show that ~75% of HOE is released for the first 2 h of illumination. These results contrast with those obtained for the same nanomaterial but in the absence of continuous illumination. At time 0 h and after 8 h SERS spectra show clear HOE signals, indicating that the integrity of the drug carrier was not compromised.
 - 3.2) SERS data fully agree with equivalent studies by confocal microscopy. From *Figure 4.22d*, NC-HOE-PMA showed HOE accumulation (blue colored dots) in the vicinity of the nuclei, which were not blue-stained due to the lack of HOE leakage. On the other hand, the non-PMA-coated sample showed bright nucleus

blue staining as a consequence of HOE leakage as a consequence of the lack of NC integrity in cell medium (see *Figure 4.22e*).

- 3.3) Finally, cells containing NC-HOE-PMA were irradiated with the NIR illumination setup (5 min, 7 W/cm², beam diameter ~1 cm²). A stained nucleus was observed thanks to controlled HOE release (see *Figure 4.22f*).

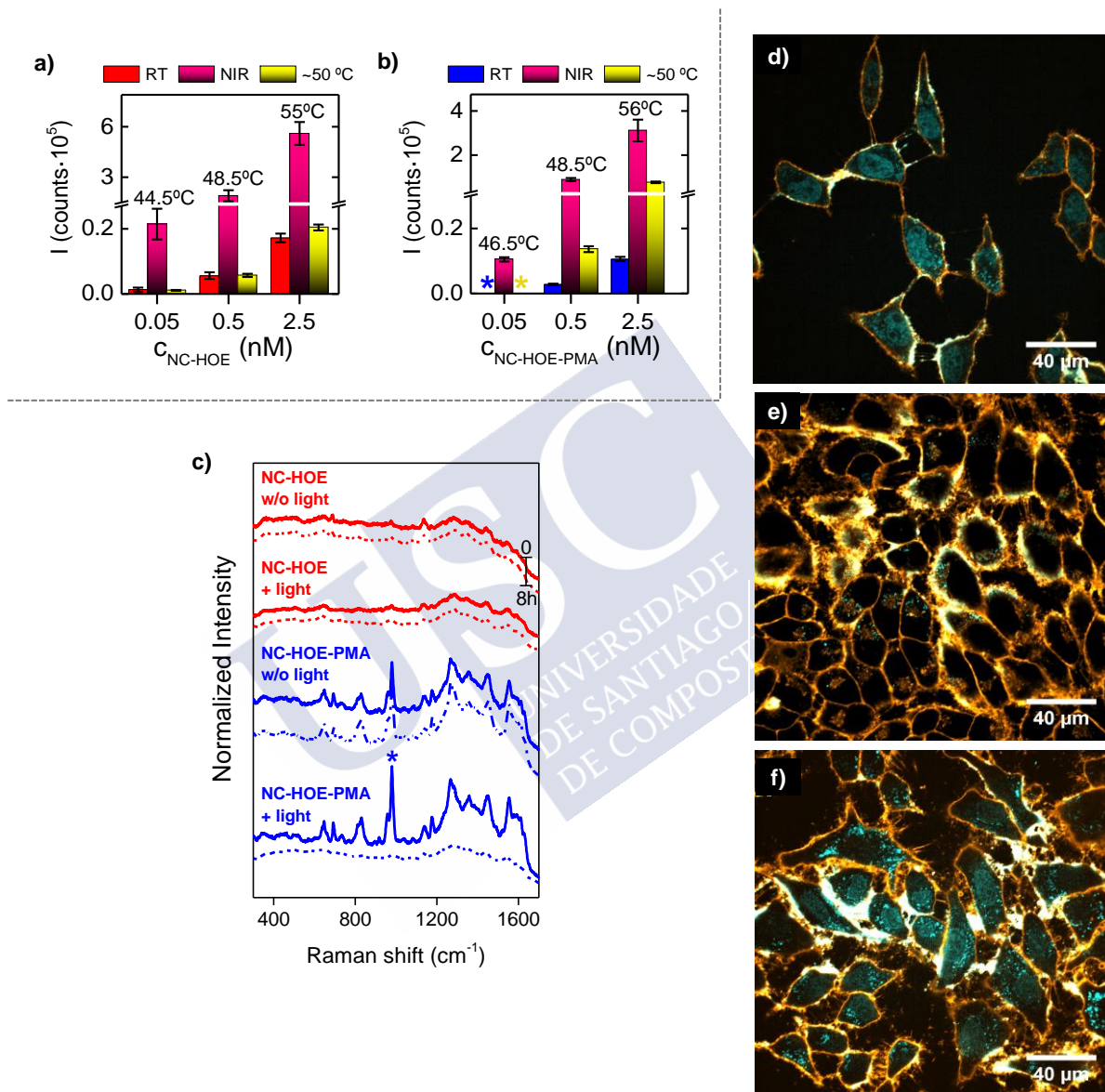


Figure 4.22. a) HOE release in methanol by fluorescence (I) after NIR illumination of the NC-HOE system (pink) at different concentrations (c); as controls, NC-HOE was heated in a thermostatic bath (50 °C, 1 min, yellow) or non-heated (red). b) Equivalent HOE release (I) in water for the NC-HOE-PMA system (blue); control samples at $c=0.05$ nM did not show any significant HOE release (*below the detection limit). c) SERS spectra of NCs after incubation with cells. Spectra were acquired in the presence and absence of NIR illumination (785 nm); solid and dashed lines represent the time points 0 h and 8 h, respectively. d-f) Confocal microscopy image of cells incubated with NC-HOE (d), NC-HOE-PMA (e) and NC-HOE-PMA after NIR treatment (f). In d-f), blue and orange color represent HOE and cell membrane staining (CellMask™ Deep Red), respectively; scale bar is 40 μm (adapted with permission from ref. [245]. Copyright 2019, Wiley-VCH Verlag GmbH & Co. KGaA).

4.3. Conclusions

In this chapter, we demonstrated the development of a ZIF-8-nanomaterial combined with thermoplasmonic and high drug-loading capabilities that are stable in both aqueous solutions and cells. Zeolitic imidazolate Frameworks -8 and -67 (*i.e.*, ZIF-8 and ZIF-67) particles were produced with very high monodispersity and precise size using cetyltrimethylammonium bromide (CTAB) as a growth-arresting surfactant. The ZIF-8 particles comprised a core of gold nanostar (NS) that was encapsulated during the synthesis. The nanostructures were loaded with bisbenzimidazole molecules as a functional cargo. The stability of the particles in aqueous medium was achieved by coating them with the amphiphilic polymer PMA (poly-[isobutylene-alt-maleic anhydride]-graft-dodecyl), which also prevents the drug from being uncontrollably released. After PMA functionalization and redispersion in water, the purified nanocomposites retained the polyhedral morphology and the hydrodynamic diameter ($d_h = 235 \pm 85$ nm). From N_2 sorption isotherms data it was observed that as the complexity of the system grows, the porosity of the samples decreases. The crystallinity of the ZIF-8 shell was not affected by the PMA functionalization, in agreement with XRD results. SERS data and confocal microscopy studies on living cells agree with the fact that bare samples (uncoated) showed bright nucleus staining as a consequence of HOE leakage. On the other hand, NCs with the PMA coating only showed accumulation (blue-colored dots) in the vicinity of the nuclei, due to the lack of HOE leakage; conversely, after NIR light irradiation the samples showed clear nuclei staining thanks to the light-induced HOE release.





Chapter 5

5. CaCO₃ Sub-Micrometric Capsules for Ultrasound Triggered Release: in Vitro and in Vivo

5.1. Introduction

Self-assembly of macromolecules, therapeutics, and/or inorganic nanoparticles into multifunctional drug delivery systems allow unique opportunities to developed next-generation theranostic nanomedicines.^[251, 252] There are a wide variety of well-established nanocarriers such as those based on liposomes, polymeric micelles, microemulsion droplets, polymersomes, metal-organic-frameworks (MOFs), and so forth.^[6,7] However, the layer-by-layer (LbL) assembly of polymers onto porous templates allows the fabrication of ultrathin polymer shell capsules that can be loaded with drugs,^[25, 253-255] therefore, LbL capsules are highly versatile in the field of drug delivery.^[33, 61, 65, 108, 256, 257] LbL method offers versatility and flexibility that allows to (i) encapsulate almost any drug, from small molecules (*e.g.*, dyes) to large macromolecules (*e.g.*, proteins, enzymes, oligonucleotides, etc.),^[258] (ii) layer self-assembly by charge, hydrogen bonding, host-guest interactions, etc. of a wide variety of polymers (*e.g.*, biodegradable, stimuli-responsive, bearing therapeutic function),^[259] and (iii) to incorporate inorganic NPs into its shell to provide multimodal imaging and/or stimuli-responsive capabilities.^[256, 260]

LbL assembly is performed by the addition of alternating charged polyelectrolyte layers onto the sacrificial macromolecule-loaded cores. The PSS/PDADMAC polyelectrolyte system (polyanion PSS: poly (sodium 4-styrene sulfonate); polycation PDADMAC: poly(diallyl dimethylammonium chloride) have been extensively used in in vitro studies, showing negligible toxicity compared to the toxic individual polyelectrolytes.^[261, 262] However, biodegradable polymers have drawn important attention due to their biocompatibility. Thus, a large variety of biodegradable LbL systems, even more biocompatible than the PSS/PDADMAC system, have been also reported.^[24, 263, 264] Dextran, poly-L-arginine, and poly-L-lysine, amongst others, are some of the biodegradable polymers that have been already used.^[31, 265, 266]

The change of the surface charge after the deposition of alternating polymeric layers of opposite charge can be confirmed by zeta potential measurements. It is important to say that, to avoid the dissolution of the cores (*i.e.*, sacrificial template) during LbL, the combination of polyelectrolytes must be carried out at a mildly alkaline pH value (pH 9).

CaCO₃ (Sacrificial Template)

CaCO₃ particles have been used as sacrificial templates to prepare micro- and nano-capsules, as well as silica and polystyrene particles, amongst others.^[22, 267] Compared to silica or polystyrene, CaCO₃ ones are promising as drug reservoirs with high-loading capacities (*i.e.*,

macromolecule per particle) because the cargo is added during the CaCO_3 particle formation (*i.e.*, pre-loading)^[23] CaCO_3 has three anhydrous crystalline polymorphs, including calcite, aragonite, and vaterite. Typically, vaterite has a spherical crystal form called framboid or raspberry^[268] (see *Figure 5.1a*). Many authors claim that the vaterite sphere is the result of smaller single-crystal subunits arranged with some degree of order.^[269-271] *Figures 5.1b-c* show a detailed examination of the CaCO_3 particle surface^[272] and the radial fiber-like internal structure of CaCO_3 particles,^[273] respectively.

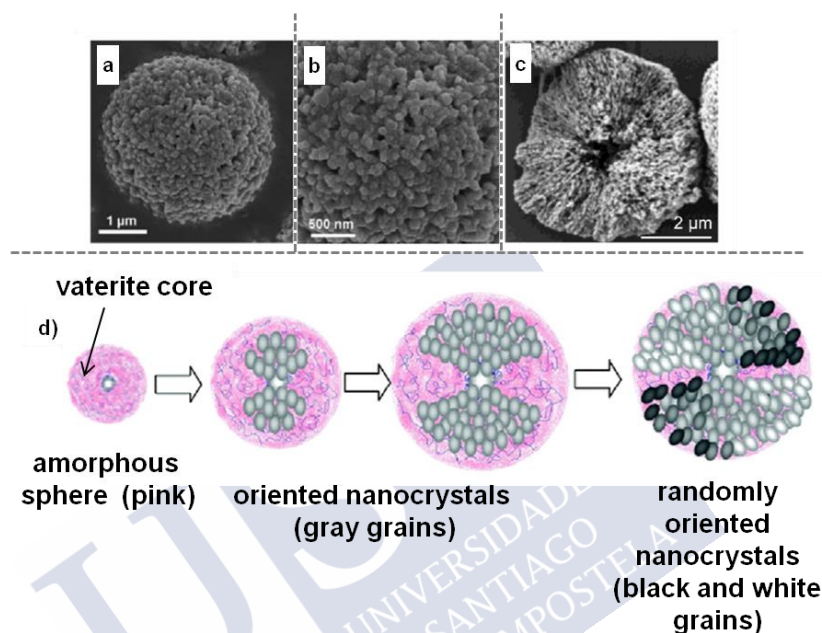


Figure 5.1. Scanning electron microscope (SEM) images of different vaterite particle shape: a) CaCO_3 vaterite crystals (adapted with permission from ref.[272] Copyright 2010, The Royal Society of Chemistry). b) Core particle surface (adapted with permission from ref. [272] Copyright 2010, The Royal Society of Chemistry). c) Core particle interior (adapted with permission from ref. [273] Copyright 2004, American Chemical Society). d) Schematic illustration of the formation process of a vaterite microsphere (adapted with permission from ref. [274] Copyright 2012, American Chemical Society).

Imai *et al.* studied the particle growth scenario of monodispersed microspheres of vaterite, called the “sphere-to-dumbbell-to-sphere”.^[274] The formation pathway of an amorphous microsphere includes a small vaterite core formed with polystyrene sulfonate (PSS); then, oriented nanocrystals grow in the amorphous sphere, and these, in turn, are covered with randomly oriented nanocrystals (see *Figure 5.1d*). As we mentioned before, vaterite has a typical spheroidal structure, however, other complex shapes have been also reported: flower-like shaped^[275] (see *Figure 5.2a*), rosette-shaped^[276] (see *Figure 5.2b*), hexagonal-shaped^[274] (see *Figure 5.2c*), lens-shaped^[277] (see *Figure 5.2d*) and plate-shaped^[208, 278] (see *Figure 5.2e*) ones.

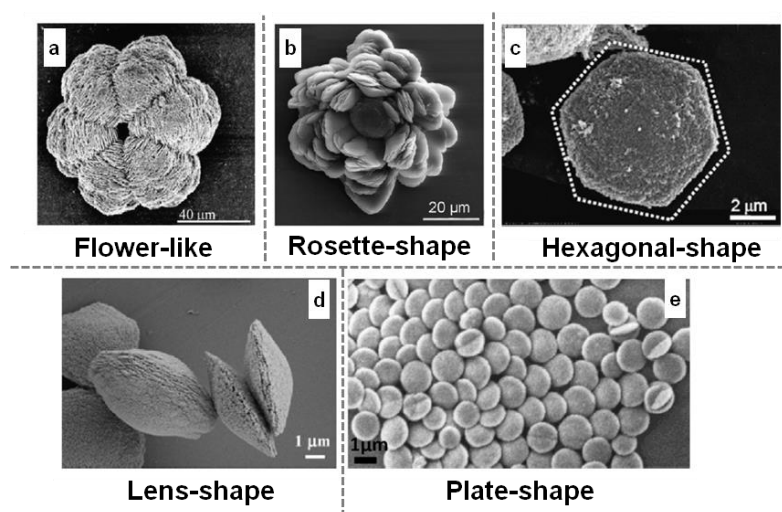


Figure 5.2. a) Flower-like shaped vaterite (adapted with permission from ref. [275] Copyright 2010, Materials Research Society). b) Rosette-shaped vaterite. (adapted with permission from ref. [276] Copyright 2006, American Chemical Society). c) Hexagonal shaped vaterite (adapted with permission from ref. [274] Copyright 2012, American Chemical Society). d) Lens-shaped vaterite (adapted with permission from ref. [277] Copyright 2005, American Chemical Society). e) Plate-shaped vaterite (adapted with permission from ref. [279] Copyright 2002, WILEY-VCH Verlag GmbH).

Vaterite has been used for the preparation of controlled drug delivery carriers thanks to its large porosity and surface area, but also, it is worth mentioning that it has a very low stability which results in a rapid disintegration under relatively mild conditions.^[280, 281] Therefore, CaCO₃ particles can be easily removed after a layer-by-layer assembly process, LbL, using, in general, a Ca²⁺ chelating agent (*i.e.*, ethylenediaminetetraacetic acid - EDTA).^[32] In contrast, polystyrene- and silica-templated particle cores require more aggressive conditions for their dissolution as, for example, organic solvents (*i.e.*, tetrahydrofuran or dichloromethane) and buffered hydrofluoric acid, respectively.^[27]

The use of CaCO₃ particles as sacrificial templates offers interesting prospects to encapsulate macromolecules in polyelectrolyte micro-and-nano-capsules.^[30, 31, 265] Two different approaches have been used to encapsulate molecules of interest within the polymeric capsules made from CaCO₃ particle templates: “preloading” and “post-loading”. Preloading strategies required porous templates. In contrast to silica- or polystyrene-templated LbL particles, CaCO₃ particles allows for achieving high-loading capacities (*i.e.*, macromolecules per particle) because the cargo is added during the formation of the CaCO₃ particles (pre-loading).^[23] Moreover, the bioactivity of the encapsulated macromolecules into CaCO₃ particles is not affected by macromolecule encapsulation and subsequent LbL polymer deposition. Petrov *et al.* found that, in the case of calcium carbonate microparticles, the coprecipitation method was five times more effective than cargo physical adsorption.^[282] In the coprecipitation method, the molecule of interest is captured during the growth process by CaCO₃ particles through the combination of aqueous solutions of CaCl₂ and Na₂CO₃.^[32, 282] On the other hand, in the “post-loading” techniques, prefabricated polymeric capsules are loaded with macromolecules or low

molecular-weight compounds by modifying the physicochemical environment. To achieve this goal, the capsule shell is permeable to small molecules but not for macromolecules.^[22] The encapsulation of small molecules is possible through shrinking (*i.e.*, with temperature),^[30] and that of large molecules by changing the pH, ionic strength, or solvent polarity. The capsule loading efficiency depends on the polymeric groups present in the outer charge compensation layer and on the multilayer construction.^[283]

The cargo release from capsules can occur by simple diffusion,^[22, 267, 284] or by biodegradation of the polymeric shell from both internal or external triggers^[22, 267, 284] Triggering from internal factors involves predetermined conditions that change the capsule's surrounding environment, and the subsequent release of the cargo can occur. These include a change in pH,^[285] enzymatic degradation,^[286] and redox processes. The use of external stimuli such as light, magnetic fields, or ultrasounds (US) appears to be especially attractive for creating local stimuli to induce a controlled cargo release. Hence, stimuli-controlled drug delivery systems can enhance targeted delivery of nanomedicines by choosing when (temporal resolution) and where (spatial resolution) to trigger drug release. For example, Elbaz *et al.* found different curcumin release profiles when changing the composition of the polymeric layers. The nanocapsules composed by chitosan and Eudragit L100 as the fifth and sixth-layer, respectively, showed a delayed drug release at two pH values (*i.e.*, 1.2 and 7.4), and demonstrating the capacity to protect the drug in the stomach (pH 1.2) and the restricted release in the intestine at neutral pH.^[287] Although the release of macromolecules produced by external stimuli has been extensively demonstrated *in vitro* with LbL microcapsules,^[254, 258] *in vivo* studies remains still relatively unexplored.

Motivation

The biological studies employing micrometric size of CaCO₃-derived capsules (typically, having diameters from 3 to 10 µm)^[288] present one main limitation as *in vivo* i.v. injectable medicinal products. As to safety issues, due to their large size, LbL capsules are likely to be rapidly sequestered within the capillaries in the lungs and by the organs of the reticuloendothelial system.^[288, 289] Microvascular occlusion that may lead to thrombotic side effects is also a concern, especially if the microparticle system lacks enough elasticity to pass through pores smaller than their diameter.^[289]

Therefore, in the present chapter, we produced sub-micrometric CaCO₃-templated polymer capsules (NCs) of approximately 600 nm in diameter using the LbL technique. The NCs were composed of non-biodegradable PSS and PDADMAC polymers. Additionally, to optimize the encapsulation protocol, as well as to investigate a potential macromolecule's role in the encapsulation process, three fluorescently labeled macromolecules were encapsulated: dextran (70 kDa), bovine serum albumin (BSA, 66.5 kDa) and recombinant tissue plasminogen activator (rtPA) (70 kDa). The rtPA is an extremely "fragile" serine protease^[290-292] involved in the breakdown of blood clots, being its systemic administration among the main effective treatments during the acute phase of ischemic stroke, and also applicable in the treatment of

acute myocardial infarctions, pulmonary thromboembolism, peripheral arterial thrombosis, and leg vein thrombosis.^[293]

Herein, we explore an original approach based on sonosensitive LbL NCs, where NCs were used as a multifunctional carrier for rtPA, which retained its enzymatic activity while encapsulated, even in the presence of a plasminogen activator inhibitor. For tracking purposes, the cargoes were fluorescently labeled (rtPA or other model macromolecules used herein) and the NCs were tagged with magnetic NPs. Also, the use of ultrasound (US) to trigger the release of fully functional rtPA from multilayer capsules was demonstrated *in vitro* and *in vivo* in mice.

5.2. Results and Discussions

5.2.1. The Influence of the Synthesis Parameters: PVSA to control growth formation of CaCO₃ particles

Coprecipitation is the most common method for the synthesis of sacrificial porous CaCO₃ cores, in which aqueous equimolar solutions of CaCl₂ and Na₂CO₃ are mixed at room temperature. This method is commonly used to fabricate porous CaCO₃ microparticles (3–10 μm),^[99] typically made of calcite, the most stable polymorph of CaCO₃.^[294, 295] During the first 60 minutes of Ca²⁺-CO₃²⁻ mixing, the thermodynamically unstable amorphous CaCO₃ transforms into a metastable polymorph of CaCO₃ (*i.e.*, nanocrystalline vaterite), which later (~20 h) transforms to calcite via a dissolution-reprecipitation mechanism.^[280] Researchers have reported that the use of additives such as polymers and copolymers can preferably promote the growth of calcite or vaterite.^[279, 296] Poly(vinyl sulfonic acid) (PVSA) has been used during the CaCO₃ growth to control growth formation and to stabilize the initially formed vaterite cores, delaying calcite transformation.^[32, 297] Usually, 330 mM solutions of the precursors (CaCl₂ and Na₂CO₃) are used for the fabrication of CaCO₃ microparticles.^[99, 298] However, we used relatively much lower concentrations (20 mM) of CaCl₂ and Na₂CO₃ to produce our cores. Thus, 1 mL of 20 mM CaCl₂·2H₂O (147.01 g/mol) solution and poly (vinylsulfonic acid) (PVSA, different concentrations, see *Table 5.1*) were mixed under continuous stirring (550 rpm) in a beaker. Then, 1 mL of 20 mM Na₂CO₃ (105.99 g/mol) solution was added rapidly, and the solution was mixed (550 rpm) for 30 min at RT. The cores were obtained by precipitation at 3×10³ rcf (5 min). After centrifugation, the precipitate was washed with water and washed/precipitated one more at 3×10³ rcf (5 min) to further characterize them.

Dynamic light scattering (DLS) showed the change in the number-weighted size population distribution of the resulting particles for different PVSA concentrations used (see *Table 5.2*). As the concentration of PVSA increases, the peak size decreases, in agreement with previous results (see *Figure 5.3*).^[297] Moreover, it was confirmed by SEM imaging that samples in the absence of PVSA exhibit a cubic morphology (see *Figures 5.4a-b*) associated with calcite,^[268, 299] having an average diameter of $d_{CC_0} = 3163 \pm 709$ nm (see *Figure 5.4 c*).

Table 5.1. PVSA concentrations to produce different particles.

Sample	CaCl ₂ ·2H ₂ O [mM]	Na ₂ CO ₃ [mM]	PVSA [μ M]	Reaction time (min)
CC_0	20	20	0	30
CC_0.1	20	20	50	
CC_0.2	20	20	100	
CC_1	20	20	500	

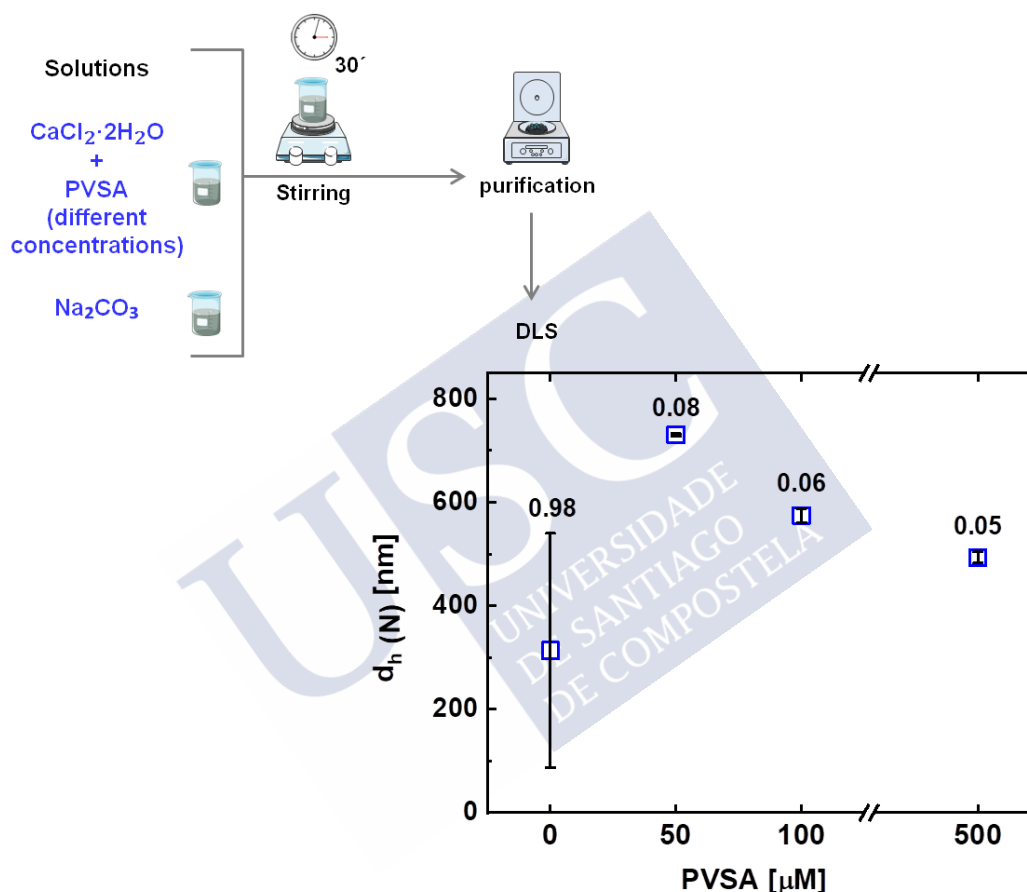


Figure 5.3. Schematic representation of the experimental setup for the synthesis of CaCO₃ particles at different PVSA concentrations and DLS data of the number-weighted average size peak for particles at different PVSA concentrations; the number on top of each square corresponds to the polydispersity index (PDI).

On the other hand, samples in the presence of PVSA display a spherical morphology (see Figures 5.4d, e, g, h, j, k) that is associated with vaterite,^[268, 297] having an average diameter of: $d_{CC_0.1} = 693 \pm 124$ nm, $d_{CC_0.2} = 541 \pm 83$ and $d_{CC_1} = 518 \pm 108$ nm (see Figures 5.4 f, i, l). These results indicate that PVSA not only acts as a surfactant but also has an active role in the formation of the cores. Figure 5.4 shows the SEM images of all the samples shown in Table 5.1.

Table 5.2. Mean average hydrodynamic diameters and ζ -potential values of CaCO₃ particles at different PVSA concentrations.

Sample name	$d_{h(I)}$ (nm)	$d_{h(N)}$ (nm)	PDI	ζ -potential (mV)
CC_0	313.0 \pm 225.6	313.5 \pm 226.6	0.98 \pm 0.05	-28.5 \pm 0.9
CC_0.1	746.4 \pm 21.6	730.5 \pm 2.4	0.08 \pm 0.04	-13.9 \pm 0.4
CC_0.2	620.1 \pm 33.2	574.3 \pm 13.5	0.06 \pm 0.05	-14.3 \pm 0.7
CC_1	550.5 \pm 14.8	493.3 \pm 10.7	0.05 \pm 0.04	-13.8 \pm 0.2

$d_{h(I)}$ and $d_{h(N)}$ refer to the mean average hydrodynamic diameter from the intensity and number-weighted DLS size distributions, respectively. PDI refers to the polydispersity index. Standard deviation values were calculated from three independent measurements.

5.2.2. Structural Characterization: CaCO₃ particles

i) Powder X-Ray Diffraction (PXRD)

To study the crystal structure of the CaCO₃ cores and their stability over time, freshly prepared cores (in the presence of PVSA, 50 μ M) were freeze-dried (during *approx.* 12 h) immediately after purification of the cores (sample 0 h), after 6 h (sample 6 h) or after 1 month of the core's preparation-purification process (see *Figure 5.5*). Freeze-dried samples (whitish powders) were studied by powder x-ray diffraction (PXRD). In freshly prepared samples (samples 0 h or 6 h), PXRD showed that the major crystalline component of our CaCO₃ is mostly composed of the polymorph vaterite, as indicated by the characteristic major diffraction peaks at 24.9°, 27° and 32.8° (see green marks in *Figure 5.5*), which correspond to [110], [112] and [114] reflections. Although very weak at 0 h, we can observe in samples at 6 hours and 1 month a stronger peak calcite (29.4°) is formed. In all the cases, the diffraction pattern shows a combination of vaterite and calcite, with varying weights.

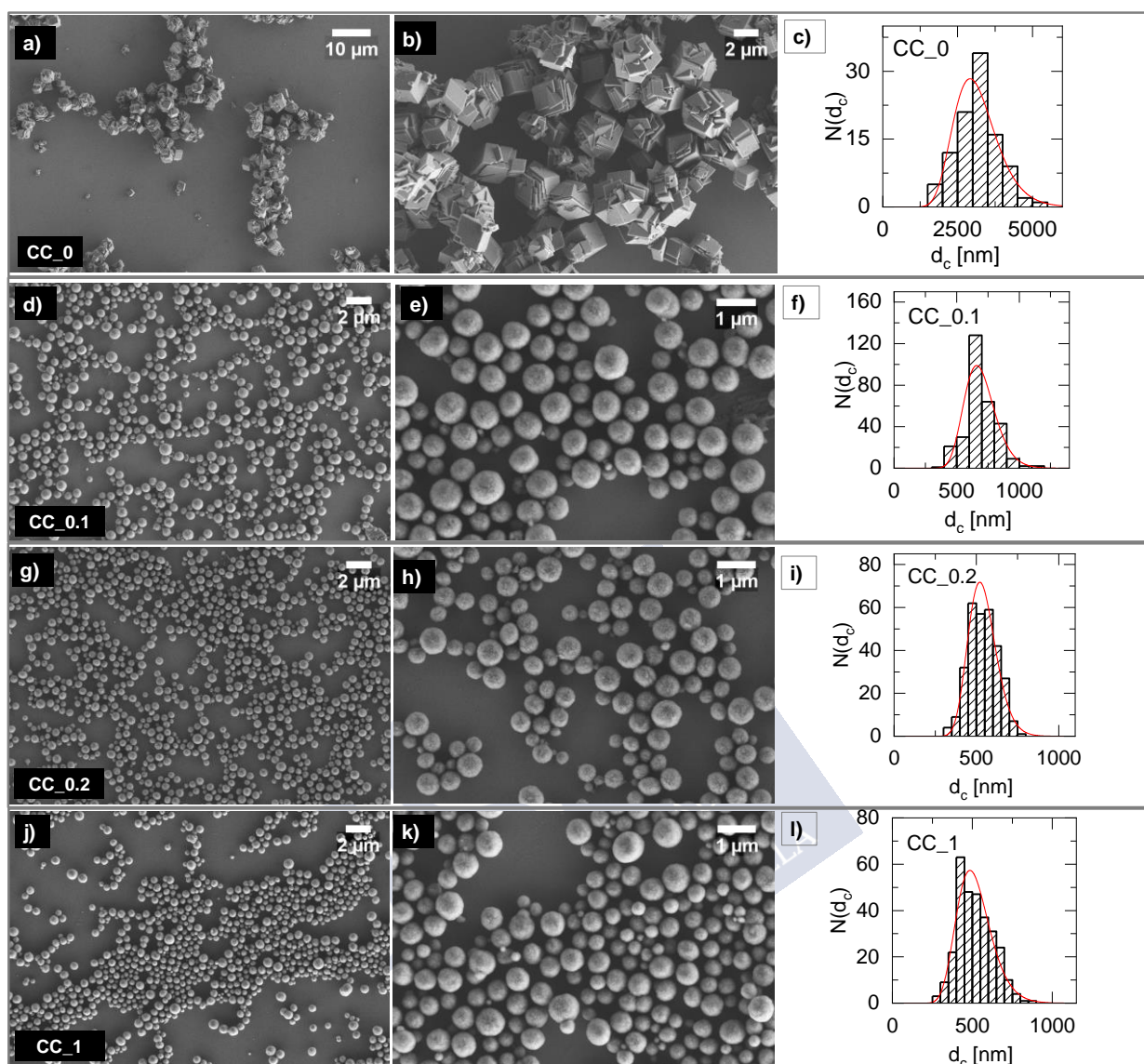


Figure 5.4. Low and high magnification SEM micrographs of different species of CaCO_3 particles from *Table 1* after drop casting on Si substrates: a-b) CC_0, d-e) CC_0.1, g-h) CC_0.2 and j-k) CC_1 (SE2, 3kV). c) Size histogram (d_{CC_0} : mean diameter of CC_0) obtained after measuring the diameter of over 100 CC_0 particles using ImageJ; $d_{\text{CC}_0} = 3163 \pm 709$ nm. f-l) Size histogram ($d_{\text{CC}_0.1}$, $d_{\text{CC}_0.2}$, d_{CC_1} : mean diameter of CC_0.1, CC_0.2 and CC_1, respectively) obtained after measuring the diameter of over 300 CC_0.1, CC_0.2 and CC_1 particles using ImageJ; $d_{\text{CC}_0.1} = 693 \pm 124$ nm, $d_{\text{CC}_0.2} = 541 \pm 83$ and $d_{\text{CC}_1} = 518 \pm 108$ nm.

However, PXRD suggested that vaterite-type CaCO_3 particles are partially or totally transformed into calcite after 1 month in aqueous solution. To our knowledge, peaks at 30.4° and 34.5° (red marks in *Figure 5.5*) cannot be explained by the polymorphs calcite or aragonite, and we ascribe them to crystallization intermediates or any of the several forms of vaterite; vaterite has been suggested as a group of related structures that differ in the order of stacking within the carbonate layers, rather than as a single disordered material.^[300] Therefore, freshly prepared cores were used in all the preparations.

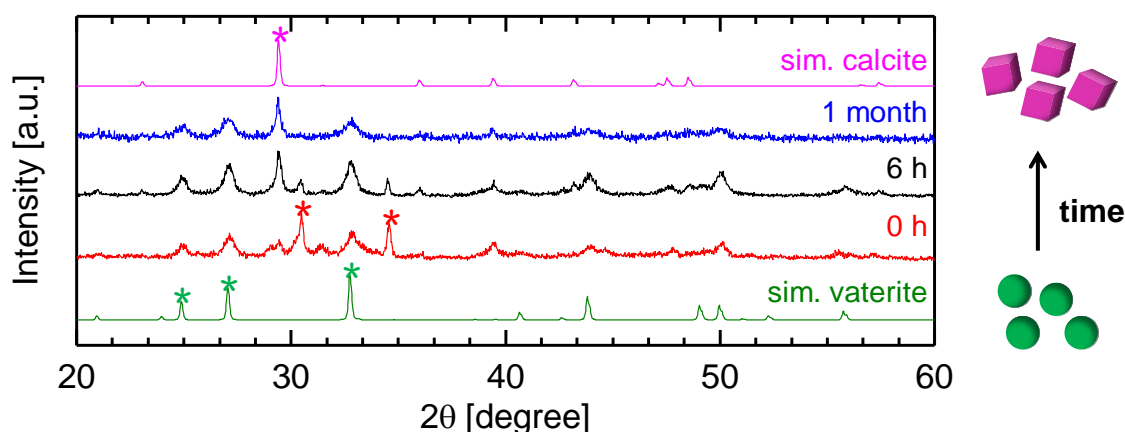


Figure 5.5. PXRD of samples 0 h (red line), 6h (black line) and 1 month (blue line). For comparison we added simulations of calcite (pink line, ICDD PDF: 98-007-9674) and vaterite (green line; ICDD PDF: 98-002-7827). Pink, green and red asterisks sit at characteristic peaks of calcite, vaterite and “unknown” phases, respectively (adapted with permission from ref. [301]. Copyright 2019, Elsevier B.V.).

ii) Fourier Transform Infrared Spectroscopy (FTIR)

Furthermore, Fourier transform infrared spectroscopy (FTIR) was used to identify the presence of vaterite in the CaCO₃ cores. Freshly prepared cores (in the presence of PVSA, 50μM) were freeze-dried (during *approx.* 12 h) immediately after purification of the cores (sample 0 h). The FTIR spectra of the precursors: CaCl₂, Na₂CO₃, PVSA, and the calcium carbonate particles (CaCO₃ cores) in the presence of PVSA (50 μM) are shown in *Figure 5.6a*. The band assignments of the FTIR vibrations of the three different types of calcium carbonate particles are presented in *Table 5.3*. According to the data shown in *Figure 5.6b*, the bands at around 875 cm⁻¹ (v₂) and 745 cm⁻¹ (v₄), correspond to CO₃²⁻ vibrations associated to vaterite.^[302, 303] The band at 1087 cm⁻¹ (v₁) also corresponds to the vaterite form;^[269] however, we noted a shift of the band v₁ to 1034 cm⁻¹ that can be related to the presence of PVSA in the sample. Thus, the presence of vaterite in the CaCO₃ cores was confirmed by both PXRD and FTIR analysis.

Table 5.3. Assignment of FTIR absorption bands of vaterite, calcite and aragonite.

	IR absorption band				Reference
	v ₁ (cm ⁻¹)	v ₂ (cm ⁻¹)	v ₃ (cm ⁻¹)	v ₄ (cm ⁻¹)	
vaterite	1034	875	-	745	Experimental data from this work
vaterite	1087	877, 876	-	745, 744	[269, 304, 305]
calcite	1080	879, 877, 874	1492-1429	713, 712, 706	[29, 304, 305]
aragonite	1083, 1080	866, 858, 844	1504, 1492	713-11, 706, 700	[29, 304, 305]

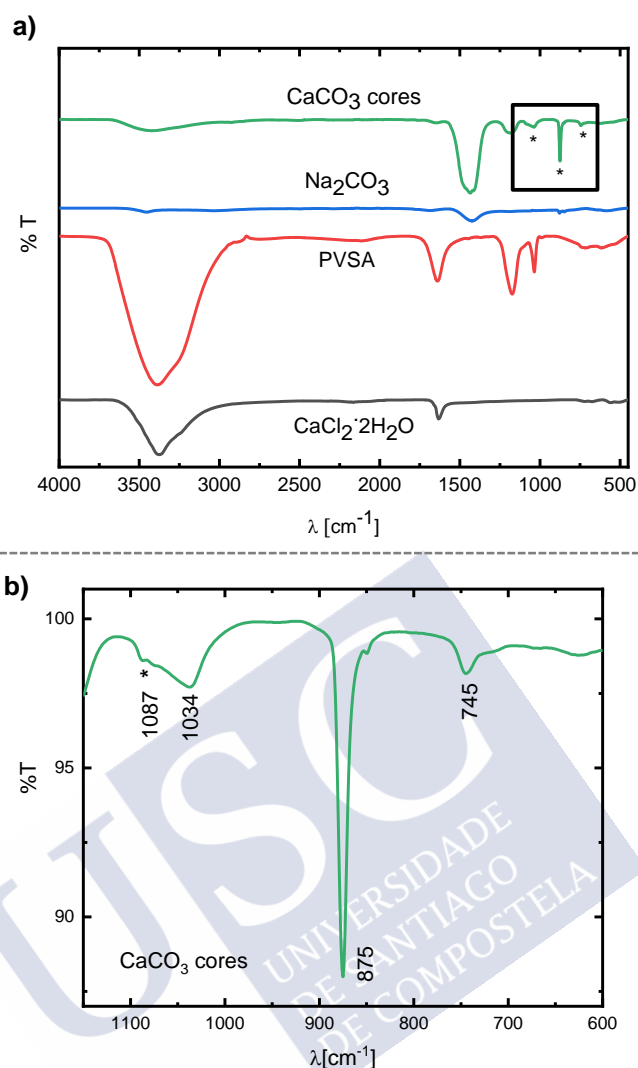


Figure 5.6. FTIR spectra of the a) CaCl_2 , Na_2CO_3 , PVSA precursors, and the calcium carbonate particles (CaCO_3 cores) in the presence of PVSA (50 μM). b) Zoomed area of FTIR spectra of the CaCO_3 cores at $\approx 600\text{--}1200$ cm^{-1} , showing characteristics carbonate vibrational bands of vaterite.

5.2.3. CaCO_3 Macromolecule-Loaded Particles

i) *Dye-labeling*

Protein labeling efficiency depends on the type of protein labeled, so the degree of labeling is the average number of dye molecules coupled to each protein molecule *i.e.*, the dye: protein molar ratio and can be controlled by varying the ratio of dye labeling to the protein.^[306] Thus, a high level of labeling is advantageous because it allows high sensitivity. However, over-labeling may cause either quenching, decreased solubility, or loss of biological activity; and on the other hand, too low dye-protein labels will lead to weak fluorescence emission.^[307] Here, we selected 25 dyes per protein (*i.e.*, 25:1) as the optimal molar ratio.

Dextran labeled with rhodamine B isothiocyanate (RBITC, Dextran-RBITC) was used as received (average MW = 70 kDa). In the case of rtPA, we used Alteplase (trade name Actilyse®) as a raw active ingredient. This commercial injectable formulation of rtPA contains as excipients polysorbate 80 (0.1 g per g of rtPA) and arginine (34 g per g of rtPA). These are crucial to prevent precipitation of rtPA and, therefore, had to be included during dye-labeling or cores formation, as otherwise, rtPA formed visible aggregates. In the case of BSA (66 kDa) and rtPA (70 kDa), proteins were mixed with fluorescein-5-isothiocyanate (FITC) in phosphate-buffered saline (PBS, pH = 8) at a ratio of 25 dye molecules per 1 protein molecule, and left to react protected from light for 4 h.

The dye-protein was collected according to the manufacturer's instructions (see *section 2.2.3*).

ii) The Bradford Assay

Bradford assay was used to determine the protein concentrations c_M (see *Figure 5.7*) after dye-labeling in the buffer used in the column (*i.e.*, PBS or PBS + arginine for BSA or rtPA, respectively). The respective calibration curves were prepared by measuring the fluorescence of different samples of known concentration c_M . The fluorescence was measured using a plate reader, which allowed to correlate protein (or dextran) concentration and fluorescent signal. The samples of dye-labeled protein were protected from light and stored (4°C) at $c_M = 1$ mg/mL. Notice that although the ratio dye-to-protein was kept constant (*approx.* 25), in the case of BSA the labeling efficiency was higher (see slopes 5.7 vs. 1.5 for BSA and rtPA, respectively). This was because BSA presents a higher number of lysine residues than rtPA (60 vs. 22).

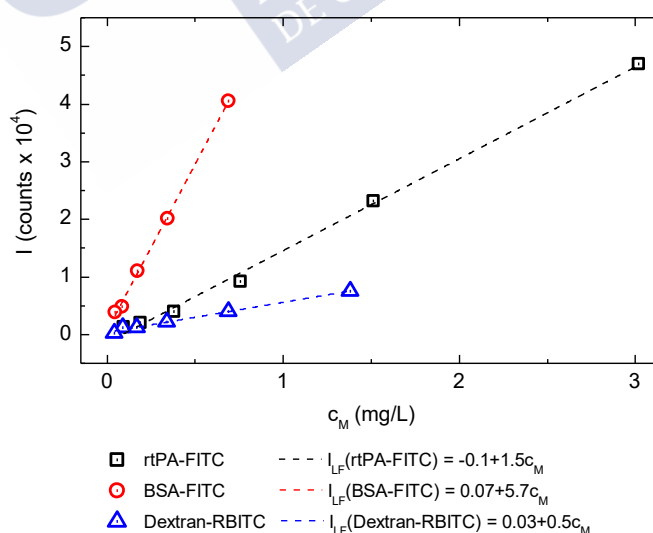


Figure 5.7. Examples of correlation between concentration c_M (as determined by the Bradford assay in case of dye-labeled proteins, or as prepared in the case of dextran-RBITC) and fluorescence counts I ($\times 10^4$). Linear fits (LF) in each case were used to calculate unknown concentrations c_M of rtPA-FITC, BSA-FITC, or dextran-RBITC, from fluorescence readings (adapted with permission from ref. [301]. Copyright 2019, Elsevier B.V.).

iii) *Synthesis of Macromolecule-Loaded CaCO₃ particles*

Vaterite was preferred over calcite because of its higher porosity and rapid degradation in mildly acidic media.^[280, 281] Using mild conditions to “dissolve” the cores is important to prevent bioactivity draining of the encapsulated proteins, as well as to speed up the NCs’ production. The concentration of PVSA (50 μM) was optimized to achieve as much cargo (i.e., number of macromolecules per NC) as possible, while keeping sub-micrometric sizes (< 700 nm).

A schematic representation of the macromolecule-loaded core process is depicted in *Figure 5.8*.

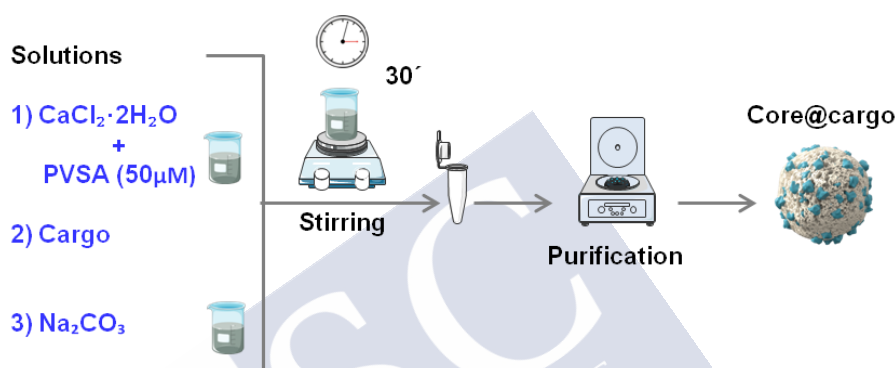


Figure 5.8. Schematic representation of the synthesis of the macromolecule loaded CaCO₃ particles.

iv) *Quantification of Cargo*

To optimize the encapsulation protocol, as well as to investigate a potential macromolecule’s role in the encapsulation process, three fluorescently labeled macromolecules were encapsulated, namely dextran (70 kDa), bovine serum albumin (BSA, 66.5 kDa) and rtPA (70 kDa).

BSA-FITC, rtPA-FITC or dextran-RBITC content (*i.e.*, loading efficiency LE) was done in all cases as an indirect measurement of the mass of cargo based on fluorescence, using the calibration curves previously described (see *Figure 5.7*). We used the following expression:

$$\text{LE (\%)} = \frac{\text{mass of cargo in purified cores}}{\text{mass of cargo added}} \times 100 \quad (5.1)$$

and obtained, using equivalent synthetic conditions by varying loading efficiencies (LEs) (*i.e.*, encapsulated-to-added macromolecule) depending on the cargo: LE(core@rtPA-FITC) = 24.5 %; LE(core@BSA-FITC) = 1.5 %; LE(core@dextran-RBITC) = 11.9 %.

The loading efficiency of rtPA was outstanding, which is very important to produce a cost-viable thrombolytic nanomedicine. We ascribe the highly efficient rtPA loading to a more favorable CaCO₃ interaction than in case of BSA or dextran, which is somehow not surprising since the influence of specific proteins in the biomineralization of CaCO₃ is well known.^[308]

From now on, only cores loaded with BSA and rtPA will be used for further fabrication of the nanocapsules (NCs) and experiments, where the NCs loaded with BSA will be used as a model during this work.

v) **Structural Characterization: CaCO₃ particles**

Moreover, scanning electron microscopy (SEM) revealed the formation of sub-micrometric spherical cores (only cores loaded with BSA and rtPA, see *Figures 5.9a* and *c*): mean core diameter $d_{C@BSA} = 617 \pm 80$ nm and $d_{C@rtPA} = 651 \pm 76$ nm for cores loaded with BSA and rtPA, respectively (see *Figures 5.9b* and *d*). Dynamic light scattering (DLS) analysis also revealed highly monodisperse sub-micrometric colloids: mean average hydrodynamic diameter (number distribution) $d_{C,BSA(N)} = 623.4 \pm 19.3$ and $d_{C,rtPA(N)} = 592 \pm 17$. Additionally, cores loaded with rtPA resulted in a more negative zeta potential compare to the ones loaded with BSA: $\zeta_{CrtPA} = -48.9$ mV \pm 5.5, and $\zeta_{CBSA} = -41.7$ mV \pm 2.6 (see *Table 5.4*).

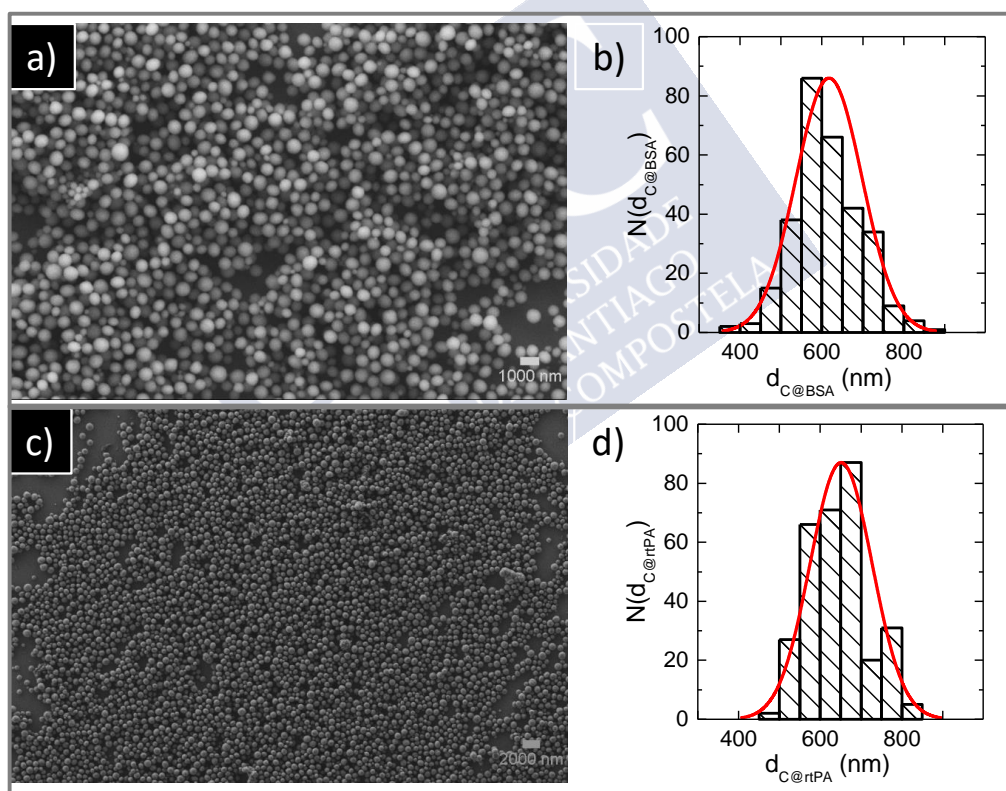


Figure 5.9. a) SEM micrograph of core@BSA particles (scale bar is 1000 nm) (SE2, 10kV). b) Size histogram ($d_{C@BSA}$: mean diameter of core@BSA) obtained after measuring the diameter of 300 core@BSA particles using ImageJ; $d_{C@BSA} = 617 \pm 80$ nm. c) SEM micrograph of core@rtPA particles (scale bar is 2000 nm) (SE2, 3kV). d) Size histogram ($d_{C@rtPA}$: mean diameter of core@rtPA) obtained after measuring the diameter of over 300 core@rtPA particles using ImageJ; $d_{C@rtPA} = 651 \pm 76$ nm. In a,b) samples after drop casting on Si substrates are shown (adapted with permission from ref. [301]. Copyright 2019, Elsevier B.V.).

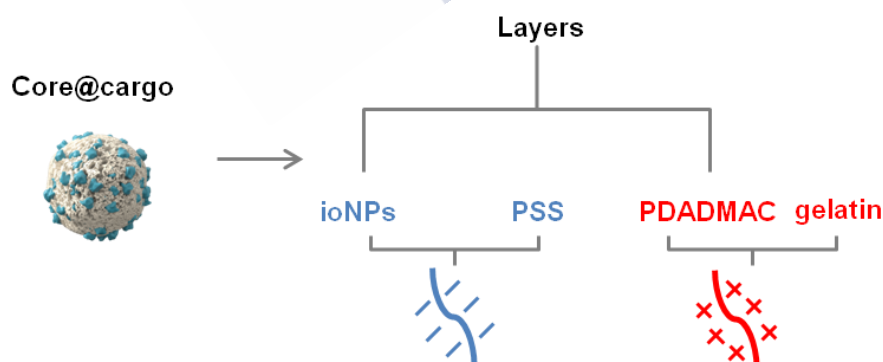
Table 5.4. Mean average hydrodynamic diameters and ζ -potential of nanocores.

Sample	$d_{h(I)}$ (nm)	$d_{h(N)}$ (nm)	PDI	ζ -potential (mV)
core@rtPA	648 ± 26	592 ± 17	0.09	-48.9 ± 5.5
core@BSA	664.4 ± 9.4	623.4 ± 19.3	0.14	-41.7 ± 2.6

5.2.4. Multifunctional Sub-Micrometric Capsules (NCs)

After macromolecule trapping, LbL assembly was performed by the addition of alternating charged polyelectrolyte layers onto the sacrificial macromolecule-loaded cores. The cores were loaded with BSA and rtPA, and then, the multilayer films were constructed with layers of poly(sodium 4-styrene sulfonate) (PSS) and poly(diallyl dimethylammonium chloride) (PDADMAC) polyelectrolytes, with Mn/Zn doped iron oxide nanoparticles (ioNPs) as an alternating layer, and an outermost layer of gelatin. PSS and ioNPs were used as negatively charged layers, and PDADMAC and gelatin as positively charged layers (see *Figure 5.10*). The outmost layer of gelatin was added aiming to provide our nanocarriers with targeting capabilities. We adopted basic gelatin, heat-denatured collagen, which binds to von Willebrand factor (vWF), a key component of platelet-rich thrombi.^[309, 310] VWF-targeting strategies have been considered as promising candidates for strokes therapy to restore cerebral blood flow without increasing intra-cerebral bleeding complications.^[311]

The layer of Mn/Zn doped iron oxide NPs was added to confer magnetic resonance imaging (MRI) capabilities to our system. Thus, the synthesis and characterization of ioNPs will be firstly discussed and the preparation of the gelatin layer.


Figure 5.10. Schematic illustration of the description of the layers in the NCs used in this work.

i) Synthesis, Polymer Coating and Characterization of Mn/Zn-doped Fe oxide NPs (ioNPs)

ioNPs were synthesized by a thermal decomposition method adapted from a previous work^[312] (see section 2.3.3).

The resulting colloids (oleic acid/oleylamine stabilized Mn/Zn ioNPs) were analyzed by transmission electron microscopy (TEM). The average ioNP core diameter d_{NP} was measured with Image J software (see Figure 5.11b), resulting in $d_{NP} = 13.03 \pm 1.08$ nm.

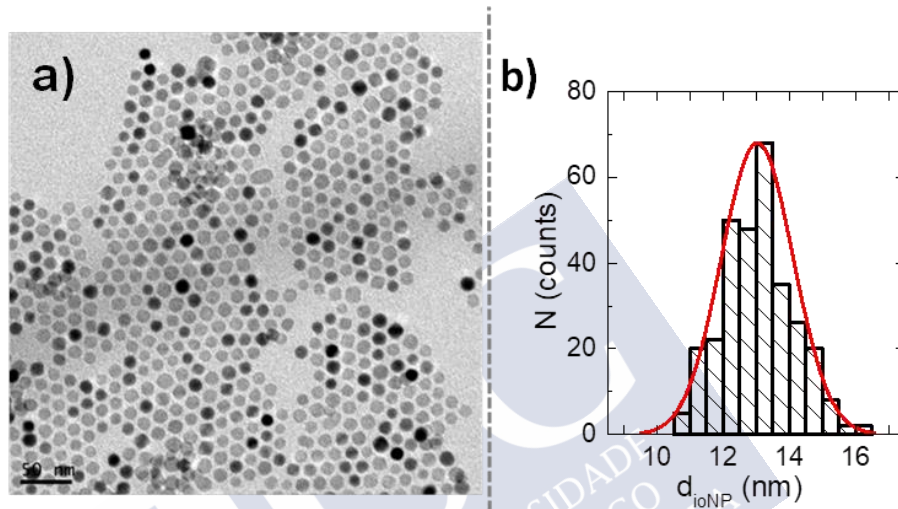


Figure 5.11. a) TEM micrograph of ioNPs; b) Size histogram obtained with ImageJ software after measuring the core diameter of 300 ioNPs. Scale bar corresponds to 50 nm (adapted with permission from ref. [301]. Copyright 2019, Elsevier B.V.).

Inductively coupled plasma mass spectrometry (ICP-MS) was used to determine the ioNP composition and the ioNPs mass concentration (m). The stoichiometry found was $Zn_{0.1}Mn_{0.2}Fe_{2.7}O_4$ and the inorganic concentration (including the oxygen content) was 0.9 g/L. The ioNP molar concentration (C_{NP}) was calculated as follows (please note that the organic contribution is not considered): The mass of a single NP m_{NP} was determined as the product of the core material density (ρ) and the core volume (V_{NP}). Therefore, the molar mass of the ioNPs M_{NP} can be calculated by multiplying the m_{NP} by N_A . Since Fe is the most predominant metal in the core ferrite, the magnetite (Fe_3O_4) density value ($5.18 \text{ g}\cdot\text{cm}^{-3}$) was used for these calculations.

$$M_{NP} = \rho \cdot V_{NP} \cdot N_A \quad (5.2)$$

The volume of a single ioNP V_{NP} was calculated as follows. The d_{NP} value used was the determined by TEM (see Figure 5.11a). The V_{NP} is equal to $1.15 \times 10^{-18} \text{ cm}^3$.

$$V_{NP} = \frac{4}{3} \cdot \pi \cdot \left(\frac{d_{NP}}{2} \right)^3 \quad (5.3)$$

Thus, the M_{NP} was 3.61×10^6 g/mol. Then, the molar NP concentration C_{NP} was determined as follows, resulting in a concentration of 2.50×10^{-7} M (0.25 μ M).

$$C_{NP} = \frac{m}{M_{NP} \cdot V} \quad (5.4)$$

In order to make the oleic acid/oleylamine capped ioNPs stable in aqueous solution, NPs were coated with the amphiphilic polymer dodecyl grafted-poly(isobutylene-alt-maleic anhydride), hereinafter referred to as PMA (*i.e.*, ioNP@PMA), following previous.^[17]

The PMA-coated ioNPs were done considering an experimental parameter, $R_{P/area}$ which refers to the number of polymer monomers added per nm^2 of NP surface. This experimentally determined parameter was fixed at 2000, below which PMA-coated ioNPs may form aggregates (*i.e.*, grouping of NPs coated with PMA). Then, for a specific volume of ioNP solution (V_{NP}) of a known concentration C_{NP} , and using an effective diameter d_{eff} which comprises the d_{NP} plus twice the length of the organic ligands (*approx.* 1.2 x 2 nm, *i.e.*, oleic acid and oleylamine), the volume of polymer V_P needed is determined as follows, for more details see a previous work.^[17]

$$V_P = \frac{R_{P/area} \cdot \pi \cdot d_{eff}^2 \cdot C_{NP} \cdot V_{NP}}{C_P} \quad (5.5)$$

Hydrodynamic size and surface zeta potential were measured in a Zetasizer Nano ZSP. The results showed a hydrodynamic diameter (in number) of *approx.* 22.3 ± 1.7 nm (polydispersity index= 0.24) and a zeta potential value of -56.4 ± 1.7 mV.

ii) **Layer-by-Layer Assembly (LbL)**

It is worth emphasizing that a wide range of biodegradable LbL systems, more biocompatible than the PSS/PDADMAC system, have been reported.^[24, 263, 264] However, the objective in this work is to demonstrate the US-triggered rtPA delivery *in vivo* and, therefore, the robustness of the non-biodegradable PSS/PDADMAC system is well-suited to such end. Thus, the methodology should be easily extended to other biodegradable polymers such as dextrane, poly-L-arginine, poly-L-lysine, and others with no protocol modification or only slight modifications, mostly concerning to the polymer concentration, the buffer nature and the NaCl concentration used during the layer-by-layer assembly.

Nanocapsules of Non-Biodegradable Polymers

Poly (sodium 4-styrenesulfonate) (PSS) and poly (diallyldimethylammonium chloride) (PDADMAC) were used as polyanion and polycation, respectively. PSS/PDADMAC LbL systems have been extensively used *in vitro*, showing negligible toxicity compared to the toxic individual polyelectrolytes, as mentioned before.^[261, 262] This combination of polyelectrolytes allows to sequentially deposit polymeric layers at a mildly alkaline pH value (pH 9), which prevents the dissolution of the nanocores during LbL assembly.

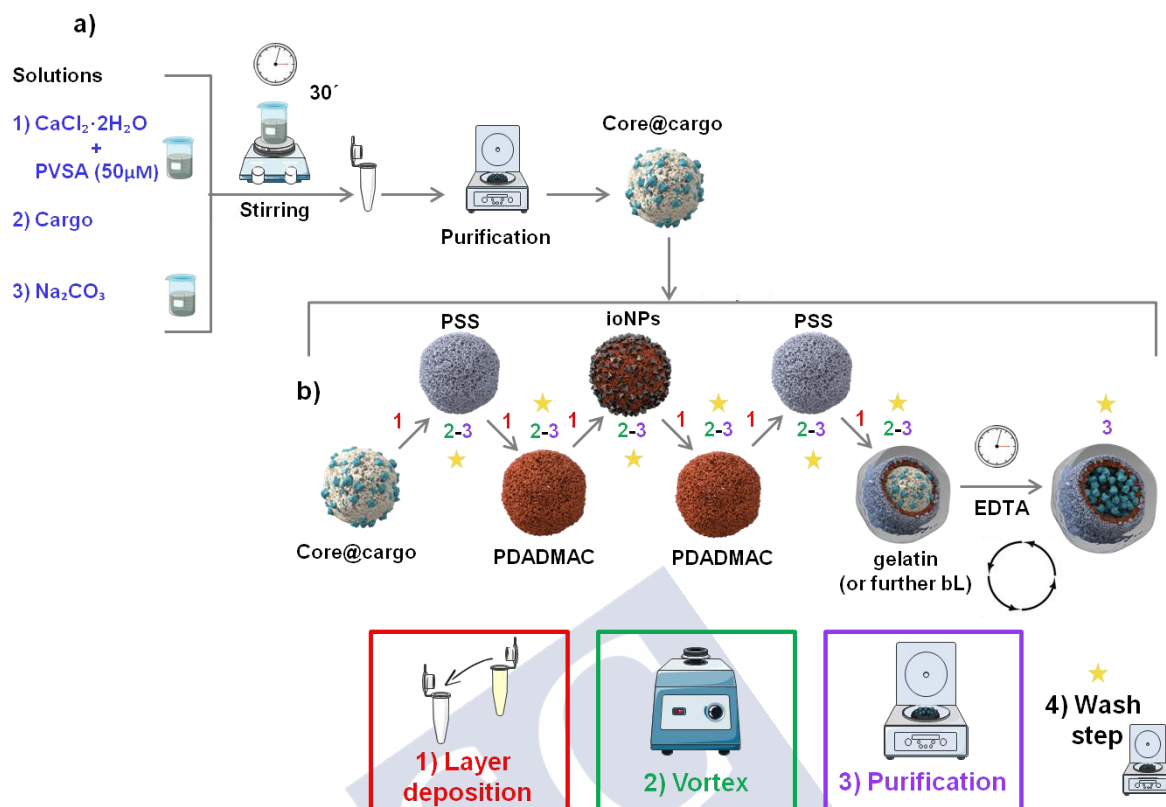


Figure 5.12. Schematic representation of the LbL process starting with A) CaCO₃ cores loaded with macromolecules (core@cargo), which after coating with 2 bL of PSS/PDADMAC, ioNPs and an outermost gelatin-based bL (gelatin), and “EDTA-dissolution” of the CaCO₃ matrix, yield NCs loaded with macromolecules (NC@cargo). Arrows and numbers represent the different synthetic steps, including purification of the colloids by centrifugation. b) Schematic representation of LbL steps (layers of PSS or PDADMAC or ioNPs or gelatin): from cores to NCs.

LbL deposition of polymers and ioNPs was carried out onto freshly prepared macromolecule-loaded cores (see Figure 5.12a). A schematic representation of the LbL process is depicted in Figure 5.12b (see Chapter 2 for the synthesis details).

Nanocapsules of Biodegradable Polymers

The strategy of the electrostatic layer-by-layer self-assembly technique for multilayer film fabrication presented before can be applied in a straightforward way to assembly capsules from CaCO₃ particles and as well alternating layers with other types of metal particles or molecules for preparing functional materials. Thus, Figure 5.13 shows one example of the morphological characteristics, using scanning electron microscopy (SEM), of hollow capsules, loaded with atorvastatin generated from CaCO₃ particles via a layer-by-layer route with biodegradable polyelectrolytes (*i.e.*, dextran sulfate and poly-L-arginine) and with gold nanorods (AuNRs) and miRNA as alternating layer (see Chapter 2 for the synthesis details).

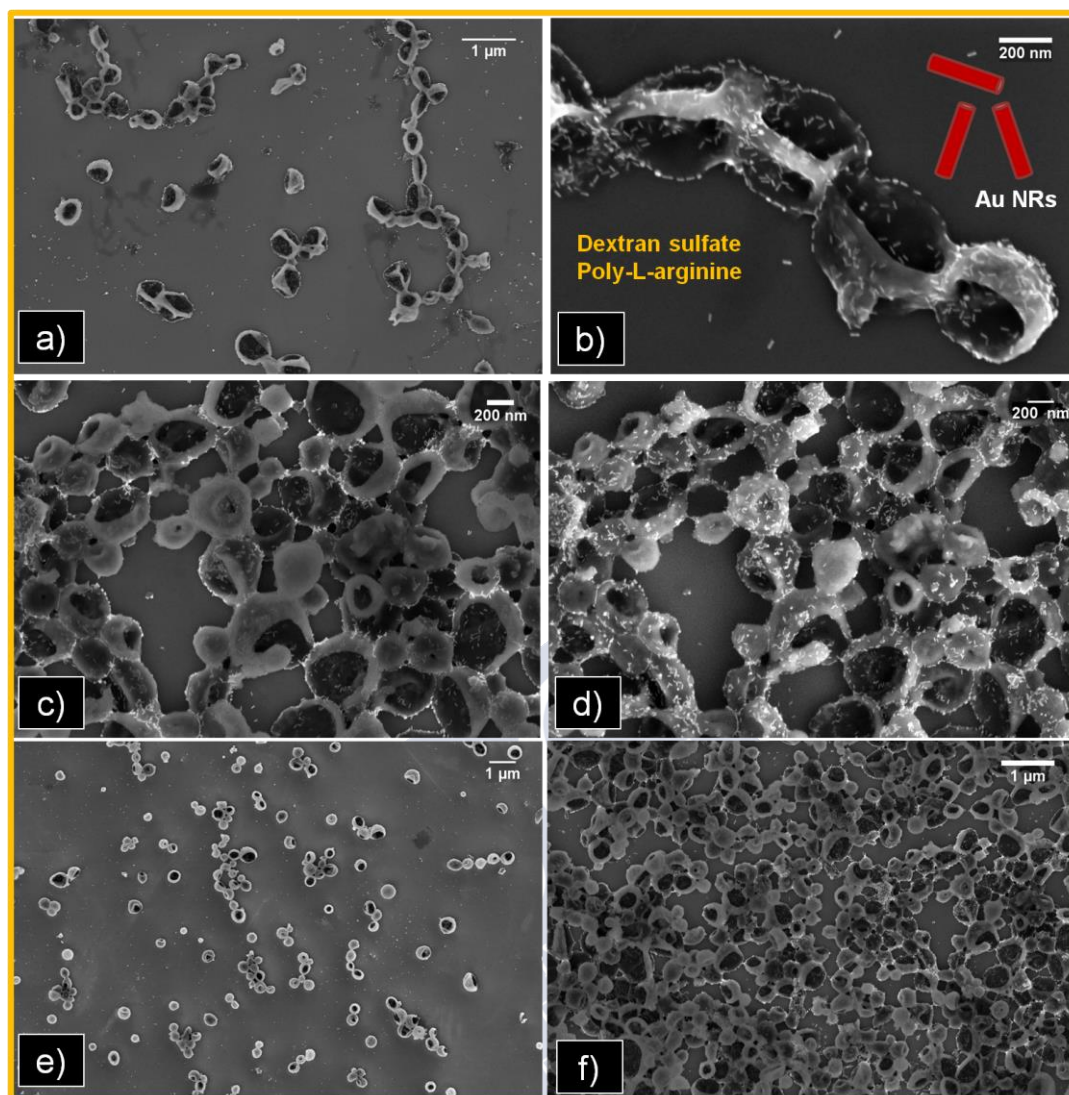


Figure 5.13. Low and high magnification SEM micrographs of LbL assembled polymer hollow capsules generated from CaCO_3 template: a-f) hollow capsules containing 6 layers (poly-L-arginine/dextran sulfate/poly-L-arginine/AuNRs/poly-L-arginine/miRNA) (0.5M NaCl, poly-L-arginine at 1mg/mL, dextran sulfate at 2mg/mL) (a, b, c: InLens, 3kV, d: SE2, 3kV, e, f: InLens, 3kV).

5.2.5. Optimization of Capsule Shell

After LbL onto the nanosystems, the macromolecule-leakage was estimated by comparing the fluorescence intensity (I) in the precipitated systems (*i.e.*, mass of cargo) and the fluorescent intensity in the supernatants (SN, *i.e.*, mass of cargo leakage). The leaking experiments were carried out in PBS under continuous agitation and at room temperature. Notice that rtPA or BSA remained stable in the loading buffer (absence of precipitation even after centrifugation at 10^4 rcf) and, therefore, the intensity measured in the precipitated material represents a good estimation of the encapsulated cargo.

Typically, macromolecules having relatively high molecular weights (*approx.* above 1-10 kDa) cannot diffuse in or out through the semipermeable LbL shell (pores size *approx.* 3-5

nm),^[313, 314] as shown extensively with different macromolecules encapsulated in LbL microcapsules.^[258, 315] The permeability of LbL microcapsules to small molecules (*e.g.*, approx. 0.4 kDa) can be reduced by heat treatment, which reduces the pore size of the LbL shell.^[313] In the case of microcapsules (*i.e.*, diameter around 5 μ m) at least a 4 bilayer (bL) structure is typically used to prevent cargo leakage.^[316]

Thus, to establish the NC's robustness for reliable macromolecule encapsulation and to determine the minimum suitable number of polyelectrolyte bilayers, the potential leakage of model dye-labeled BSA from NCs (NC@BSA) with two, four and six bilayers (2 bL, 4 bL, and 6 bL, respectively) was investigated.

Table 5.5. Fluorescence data expressed in % corresponding to loading/leakage of macromolecules encapsulated in NCs.

Sample		I (%)				
		0 h	24 h	48 h	72 h	7 days
Core@BSA-FITC 2bL	SN	21 \pm 3	18 \pm 2	19 \pm 8	21 \pm 1	25 \pm 1
	C	79 \pm 7	82 \pm 7	81 \pm 3	79 \pm 3	75 \pm 3
NC@BSA-FITC 2bL	SN	24 \pm 1	8 \pm 1	18 \pm 3	11 \pm 0	18 \pm 0
	C	76 \pm 5	92 \pm 13	82 \pm 14	89 \pm 6	82 \pm 5
Core@BSA-FITC 4bL	SN	8 \pm 2	19 \pm 4	23 \pm 1	40 \pm 10	30 \pm 4
	C	92 \pm 2	81 \pm 5	77 \pm 5	60 \pm 6	70 \pm 7
NC@BSA-FITC 4bL	SN	17 \pm 2	20 \pm 3	23 \pm 5	10 \pm 0	21 \pm 4
	C	83 \pm 2	80 \pm 9	77 \pm 1	90 \pm 1	79 \pm 2
Core@BSA-FITC 6bL	SN	18 \pm 7	26 \pm 3	16 \pm 3	26 \pm 0	18 \pm 3
	C	82 \pm 2	74 \pm 14	84 \pm 8	74 \pm 3	82 \pm 7
NC@BSA-FITC 6bL	SN	3 \pm 1	24 \pm 1	12 \pm 1	14 \pm 2	25 \pm 2
	C	97 \pm 5	76 \pm 4	88 \pm 4	86 \pm 4	75 \pm 1

C: cargo; SN: supernatant.

To quantify the leakage of the encapsulated dye-labeled cargo after LbL, both before or after “dissolving” the CaCO₃ core matrix, the nanosystems were precipitated, and the cargo was quantified in both the precipitates and the supernatants by fluorescence. *Figures 59a-c* show the BSA encapsulation stability for nanosystems with different shell compositions: 2, 4, and 6 bilayers, respectively (see *Figure 5.14d*). As can be seen from *Table 5.5* at the time 0 h, the supernatant from NCs (*i.e.*, without the CaCO₃ core) reduces gradually as the number of bilayers increases from 2 to 6. The difference in BSA leakage between the nanosystems before and after “dissolving” the CaCO₃ core matrix might arise from both the “dissolution of the cores” and the purification (*i.e.*, centrifuge and washing) method.

Then, over time, the nanosystems exhibited a fluctuating loading/leakage of BSA encapsulated that can be due to shell permeability in aqueous solution. However, regardless of

the number of layers, the results show that the nanosystems can withstand up BSA without any statistically significant leakage along one week.

Table 5.5 shows the fluorescence data from Figures 5.14a-c corresponding to loading/leakage of BSA encapsulated in the nanosystems.

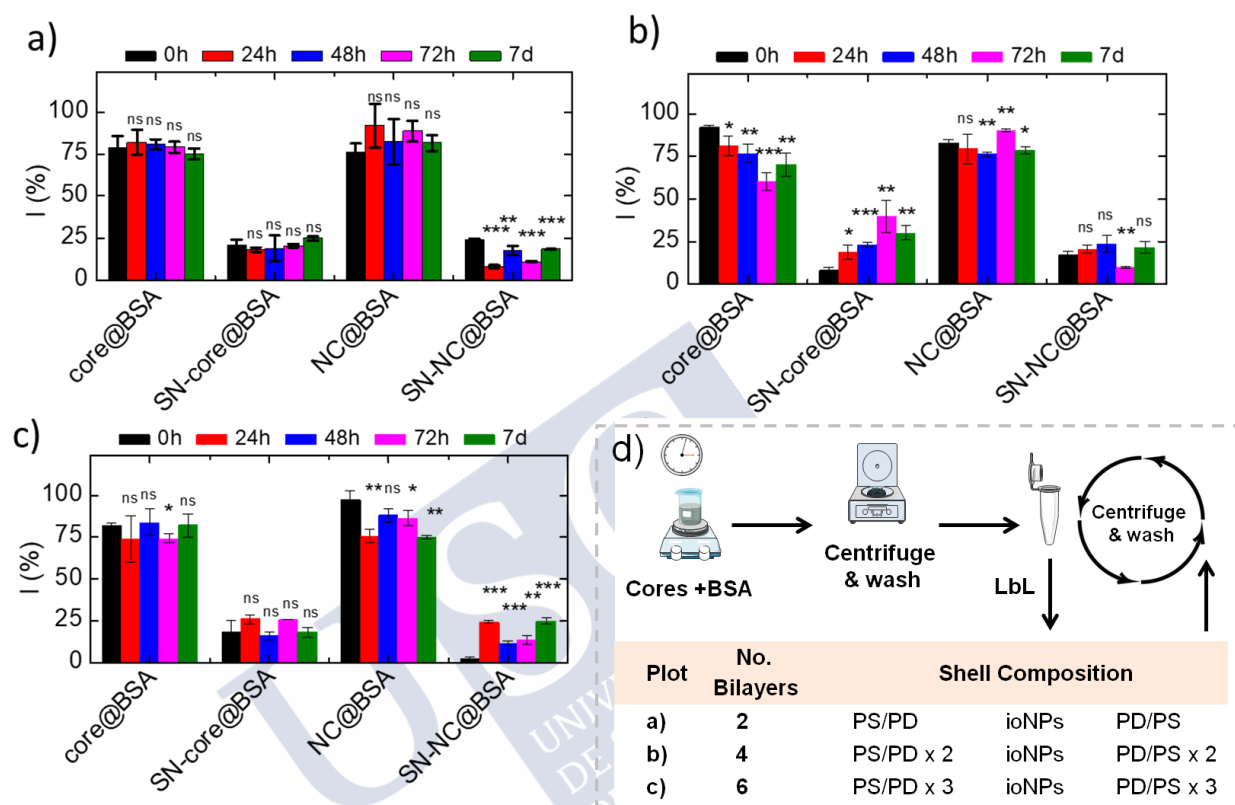


Figure 5.14. BSA encapsulation stability after LbL in CaCO_3 cores (without “dissolving” the CaCO_3 core matrix) or NCs (that is, the core dissolved), both nanosystems with increasing bL configurations: a) 2 bL, b) 4 bL and c) 6 bL for one week in PBS; Core or NC refer to the precipitated sample, and SN refers to the supernatant. All data represent mean \pm s.d. (three independent measurements). In all data, statistical significance was assessed by the *t*-test: each sample was compared with the basal level at 0 h (ns, not significant; **P* < 0.05; ***P* < 0.01; ****P* < 0.001). d) Shell composition information: PS: PSS, PD: PDADMAC and ioNPs: iron nanoparticles; for example, 2bL: PSS/PDADMAC/ioNPs/PDADMAC/PSS (adapted with permission from ref. [301]. Copyright 2019, Elsevier B.V.).

Based on these results, we chose the 2bL shell composition to evaluate the stability of nanosystems loaded with rtPA. Thus, the LbL assembly of the system loaded with rtPA was performed as follows (from the core to the outermost layer): macromolecule-loaded CaCO_3 core – (PSS/PDADMAC) – ioNPs – (PDADMAC/PSS) – gelatin (see Figure 5.15b).

To quantify the leakage of the encapsulated dye-labeled cargo after LbL, both before or after “dissolving” the CaCO_3 core matrix, the nanosystems were precipitated, and the cargo was quantified in both the precipitates and the supernatants by fluorescence over one week.

Table 5.6. Fluorescence data expressed in % corresponding to loading/leakage of macromolecules encapsulated in NCs.

Sample		I (%)				
		0 h	24 h	48 h	72 h	7 days
Core@rtPA-FITC	SN	4 ± 4	7 ± 1	13 ± 3	10 ± 1	14 ± 5
2bL	C	96 ± 29	93 ± 5	87 ± 3	90 ± 9	86 ± 1
NC@rtPA-FITC	SN	28 ± 2	22 ± 4	29 ± 1	31 ± 2	38 ± 3
2bL	C	72 ± 2	78 ± 3	71 ± 7	69 ± 7	62 ± 2

C: cargo; SN: supernatant.

The difference in rtPA leakage between the nanosystems before and after “dissolving” the CaCO₃ core matrix led to the same assumption that might arise from the “dissolution of the cores” process (*i.e.*, centrifuge and washing steps). Like the BSA leakage-profile, the nanosystems exhibited a fluctuating loading/leakage of rtPA encapsulated that can be due to the shell permeability in aqueous solution over time (see Table 5.6). According to Figure 5.15a, the nanosystem only showed residual rtPA leakage after one week, both in the case of keeping or removing the CaCO₃ core matrix. Table 5.6 shows the fluorescence data from Figure 5.15a corresponding to loading/leakage of rtPA encapsulated in the nanosystems.

These results demonstrated here that two polymer bilayers (with or without an outermost gelatin layer) are robust enough to prevent cargo leakage from the NCs either loaded with BSA or rtPA.

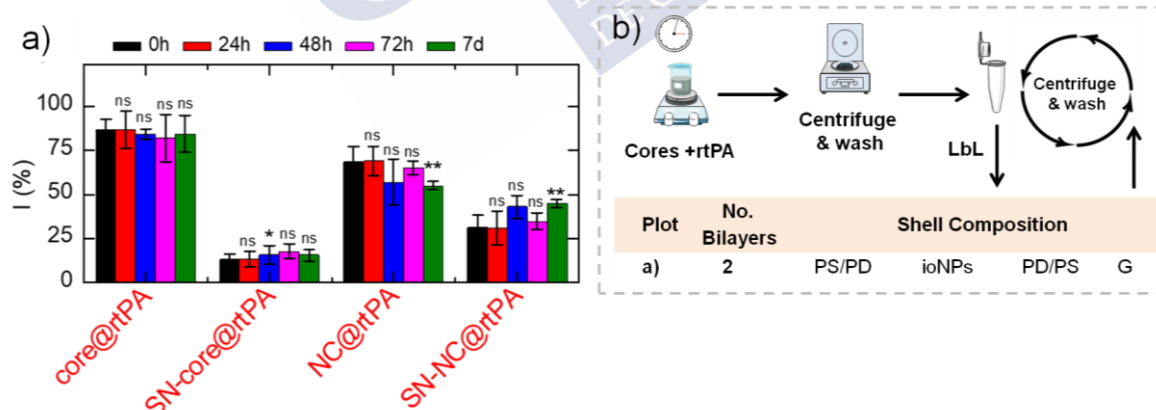


Figure 5.15. a) rtPA encapsulation stability in cores (without “dissolving” the CaCO₃ matrix) or NCs (that’s is, with dissolved cores) for one week in PBS. Core or NC refer to the precipitated sample, and SN refers to the supernatant. All data represent mean ± s.d. (three independent measurements). In all data, statistical significance was assessed by the *t*-test: each sample was compared with the basal level at 0 h (ns, not significant; **P* < 0.05; ***P* < 0.01; ****P* < 0.001). b) Shell composition information: PS: PSS, PD: PDADMAC, ioNPs: iron nanoparticles and G: gelatin (adapted with permission from ref. [301]. Copyright 2019, Elsevier B.V.).

5.2.6. Characterization of the Multifunctional Sub-Micrometric Capsules (NCs)

i) Structural Characterization

The deposition of each layer was followed by dynamic light scattering and zeta potential (ζ -potential) measurements for the system with rtPA. Layer-by-layer coated CaCO_3 particles with gelatin as the top layer show a reversal in ζ -potential after each layer deposition. The CaCO_3 templates had a negative ζ -potential of ~ -49 mV. The ζ -potential of the particles shifted from ~ -49 mV to ~ -34 mV with the deposition of the first PSS layer; then, from ~ -34 mV to $+24$ mV with the deposition of the second layer PDADMAC, and finally, to $\sim +15$ mV when terminated with gelatin (see *Figure 5.16* and *Table 5.7*). Instead, the CaCO_3 templates loaded with BSA had a negative ζ -potential of ~ -42 mV. The ζ -potential of the particles shifted from ~ -42 mV to ~ -17 mV when terminated with PSS (see *Table 5.7*).

Dynamic light scattering (DLS) analysis also revealed the formation of monodisperse sub-micrometric colloids; the addition of the layers increased the hydrodynamic diameter (number distribution) of the CaCO_3 templates loaded with rtPA from ~ 592 nm to ~ 890 nm with most of the increases attributed to the 1st PDADMAC layer and to the terminal gelatin layer. In the case of CaCO_3 templates loaded with BSA, the hydrodynamic diameter (number distribution) of the cores increased from ~ 623 nm to ~ 850 nm to the terminal PSS layer (see *Table 5.7*).

Scanning electron microscopy (SEM) inspection of NCs loaded with BSA, rtPA and rtPA + gelatin (NC@BSA or NC@rtPA, and NC@rtPA_gelatin, respectively) after drop casting on silicon substrates also confirmed the NCs morphology and size ($d_{\text{NC@BSA}} = 735 \pm 130$ nm, $d_{\text{NC@rtPA}} = 549 \pm 88$ nm and $d_{\text{NC@rtPA+gelatin}} = 780 \pm 210$ nm; see *Figure 5.17*).

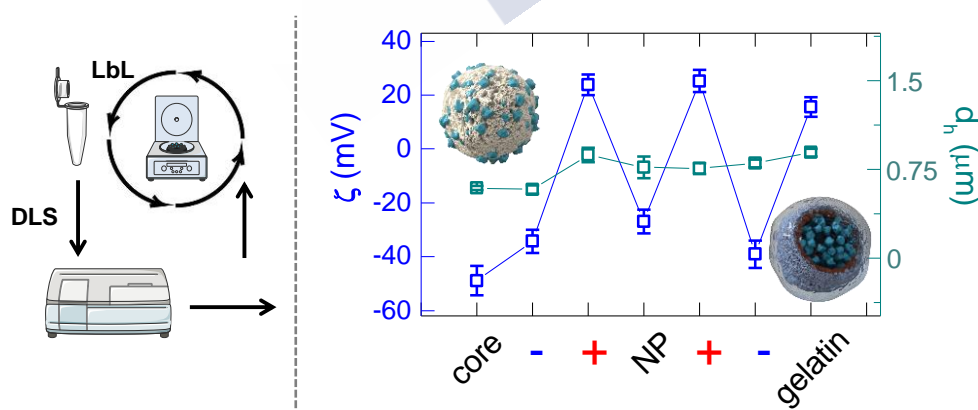


Figure 5.16. Mean values of ζ -potential (blue colored square symbols) and hydrodynamic diameter (green colored square symbols) evolution after each layer deposition of rtPA-loaded NCs (adapted with permission from ref. [301]. Copyright 2019, Elsevier B.V.).

Table 5.7. Mean average hydrodynamic diameters and ζ -potential of nanocores and NCs.

Sample	LbL-step	$d_{H(I)}$ (nm)	$d_{H(N)}$ (nm)	PDI	ζ -potential (mV)
NC@rtPA	core-rtPA	648 \pm 26	592 \pm 17	0.09	-48.9 \pm 5.5
	1 st PSS	638.1 \pm 34.3	577.6 \pm 35.5	0.13	-34.3 \pm 4.3
	1 st PDADMAC	909.4 \pm 73.8	869.9 \pm 61.4	0.30	23.9 \pm 3.8
	1 st ioNPs	796.0 \pm 11.3	765.7 \pm 91.4	0.28	-26.9 \pm 4.4
	2 nd PDADMAC	821.1 \pm 77.3	755.5 \pm 44.4	0.30	25.2 \pm 4.1
	2 nd PSS	834.6 \pm 36.3	799.6 \pm 32.3	0.18	-39.1 \pm 5.1
	gelatin+EDTA	890.0 \pm 34.9	890.4 \pm 33.3	0.62	15.6 \pm 3.6
	gelatin+EDTA	883.1 \pm 46.5	802.1 \pm 44.5	0.24	-
	gelatin+EDTA	853.7 \pm 48.5	835.7 \pm 43.9	0.23	-
NC@BSA	core-BSA	664.4 \pm 9.4	623.4 \pm 19.3	0.14	-41.7 \pm 2.6
	6 bL	864.4 \pm 38.9	851.7 \pm 38.4	0.09	-17.3 \pm 0.90
	6bL + EDTA	1119 \pm 80.41	1080 \pm 64.30	0.08	-16.8 \pm 0.7

$d_{H(I)}$ and $d_{H(N)}$ refer to the mean average hydrodynamic diameter from the intensity and number weighted DLS size distributions. PDI refers to polydispersity index. Standard deviation values were calculated from three independent measurements.

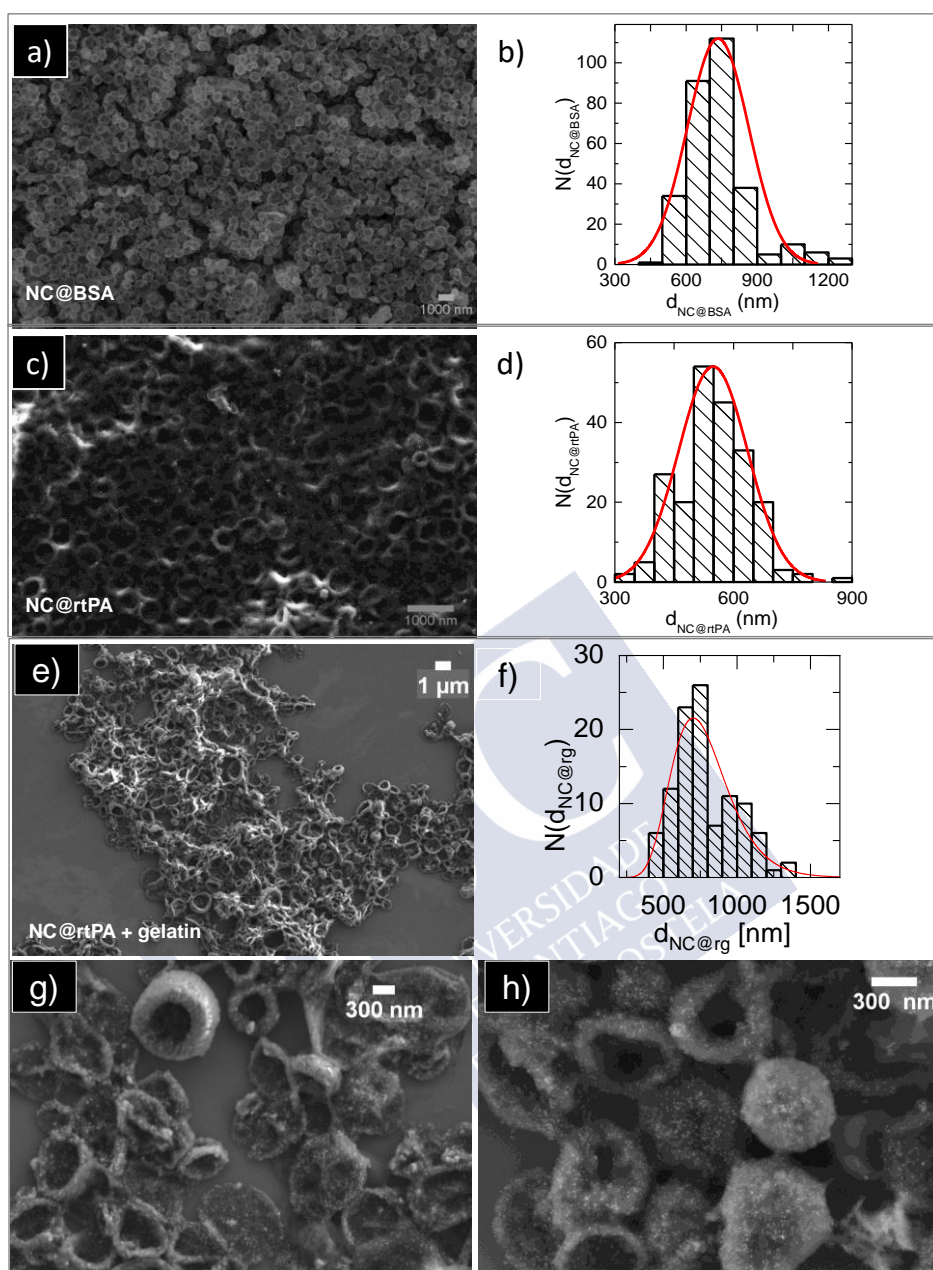


Figure 5.17. a) SEM micrograph of NC@BSA particles (scale bar is 1000 nm) (InLens, 10kV). b) Size histogram ($d_{NC@BSA}$: mean diameter of NC@BSA) obtained after measuring the diameter of over 300 NC@BSA particles using ImageJ; $d_{NC@BSA} = 735 \pm 130$ nm. c) SEM micrograph of NC@rtPA particles without the outermost gelatin layer (scale bar is 1000 nm) (SE2, 3kV). d) Size histogram ($d_{NC@rtPA}$: mean diameter of NC@rtPA without the gelatin layer) obtained after measuring the diameter of over 150 NC@rtPA particles (no gelatin) using ImageJ; $d_{NC@rtPA} = 549 \pm 88$ nm. e) SEM micrographs of NC@rtPA particles with the outermost gelatin layer (SE2, 3kV). f) Size histogram ($d_{NC@rg}$: mean diameter of NC@rtPA+gelatin with the outermost gelatin layer) obtained after measuring the diameter of over 100 NC@rtPA+gelatin particles using ImageJ; $d_{NC@rg} = 780 \pm 210$ nm. g-h) High magnification SEM micrographs of NC@rtPA+gelatin particles with the outermost gelatin layer, ioNPs are distinguishable as bright dots in the polymer shell of collapsed NCs (SE2, 3kV) (adapted with permission from ref. [301]. Copyright 2019, Elsevier B.V.).

ii) Flow Cytometry (FC)

Measurements were performed to determine the NCs concentration (i.e., NC/mL). The lower size detection limit for light scattering of conventional flow cytometers is typically in the order of 300-500 nm. Fluorescence and SSC signals were recorded to gather information of the fluorescently labeled encapsulated cargo (BSA or rtPA). Dispersions of 600 nm NCs were analyzed by FC, generating a distinctive side scattering signal from the background (PBS buffer). Concentrations between 100 to 1000 NCs / μ L for 600 nm NCs were analyzed, *cf.* Figure 5.18. The number of events measured in the corresponding NC gate divided by the acquired volume gives the final NC concentration.

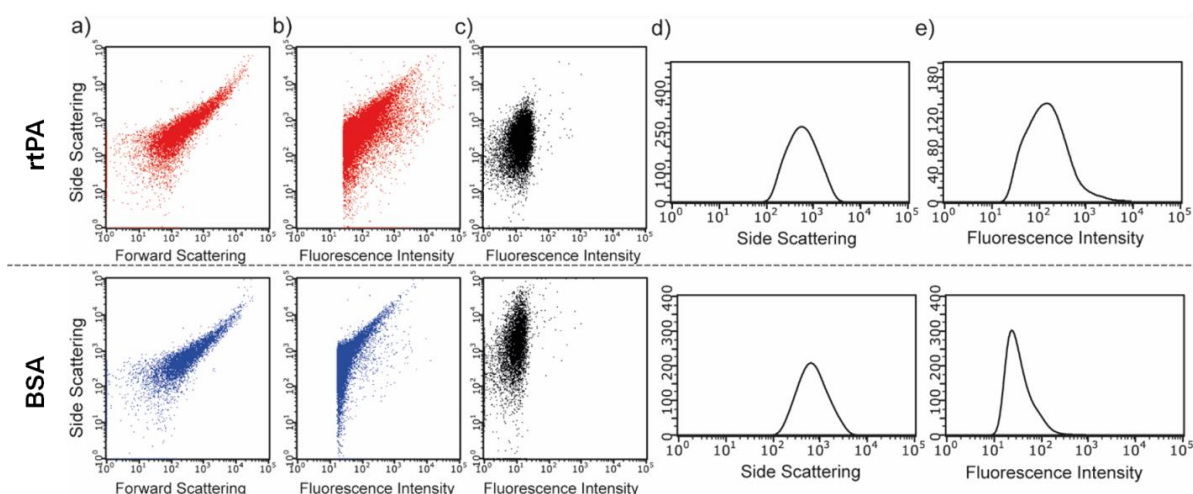


Figure 5.18. NCs dispersion analysis by flow cytometry. The variation of the flow cytometry SSC and the fluorescence signal as a function of the fluorescently-labeled encapsulated molecules are shown. a) Scatter density plots of SSC signal versus FSC signal for different NCs with diverse cargos: rtPA (red) and BSA (blue). b) Scatter density plots of SSC signal versus fluorescence signal (from the corresponding channel, 512/18 nm for FITC for the NCs with the different cargos: rtPA (red), and BSA (blue). c) Scatter density plots of SSC signal versus fluorescence signal (from the corresponding channel, 512/18 nm for FITC for the non-fluorescent NCs. d) Representative histograms of side scattering distributions of different loaded-NCs samples (rtPA and BSA). e) Representative histograms of MFI from the different channels (512/18 nm for FITC) associated with the encapsulated cargo (adapted with permission from ref. [301]. Copyright 2019, Elsevier B.V.).

iii) Quantification of the Cargo Content per NC

Quantification of the cargo content per NC was done in all cases as an indirect measurement of the mass of cargo based on fluorescence using the calibration curves previously described (see Figure 5.7), and the quantification of the NC per mL obtained by Flow Cytometry. The following expression was used:

$$\text{Cargo/NC} = \frac{\text{mass of cargo in purified NC/mL}}{\text{Number of NC / mL}} \times \frac{\text{Avogadro Number}}{\text{MW (cargo)}} \quad (5.6)$$

Moreover, NCs concentration and quantification of macromolecules per NC were evaluated by flow cytometry as described before (see *Table 5.8*).

Table 5.8. Number of macromolecules encapsulated per NCs for different NC@rtPA batches.

Sample	NC/mL	µg rtPA/mL	pg rtPA / NC	No. protein/NC
NC@rtPA	4.71×10^8	12.9	0.03	2.09×10^5
	4.38×10^8	14.7	0.03	2.56×10^5
	4.54×10^8	15.3	0.03	2.58×10^5
	4.95×10^8	10.5	0.02	1.61×10^5
	4.04×10^8	18.7	0.05	3.53×10^5
	4.60×10^8	11.4	0.02	1.89×10^5
	4.72×10^8	13.2	0.03	2.13×10^5
	4.64×10^8	16.1	0.03	2.65×10^5

5.2.7. Bioactivity of Encapsulated and Ultrasound-Loading Released

Different enzymatic assays were carried out to evaluate the bioactivity (*i.e.*, enzymatic activity) of rtPA, both inside the NCs and once released from the NCs by means of the application of US. Three different assays were used to test the rtPA activity. The amidolytic (*i.e.*, amide bond) activity of rtPA was studied using chromogenic and fluorogenic substrates, whereas the rtPA fibrinolytic (*i.e.*, thrombolytic) activity was tested using preformed rat-blood clots. It should be mentioned that the US were applied to NCs in Eppendorf tubes (see *Figure 5.19c*). Chromogenic substrates are peptides that after reaction with enzymes give rise to a colored product and are used to determine the activity of proteinase inhibitors by adding an active enzyme to the analyzed sample. A fluorogenic substrate allows the detection of the enzymatic activity by a fluorescent signal.^[317]

In particular, spectroscopic methods are used for studying the hydrolysis of peptides substrates, to determine the activity of proteolytic enzymes, based on the change of absorption spectrum of the solution studied or on the change of its fluorescence after enzymatic hydrolysis of chromogenic or fluorogenic substrate.^[318]

i) Chromogenic Assay

Firstly, a rtPA chromogenic peptide substrate (see *Figure 5.19a*) was used to quantify the amidolytic activity of a free FITC-labeled rtPA in solution (rtPA-FITC), inside the CaCO₃ cores (without CaCO₃ removal, *i.e.*, core@rtPA), and in the cavity of NCs (*i.e.*, NC@rtPA), as shown in *Figure 5.19b*.^[319] Due to the low molecular weight (MW) of the chromogenic substrate (MW = 659 Da), this can pass through the pores of both the microporous CaCO₃ cores and the semipermeable LbL shell, thereby allowing for the quantification of rtPA activity. In addition, the rtPA and BSA activity of NCs without the outmost gelatin layer also was quantified.

Free Alteplase (*i.e.*, thrombolytic agent also referred to as tissue plasminogen activator) was used as reference (100 %). From Table 5.9 we observed that the absorbance of the free Alteplase was equal to that created by free FITC-labeled rtPA in solution. Samples, with zero concentration of rtPA, did not exhibit a significant absorbance. Moreover, samples with cores, without cores and after US treatment showed similar absorbance values, as well as higher compared to samples with gelatin.

Therefore, compared with free Alteplase (taken as reference, 100 %) we found virtually the same rtPA amidolytic activity among all samples, which confirms the following:

- i) FITC-labeling of rtPA does not affect its enzymatic activity,
- ii) rtPA supported in the cores is fully active,
- iii) after CaCO₃ removal, rtPA keeps its activity inside the NCs, and
- iv) after US treatment, rtPA keeps its activity inside the NCs.

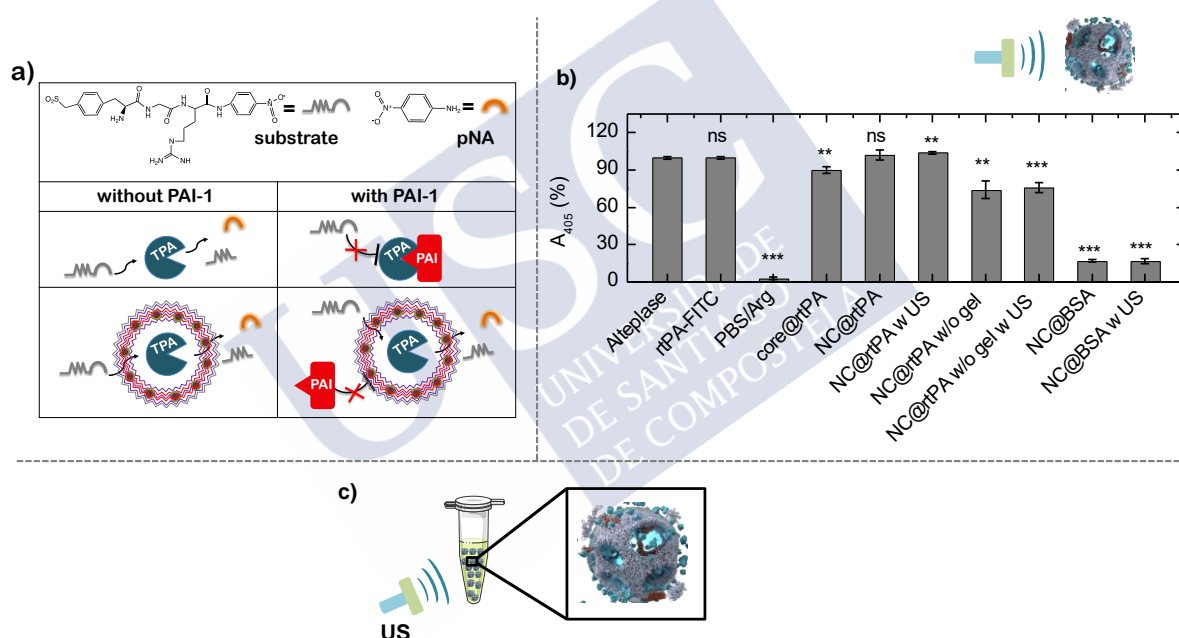


Figure 5.19. a) Scheme of the bioactivity assay (upon binding of the chromogenic substrate, rtPA releases p-nitroalanine - pNA) to determine the rtPA amidolytic activity upon set-up: US were applied to the NCs in Eppendorf tubes (adapted with permission from ref. [301]. Copyright 2019, Elsevier B.V.).

Moreover, to analyze if the encapsulated rtPA is protected from its natural inhibitor, which is the plasminogen activator inhibitor-1 (PAI-1; MW = 43 kDa), a member of the serine protease inhibitor (serpin) superfamily,^[291] FITC-labeled rtPA free in solution (rtPA-FITC) or encapsulated (NC@rtPA) were mixed with PAI-1 and the rtPA chromogenic peptide substrate (with PAI-1) (see Figure 5.19a).^[291]

Table 5.9. Raw absorbance data and corresponding % values obtained for the chromogenic rtPA substrate. Free Alteplase was used as reference (100 %).

Sample	A ₄₀₅ (a.u.)	A (%)
Alteplase	3.6 ± 0.1	100 ± 1
rtPA-FITC	3.6 ± 0.1	100 ± 1
PBS/Arg	0.1 ± 0.1	3 ± 1
core@rtPA-FITC	3.2 ± 0.1	90 ± 3
NC@rtPA-FITC	3.6 ± 0.2	102 ± 4
NC@rtPA-FITC w US	3.7 ± 0.0	104 ± 1
NC@rtPA-FITC w/o gelatin	2.7 ± 0.3	74 ± 7
NC@rtPA-FITC w/o gelatin w US	2.7 ± 0.1	76 ± 4
NC@BSA-FITC	0.6 ± 0.1	17 ± 1
NC@BSA-FITC w US	0.6 ± 0.1	17 ± 2

As shown in *Figure 5.20* and *Table 5.10*, PAI-1 inhibited the amidolytic activity (~ 17%) of non-encapsulated rtPA. In contrast, encapsulated rtPA kept its amidolytic activity (~ 78%) because PAI-1 cannot diffuse through the LbL porous shell due to its size (*i.e.*, 43kDa), similar as rtPA, which cannot diffuse out.

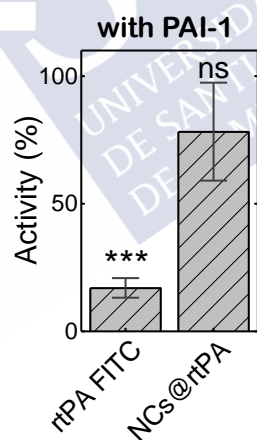


Figure 5.20. PAI-1 inhibition assay results of selected samples of free rtPA (rtPA-FITC) and encapsulated rtPA (NC@rtPA). All data represent mean ± s.d. (three independent measurements). In all data statistical significance was assessed by the t-test: each sample was compared with Alteplase (adapted with permission from ref. [301]. Copyright 2019, Elsevier B.V.).

These confirmed findings are particularly relevant as they anticipate the potential benefits of using *in vivo* the nanosystems proposed, *i.e.*, the rtPA half-life in blood may be greatly improved by encapsulation in NCs.

Table 5.10. Raw absorbance data and the corresponding % values obtained for the chromogenic rtPA substrate and PAI-1.

Sample	A ₄₀₅ (a.u.)		A (%)	
	w/o PAI-1	w PAI-1	w/o PAI-1	w PAI-1
rtPA-FITC	3.6 ± 0.1	0.6 ± 0.1	100 ± 1	17 ± 4
NC@rtPA-FITC	3.4 ± 0.2	2.8 ± 0.7	95 ± 4	78 ± 19

ii) SensoLyte® assay

Then, to produce a more efficient sonosensitive nanocarrier, the US-triggered protein release from the cavity of NCs was studied by firstly preparing dye-labeled BSA-loaded NCs (*i.e.*, NC@BSA) with different number of polyelectrolyte bilayers as a model system (*i.e.*, 2 bL, 4 bL and 6 bL), and exposed them to US during 15 or 120 min. The selected US application parameters (720 mW/cm², 2 MHz, 15 or 120 min) have been confirmed safe in rodent models,^[320] and are in the range of parameters used in clinical transcranial Doppler sonography.^[321] For example, similar parameters have been previously confirmed for US-triggered release of doxorubicin from LbL microcapsules (diameter of *approx.* 5 µm, 4 bL).

Here, the quantification of US-triggered release of macromolecules (BSA and rtPA) from the cavity of NCs was estimated from fluorescence measurements: relative fluorescence (*i.e.*, macromolecule-FITC) of the supernatant (SN, US-release) to the fluorescence of the precipitated product (cargo non-released).

As is shown in *Figures 5.21a-b* and *Table 5.11* it was found that within 15 min of US application, fluorescence analysis showed that the NCs with 2 bL exhibited notably BSA release (~ 50 %) in the supernatant (*i.e.*, the release of the dye-labeled BSA), after precipitation of the NCs. On the other hand, NCs with 4L and 6L both exhibited BSA release of ~ 22% in the supernatant. After 120 min US application, again, only the 2 bL system showed significant BSA release (~ 60 %).

Finally, based on these results, we performed similar experiments with capsules loaded with rtPA (*i.e.*, NC@rtPA) with 2 bL plus gelatin, and results confirmed that after 15 min of US application, *approx.* 50 % of the encapsulated rtPA (*i.e.*, the fluorescence of FITC-labeled rtPA) was found in the supernatant (see *Table 5.11* and *Figure 5.21b*).

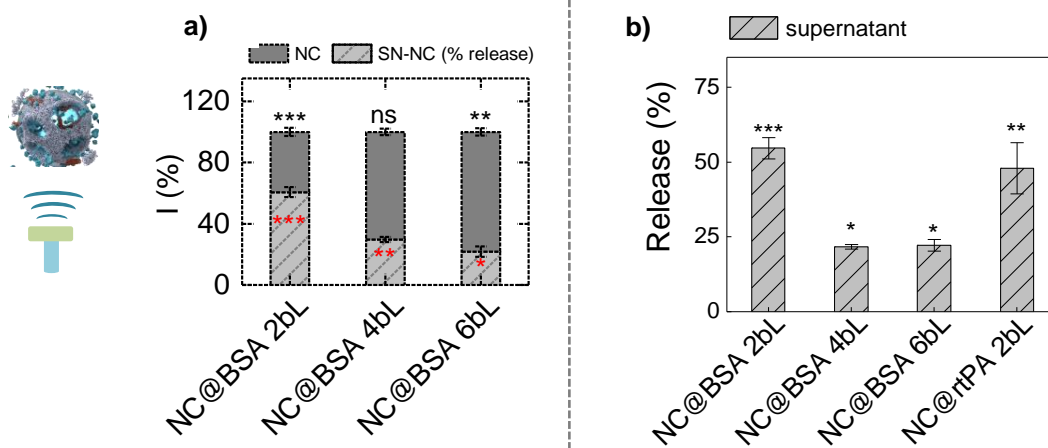


Figure 5.21. a) NC@BSA with two, four and six bL (2bL, 4bL and 6bL), and exposed to US for 120 min (720 mW/cm², 2 MHz, 120-min). b) Fluorescence-quantified (Intensity, %) US-triggered delivery into the supernatant of BSA or rtPA for NC with different number of bL after 15 min of US application (720 mW/cm², 2 MHz). In all data, statistical significance was assessed by the *t*-test: each sample was compared with the corresponding sample without US (ns, not significant; **P* < 0.05; ***P* < 0.01; ****P* < 0.001) (adapted with permission from ref. [301]. Copyright 2019, Elsevier B.V.).

Table 5.11. Fluorescence quantification of US-induced cargo release from NC@BSA (2-, 4- and 6-bL) and NC@rtPA particles (three independent experiments using different NC@rtPA concentrations).

Sample		I (counts)			I (%)		
		w/ot US	15 min	120 min	w/o US	15 min	120 min
NC@BSA -FITC 2bL	SN	199 ± 17	563 ± 37	455 ± 25	26 ± 2	55 ± 4	61 ± 3
	cargo	564 ± 23	468 ± 13	295 ± 21	74 ± 3	45 ± 1	39 ± 3
	SN1	13194	45191	x			
	SN2	10473	19665	x	13 ± 1	48 ± 9	x
NC@rtPA -FITC 2bL	SN3	2558	49320	x			
	cargo1	77844	57853	x			
	cargo2	69379	26907	x	87 ± 1	52 ± 9	x
	cargo3	19436	35880	x			
NC@BSA -FITC 4bL	SN	45 ± 21	65 ± 2	129 ± 8	11 ± 5	22 ± 1	30 ± 2
	cargo	380 ± 101	234 ± 16	305 ± 9	89 ± 24	78 ± 5	70 ± 2
NC@BSA -FITC 6bL	SN	29 ± 15	74 ± 6	80 ± 13	9 ± 5	22 ± 2	22 ± 3
	cargo	285 ± 7	257 ± 20	286 ± 8	91 ± 2	78 ± 6	78 ± 2

Once US-triggered rtPA release was confirmed and quantified by fluorescence measurements, the enzymatic activity (amidolytic) of the released rtPA was quantified by a fluorogenic assay (SensoryLyte® AMC tPA activity assay). According to Figure 5.22 and Table 5.12, the released rtPA is fully bioactive, in agreement with the fluorescence quantification of

the supernatants. The fluorogenic assay allows for reliable measurements in physiological media such as blood and plasma. Thus, later, this assay was also used to quantify rtPA activity after US application *in vivo* (see section US-triggered delivery of rtPA *in vivo*).

Table 5.12. Sensolyte activity assay performed in NC@rtPA particles in the supernatant (SN) and precipitate (cargo) after 15 min of US.

Sample		I ₄₄₂ (counts)		I ₄₄₂ (%)	
		w/o US	15 min	w/o US	15 min
NC@rtPA	SN	423 ± 44	989 ± 31	19 ± 2	43 ± 1
	cargo	1841 ± 215	1289 ± 83	81 ± 9	57 ± 4

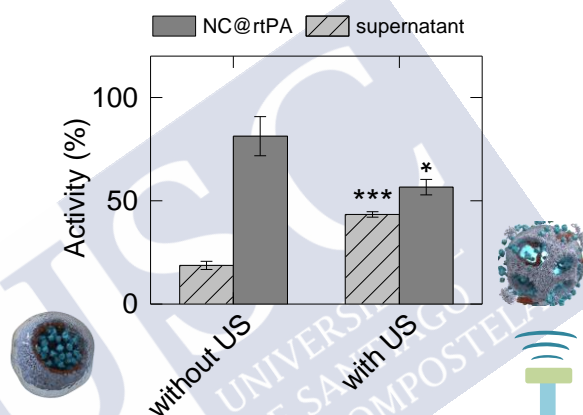


Figure 5.22. Enzymatic activity of rtPA released from NC@rtPA particles quantified in the supernatant by the fluorogenic assay Sensolyte® upon US application. In all data, statistical significance was assessed by the *t*-test: each sample was compared with the corresponding sample without US (ns, not significant; **P* < 0.05; ***P* < 0.01; ****P* < 0.001) (adapted with permission from ref. [301]. Copyright 2019, Elsevier B.V.).

iii) Clot Assay

The final test done was a clot assay following previous reports.^[322] Here, the efficiency (*i.e.*, bioactivity) of the US-released rtPA to reduce the size of clots (artificially pre-formed in microwell plates) was evaluated indirectly by measuring the absorbance of hemoglobin at 520 nm (*i.e.*, red) that increases as the clots dissolve.

Initially, as a calibration curve, solutions of free rtPA solutions of increasing concentrations (*i.e.*, 0-100 µg/mL) were added to preformed clots at the bottom of microwell plates. Then, after 1 h of incubation, the absorbance at 520 nm (*i.e.*, red) of differently colored solutions (extracted from the clot wells) was measured, which showed an enhanced absorbance with increasing rtPA concentrations (see *Figure 5.23a*). NCs without cargo (*i.e.*, 100 µL, 4.2 × 10⁷ NC/mL) were added as a control, showing negligible effects as expected (see *Figure 5.23b*). In addition, we added NCs with the following characteristics: the supernatant (SN) or precipitate (PPT) of the

sample NC@rtPA (1 $\mu\text{g/mL}$) with US (15 min), NC@rtPA (1 $\mu\text{g/mL}$) w/o US, NC@rtPA (1 $\mu\text{g/mL}$) with US (15 min) (see Table 5.13).

In the case of NC@rtPA (100 μL , 4.2×10^7 NC/mL), rtPA encapsulated (1 $\mu\text{g/mL}$) was added; without US application, clots were only partially dissolved, which we ascribe to residual rtPA leaking. In the case of US application, clots were as dissolved as the same amount of non-encapsulated rtPA, showing a similar activity (increased 520 nm-absorbance) (see Figure 5.23b).

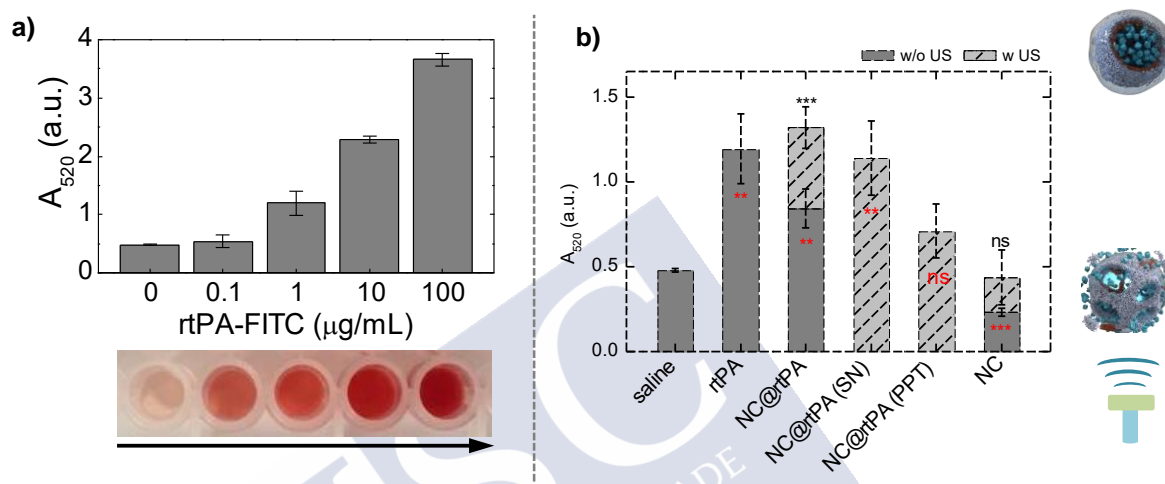


Figure 5.23. Clots assay: a) Calibration curve of clot dissolution using increasing free rtPA concentrations. b) Absorption at 520 nm, A_{520} , after addition to the clots of: saline, free rtPA (1 $\mu\text{g/mL}$), NC@rtPA particles with encapsulated rtPA (1 $\mu\text{g/mL}$) in the presence and absence of US, and non-loaded NC in the presence and absence of US (absorbance A_{520} measurements illustrate the ability of the different samples to dissolve the clots). All data represent mean \pm s.d. (three independent measurements). In all data, statistical significance was assessed by the *t*-test: each sample was compared with the saline group (ns, not significant; **P* < 0.05; ***P* < 0.01; ****P* < 0.001) (adapted with permission from ref. [301]. Copyright 2019, Elsevier B.V.).

Table 5.13. Clots assay data.

Sample	A_{520} (a.u.)	
	w/o US	w US
saline	0.48 ± 0.01	
rtPA-FITC 0.1 $\mu\text{g/mL}$	0.54 ± 0.10	
rtPA-FITC 1 $\mu\text{g/mL}$	1.19 ± 0.21	None
rtPA-FITC 10 $\mu\text{g/mL}$	2.28 ± 0.05	
rtPA-FITC 100 $\mu\text{g/mL}$	3.66 ± 0.11	
NC@rtPA 1 mg/mL	0.84 ± 0.12	1.32 ± 0.12
NC@rtPA 1 $\mu\text{g/mL}$ SN		1.14 ± 0.22
NC@rtPA 1 $\mu\text{g/mL}$ PPT	None	0.71 ± 0.16
NC	0.23 ± 0.02	0.44 ± 0.16

5.2.8. NCs Dispersion and Fluorescence Analysis after US Treatment

i) *Flow Cytometry*

Flow cytometry assay was performed to characterize the NCs dispersion and fluorescence without (w/o) and with US treatment (see *Figure 5.24*).

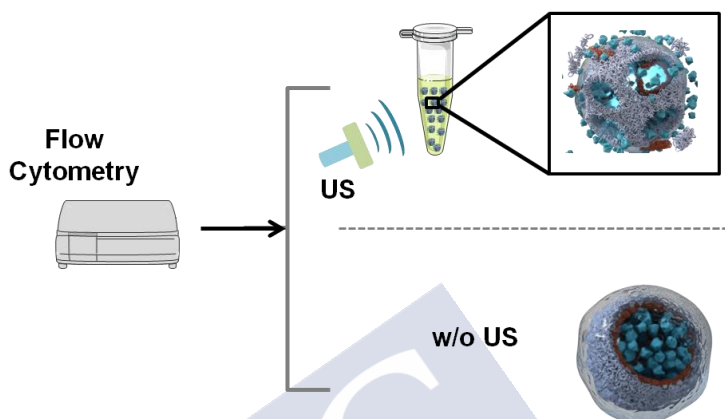


Figure 5.24. Schematic Illustration of the characterization of NCs before and after US treatment. US were applied to the NCs in Eppendorf tubes (adapted with permission from ref. . Copyright 2019, Elsevier B.V.).

Flow cytometry data from the forward and side scatter channels (FSC and SSC) showed a significant change in the NCs after US application (see *Figure 5.25*). The scattering (forward and side-) and fluorescence intensity of the NCs samples and the SN in the presence and absence of US treatment were measured with a Guava® easyCyte BG HT flow cytometer (Millipore®), at a constant flow rate of 0.12 $\mu\text{L/s}$, using a blue laser emitting at 488 nm and a green laser emitting at 532 nm as excitation sources. FSC and SSC signals were recorded to gather information of the NC concentration and dispersion. Fluorescence and SSC signals were recorded to gather information of the fluorescently labeled encapsulated cargo (rtPA).

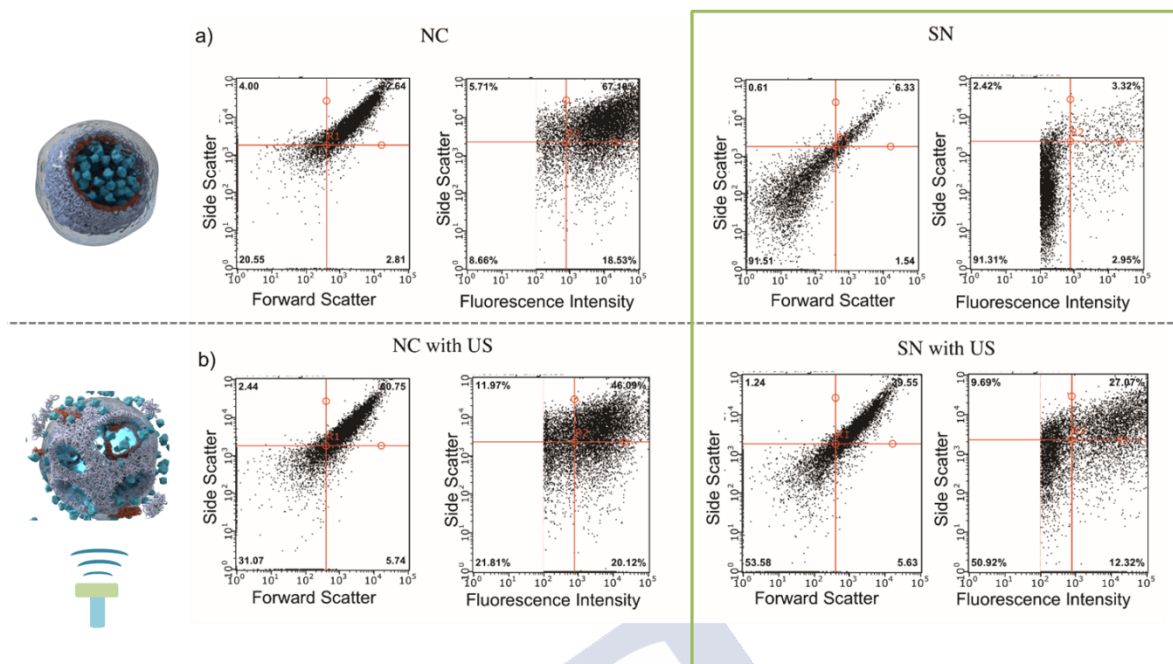


Figure 5.25. NCs dispersion analysis after US treatment by flow cytometry. The variation of the FCS and the SSC signals of the NC and SN as a function of the US application are shown. a) Scatter density plots of FSC signal versus SSC signal, and SSC signal versus fluorescence signal (corresponding to the 512/18 nm channel for control NCs with rtPA in the supernatant. b) Scatter density plots of FSC signal versus SSC signal, and SSC signal versus fluorescence signal (corresponding to the 512/18 nm channel for control NCs with rtPA in the supernatant after US treatment. This assay confirms the US-triggered release of rtPA by fluorescence increases in the supernatant of NC after US treatment (adapted with permission from ref. [301]. Copyright 2019, Elsevier B.V.).

5.2.9. Ultrasound-Triggered *in vivo* Delivery of rtPA

All previous US-controlled release results illustrated that a system with 2bL is a suitable carrier for *in vivo* drug delivery. Therefore, a capsule-based on 2bL plus gelatin was selected for the *in vivo* experiments.

Ultrasound triggered release characterization and the entire experimental work *in vitro* and *in vivo* were part of the Ph.D. thesis of Clara Correa Paz (Completed).

Swiss mice (male, 25-30 g) were used as the animal model to investigate the *in vivo* performance of the NC@rtPA particles for the US-controlled release of rtPA. Treatments were administered through the femoral vein, and blood samples were further obtained from the carotid artery. This approach allowed us to analyze the *in vivo* stability of the rtPA-encapsulation and to evaluate the US-induced drug release. For more details concerning animal procedures and results obtained from the *in vivo* experiments see Chapter 6 Appendix 6.2.

Results arising from the *in vivo* delivery of rtPA in mice by US application can be summarized as follows:

- 1) Three standard toxicity markers were evaluated after *i.v.* administration of NC@rtPA particles (1 mg/kg rtPA dose, bolus, approx. 5.1 mg/kg Fe) and, in all cases, whole blood analysis showed normal enzymatic levels.

- 2) The enzymatic activity of *in vivo* US-released rtPA was quantified with the SensoLyte assay in freshly extracted plasma samples.
- 3) Blood extractions were done through a cannula inserted in the carotid artery. Blood samples were taken before administering the treatments (basal) and 5, 20, and 40 minutes after the administration. The US was continuously applied (40 min) in the abdominal region, as shown in *Figure 5.26a*. For comparison, different samples were tested: non-encapsulated rtPA (1 or 10mg/kg), NC@rtPA (1 mg rtPA/kg) and NC@rtPA (1 mg rtPA/kg) with US-application.
- 4) After 40 min of administration of non-encapsulated (free) rtPA, its activity is, in either case, no significant compared to basal levels. In the case of NC@rtPA particles (1 mg/kg) in the absence of US application, rtPA activity is in the order of the non-encapsulated rtPA sample (1 mg/kg), which may be due to some rtPA leakage *in vivo*. After 40 min, rtPA activity in the NC@rtPA group dropped to basal levels. In the case of US-application (40 min) after administration of NC@rtPA (1 mg/kg), the rtPA activity increased over time, reaching about 7-fold for basal levels after 40 min. These results demonstrate that the half-life of rtPA can be greatly enhanced by encapsulation in our sonosensitive NCs (see *Figure 5.26b*).
- 5) The *in vivo* fate (biodistribution) of the NCs was investigated by MRI and ICP-MS; no MRI contrast differences were found among treated (*i.v.* NC@rtPA, 1 mg rtPA/kg mouse) or non-treated (saline) animals. Regarding ICP-MS analysis, significant increases of Fe concentration were not found in the brain, heart, liver, spleen, or kidneys in any case. On the other hand, the Fe concentration in the lungs of animals treated with NC@rtPA particles plus applied US was slightly higher than in control animals.

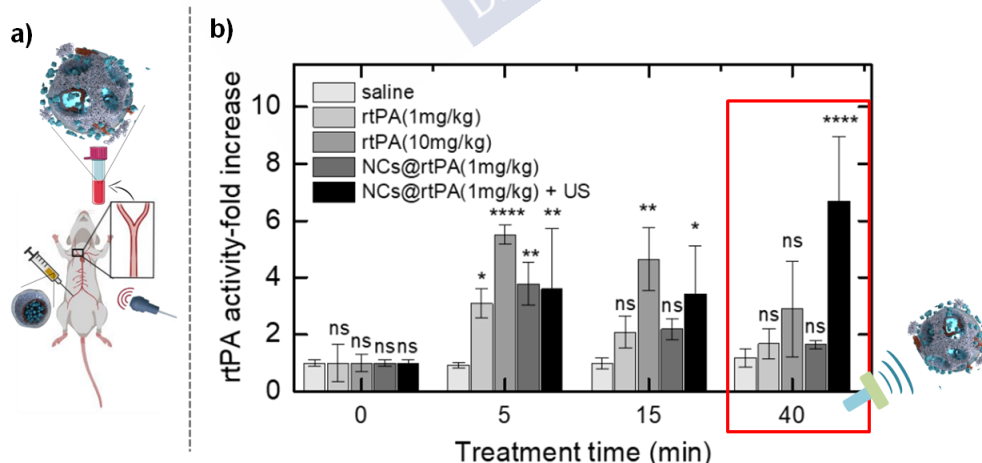


Figure 5.26. a) *In vivo* scheme to evaluate the rtPA encapsulation and the US drug release. b) Blood rtPA activity was determined in the 5 groups tested ($n = 3$), before treatment administration (blood rtPA basal levels), and 5, 15 and 40 min later on. All data represent mean \pm s.d. Statistical significance was assessed by two-way analysis of variance followed by Dunnett's multiple comparisons test. In b), each treatment time (5, 15 or 40 min) was compared with rtPA levels in the saline group; in c) each treatment was compared with the corresponding rtPA basal levels (ns, not significant; * $P < 0.05$; ** $P < 0.01$; *** $P < 0.001$; **** $P < 0.0001$) (adapted with permission from ref. [301]. Copyright 2019, Elsevier B.V.).

5.3. Conclusions

In this chapter, we demonstrated that the addition of PVSA [poly (vinylsulfonic acid)] in the course of CaCO_3 nanoparticle synthesis lowered the nucleation rate, stabilized the particle surface, and served as particle size modulator. PRXD and FTIR results confirmed that the major crystalline component of our CaCO_3 cores is the polymorph vaterite. However, the characteristic calcite peak grows along time. The successful incorporation of delicate biomolecules such as rtPA, (recombinant tissue plasminogen activator), BSA, and dextran into monodisperse CaCO_3 particles with loading efficiencies of: $\text{core@rtPA-FITC} = 24.5 \%$; $\text{LE}(\text{core@BSA-FITC}) = 1.5 \%$; $\text{LE}(\text{core@dextran-RBITC}) = 11.9 \%$ was demonstrated. Moreover, CaCO_3 sub-micrometric polymer capsules via the layer-by-layer technique based on the deposition of both non-biodegradable PDADMAC/PSS and biodegradable poly-L-arginine/dextran sulfate polymers were presented. The PDADMAC/PSS multilayer capsules were prepared with the addition of ioNPs and gelatin layers. The capsules loaded with rtPA were approximately 600 nm in size, and it was found that rtPA retained its enzymatic activity inside the NCs. We were able to optimize the NCs shell thickness, with two bilayers (with or without an outermost gelatin layer) being the most suitable system that allows the ultrasound-induced release of fully functional rtPA in vitro and in vivo (in mice), whilst preventing leakage. The inversion of the surface charge after each deposited layer was confirmed by ζ -potential measurements. The activity of the released rtPA from the NCs was approx. 3.5-fold-improved compared to a similar amount of non-encapsulated rtPA (1 mg/kg). The proposed research strategy presented in this study significantly extended the half-life and activity of rtPA in mice compared to non-encapsulated rtPA.





Chapter 6

6. Appendix

6.1. Chapter 4 Appendix

6.1.1. Cell Studies

i) Cell Culture

Hela (cervical cancer cell line) and A549 cells (adenocarcinomic human alveolar basal epithelial cell line) were cultured in DMEM with phenol red, 4.5 g/L D-glucose, L-glutamine and pyruvate (DMEM, 1X, Gibco, #41966-029) supplemented with 10 % Fetal Bovine Serum (FBS, Gibco, #10270-106) and 1% Penicillin Streptomycin (P/S, Corning, 100X, #30-002-CI). Cells were maintained under humid conditions at 37 °C and 5 % of CO₂. Cells were passaged after cleaning Dulbecco's Phosphate Buffered Saline (DPBS, 1X, Gibco, #14190-094) with 0.25 % Trypsin-EDTA (1X, Gibco, 25200-056) when the culture reached confluency.

ii) Cell Viability

In order to study the number of viable cells after NPs exposure, we carried out the resazurin assay, *cf. Figure 6.1*. HeLa and A549 were seeded in 96-well plates (NEST Scientific, #701001), 7500 cells per well in 100 µL of cell growth medium (0.3 cm² per well) 24 h before NPs exposition. Then, medium was removed and 100 µL of cell culture growth medium with the desired concentration of NPs were added. We incubated the cells with the NPs the time of interest (4 and 24 h) at 37 °C and 5 % CO₂. After that, we rinsed each well three times with phosphate buffered saline (PBS) and added 100 µL of freshly prepared solution with 90 % of media and 10 % of resazurin (resazurin sodium salt in water 0.2 mg/mL filtered; Resazurin Sodium Salt, Sigma Aldrich, #199303-1G). Cells were incubated during 3 h at 37 °C and 5 % CO₂ under dark conditions.

Non-fluorescent resazurin (Alamar blue) is oxidized by living cells into its fluorescent product resorufin (excitation at 579 nm and emission at 584 nm). In this way, the fluorescence intensity of each well is proportional to the number of living cells there. After the incubation time, plates were measured with a plate reader (Infinite® 200 PRO, Tecan, Switzerland) under 560 ± 20 nm excitation and fluorescence was collected with a 610 ± 20 nm filter. The fluorescence value of each well provided by the instrument is an average of nine consecutive measures in the same well. Final intensity value for control cells (I_C), the ones that were not treated, is an average of, at least, nine different well values. Final intensity values for samples (I_S) are a mean of three independent wells values. So, we can calculate the final cell viability values as:

$$\text{cell viability (\%)} = \frac{I_S}{I_C} \cdot 100 \quad (6.1)$$

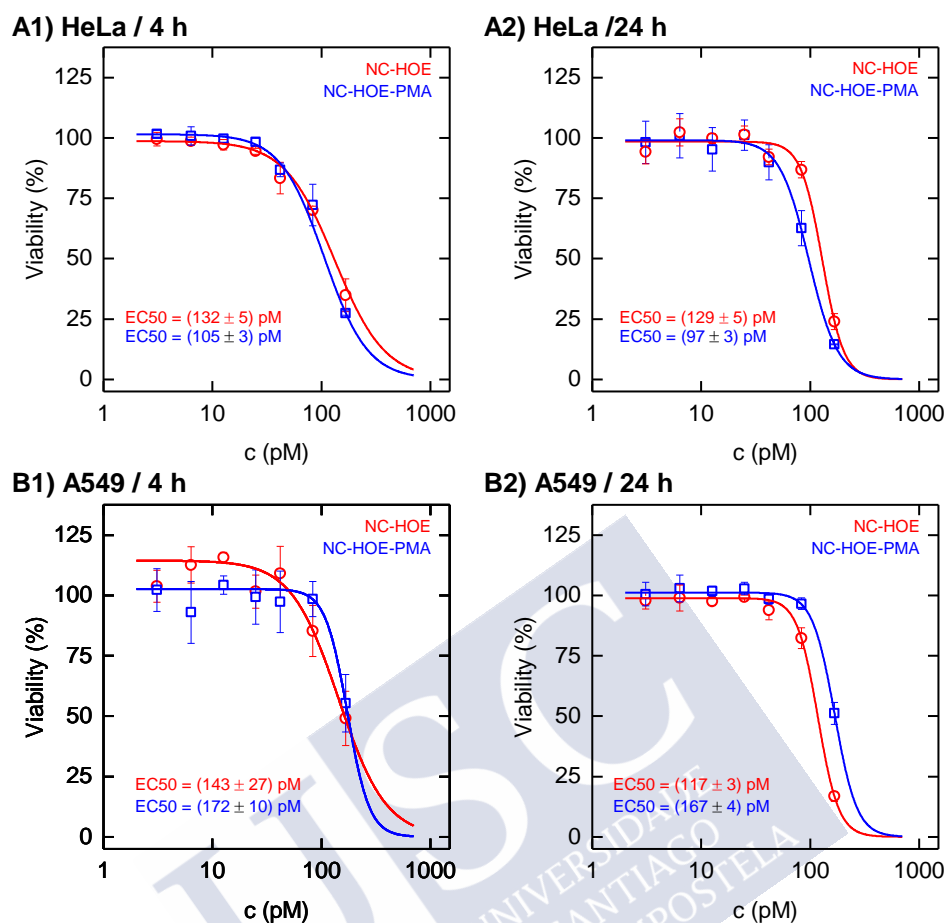


Figure 6.1. Cell viability using the resazurin assay of HeLa cells (A) and A549 cells (B) under exposure to increasing concentrations of the particles before (NC-HOE) and after PMA-functionalization (NC-HOE-PMA), and evaluated at two incubation times: 4 h (1) and 24 h (2). Half-maximal responses (EC50 values) were calculated by fitting (logistic function in OriginLab, fixing minimum viability to 0 %) (adapted with permission from ref. [245]). Copyright 2019, Wiley-VCH Verlag GmbH & Co. KGaA).

iii) Confocal Imaging

In order to perform all the confocal imaging experiments with living cells, 20000 HeLa cells in 200 μ L were seeded on μ -Slide 8 well-ibiTreat chambers (1 cm^2 per well, Ibidi, Germany, #80826) at least 12 h before the particle exposure. Our nanosystems were diluted to a concentration of 50 pM in culture media. After 4 h, cells were cleaned three times with fresh PBS to remove particles non-associated with cells. For cell membrane staining, we made a CellMask™ Deep Red (ThermoFisher, #C10046) dilution with 1 μ L in 1000 μ L of DMEM. We added 100 μ L of this staining solution to the cells and we incubated them during 3 minutes at 37 °C in dark conditions. After this, we cleaned again three times with PBS and added HEPES (4-(2-hydroxyethyl)-1-piperazineethanesulfonic acid) supplemented media to cells (Dulbecco's Modified Eagle Medium without phenol red, +4.5 g/L D-glucose and L-glutamine, 25 mM

HEPES and without pyruvate, 1X, Gibco, 21063-029). Confocal images of living cells were captured on an Andor Dragonfly spinning disk confocal system mounted on a Nikon TiE microscope equipped with a Zyla 4.2 PLUS camera (Andor, Oxford Instruments) and an OKO-lab incubator to keep cells at 37 °C during all the experiment. Images were taken with different magnification objectives (20X, 60X, 100X). HOE fluorescence was measured with an excitation of a 405 nm laser and a 450(50) nm filter. CellMask™ Deep Red channel was obtained under the excitation with a 637 nm laser and using the 725(40) nm filter. All the images were processed with ImageJ.

iv) *Laser Irradiation*

After checking the cells with the NC-HOE-PMA nanosystems to the microscope without irradiation, we performed an irradiation protocol as follows: we used an 808 nm laser (Lasing, #FC-W-808A) with a zoom fiber collimator (Thorlabs, #ZC618SMA-B) to control the spot size as well as irradiate cells homogeneously, *cf. Figure 6.2*. In order to calculate the intensity in W/cm^2 that cells received, a power energy meter was used (Thorlabs, #PM100D) with a thermal power head (10 W, 25 mm, Thorlabs, #S425C) to measure the output power. To obtain the spot size a viewing card was used (Thorlabs, #VRC4) to see the spot and ImageJ to measure it. Since the beam is collimated, we consider a homogeneous spot and, thus, the fluency was obtained just dividing the power by the surface (in cm^2) of the spot. Different time and power conditions were analyzed and 5 minutes at $7 \text{ W}/\text{cm}^2$ selected as the optimal conditions.

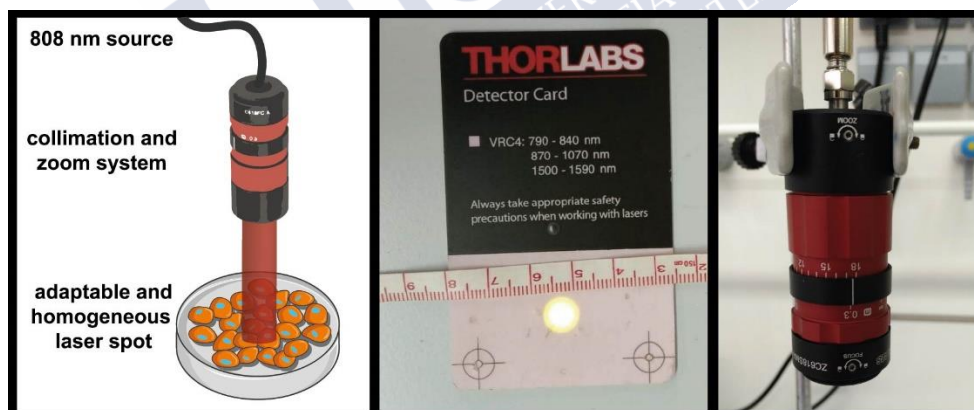


Figure 6.2. Left: Schematic representation of the NIR irradiation set-up used to activate HOE-release from the NC-HOE-PMA particles inside living cells; middle: beam diameter; right: actual image of the collimation/zoom system (adapted with permission from ref. [245]. Copyright 2019, Wiley-VCH Verlag GmbH & Co. KGaA).

v) *SERS Imaging*

To perform SERS imaging with living cells, A549 cells were seeded at a density of 60000 cells/ cm^2 onto a Nunc™ Δ -Petri Dishes (Thermo Fisher Scientific) in DMEM medium without red phenol, 4.5 g/L D-glucose, 4 mM L-glutamine and 25 mM HEPES (DMEM, 1X, Gibco, #21063-029) supplemented with 10% heat-inactivated Fetal Bovine Serum (Gibco, #10270-106) and 1% Penicillin Streptomycin (P/S, Corning, 100X, #30-002-CI). After 16 h of culture,

A549 cells displayed a semi-confluent (75%) phenotype under phase-contrast microscopy (IMT2 microscope by Olympus; Barcelona, Spain). Experiments were carried out at this semi-confluent state. NC-HOE and NC-HOE-PMA systems were redispersed in MeOH or in sterile Milli-Q water, respectively, at a concentration of 0.5 nM. NCs were added to A549 cells to a final concentration of 50 pM and kept in the incubator for 4 h. At the end of the experiment, culture medium with non-internalized NCs was discarded, and cells were inspected in the SERS confocal microscope. A control consisting of a Petri dish with no cells but containing complete medium also incubated at 37°C, was included in this set of experiments to subtract the background signal caused by the Petri dish and the culture medium.

The laser was focused into the samples with a 5X objective, providing an optical resolution of 1 μm . The inelastic radiation was collected with a Renishaw Invia system by using a high-resolution grating of 1200 g cm^{-1} and a NIR laser (785 nm). Samples were studied in single points or by mapping extended areas with the Renishaw StreaLine accessory. For the SERS characterization of the nanomaterials, samples were studied in powder. For quantitative analysis, bands were deconvoluted by curves of Lorentzian shape, where the band position and the full widths at half maxima were fixed after applying a linear baseline. Experiments in the presence and absence of light were carried out as follows: For NIR illumination, cells were placed under the microscope and illuminated continuously with 3 mW at the sample. Spectra were collected every hour at 0.3 mW with acquisition times of 10 s. This difference of power was set to minimize the effect of the laser on the nanocomposites during data collection. In the case of the experiments without light, the same scheme was repeated but with no exposition of the sample to light (only for the spectral acquisition).

The following collage images, at different magnifications provide an overview of the behavior of the NC-HOE (see *Figure 6.3*) and NC-HOE-PMA nanosystems (see *Figure 6.4*). Confocal imaging was used to assess the effect of laser irradiation on the NC-HOE-PMA system inside HeLa cells, *cf. Figure 6.5*.

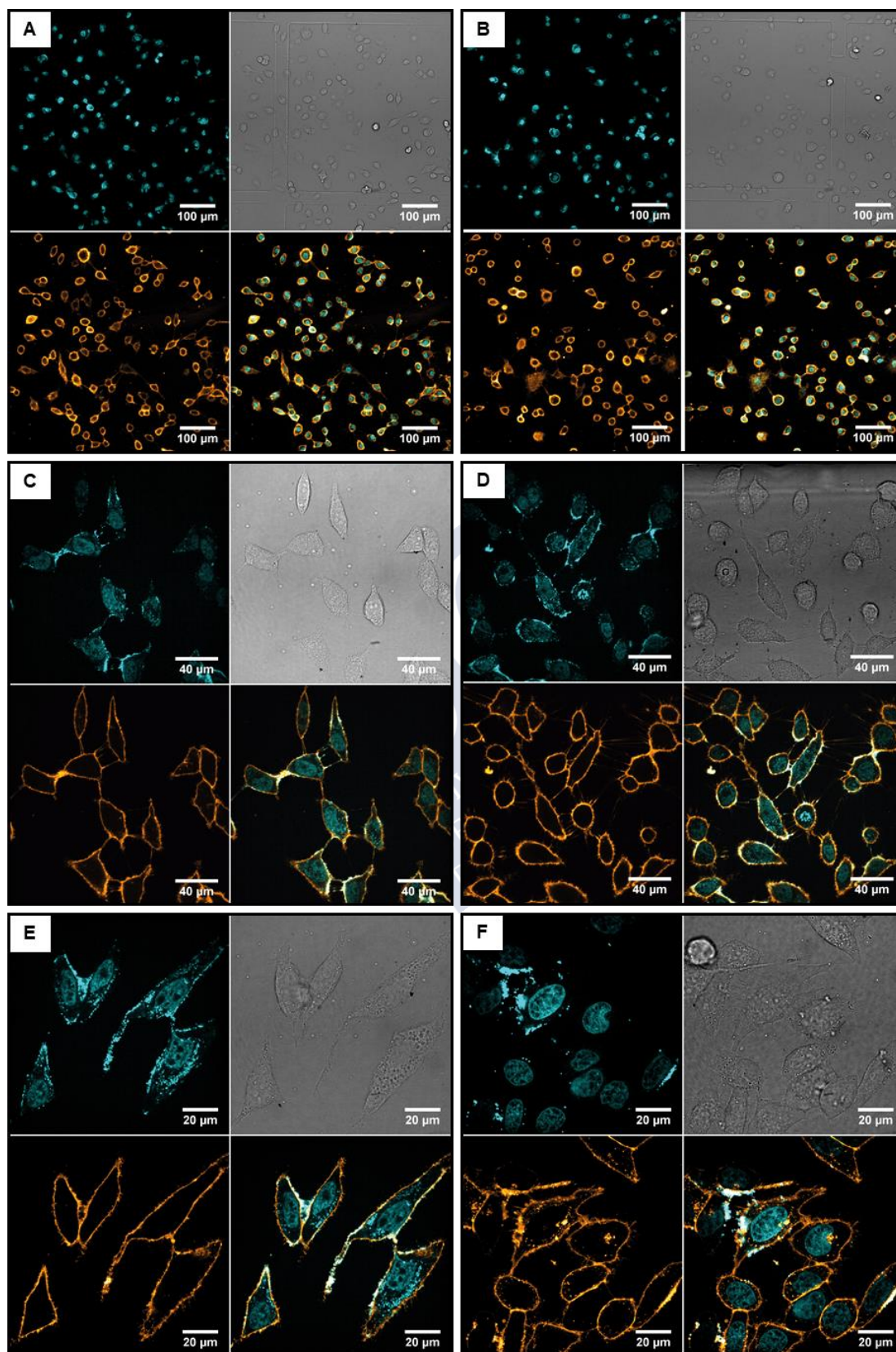


Figure 6.3. Collage of confocal microscopy images (top-left: blue channel; top-right: bright field; bottom-left: orange channel; bottom-right: merged blue + orange) at different magnifications (A,B: 20X; C,D: 60X; E,F: 100X) for the NC-HOE nanosystem (adapted with permission from ref. [245]). Copyright 2019, Wiley-VCH Verlag GmbH & Co. KGaA).

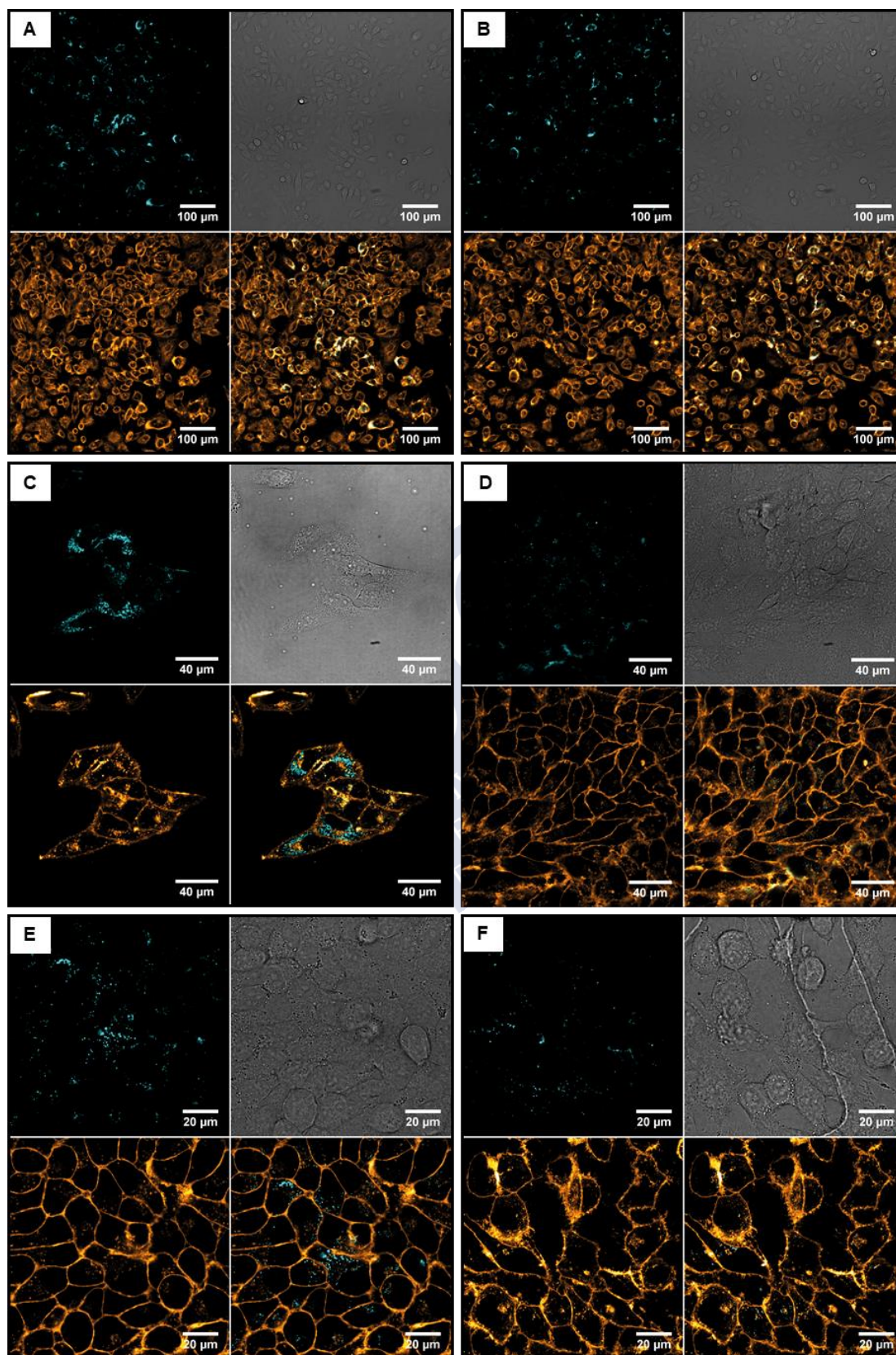


Figure 6.4. Collage of confocal microscopy images (top-left: blue channel; top-right: bright field; bottom-left: orange channel; bottom-right: merged blue + orange) at different magnifications (A,B: 20X; C,D: 60X; E,F: 100X) for the NC-HOE-PMA nanosystem (adapted with permission from ref. [245]). Copyright 2019, Wiley-VCH Verlag GmbH & Co. KGaA).

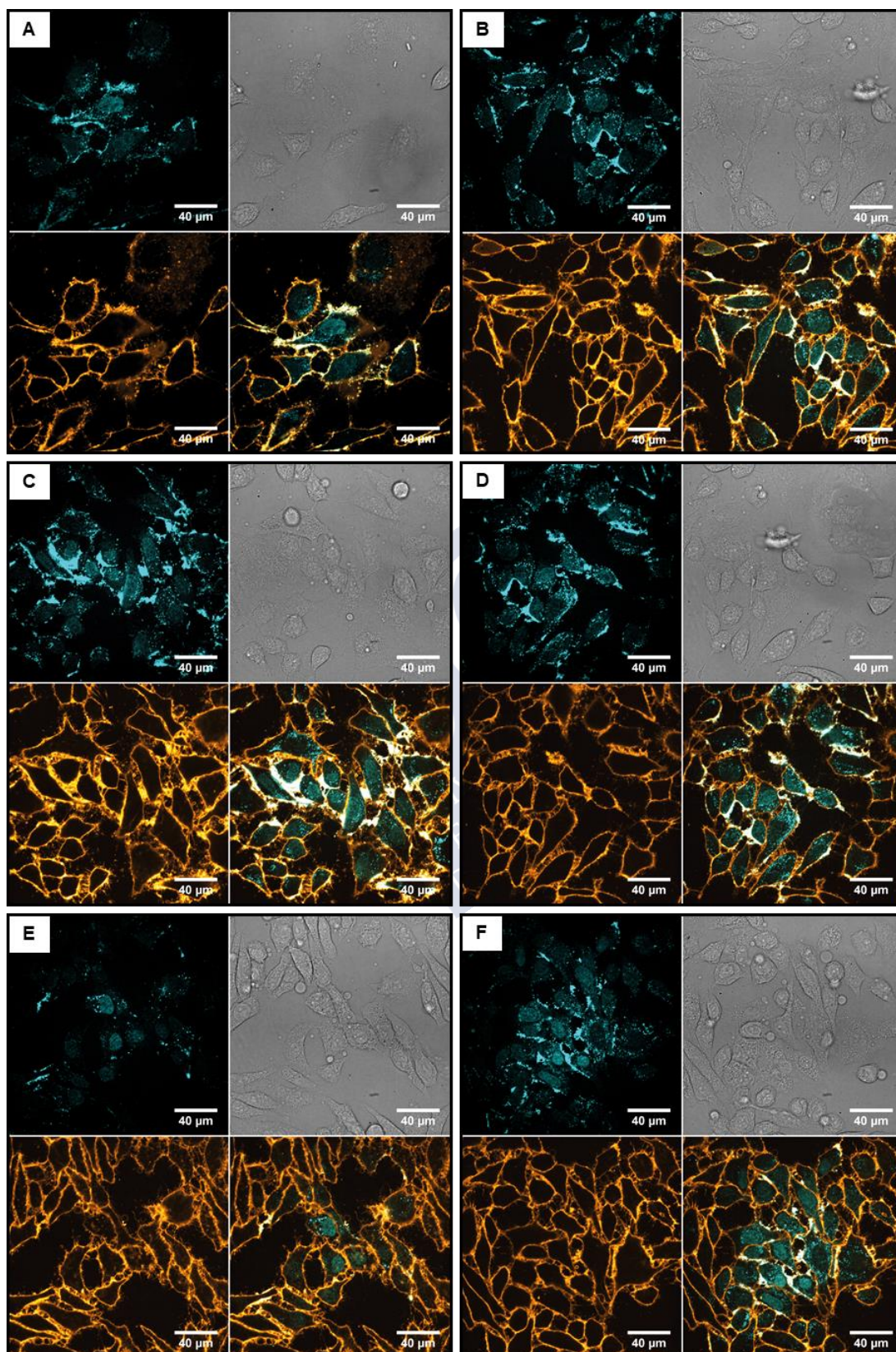


Figure 6.5. Collage of confocal microscopy images (top-left: blue channel; top-right: bright field; bottom-left: orange channel; bottom-right: merged blue + orange) at 60X magnification for the NC-HOE-PMA nanosystem after NIR treatment (adapted with permission from ref. [245]. Copyright 2019, Wiley-VCH Verlag GmbH & Co. KGaA).

6.2. Chapter 5 Appendix

6.2.1. In Vivo Studies

i) Materials and Methods

Swiss male mice (25 to 30 g, Harlan Laboratories, Barcelona, Spain) were maintained at controlled conditions of temperature ($22\text{ }^{\circ}\text{C} \pm 1^{\circ}\text{C}$) and humidity ($60\% \pm 5\%$) with a 12/12 h light/dark cycle for a week prior to surgery and up to 7 days after surgery. Mice had access to food and water ad libitum. Anesthesia was induced by the inhalation of 5 % sevoflurane in a nitrous oxide/oxygen mixture (70/30). Rectal temperature was monitored and maintained at $37\text{ }^{\circ}\text{C} \pm 0.5\text{ }^{\circ}\text{C}$ by using a feedback-controlled heating system. At the end of the procedures, mice were sacrificed under deep anesthesia (8 % sevoflurane). Experiments were conducted according to protocols approved by the local Animal Care Committee according to the European Union (EU) rules (86/609/CEE, 2003/65/CE, and 2010/63/EU).

Intravenous (*i.v.*) treatment administration was performed under anesthetic conditions, as follows: a 0.5 cm incision was made on the right paw; the femoral vein was exposed and cannulated with a 30-gauge needle for treatment administration. For arterial blood sampling, a catheter (polythene tube of 80 cm of length and 0.28 mm ID and 0.61 mm OD from Smiths) was introduced 0.3 mm (approx.) in the external common artery until the bifurcation of the carotid common artery. Group treated with rtPA and US, Doppler probe was applied on the abdominal region. For US application, an ultrasound gel (Transonic Gel®) was used. After blood sampling (40 min after treatments administration), the catheters were removed, and the animals were sacrificed for further ICP-MS organs (brain, heart, liver, lungs, spleen and kidneys) analysis. The organ preparation for ICP-MS and evaluation of the results were done following the methods reported by Talamini *et al.*^[323]

Five different treatments were tested in Swiss male mice ($n = 3$): 1) 200 μL of saline (used as vehicle control group), 2) 200 μL rtPA (1 mg/kg, bolus administration), 3) 200 μL rtPA (10 mg/g, 10 % bolus administration + 90 % infusion during 40 min), 4) 200 μL NCs@rtPA (1 mg/kg rtPA, bolus administration), and 5) 200 μL NCs@rtPA particles (1 mg/kg rtPA, bolus administration) combined with US (applied during 40 min). Intravenous (*i.v.*) treatment administration was performed through the right femoral vein, and the blood samples (150-200 μL) were obtained from the right common carotid artery in healthy animals. An independent group of 3 animals were used to evaluate the *in vivo* toxicity and potential brain lesion caused by NCs. For that aim, blood samples were obtained before NCs administration (basal levels) and 1, 3 and 7 days later. Toxicity was determined in blood samples using hepatic enzymes release (GOT and GPT) and renal enzymes (creatinine).

ii) Results and Discussions

• In Vivo Performance of the NC@rtPA Particles

Swiss mice (male, 25-30 g) were used as animal model to investigate the *in vivo* performance of the NC@rtPA particles for US-controlled release of rtPA. First, three standard toxicity markers were evaluated after *i.v.* administration of NC@rtPA particles (1 mg/kg rtPA dose, bolus, *approx.* 5.1 mg/kg Fe): glutamate oxaloacetate transaminase (GOT) and glutamate pyruvate transaminase (GPT) levels as hepatotoxicity markers, and creatinine levels as nephrotoxicity marker. These markers are widely used to assess toxicity after administration of nanomaterials in rodent models, being the liver and kidneys the most likely recipients of the nanoparticles after *i.v.* administration.^[324] Briefly, blood extractions (32 μ L) were carried out before (basal level) and after administration of the NC@rtPA particles (24 hours, 3 days and 7 days). In all cases, whole blood analysis showed normal enzymatic levels (*i.e.*, within limits of healthy animals; see *Figure 6.6* and *Table 6.1*).

Table 6.1. Hepatotoxicity and nephrotoxicity markers: GOT, GPT, and creatinine levels.

ID	GOT				GPT				Creatinine			
	Basal	24h	3 days	7 days	Basal	24h	3 days	7 days	Basal	24h	3 days	7 days
882	80.2	91.4	96.6	78.2	24.6	38.8	10	17.98	<0.5	<0.5	<0.5	<0.5
829	62.2	108.4	x	x	12.34	34.8	x	x	<0.5	<0.5	x	x
830	91.8	90	81.6	79	15.4	35.4	20.6	25.8	<0.5	<0.5	<0.5	<0.5
Average \pm s.d.	78 \pm 15	97 \pm 10	89 \pm 11	79 \pm 1	17 \pm 6	36 \pm 2	15 \pm 8	22 \pm 6	x	x	x	x

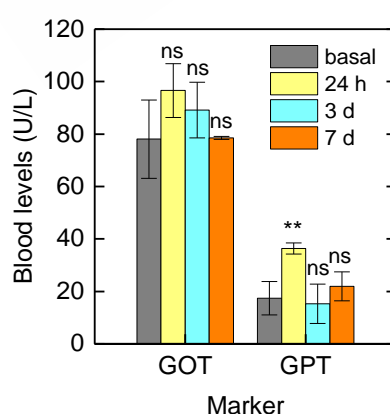


Figure 6.6. GOT and GPT levels in mice. In all data statistical significance was assessed by the *t*-test; each sample was compared with the corresponding basal level (ns, not significant; **P* < 0.05; ***P* < 0.01) (adapted with permission from ref. [301]. Copyright 2019, Elsevier B.V.).

- **In Vivo Fate (Biodistribution)**

The *in vivo* fate (biodistribution) of the NCs was investigated by MRI and ICP-MS. NCs contained a layer of NPs (*approx.* 0.15 pg Fe/NC, *approx.* 128 µg Fe per mouse) were used for contrast purposes. Although these may be clearly detected at a very low dose of NCs (2 µL of NCs, 4.2×10^7 NC/mL, *approx.* 13 ng Fe) after intracerebral injection by MRI, no MRI contrast differences were found among treated (*i.v.* NC@rtPA, 1 mg rtPA/kg mouse) or non-treated (saline) animals.

ICP-MS

Animals ($n = 3$) were euthanized *approx.* 1 h after the administration (in the presence and absence of US-application) of the NC@rtPA particles (or non-encapsulated rtPA), and brain, liver, spleen, lungs, heart and kidneys were extracted to study the biodistribution (*i.e.*, Fe content in selected organs) of the NCs by ICP-MS. A significant increased Fe concentration was found neither in brain, heart, liver, spleen nor kidneys. In contrast, the Fe concentration in the lungs of animals treated with NC@rtPA particles plus US was slightly higher than in control animals (see *Figure 6.7a*). Equivalent inductively coupled plasma mass spectrometry (ICP-MS) biodistribution studies in animals euthanized 7 days after NCs administration were done, showing no difference in Fe concentration in selected organs with respect to control animals treated with saline (see *Figure 6.7b*).

MRI Studies

MRI studies were conducted on a 9.4 T horizontal bore magnet (BrukerBioSpin, Ettlingen, Germany) with 12 cm wide actively shielded gradient coils (440 mT/m). Radiofrequency (RF) transmission was achieved with a birdcage volume resonator; signal was detected using a two-element arrayed surface coil (RAPID Biomedical, Germany), positioned over the head of the animal, which was fixed with a teeth bar, earplugs and adhesive tape. Respiratory frequency and body temperature were monitored throughout the experiment. Transmission and reception coils were actively decoupled from each other. Gradient-echo pilot scans were performed at the beginning of each imaging session for accurate positioning of the animal inside the magnet bore. T2-weighted images were acquired using a multi-slice multi-echo (MSME) sequence with a 11 ms echo time (TE), 2.8 s repetition time (TR), 12 echoes with 11 ms echo spacing, flip angle (FA) of 180°, 2 averages, 50 KHz spectral bandwidth (SW), 16 slices of 0.5 mm, 19.2×19.2 mm² field of view (FOV) with saturation bands to suppress signal outside this FOV, a matrix size of 256×256 (isotropic in-plane resolution of 75 µm/pixel \times 75 µm/pixel) and implemented without fat suppression option.

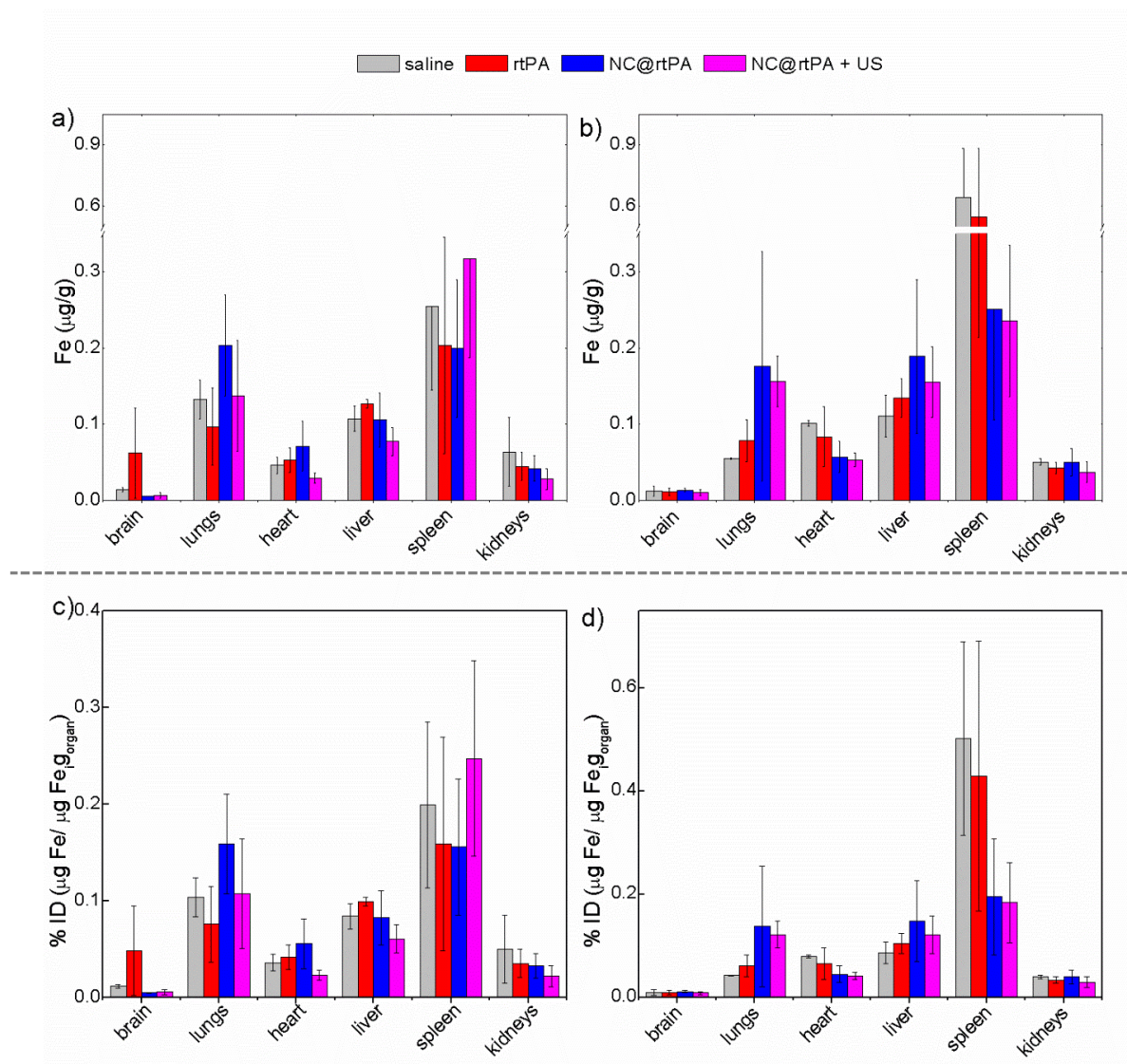


Figure 6.7. ICP-MS NCs Fe organ biodistribution in a) animals sacrificed 40 min after treatments or b) animals sacrificed 7 d after the treatments. ICP-MS data expressed as percentage of the injected dose (%ID) per organ in c) animals sacrificed 40 min after treatments or d) animals sacrificed 7 d after the treatments. Please, note that in c) and d) even for the animals not treated with Fe-containing samples data has been corrected considering the injected Fe (Fe_i) dose (128 μ g) in order to show the endogenous Fe content. All data represent mean \pm s.d. (three independent measurements). In all data statistical significance was assessed by the *t*-test, each sample was compared with the corresponding saline control (ns, not significant; **P* < 0.05; ***P* < 0.01) (adapted with permission from ref. [301]. Copyright 2019, Elsevier B.V.).

The acquisition time was 23 min. T2*-weighted images were acquired using a multi-gradient-echo sequence (MGE) with a 5 ms echo time (TE), 1.2 s repetition time (TR), 8 echoes with 4.5 ms echo spacing, 100 KHz spectral bandwidth, flip angle (FA) of 20°, 16 slices of 0.55 mm, 2 averages, 19.2 \times 19.2 mm² field of view (FOV) with saturation bands to suppress signal outside this FOV, a matrix size of 256 \times 256 (isotropic in-plane resolution of 75 μ m/pixel \times 75 μ m/pixel) and implemented with fat suppression option. The acquisition time was 10 min. MRI post-processing was performed using ImageJ software (W. Rasband, NIH, USA) on independent workstation.

Therefore, in order to prove the MRI imaging capabilities of the NCs, a direct NCs intraparenchymal injection was performed. For intraparenchymal injection, mice were placed in a stereotaxic frame (Stoelting Co., Wood Dale, IL, USA) under sevoflurane anesthesia. A 1-cm-long midline incision was made in the scalp. Two small cranial burr holes were drilled through the skull, one on the right hemisphere and other one on the left, for the subsequently injection of the NCs@rtPA and saline, respectively. A Hamilton syringe (Hamilton, Reno, NV, USA; 10 μ L) was filled with 3.0 μ L of NCs@rtPA or vehicle (saline). The syringe was mounted onto the injection pump and the needle was slowly inserted into the brain to a depth of 3.25 mm below the surface of the skull. A volume of 2.0 μ L of NCs or vehicle was injected at a rate of 0.5 μ L/min over 4 min. The needle was left in place for 5 minutes and then removed slowly at a rate of 1 mm/min. The burr hole was filled with bone wax (Ethicon, Somerville, NJ, USA), and the scalp incision was closed and moved to the MRI for brain scan.

MRI scan was performed at 1, 3 and 7 days after the i.v. administration, however, no relevant accumulation in brain was observed (see *Figure 6.8*). Therefore, to test the NCs@rtPA contrast in brain organ, NCs@rtPA (2 μ L of NCs, 4.2×10^7 NC/mL, approx. 13 ng Fe) were injected intraparenchymally in the cerebral tissue of healthy animals (n=3) and later scanned by MRI (see *Figure 6.9*). Statistical significance was assayed by assessed by two-way analysis of variance followed by Dunnett's multiple comparisons test using GraphPad Prism 6.

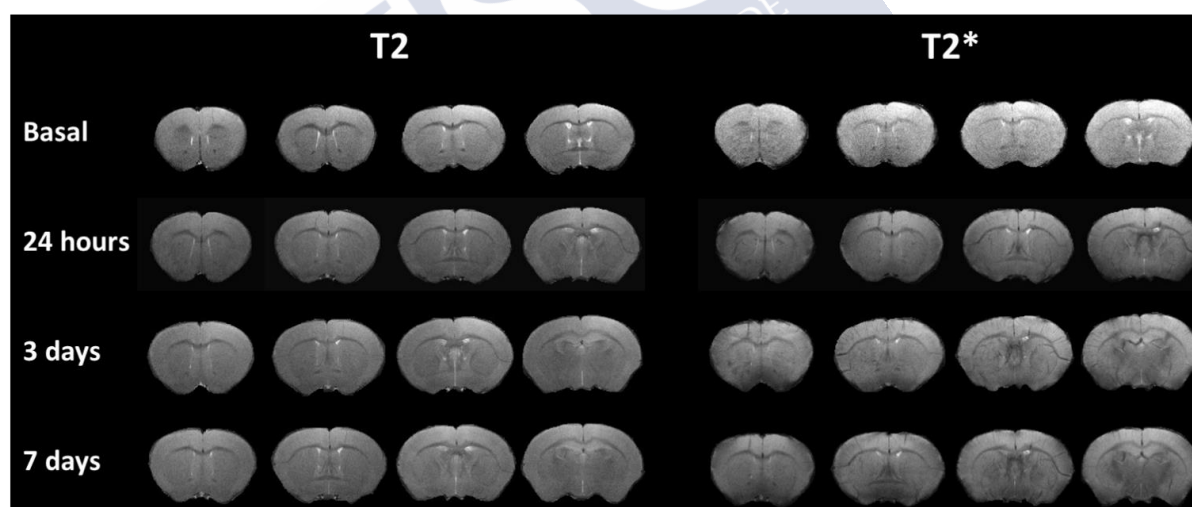


Figure 6.8. MRI image of a mouse's brain after NCs@rtPA i.v. injection at different times, left panel shows T2 MRI signal and right panel, T2* signal (adapted with permission from ref. [301]. Copyright 2019, Elsevier B.V.).

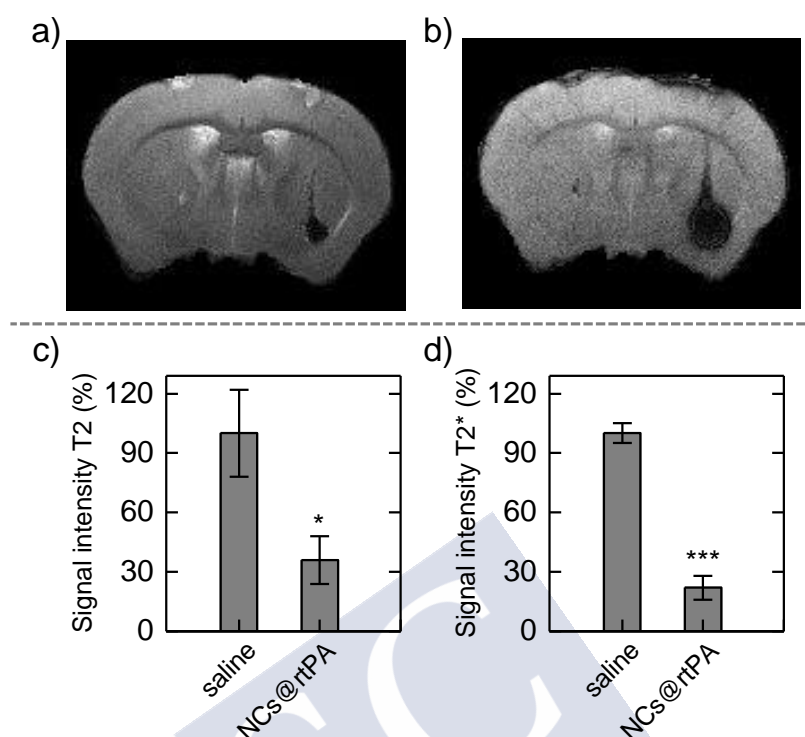


Figure 6.9. MRI image of a mouse brain after NCs@rtPA and saline intraparenchymal injection. a,c) The MRI signal in T2 decreased 65.87 % in the right hemisphere, where the NCs@rtPA particles had been injected, in comparison with the left hemisphere, where the control (saline) was injected. b, d) In T2* the NCs MRI signal decreased 79.33 % compared with control signal. In all data statistical significance was assessed by the *t*-test, each sample was compared with the corresponding saline control (**P* < 0.05; ****P* < 0.001) (adapted with permission from ref. [301]. Copyright 2019, Elsevier B.V.).

• Ultrasound-triggered *in vivo* delivery of rtPA

The enzymatic activity of *in vivo* US-released rtPA was quantified with the SensoLyte assay in freshly extracted plasma samples. For comparison between US-released (from NC@rtPA) and non-encapsulated rtPA, *i.v.* administration of free rtPA was used: 1 mg/kg dose (*approx.* 25-30 µg rtPA per mouse), as commonly used in clinical practice for treatment of acute ischemic stroke (0.9-1 mg/kg, maximum 90-100 mg rtPA, see prescribing information of Alteplase). NC@rtPA particles or non-encapsulated rtPA were administrated as *i.v.* bolus (0.2 mL) in less than 1 min. Additionally, a higher dose (10 mg/kg, *approx.* 250-300 µg rtPA per mouse) of non-encapsulated rtPA was administrated: initial 1 mg/kg (10 %) dose as *i.v.* bolus in less than 1 min, followed by a 9 mg/kg (90 %) dose as *i.v.* continuous infusion over 40 min. The latter bolus + infusion administration protocol is commonly used in preclinical mouse models (10 mg/kg) and as thrombolytic treatment in the clinic (0.9-1 mg/kg, 10 % bolus + 90 % infusion over 2 h, as described in the prescribing information of Alteplase). In preclinical mouse models, the 10-fold rtPA dose is motivated by the characteristics of the fibrinolytic

system in rodents, which is known to be about 10 times less sensitive to rtPA than in humans.^[325, 326] In all cases, 0.2 mL of sample were injected (bolus or bolus + infusion) in the femoral vein. Blood extractions were done through a canula inserted in the carotid artery. Blood samples were taken prior to administering the treatments (basal) and 5, 20 and 40 minutes after the administration. US were continuously applied (40 min) in the abdominal region (see *Figure 6.10a*).

In the case of non-encapsulated rtPA (1 or 10 mg/kg), as expected, rtPA activity rapidly decreases due to the low half-life of rtPA (*approx.* 5 min). Such decay is less pronounced after the 10 mg/kg administration (*i.e.*, 10 % bolus + 90 % infusion over 40 min). After 40 min of administration of non-encapsulated rtPA, its activity is in either case no significant compared to basal levels. In the case of NC@rtPA particles (1 mg/kg), rtPA activity is in the order of the non-encapsulated rtPA (1 mg/kg), which may be due to some rtPA leakage *in vivo*. After 40 min, rtPA activity in the NC@rtPA group dropped to basal levels. In the case of US-application (40 min) after administration of NC@rtPA (1 mg/kg), a completely new trend arose: rtPA activity increased over time, reaching about 7-fold with respect to basal levels after 40 min. This result is particularly important as it demonstrates that the half-life of rtPA can be greatly enhanced by encapsulation in our sonosensitive NCs (see *Figures 6.10b-c*).



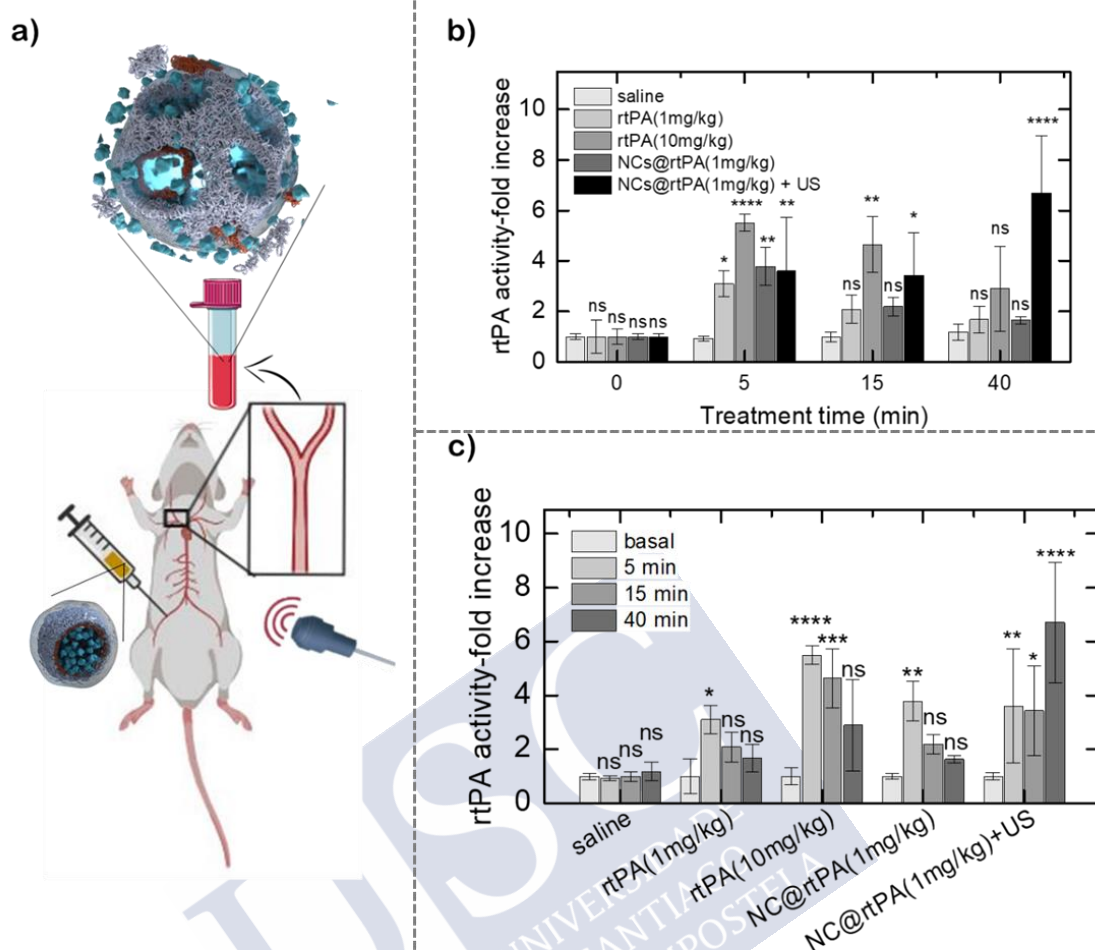


Figure 6.10. a) *In vivo* scheme to evaluate the rtPA encapsulation and the US drug release. Treatments were administered through the femoral vein, and blood samples were further obtained from the carotid artery. This approach allowed to analyze the *in vivo* stability of the rtPA-encapsulation and to evaluate the US-induced drug release. b, c) Blood rtPA activity was determined in the 5 groups tested ($n = 3$), before treatment administration (blood rtPA basal levels), and 5, 15 and 40 min later. All data represent mean \pm s.d. Statistical significance was assessed by two-way analysis of variance followed by Dunnett's multiple comparisons test. In b), each treatment time (5, 15 or 40 min) was compared with rtPA levels in the saline group; in c) each treatment was compared with the corresponding rtPA basal levels (ns, not significant; * $P < 0.05$; ** $P < 0.01$; *** $P < 0.001$; **** $P < 0.0001$) (adapted with permission from ref. [301]. Copyright 2019, Elsevier B.V.).





Chapter 7

7. General Conclusions

This chapter presents the main conclusions arising from this Ph.D. thesis. The overall aim of this thesis was to highlight the controlled synthesis and functionalization of two specific porous materials based on calcium carbonate polymeric nanoparticles (CCPNs) and porous coordination polymers (PCPs) at the nanoscale level, mainly for its use in biological applications.

Although previous works have been proposed different methodologies for the fabrication of CCPNs and PCPs, our research documented straightforward methods that allow controlling the morphology and functionalization of the particles (i.e., CCPN, ZIF-8, and Cu-based CP) at the nanoscale with high monodispersity, and potential applications in biomedicine and catalysis.

The protocols in Chapters 3, 4 and 5 gave rise to nanoparticles of adequate morphology and size for each study. The first project entitled “Copper Based Coordination Polymer Nanoparticles for Catalytic Reduction: Methylene Blue into Leucomethylene Blue” in Chapter 3 showed the preparation of a novel porous coordination polymer nanoparticles composed of Cu^{2+} and imidazolate with different shapes. The addition of CTAB, the reaction time, and the effect of the solvent during the synthesis determines the size, morphology, and structure of the highly monodisperse nanospheres. These nanospheres (NP1) evolve into larger nanosheets (NP2) if the reaction time is 72 hours or even longer which have similar porosity, crystalline structure, and good activity towards catalysis in the reduction of methylene blue. The presence of water on the nanospheres leads to a change in morphology, starting with the formation of nanofibers, which evolve into nanospikes (NP3) which have low-porosity and a kinetic constant value like the control.

The second project entitled “Gold Nanostars@Zeolitic Imidazolate Framework 8 Core-Shell Nanostructures for Light Triggered Release: in Vitro” in Chapter 4 demonstrated the development of a ZIF-8-nanomaterial with combined thermoplasmonic and high drug-loading capabilities that is stable in aqueous solution and when stored in cells. The ZIF-8 particles comprise a core of gold nanostars (NSs). The stability of the particles in aqueous medium was achieved by coating them with the amphiphilic polymer PMA (poly-[isobutylene-alt-maleic anhydride]-graft-dodecyl). The ZIF-8-based nanomaterial was produced with very high monodispersity and precise shape using the surfactant CTAB (hexadecyltrimethylammonium bromide). The obtained monodisperse ZIF-8-based nanomaterial released its cargo upon illumination with near-IR (NIR) light in aqueous solution and inside living cells.

The third project entitled “ CaCO_3 Sub-Micrometric Capsules for Ultrasound Triggered Release: in Vitro and in Vivo” in Chapter 5 demonstrated demonstrated the successful incorporation of delicate biomolecules such as rtPA (recombinant tissue plasminogen activator) into monodisperse CaCO_3 sub-micrometric polymer capsules via layer-by-layer technique. The addition of PVSA [poly(vinylsulfonic acid)] in the course of the CaCO_3 nanoparticle synthesis was found to lower the nucleation rate, stabilize the surface, and also serve as size modulator. The capsules were approximately 600nm in size, where rtPA retains its enzymatic activity while

trapped. We were able to optimize the NC's shell thickness, allowing us the ultrasound-induced release of fully functional rtPA in vitro and in vivo in mice, while at the same time preventing leakage. The proposed research strategy presented in this study significantly extended the half-life and activity of rtPA in mice compared to non-encapsulated rtPA. Therefore, the results obtained indicate that this strategy could be applied in a straightforward way for preparing thin films of various molecules such as polymers, nanoparticles, etc. as well to incorporate different kinds of drugs or combination of drugs.





References

1. Sharma, S., et al., *Copper-Gallic Acid Nanoscale Metal–Organic Framework for Combined Drug Delivery and Photodynamic Therapy*. ACS Applied Bio Materials, 2019. **2**(5): p. 2092-2101.
2. Thanh, N.T.K., N. Maclean, and S. Mahiddine, *Mechanisms of Nucleation and Growth of Nanoparticles in Solution*. Chemical Reviews, 2014. **114**(15): p. 7610-7630.
3. Awan, I.Z., et al., *Wondrous Nanotechnology*. Journal of the Chemical Society of Pakistan, 2016. **38**(6): p. 1026-1055.
4. Griffin, S., et al., *Natural Nanoparticles: A Particular Matter Inspired by Nature*. Antioxidants (Basel, Switzerland), 2017. **7**(1): p. 3.
5. Jeevanandam, J., et al., *Review on nanoparticles and nanostructured materials: history, sources, toxicity and regulations*. Beilstein journal of nanotechnology, 2018. **9**: p. 1050-1074.
6. Wagner, S., et al., *Spot the Difference: Engineered and Natural Nanoparticles in the Environment—Release, Behavior, and Fate*. Angewandte Chemie International Edition, 2014. **53**(46): p. 12398-12419.
7. Gleiter, H., *Nanostructured materials: basic concepts and microstructure*. Acta Materialia, 2000. **48**(1): p. 1-29.
8. Pokropivny, V.V. and V.V. Skorokhod, *Classification of nanostructures by dimensionality and concept of surface forms engineering in nanomaterial science*. Materials Science and Engineering: C, 2007. **27**(5): p. 990-993.
9. Tiwari, J.N., R.N. Tiwari, and K.S. Kim, *Zero-dimensional, one-dimensional, two-dimensional and three-dimensional nanostructured materials for advanced electrochemical energy devices*. Progress in Materials Science, 2012. **57**(4): p. 724-803.
10. Abbasi, A.R., K. Akhbari, and A. Morsali, *Dense coating of surface mounted CuBTC Metal–Organic Framework nanostructures on silk fibers, prepared by layer-by-layer method under ultrasound irradiation with antibacterial activity*. Ultrasonics Sonochemistry, 2012. **19**(4): p. 846-852.
11. Khan, I., K. Saeed, and I. Khan, *Nanoparticles: Properties, applications and toxicities*. Arabian Journal of Chemistry, 2019. **12**(7): p. 908-931.
12. Wang, Y. and Y. Xia, *Bottom-Up and Top-Down Approaches to the Synthesis of Monodispersed Spherical Colloids of Low Melting-Point Metals*. Nano Letters, 2004. **4**(10): p. 2047-2050.
13. Sperling, R.A. and W.J. Parak, *Surface modification, functionalization and bioconjugation of colloidal inorganic nanoparticles*. Philosophical Transactions of the Royal Society A: Mathematical, Physical and Engineering Sciences, 2010. **368**(1915): p. 1333-1383.
14. Polte, J., *Fundamental growth principles of colloidal metal nanoparticles – a new perspective*. CrystEngComm, 2015. **17**(36): p. 6809-6830.

15. Sugimoto, T., *CHAPTER 8 - CONTROL OF PARTICLE CHARACTERISTICS*, in *Monodispersed Particles*, T. Sugimoto, Editor. 2001, Elsevier: Amsterdam. p. 368-452.
16. Mosnáčková, K., et al., *1 - Synthesis Routes of Functionalized Nanoparticles*, in *Polymer Composites with Functionalized Nanoparticles*, K. Pielichowski and T.M. Majka, Editors. 2019, Elsevier. p. 1-46.
17. Hühn, J., et al., *Selected Standard Protocols for the Synthesis, Phase Transfer, and Characterization of Inorganic Colloidal Nanoparticles*. Chemistry of Materials, 2017. **29**(1): p. 399-461.
18. Lin, C.-A.J., et al., *Design of an Amphiphilic Polymer for Nanoparticle Coating and Functionalization*. Small, 2008. **4**(3): p. 334-341.
19. Iler, R.K., *Multilayers of colloidal particles*. Journal of Colloid and Interface Science, 1966. **21**(6): p. 569-594.
20. Decher, G., J.D. Hong, and J. Schmitt, *Buildup of ultrathin multilayer films by a self-assembly process: III. Consecutively alternating adsorption of anionic and cationic polyelectrolytes on charged surfaces*. Thin Solid Films, 1992. **210-211**: p. 831-835.
21. Decher, G., *Fuzzy Nanoassemblies: Toward Layered Polymeric Multicomposites*. Science, 1997. **277**(5330): p. 1232-1237.
22. De Cock, L.J., et al., *Polymeric Multilayer Capsules in Drug Delivery*. Angewandte Chemie International Edition, 2010. **49**(39): p. 6954-6973.
23. Larrañaga, A., et al., *Polymer capsules as micro-/nanoreactors for therapeutic applications: Current strategies to control membrane permeability*. Progress in Materials Science, 2017. **90**: p. 325-357.
24. Yan, Y., et al., *Toward Therapeutic Delivery with Layer-by-Layer Engineered Particles*. ACS Nano, 2011. **5**(6): p. 4252-4257.
25. Yan, Y., M. Björnmalm, and F. Caruso, *Assembly of Layer-by-Layer Particles and Their Interactions with Biological Systems*. Chemistry of Materials, 2014. **26**(1): p. 452-460.
26. Wang, Y., A.S. Angelatos, and F. Caruso, *Template Synthesis of Nanostructured Materials via Layer-by-Layer Assembly*. Chemistry of Materials, 2008. **20**(3): p. 848-858.
27. Trofimov, A.D., et al., *Porous inorganic carriers based on silica, calcium carbonate and calcium phosphate for controlled/modulated drug delivery: Fresh outlook and future perspectives*. Pharmaceutics, 2018. **10**(4): p. 1.-35.
28. Xiao, F.-X., et al., *Layer-by-layer assembly of versatile nanoarchitectures with diverse dimensionality: a new perspective for rational construction of multilayer assemblies*. Chemical Society Reviews, 2016. **45**(11): p. 3088-3121.
29. Marchenko, I., et al., *Controlled enzyme-catalyzed degradation of polymeric capsules templated on CaCO₃: Influence of the number of LbL layers, conditions of degradation, and disassembly of multicompartments*. Journal of Controlled Release, 2012. **162**(3): p. 599-605.
30. Novoselova, M.V., et al., *Biodegradable Polymeric Multilayer Capsules for Therapy of Lung Cancer*. ACS Applied Materials & Interfaces, 2020. **12**(5): p. 5610-5623.

31. De Temmerman, M.-L., et al., *Encapsulation Performance of Layer-by-Layer Microcapsules for Proteins*. Biomacromolecules, 2011. **12**(4): p. 1283-1289.
32. Biswas, A., A.T. Nagaraja, and M.J. McShane, *Fabrication of Nanocapsule Carriers from Multilayer-Coated Vaterite Calcium Carbonate Nanoparticles*. ACS Applied Materials & Interfaces, 2014. **6**(23): p. 21193-21201.
33. Donath, E., et al., *Novel Hollow Polymer Shells by Colloid-Templated Assembly of Polyelectrolytes*. Angewandte Chemie International Edition, 1998. **37**(16): p. 2201-2205.
34. Kantak, C., et al., *A 'microfluidic pinball' for on-chip generation of Layer-by-Layer polyelectrolyte microcapsules*. Lab on a Chip, 2011. **11**(6): p. 1030-1035.
35. Richardson, J.J., et al., *Preparation of Nano- and Microcapsules by Electrophoretic Polymer Assembly*. Angewandte Chemie International Edition, 2013. **52**(25): p. 6455-6458.
36. Mourdikoudis, S., R.M. Pallares, and N.T.K. Thanh, *Characterization techniques for nanoparticles: comparison and complementarity upon studying nanoparticle properties*. Nanoscale, 2018. **10**(27): p. 12871-12934.
37. Copéret, C., et al., *Homogeneous and Heterogeneous Catalysis: Bridging the Gap through Surface Organometallic Chemistry*. Angewandte Chemie International Edition, 2003. **42**(2): p. 156-181.
38. Zhang, Y., et al., *Synthesis of a molecularly defined single-active site heterogeneous catalyst for selective oxidation of N-heterocycles*. Nature Communications, 2018. **9**(1): p. 1465.
39. *Concepts in Nanocatalysis*, in *Nanomaterials in Catalysis*. p. 1-54.
40. Astruc, D., F. Lu, and J.R. Aranzas, *Nanoparticles as Recyclable Catalysts: The Frontier between Homogeneous and Heterogeneous Catalysis*. Angewandte Chemie International Edition, 2005. **44**(48): p. 7852-7872.
41. Navalón, S. and H. García, *Nanoparticles for Catalysis*. Nanomaterials (Basel, Switzerland), 2016. **6**(7): p. 123.
42. Lane, L.A., et al., *Physical Chemistry of Nanomedicine: Understanding the Complex Behaviors of Nanoparticles in Vivo*. Annual Review of Physical Chemistry, 2015. **66**(1): p. 521-547.
43. Albanese, A., P.S. Tang, and W.C.W. Chan, *The Effect of Nanoparticle Size, Shape, and Surface Chemistry on Biological Systems*. Annual Review of Biomedical Engineering, 2012. **14**(1): p. 1-16.
44. Sun, T., et al., *Engineered Nanoparticles for Drug Delivery in Cancer Therapy*. Angewandte Chemie International Edition, 2014. **53**(46): p. 12320-12364.
45. Martínez, R., et al., *Chapter 2 - Nanoparticle behavior and stability in biological environments*, in *Nanoparticles for Biomedical Applications*, E.J. Chung, L. Leon, and C. Rinaldi, Editors. 2020, Elsevier. p. 5-18.
46. Sahay, G., D.Y. Alakhova, and A.V. Kabanov, *Endocytosis of nanomedicines*. J Control Release, 2010. **145**(3): p. 182-95.

47. Blanco, E., H. Shen, and M. Ferrari, *Principles of nanoparticle design for overcoming biological barriers to drug delivery*. Nature biotechnology, 2015. **33**(9): p. 941-951.
48. Zhao, J. and M.H. Stenzel, *Entry of nanoparticles into cells: the importance of nanoparticle properties*. Polymer Chemistry, 2018. **9**(3): p. 259-272.
49. Oh, N. and J.-H. Park, *Endocytosis and exocytosis of nanoparticles in mammalian cells*. International journal of nanomedicine, 2014. **9 Suppl 1**(Suppl 1): p. 51-63.
50. Wang, Z., et al., *Size and dynamics of caveolae studied using nanoparticles in living endothelial cells*. ACS Nano, 2009. **3**(12): p. 4110-6.
51. Rothen-Rutishauser, B., J. Bourquin, and A. Fink, *Nanoparticle-Cell Interactions: Overview of Uptake, Intracellular Fate and Induction of Cell Responses*. 2019. p. 153-170.
52. Septiadi, D., et al., *Nanoparticle–Cell Interaction: A Cell Mechanics Perspective*. Advanced Materials, 2018. **30**(19): p. 1704463.
53. Fletcher, D.A. and R.D. Mullins, *Cell mechanics and the cytoskeleton*. Nature, 2010. **463**(7280): p. 485-492.
54. Caracciolo, G., O.C. Farokhzad, and M. Mahmoudi, *Biological Identity of Nanoparticles In Vivo: Clinical Implications of the Protein Corona*. Trends in Biotechnology, 2017. **35**(3): p. 257-264.
55. Polyak, B. and B. Cordovez, *How can we predict behavior of nanoparticles in vivo?* Nanomedicine, 2016. **11**(3): p. 189-192.
56. Soo Choi, H., et al., *Renal clearance of quantum dots*. Nature Biotechnology, 2007. **25**(10): p. 1165-1170.
57. Kumari, A., S.K. Yadav, and S.C. Yadav, *Biodegradable polymeric nanoparticles based drug delivery systems*. Colloids and Surfaces B: Biointerfaces, 2010. **75**(1): p. 1-18.
58. Docter, D., et al., *The nanoparticle biomolecule corona: lessons learned – challenge accepted?* Chemical Society Reviews, 2015. **44**(17): p. 6094-6121.
59. Moussa, H., A. Martins, and G. Hussein, *Review on Triggered Liposomal Drug Delivery with a Focus on Ultrasound*. Current cancer drug targets, 2015. **15**.
60. Wang, Y. and D.S. Kohane, *External triggering and triggered targeting strategies for drug delivery*. Nature Reviews Materials, 2017. **2**(6): p. 17020.
61. Liang, K., et al., *Endocytic pH-Triggered Degradation of Nanoengineered Multilayer Capsules*. Advanced Materials, 2014. **26**(12): p. 1901-1905.
62. Shutava, T., et al., *pH Responsive Decomposable Layer-by-Layer Nanofilms and Capsules on the Basis of Tannic Acid*. Macromolecules, 2005. **38**(7): p. 2850-2858.
63. Wang, Z., et al., *Near-infrared light-induced dissociation of zeolitic imidazole framework-8 (ZIF-8) with encapsulated CuS nanoparticles and their application as a therapeutic nanoplatfrom*. Chemical Communications, 2016. **52**(82): p. 12210-12213.
64. Muñoz Javier, A., et al., *Photoactivated Release of Cargo from the Cavity of Polyelectrolyte Capsules to the Cytosol of Cells*. Langmuir, 2008. **24**(21): p. 12517-12520.

65. Delcea, M., H. Möhwald, and A.G. Skirtach, *Stimuli-responsive LbL capsules and nanoshells for drug delivery*. Advanced Drug Delivery Reviews, 2011. **63**(9): p. 730-747.
66. Polo, E., et al., *Colloidal bioplasmonics*. Nano Today, 2018. **20**: p. 58-73.
67. Liz-Marzán, L.M., *Tailoring Surface Plasmons through the Morphology and Assembly of Metal Nanoparticles*. Langmuir, 2006. **22**(1): p. 32-41.
68. Koppens, F.H.L., D.E. Chang, and F.J. García de Abajo, *Graphene Plasmonics: A Platform for Strong Light–Matter Interactions*. Nano Letters, 2011. **11**(8): p. 3370-3377.
69. Comin, A. and L. Manna, *New materials for tunable plasmonic colloidal nanocrystals*. Chemical Society Reviews, 2014. **43**(11): p. 3957-3975.
70. Lindquist, N.C., et al., *Engineering metallic nanostructures for plasmonics and nanophotonics*. Rep Prog Phys, 2012. **75**(3): p. 036501.
71. Stockman, M.I., *Nanoplasmonics: past, present, and glimpse into future*. Optics Express, 2011. **19**(22): p. 22029-22106.
72. Jain, P.K., et al., *Calculated Absorption and Scattering Properties of Gold Nanoparticles of Different Size, Shape, and Composition: Applications in Biological Imaging and Biomedicine*. The Journal of Physical Chemistry B, 2006. **110**(14): p. 7238-7248.
73. Jain, P.K., et al., *Noble Metals on the Nanoscale: Optical and Photothermal Properties and Some Applications in Imaging, Sensing, Biology, and Medicine*. Accounts of Chemical Research, 2008. **41**(12): p. 1578-1586.
74. Bruzzone, S., et al., *Comparative study of near and far field e.m. scattering response by Au/Ag alloy and core-shell nanoparticles*. Materials Science and Engineering: C, 2007. **27**(5): p. 1015-1021.
75. Schuller, J.A., et al., *Plasmonics for extreme light concentration and manipulation*. Nat Mater, 2010. **9**(3): p. 193-204.
76. Anker, J.N., et al., *Biosensing with plasmonic nanosensors*. Nat Mater, 2008. **7**(6): p. 442-453.
77. Perez-Hernandez, M., et al., *Dissecting the Molecular Mechanism of Apoptosis during Photothermal Therapy Using Gold Nanoprisms*. ACS Nano, 2015. **9**(1): p. 52-61.
78. Bao, C., et al., *Gold Nanoprisms as Optoacoustic Signal Nanoamplifiers for In Vivo Bioimaging of Gastrointestinal Cancers*. Small, 2013. **9**(1): p. 68-74.
79. Wang, H., et al., *In vitro and in vivo two-photon luminescence imaging of single gold nanorods*. Proceedings of the National Academy of Sciences of the United States of America, 2005. **102**(44): p. 15752-15756.
80. Ferry, V.E., J.N. Munday, and H.A. Atwater, *Design Considerations for Plasmonic Photovoltaics*. Advanced Materials, 2010. **22**(43): p. 4794-4808.
81. Kievit, F.M., et al., *Targeting of Primary Breast Cancers and Metastases in a Transgenic Mouse Model Using Rationally Designed Multifunctional SPIONs*. ACS Nano, 2012. **6**(3): p. 2591-2601.

82. Storhoff, J.J., et al., *One-Pot Colorimetric Differentiation of Polynucleotides with Single Base Imperfections Using Gold Nanoparticle Probes*. Journal of the American Chemical Society, 1998. **120**(9): p. 1959-1964.
83. Elghanian, R., et al., *Selective Colorimetric Detection of Polynucleotides Based on the Distance-Dependent Optical Properties of Gold Nanoparticles*. Science, 1997. **277**(5329): p. 1078-1081.
84. Bao, C., et al., *A promising road with challenges: where are gold nanoparticles in translational research?* Nanomedicine, 2014. **9**(15): p. 2353-2370.
85. Álvarez-Puebla, R.A., *Effects of the Excitation Wavelength on the SERS Spectrum*. The Journal of Physical Chemistry Letters, 2012. **3**(7): p. 857-866.
86. Ren, B., et al., *Surface-Enhanced Raman Scattering in the Ultraviolet Spectral Region: UV-SERS on Rhodium and Ruthenium Electrodes*. Journal of the American Chemical Society, 2003. **125**(32): p. 9598-9599.
87. Ross, M.B. and G.C. Schatz, *Aluminum and Indium Plasmonic Nanoantennas in the Ultraviolet*. The Journal of Physical Chemistry C, 2014. **118**(23): p. 12506-12514.
88. Townsend, E. and G.W. Bryant, *Plasmonic Properties of Metallic Nanoparticles: The Effects of Size Quantization*. Nano Letters, 2012. **12**(1): p. 429-434.
89. Njoki, P.N., et al., *Size Correlation of Optical and Spectroscopic Properties for Gold Nanoparticles*. The Journal of Physical Chemistry C, 2007. **111**(40): p. 14664-14669.
90. Myroshnychenko, V., et al., *Modelling the optical response of gold nanoparticles*. Chemical Society Reviews, 2008. **37**(9): p. 1792-1805.
91. Alvarez-Puebla, R., L.M. Liz-Marzán, and F.J. García de Abajo, *Light Concentration at the Nanometer Scale*. The Journal of Physical Chemistry Letters, 2010. **1**(16): p. 2428-2434.
92. Fang, Q., et al., *5.01 - Porous Metal–Organic Frameworks*, in *Comprehensive Nanoscience and Technology*, D.L. Andrews, G.D. Scholes, and G.P. Wiederrecht, Editors. 2011, Academic Press: Amsterdam. p. 1-20.
93. Kitagawa, S., R. Kitaura, and S.-i. Noro, *Functional Porous Coordination Polymers*. Angewandte Chemie International Edition, 2004. **43**(18): p. 2334-2375.
94. Sher, P., et al., *Low density porous carrier: Drug adsorption and release study by response surface methodology using different solvents*. International Journal of Pharmaceutics, 2007. **331**(1): p. 72-83.
95. Thommes, M., et al., *Physisorption of gases, with special reference to the evaluation of surface area and pore size distribution (IUPAC Technical Report)*, in *Pure and Applied Chemistry*. 2015. p. 1051.
96. Sing, K., *Reporting physisorption data for gas/solid systems with special reference to the determination of surface area and porosity (Recommendations 1984)*. Pure and Applied Chemistry, 1985. **57**: p. 603.
97. Boucher, E.A., *Porous materials: structure, properties and capillary phenomena*. Journal of Materials Science, 1976. **11**(9): p. 1734-1750.

98. Thommes, M., *Physical Adsorption Characterization of Nanoporous Materials*. Chemie Ingenieur Technik, 2010. **82**(7): p. 1059-1073.
99. Sukhorukov, G.B., et al., *Porous calcium carbonate microparticles as templates for encapsulation of bioactive compounds*. Journal of Materials Chemistry, 2004. **14**(14): p. 2073-2081.
100. Horcajada, P., et al., *Metal–Organic Frameworks in Biomedicine*. Chemical Reviews, 2012. **112**(2): p. 1232-1268.
101. McKinlay, A.C., et al., *BioMOFs: Metal–Organic Frameworks for Biological and Medical Applications*. Angewandte Chemie International Edition, 2010. **49**(36): p. 6260-6266.
102. Sampath, U.G.T.M., et al., *Fabrication of Porous Materials from Natural/Synthetic Biopolymers and Their Composites*. Materials (Basel, Switzerland), 2016. **9**(12): p. 991.
103. Wang, B., et al., *Macroporous materials: microfluidic fabrication, functionalization and applications*. Chemical Society Reviews, 2017. **46**(3): p. 855-914.
104. Zhou, M., et al., *Design and pharmaceutical applications of porous particles*. RSC Advances, 2017. **7**(63): p. 39490-39501.
105. Irvine, W.M., *Adsorption*, in *Encyclopedia of Astrobiology*, M. Gargaud, et al., Editors. 2011, Springer Berlin Heidelberg: Berlin, Heidelberg. p. 21-21.
106. Nasalevich, M.A., et al., *Enhancing optical absorption of metal–organic frameworks for improved visible light photocatalysis*. Chemical Communications, 2013. **49**(90): p. 10575-10577.
107. Sing, K.S.W., et al., *Reporting Physisorption Data for Gas/Solid Systems With Special Reference to the Determination of Surface Area and Porosity*.
108. Sukhorukov, G.B., et al., *Stepwise polyelectrolyte assembly on particle surfaces: a novel approach to colloid design*. Polymers for Advanced Technologies, 1998. **9**(10 - 11): p. 759-767.
109. Ambroz, F., et al., *Evaluation of the BET Theory for the Characterization of Meso and Microporous MOFs*. Small Methods, 2018. **2**(11): p. 1800173.
110. White, J., *LITERATURE REVIEW ON ADSORPTION COOLING SYSTEMS*. Latin American and Caribbean Journal of Engineering Education (378-884-1-RV) (2013), 2013.
111. Brunauer, S., et al., *On a Theory of the van der Waals Adsorption of Gases*. Journal of the American Chemical Society, 1940. **62**(7): p. 1723-1732.
112. Kumar, K.V., et al., *Characterization of the adsorption site energies and heterogeneous surfaces of porous materials*. Journal of Materials Chemistry A, 2019. **7**(17): p. 10104-10137.
113. Gawande, M.B., et al., *Cu and Cu-Based Nanoparticles: Synthesis and Applications in Catalysis*. Chemical Reviews, 2016. **116**(6): p. 3722-3811.
114. *Nanostructured Porous Materials: Synthesis and Catalytic Applications*, in *Nanotechnology in Catalysis*. p. 119-144.

- 115.Xu, Y., et al., *Nanoparticle-Encapsulated Hollow Porous Polymeric Nanosphere Frameworks as Highly Active and Tunable Size-Selective Catalysts*. ACS Macro Letters, 2019. **8**(10): p. 1263-1267.
- 116.Poupart, R., et al., *Porous polymers and metallic nanoparticles: A hybrid wedding as a robust method toward efficient supported catalytic systems*. Progress in Polymer Science, 2019. **96**: p. 21-42.
- 117.Chaturvedi, S., P.N. Dave, and N.K. Shah, *Applications of nano-catalyst in new era*. Journal of Saudi Chemical Society, 2012. **16**(3): p. 307-325.
- 118.Ashik, U.P.M., et al., *Chapter 3 - Nanomaterials as Catalysts*, in *Applications of Nanomaterials*, S. Mohan Bhagyaraj, et al., Editors. 2018, Woodhead Publishing. p. 45-82.
- 119.Huang, Y., et al., *Homochiral Nickel Coordination Polymers Based on Salen(Ni) Metalloligands: Synthesis, Structure, and Catalytic Alkene Epoxidation*. Inorganic Chemistry, 2011. **50**(6): p. 2191-2198.
- 120.Lee, I., et al., *New nanostructured heterogeneous catalysts with increased selectivity and stability*. Physical Chemistry Chemical Physics, 2011. **13**(7): p. 2449-2456.
- 121.Zaera, F., *Nanostructured materials for applications in heterogeneous catalysis*. Chemical Society Reviews, 2013. **42**(7): p. 2746-2762.
- 122.Robin, A.Y. and K.M. Fromm, *Coordination polymer networks with O- and N-donors: What they are, why and how they are made*. Coordination Chemistry Reviews, 2006. **250**(15): p. 2127-2157.
- 123.Fromm, K.M., J.L. Sagué, and L. Mirolo, *Coordination Polymer Networks: An Alternative to Classical Polymers?* Macromolecular Symposia, 2010. **291-292**(1): p. 75-83.
- 124.Han, H., et al., *Fe(Cu)-Containing Coordination Polymers: Syntheses, Crystal Structures, and Applications as Benzyl Alcohol Oxidation Catalysts*. European Journal of Inorganic Chemistry, 2006. **2006**(8): p. 1594-1600.
- 125.Zheng, G., et al., *Encapsulation of Single Plasmonic Nanoparticles within ZIF-8 and SERS Analysis of the MOF Flexibility*. Small, 2016. **12**(29): p. 3935-3943.
- 126.Kost, J., K. Leong, and R. Langer, *Ultrasound-enhanced polymer degradation and release of incorporated substances*. Proceedings of the National Academy of Sciences of the United States of America, 1989. **86**(20): p. 7663-7666.
- 127.Di, J., et al., *Ultrasound-triggered noninvasive regulation of blood glucose levels using microgels integrated with insulin nanocapsules*. Nano Research, 2017. **10**(4): p. 1393-1402.
- 128.Yaghi, O.M., et al., *Reticular synthesis and the design of new materials*. Nature, 2003. **423**(6941): p. 705-714.
- 129.Yaghi, O.M., G. Li, and H. Li, *Selective binding and removal of guests in a microporous metal-organic framework*. Nature, 1995. **378**(6558): p. 703-706.
- 130.Li, H., et al., *Design and synthesis of an exceptionally stable and highly porous metal-organic framework*. Nature, 1999. **402**(6759): p. 276-279.

131. Riou, D., O. Roubeau, and G. Férey, *Composite microporous compounds. Part I: Synthesis and structure determination of two new vanadium alkylidiphosphonates (MIL-2 and MIL-3) with three-dimensional open frameworks*. Microporous and Mesoporous Materials, 1998. **23**(1): p. 23-31.
132. Hoskins, B.F. and R. Robson, *Infinite polymeric frameworks consisting of three dimensionally linked rod-like segments*. Journal of the American Chemical Society, 1989. **111**(15): p. 5962-5964.
133. Kondo, M., et al., *Three-Dimensional Framework with Channeling Cavities for Small Molecules: $\{[M_2(4,4'-bpy)_3(NO_3)_4] \cdot xH_2O\}_n$ ($M = Co, Ni, Zn$)*. Angewandte Chemie International Edition in English, 1997. **36**(16): p. 1725-1727.
134. Howarth, A.J., et al., *Chemical, thermal and mechanical stabilities of metal-organic frameworks*. Nature Reviews Materials, 2016. **1**(3).
135. Zhu, Q.-L. and Q. Xu, *Metal-organic framework composites*. Chemical Society Reviews, 2014. **43**(16): p. 5468-5512.
136. Maurin, G., et al., *The new age of MOFs and of their porous-related solids*. Chemical Society Reviews, 2017. **46**(11): p. 3104-3107.
137. Cui, Y., et al., *Metal–Organic Frameworks as Platforms for Functional Materials*. Accounts of Chemical Research, 2016. **49**(3): p. 483-493.
138. Furukawa, H., et al., *The Chemistry and Applications of Metal-Organic Frameworks*. Science, 2013. **341**(6149).
139. Horike, S., S. Shimomura, and S. Kitagawa, *Soft porous crystals*. Nature Chemistry, 2009. **1**(9): p. 695-704.
140. Tominaka, S., et al., *Topochemical conversion of a dense metal-organic framework from a crystalline insulator to an amorphous semiconductor*. Chemical Science, 2015. **6**(2): p. 1465-1473.
141. McDonald, K.A., S. Seth, and A.J. Matzger, *Coordination Polymers with High Energy Density: An Emerging Class of Explosives*. Crystal Growth & Design, 2015. **15**(12): p. 5963-5972.
142. O'Neill, L., H. Zhang, and D. Bradshaw, *Macro/microporous MOF composite beads*. Journal of Materials Chemistry - J MATER CHEM, 2010. **20**.
143. Nasalevich, M.A., et al., *Enhancing optical absorption of metal-organic frameworks for improved visible light photocatalysis*. Chemical Communications, 2013. **49**(90): p. 10575-10577.
144. Stylianou, K.C., I. Imaz, and D. Maspoch, *Metal-Organic Frameworks: Nanoscale Frameworks*, in *Encyclopedia of Inorganic and Bioinorganic Chemistry*. 2011, John Wiley & Sons, Ltd.
145. Makiura, R., et al., *Surface nano-architecture of a metal–organic framework*. Nat Mater, 2010. **9**(7): p. 565-571.

- 146.Green, M.A., *Crystal engineering in two dimensions: Surface attraction*. Nat Mater, 2010. **9**(7): p. 539-540.
- 147.He, L., et al., *DNA-Assembled Core-Satellite Upconverting-Metal–Organic Framework Nanoparticle Superstructures for Efficient Photodynamic Therapy*. Small, 2017. **13**(24): p. 1700504.
- 148.Borges, M., et al., *Dual T1/T2 MRI contrast agent based on hybrid SPION@coordination polymer nanoparticles*. RSC Advances, 2015. **5**(105): p. 86779-86783.
- 149.Hu, P., J.V. Morabito, and C.-K. Tsung, *Core–Shell Catalysts of Metal Nanoparticle Core and Metal–Organic Framework Shell*. ACS Catalysis, 2014. **4**(12): p. 4409-4419.
- 150.El-Shall, M.S., et al., *Metallic and bimetallic nanocatalysts incorporated into highly porous coordination polymer MIL-101*. Journal of Materials Chemistry, 2009. **19**(41): p. 7625-7631.
- 151.Lin, W., W.J. Rieter, and K.M.L. Taylor, *Modular Synthesis of Functional Nanoscale Coordination Polymers*. Angewandte Chemie International Edition, 2009. **48**(4): p. 650-658.
- 152.Kuo, C.-H., et al., *Yolk–Shell Nanocrystal@ZIF-8 Nanostructures for Gas-Phase Heterogeneous Catalysis with Selectivity Control*. Journal of the American Chemical Society, 2012. **134**(35): p. 14345-14348.
- 153.Lu, G., et al., *Imparting functionality to a metal–organic framework material by controlled nanoparticle encapsulation*. Nature Chemistry, 2012. **4**(4): p. 310-316.
- 154.Horcajada, P., et al., *Porous metal-organic-framework nanoscale carriers as a potential platform for drug delivery and imaging*. Nat Mater, 2010. **9**(2): p. 172-178.
- 155.Wang, X.-G., et al., *A multifunctional metal-organic framework based tumor targeting drug delivery system for cancer therapy*. Nanoscale, 2015. **7**(38): p. 16061-16070.
- 156.Abánades Lázaro, I., et al., *Selective Surface PEGylation of UiO-66 Nanoparticles for Enhanced Stability, Cell Uptake, and pH-Responsive Drug Delivery*. Chem, 2017. **2**(4): p. 561-578.
- 157.Orellana-Tavra, C., et al., *Tuning the Endocytosis Mechanism of Zr-Based Metal–Organic Frameworks through Linker Functionalization*. ACS Applied Materials & Interfaces, 2017. **9**(41): p. 35516-35525.
- 158.Schaate, A., et al., *Modulated Synthesis of Zr-Based Metal–Organic Frameworks: From Nano to Single Crystals*. Chemistry – A European Journal, 2011. **17**(24): p. 6643-6651.
- 159.Zhao, M., et al., *Ultrathin 2D Metal–Organic Framework Nanosheets*. Advanced Materials, 2015. **27**(45): p. 7372-7378.
- 160.Vaucher, S., M. Li, and S. Mann, *Synthesis of Prussian Blue Nanoparticles and Nanocrystal Superlattices in Reverse Microemulsions*. Angewandte Chemie International Edition, 2000. **39**(10): p. 1793-1796.
- 161.Wee, L.H., et al., *Fine tuning of the metal-organic framework Cu₃(BTC)₂ HKUST-1 crystal size in the 100 nm to 5 micron range*. Journal of Materials Chemistry, 2012. **22**(27): p. 13742-13746.

162. Diring, S., et al., *Controlled Multiscale Synthesis of Porous Coordination Polymer in Nano/Micro Regimes*. Chemistry of Materials, 2010. **22**(16): p. 4531-4538.
163. Park, J., et al., *Size-Controlled Synthesis of Porphyrinic Metal–Organic Framework and Functionalization for Targeted Photodynamic Therapy*. Journal of the American Chemical Society, 2016. **138**(10): p. 3518-3525.
164. Li, P., et al., *Synthesis of nanocrystals of Zr-based metal-organic frameworks with csq-net: significant enhancement in the degradation of a nerve agent simulant*. Chemical Communications, 2015. **51**(54): p. 10925-10928.
165. Hirschle, P., et al., *Exploration of MOF nanoparticle sizes using various physical characterization methods - is what you measure what you get?* CrystEngComm, 2016. **18**(23): p. 4359-4368.
166. Giménez-Marqués, M., et al., *Nanostructured metal–organic frameworks and their bio-related applications*. Coordination Chemistry Reviews, 2016. **307**: p. 342-360.
167. Nune, S.K., et al., *Synthesis and properties of nano zeolitic imidazolate frameworks*. Chemical Communications, 2010. **46**(27): p. 4878-4880.
168. Barmparis, G.D., et al., *Nanoparticle shapes by using Wulff constructions and first-principles calculations*. Beilstein Journal of Nanotechnology, 2015. **6**: p. 361-368.
169. Xiao, B., Q. Yuan, and R.A. Williams, *Exceptional function of nanoporous metal organic framework particles in emulsion stabilisation*. Chemical Communications, 2013. **49**(74): p. 8208-8210.
170. Ranft, A., et al., *Additive-mediated size control of MOF nanoparticles*. CrystEngComm, 2013. **15**(45): p. 9296-9300.
171. Jiang, D., et al., *Polymer-assisted synthesis of nanocrystalline copper-based metal–organic framework for amine oxidation*. Catalysis Communications, 2011. **12**(7): p. 602-605.
172. Sanz, R., et al., *Synthesis of a honeycomb-like Cu-based metal-organic framework and its carbon dioxide adsorption behaviour*. Dalton Transactions, 2013. **42**(7): p. 2392-2398.
173. Chen, Z., et al., *A Microporous Metal–Organic Framework with Immobilized –OH Functional Groups within the Pore Surfaces for Selective Gas Sorption*. European Journal of Inorganic Chemistry, 2010. **2010**(24): p. 3745-3749.
174. Chen, Y., et al., *A Copper(II)-Paddlewheel Metal–Organic Framework with Exceptional Hydrolytic Stability and Selective Adsorption and Detection Ability of Aniline in Water*. ACS Applied Materials & Interfaces, 2017. **9**(32): p. 27027-27035.
175. Chui, S.S.-Y., et al., *A Chemically Functionalizable Nanoporous Material [Cu₃(TMA)₂(H₂O)₃]_n*. Science, 1999. **283**(5405): p. 1148-1150.
176. Karahan, Ö., et al., *Development of Efficient Copper-Based MOF-Derived Catalysts for the Reduction of Aromatic Nitro Compounds*. European Journal of Inorganic Chemistry: p. n/a-n/a.

177. Masciocchi, N., et al., *Extended Polymorphism in Copper(II) Imidazolate Polymers: A Spectroscopic and XRPD Structural Study*. Inorganic Chemistry, 2001. **40**(23): p. 5897-5905.
178. Luz, I., A. Corma, and F.X. Llabres i Xamena, *Cu-MOFs as active, selective and reusable catalysts for oxidative C-O bond coupling reactions by direct C-H activation of formamides, aldehydes and ethers*. Catalysis Science & Technology, 2014. **4**(6): p. 1829-1836.
179. Park, K.S., et al., *Exceptional chemical and thermal stability of zeolitic imidazolate frameworks*. Proceedings of the National Academy of Sciences, 2006. **103**(27): p. 10186-10191.
180. Zheng, G., et al., *Shape control in ZIF-8 nanocrystals and metal nanoparticles@ZIF-8 heterostructures*. Nanoscale, 2017. **9**(43): p. 16645-16651.
181. Samiey, B., C.H. Cheng, and J. Wu, *Effects of Surfactants on the Rate of Chemical Reactions*. Journal of Chemistry, 2014. **2014**: p. 908476.
182. Navarro Poupard, M.F., et al., *Aqueous Synthesis of Copper(II)-Imidazolate Nanoparticles*. Inorganic Chemistry, 2018. **57**(19): p. 12056-12065.
183. Wang, X., et al., *Surfactant-free Synthesis of CuO with Controllable Morphologies and Enhanced Photocatalytic Property*. Nanoscale Research Letters, 2016. **11**(1): p. 125.
184. Volanti, D.P., et al., *Efficient microwave-assisted hydrothermal synthesis of CuO sea urchin-like architectures via a mesoscale self-assembly*. CrystEngComm, 2010. **12**(6): p. 1696-1699.
185. del Pino, P., et al., *The configuration of the Cu²⁺ binding region in full-length human prion protein*. European Biophysics Journal With Biophysics Letters, 2007. **36**(3): p. 239-252.
186. El Mkami, H., et al., *EPR and magnetic studies of a novel copper metal organic framework (STAM-I)*. Chemical Physics Letters, 2012. **544**: p. 17-21.
187. Barnett, S.M., K.I. Goldberg, and J.M. Mayer, *A soluble copper-bipyridine water-oxidation electrocatalyst*. Nature Chemistry, 2012. **4**: p. 498.
188. Godlewska, S., et al., *Copper(II) complexes with substituted imidazole and chlorido ligands: X-ray, UV-Vis, magnetic and EPR studies and chemotherapeutic potential*. Polyhedron, 2013. **65**: p. 288-297.
189. Peisach, J. and W.E. Blumberg, *Structural implications derived from the analysis of electron paramagnetic resonance spectra of natural and artificial copper proteins*. Archives of Biochemistry and Biophysics, 1974. **165**(2): p. 691-708.
190. Silva, K.I., et al., *ESEEM Analysis of Multi-Histidine Cu(II)-Coordination in Model Complexes, Peptides, and Amyloid- β* . The Journal of Physical Chemistry B, 2014. **118**(30): p. 8935-8944.
191. Tran, C.D., et al., *Biocompatible Copper Oxide Nanoparticle Composites from Cellulose and Chitosan: Facile Synthesis, Unique Structure, and Antimicrobial Activity*. ACS Applied Materials & Interfaces, 2017. **9**(49): p. 42503-42515.

192. Xu, B., et al., *Monitoring thermally induced structural deformation and framework decomposition of ZIF-8 through in situ temperature dependent measurements*. Physical Chemistry Chemical Physics, 2017. **19**(40): p. 27178-27183.
193. Li, G., et al., *An ordered bcc CuPd nanoalloy synthesised via the thermal decomposition of Pd nanoparticles covered with a metal-organic framework under hydrogen gas*. Chemical Communications, 2014. **50**(89): p. 13750-13753.
194. Lin, K.-S., et al., *Synthesis and characterization of porous HKUST-1 metal organic frameworks for hydrogen storage*. International Journal of Hydrogen Energy, 2012. **37**(18): p. 13865-13871.
195. Topnani, N., S. Kushwaha, and T. Athar, *Wet Synthesis of Copper Oxide Nanopowder*. International Journal of Green Nanotechnology: Materials Science & Engineering, 2010. **1**(2): p. M67-M73.
196. Chen, L., et al., *Copper Salts Mediated Morphological Transformation of Cu₂O from Cubes to Hierarchical Flower-like or Microspheres and Their Supercapacitors Performances*. Scientific Reports, 2015. **5**: p. 9672.
197. Zoroddu, M.A., S. Medici, and M. Peana, *Copper and nickel binding in multi-histidinic peptide fragments*. Journal of Inorganic Biochemistry, 2009. **103**(9): p. 1214-1220.
198. Shahmiri, M., et al., *Preparation of PVP-coated copper oxide nanosheets as antibacterial and antifungal agents*. Journal of Materials Research, 2013. **28**(22): p. 3109-3118.
199. Suchomel, P., et al., *Simple size-controlled synthesis of Au nanoparticles and their size-dependent catalytic activity*. Scientific Reports, 2018. **8**(1): p. 4589.
200. Basu, M., et al., *Methylene Blue–Cu₂O Reaction Made Easy in Acidic Medium*. The Journal of Physical Chemistry C, 2012. **116**(49): p. 25741-25747.
201. Robina, B., et al., *Chemical reduction of methylene blue in the presence of nanocatalysts: a critical review*. Reviews in Chemical Engineering, 2019(0): p. 20180047.
202. Mehlig, J., *Colorimetric Determination of Copper with Ammonia*. Industrial & Engineering Chemistry Analytical Edition, 1941. **13**(8): p. 533-535.
203. del Pino, P., et al., *Basic Physicochemical Properties of Polyethylene Glycol Coated Gold Nanoparticles that Determine Their Interaction with Cells*. Angewandte Chemie-International Edition, 2016. **55**(18): p. 5483-5487.
204. Kurtan, U., et al., *Synthesis of magnetically recyclable MnFe₂O₄@SiO₂@Ag nanocatalyst: Its high catalytic performances for azo dyes and nitro compounds reduction*. Applied Surface Science, 2016. **376**: p. 16-25.
205. Cui, X., et al., *Novel yolk–shell-structured Fe₃O₄@ γ -AlOOH nanocomposite modified with Pd nanoparticles as a recyclable catalyst with excellent catalytic activity*. Applied Surface Science, 2017. **416**: p. 103-111.
206. Seth, S. and A.J. Matzger, *Metal–Organic Frameworks: Examples, Counterexamples, and an Actionable Definition*. Crystal Growth & Design, 2017. **17**(8): p. 4043-4048.

207. Tominaka, S., et al., *Topochemical conversion of a dense metal–organic framework from a crystalline insulator to an amorphous semiconductor*. Chemical Science, 2015. **6**(2): p. 1465-1473.
208. Horcajada, P., et al., *Porous metal–organic-framework nanoscale carriers as a potential platform for drug delivery and imaging*. Nature Materials, 2010. **9**(2): p. 172-178.
209. Cai, W., et al., *Metal–Organic Framework-Based Stimuli-Responsive Systems for Drug Delivery*. Advanced Science, 2019. **6**(1): p. 1801526.
210. Wu, M.-X. and Y.-W. Yang, *Metal–Organic Framework (MOF)-Based Drug/Cargo Delivery and Cancer Therapy*. Advanced Materials, 2017. **29**(23): p. 1606134.
211. Ayala, A., et al., *Introducing asymmetric functionality into MOFs via the generation of metallic Janus MOF particles*. Chemical Communications, 2016. **52**(29): p. 5096-5099.
212. Zhu, W., et al., *Versatile Surface Functionalization of Metal–Organic Frameworks through Direct Metal Coordination with a Phenolic Lipid Enables Diverse Applications*. Advanced Functional Materials, 2018. **28**(16): p. 1705274.
213. Li, Z. and H.C. Zeng, *Surface and Bulk Integrations of Single-Layered Au or Ag Nanoparticles onto Designated Crystal Planes {110} or {100} of ZIF-8*. Chemistry of Materials, 2013. **25**(9): p. 1761-1768.
214. Baati, T., et al., *In depth analysis of the in vivo toxicity of nanoparticles of porous iron(III) metal–organic frameworks*. Chemical Science, 2013. **4**(4): p. 1597-1607.
215. Simon-Yarza, T., et al., *The Situation of Metal-Organic Frameworks in Biomedicine*. 2017.
216. Wei, Y., et al., *Tailoring and visualizing the pore architecture of hierarchical zeolites*. Chemical Society Reviews, 2015. **44**(20): p. 7234-7261.
217. Baerlocher, C., W.M. Meier, and O. D.H., *Atlas Of Zeolite Framework Types*. Atlas of Zeolite Framework Types, Elsevier, 2001.
218. Banerjee, R., et al., *High-Throughput Synthesis of Zeolitic Imidazolate Frameworks and Application to CO₂ Capture*. Science, 2008. **319**(5865): p. 939-943.
219. Cravillon, J., et al., *Formate modulated solvothermal synthesis of ZIF-8 investigated using time-resolved in situ X-ray diffraction and scanning electron microscopy*. CrystEngComm, 2012. **14**(2): p. 492-498.
220. Zhuang, J., et al., *Optimized Metal–Organic-Framework Nanospheres for Drug Delivery: Evaluation of Small-Molecule Encapsulation*. ACS Nano, 2014. **8**(3): p. 2812-2819.
221. Zheng, H., et al., *One-pot Synthesis of Metal–Organic Frameworks with Encapsulated Target Molecules and Their Applications for Controlled Drug Delivery*. Journal of the American Chemical Society, 2016. **138**(3): p. 962-968.
222. Troyano, J., et al., *Colloidal metal–organic framework particles: the pioneering case of ZIF-8*. Chemical Society Reviews, 2019. **48**(23): p. 5534-5546.

- 223.Kaur, H., et al., *Synthesis and characterization of ZIF-8 nanoparticles for controlled release of 6-mercaptopurine drug*. Journal of Drug Delivery Science and Technology, 2017. **41**: p. 106-112.
- 224.Perro, A., et al., *Design and synthesis of Janus micro- and nanoparticles*. Journal of Materials Chemistry, 2005. **15**(35-36): p. 3745-3760.
- 225.Walther, A. and A.H.E. Müller, *Janus Particles: Synthesis, Self-Assembly, Physical Properties, and Applications*. Chemical Reviews, 2013. **113**(7): p. 5194-5261.
- 226.Nabipour, H., M.H. Sadr, and G.R. Bardajee, *Synthesis and characterization of nanoscale zeolitic imidazolate frameworks with ciprofloxacin and their applications as antimicrobial agents*. New Journal of Chemistry, 2017. **41**(15): p. 7364-7370.
- 227.Yan, L., et al., *Size Controllable and Surface Tunable Zeolitic Imidazolate Framework-8–Poly(acrylic acid sodium salt) Nanocomposites for pH Responsive Drug Release and Enhanced in Vivo Cancer Treatment*. ACS Applied Materials & Interfaces, 2017. **9**(38): p. 32990-33000.
- 228.Chen, X., et al., *MOF Nanoparticles with Encapsulated Autophagy Inhibitor in Controlled Drug Delivery System for Antitumor*. ACS Applied Materials & Interfaces, 2018. **10**(3): p. 2328-2337.
- 229.Zhang, C., et al., *pH-sensitive MOF integrated with glucose oxidase for glucose-responsive insulin delivery*. Journal of Controlled Release, 2020. **320**: p. 159-167.
- 230.Ettlinger, R., et al., *Zeolitic Imidazolate Framework-8 as pH-Sensitive Nanocarrier for "Arsenic Trioxide" Drug Delivery*. Chemistry, 2019. **25**.
- 231.Li, Y., et al., *Coordination-responsive drug release inside gold nanorod@metal-organic framework core-shell nanostructures for near-infrared-induced synergistic chemophotothermal therapy*. Nano Research, 2018. **11**(6): p. 3294-3305.
- 232.Chen, W.-H., et al., *Glucose-Responsive Metal–Organic-Framework Nanoparticles Act as “Smart” Sense-and-Treat Carriers*. ACS Nano, 2018. **12**(8): p. 7538-7545.
- 233.Sharsheeva, A., et al., *Light-controllable systems based on TiO₂-ZIF-8 composites for targeted drug release: communicating with tumour cells*. Journal of Materials Chemistry B, 2019. **7**(43): p. 6810-6821.
- 234.Liu, X., et al., *Improvement of hydrothermal stability of zeolitic imidazolate frameworks*. Chemical Communications, 2013. **49**(80): p. 9140-9142.
- 235.Zhang, H., et al., *Stability of ZIF-8 membranes and crystalline powders in water at room temperature*. Journal of Membrane Science, 2015. **485**: p. 103-111.
- 236.Karimi, M., et al., *Smart micro/nanoparticles in stimulus-responsive drug/gene delivery systems*. Chemical Society Reviews, 2016. **45**(5): p. 1457-1501.
- 237.Pan, Y., et al., *Rapid synthesis of zeolitic imidazolate framework-8 (ZIF-8) nanocrystals in an aqueous system*. Chemical Communications, 2011. **47**(7): p. 2071-2073.
- 238.Pan, Y., et al., *Tuning the crystal morphology and size of zeolitic imidazolate framework-8 in aqueous solution by surfactants*. CrystEngComm, 2011. **13**(23): p. 6937-6940.

- 239.Fu, F., et al., *Size-Controllable Synthesis of Zeolitic Imidazolate Framework/Carbon Nanotube Composites*. Crystals, 2018. **8**: p. 367.
- 240.Wan, R., et al., *Cobalt nanoparticles induce lung injury, DNA damage and mutations in mice*. Particle and Fibre Toxicology, 2017. **14**(1): p. 38.
- 241.Papageorgiou, I., et al., *The effect of nano- and micron-sized particles of cobalt–chromium alloy on human fibroblasts in vitro*. Biomaterials, 2007. **28**(19): p. 2946-2958.
- 242.Chen, Y., et al., *ZIF-67 as precursor to prepare high loading and dispersion catalysts for Fischer-Tropsch synthesis: Particle size effect*. Fuel, 2019. **241**: p. 802-812.
- 243.Schulz, F., et al., *Little Adjustments Significantly Improve the Turkevich Synthesis of Gold Nanoparticles*. Langmuir, 2014. **30**(35): p. 10779-10784.
- 244.Haiss, W., et al., *Determination of Size and Concentration of Gold Nanoparticles from UV–Vis Spectra*. Analytical Chemistry, 2007. **79**(11): p. 4215-4221.
- 245.Carrillo - Carrión, C., et al., *Aqueous Stable Gold Nanostar/ZIF - 8 Nanocomposites for Light - Triggered Release of Active Cargo Inside Living Cells*. Angewandte Chemie International Edition, 2019. **58**(21): p. 7078-7082.
- 246.Bucevičius, J., G. Lukinavičius, and R. Gerasimaitė, *The Use of Hoechst Dyes for DNA Staining and Beyond*. Chemosensors, 2018. **6**(2): p. 18.
- 247.Kumari, G., et al., *Temperature Induced Structural Transformations and Gas Adsorption in the Zeolitic Imidazolate Framework ZIF-8: A Raman Study*. The Journal of Physical Chemistry A, 2013. **117**(43): p. 11006-11012.
- 248.Knebel, A., et al., *Defibrillation of soft porous metal-organic frameworks with electric fields*. Science, 2017. **358**(6361): p. 347-351.
- 249.Fairen-Jimenez, D., et al., *Opening the Gate: Framework Flexibility in ZIF-8 Explored by Experiments and Simulations*. Journal of the American Chemical Society, 2011. **133**(23): p. 8900-8902.
- 250.Rivera_Gil, P., et al., *Plasmonic Nanoprobes for Real-Time Optical Monitoring of Nitric Oxide inside Living Cells*. Angewandte Chemie, 2013. **125**(51): p. 13939-13943.
- 251.Yahia-Ammar, A., et al., *Self-Assembled Gold Nanoclusters for Bright Fluorescence Imaging and Enhanced Drug Delivery*. ACS Nano, 2016. **10**(2): p. 2591-2599.
- 252.Huang, P., et al., *Tumor-Specific Formation of Enzyme-Instructed Supramolecular Self-Assemblies as Cancer Theranostics*. ACS Nano, 2015. **9**(10): p. 9517-9527.
- 253.Godoy-Gallardo, M., et al., *Multicompartment Artificial Organelles Conducting Enzymatic Cascade Reactions inside Cells*. ACS Applied Materials & Interfaces, 2017. **9**(19): p. 15907-15921.
- 254.Fu, X., et al., *Multi-Stimuli-Responsive Polymer Particles, Films, and Hydrogels for Drug Delivery*. Chem, 2018. **4**(9): p. 2084-2107.
- 255.Facca, S., et al., *Active multilayered capsules for in vivo bone formation*. Proceedings of the National Academy of Sciences, 2010. **107**(8): p. 3406-3411.

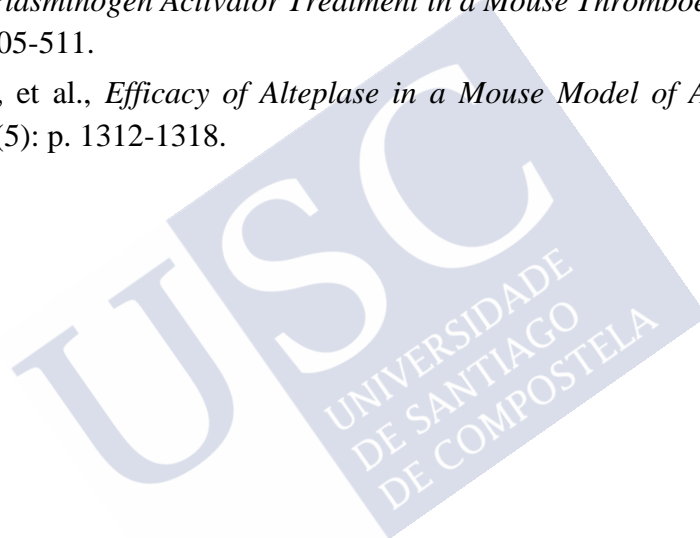
256. Zhao, S., et al., *The Future of Layer-by-Layer Assembly: A Tribute to ACS Nano Associate Editor Helmuth Möhwald*. ACS Nano, 2019. **13**(6): p. 6151-6169.
257. Dai, Q., et al., *Monoclonal Antibody-Functionalized Multilayered Particles: Targeting Cancer Cells in the Presence of Protein Coronas*. ACS Nano, 2015. **9**(3): p. 2876-2885.
258. Ochs, M., et al., *Light-Addressable Capsules as Caged Compound Matrix for Controlled Triggering of Cytosolic Reactions*. Angewandte Chemie International Edition, 2013. **52**(2): p. 695-699.
259. Oliveira, M.B., J. Hatami, and J.F. Mano, *Coating Strategies Using Layer-by-layer Deposition for Cell Encapsulation*. Chemistry – An Asian Journal, 2016. **11**(12): p. 1753-1764.
260. Gil, P.R., et al., *Nanoparticle-modified polyelectrolyte capsules*. Nano Today, 2008. **3**(3): p. 12-21.
261. Szczepanowicz, K., et al., *Biocompatible long-sustained release oil-core polyelectrolyte nanocarriers: From controlling physical state and stability to biological impact*. Advances in Colloid and Interface Science, 2015. **222**: p. 678-691.
262. Hauck, T.S., A.A. Ghazani, and W.C.W. Chan, *Assessing the Effect of Surface Chemistry on Gold Nanorod Uptake, Toxicity, and Gene Expression in Mammalian Cells*. Small, 2008. **4**(1): p. 153-159.
263. Cui, J., et al., *Nanoengineered Templated Polymer Particles: Navigating the Biological Realm*. Accounts of Chemical Research, 2016. **49**(6): p. 1139-1148.
264. Ochs, C.J., et al., *Biodegradable Click Capsules with Engineered Drug-Loaded Multilayers*. ACS Nano, 2010. **4**(3): p. 1653-1663.
265. De Koker, S., et al., *Biodegradable Polyelectrolyte Microcapsules: Antigen Delivery Tools with Th17 Skewing Activity after Pulmonary Delivery*. The Journal of Immunology, 2010. **184**(1): p. 203-211.
266. Hartmann, R., et al., *Stiffness-Dependent In Vitro Uptake and Lysosomal Acidification of Colloidal Particles*. Angewandte Chemie International Edition, 2015. **54**(4): p. 1365-1368.
267. Becker, A.L., A.P.R. Johnston, and F. Caruso, *Layer-By-Layer-Assembled Capsules and Films for Therapeutic Delivery*. Small, 2010. **6**(17).
268. Trushina, D.B., et al., *CaCO₃ vaterite microparticles for biomedical and personal care applications*. Materials Science and Engineering: C, 2014. **45**: p. 644-658.
269. Dupont, L., F. Portemer, and M. Figlarz, *Synthesis and study of a well crystallized CaCO₃ vaterite showing a new habitus*. Journal of Materials Chemistry, 1997. **7**(5): p. 797-800.
270. Andreassen, J.-P. and M.J. Hounslow, *Growth and aggregation of vaterite in seeded-batch experiments*. AIChE Journal, 2004. **50**(11): p. 2772-2782.
271. Ouhenia, S., et al., *Synthesis of calcium carbonate polymorphs in the presence of polyacrylic acid*. Journal of Crystal Growth, 2008. **310**(11): p. 2832-2841.
272. Won, Y.-H., et al., *Multifunctional calcium carbonate microparticles: Synthesis and biological applications*. Journal of Materials Chemistry, 2010. **20**(36): p. 7728-7733.

- 273.Volodkin, D.V., N.I. Larionova, and G.B. Sukhorukov, *Protein Encapsulation via Porous CaCO₃ Microparticles Templating*. Biomacromolecules, 2004. **5**(5): p. 1962-1972.
- 274.Imai, H., et al., *Oriented Nanocrystal Mosaic in Monodispersed CaCO₃ Microspheres with Functional Organic Molecules*. Crystal Growth & Design, 2012. **12**(2): p. 876-882.
- 275.Hu, Q., et al., *Growth process and crystallographic properties of ammonia-induced vaterite*. American Mineralogist, 2012. **97**(8-9): p. 1437-1445.
- 276.Fricke, M., et al., *Vaterite Polymorph Switching Controlled by Surface Charge Density of an Amphiphilic Dendron-calix[4]arene*. Crystal Growth & Design, 2006. **6**(5): p. 1120-1123.
- 277.Gehrke, N., et al., *Superstructures of Calcium Carbonate Crystals by Oriented Attachment*. Crystal Growth & Design, 2005. **5**(4): p. 1317-1319.
- 278.Qi, L., J. Li, and J. Ma, *Biomimetic morphogenesis of calcium carbonate in mixed solutions for surfactants and double-hydrophilic block copolymers*. Advanced Materials, 2002. **14**(4): p. 300-303.
- 279.Qi, L., J. Li, and J. Ma, *Biomimetic Morphogenesis of Calcium Carbonate in Mixed Solutions of Surfactants and Double-Hydrophilic Block Copolymers*. Advanced Materials, 2002. **14**(4): p. 300-303.
- 280.Rodriguez-Blanco, J.D., S. Shaw, and L.G. Benning, *The kinetics and mechanisms of amorphous calcium carbonate (ACC) crystallization to calcite, viavaterite*. Nanoscale, 2011. **3**(1): p. 265-271.
- 281.Cherkas, O., et al., *Direct Observation of Microparticle Porosity Changes in Solid-State Vaterite to Calcite Transformation by Coherent X-ray Diffraction Imaging*. Crystal Growth & Design, 2017. **17**(8): p. 4183-4188.
- 282.Petrov, A.I., D.V. Volodkin, and G.B. Sukhorukov, *Protein—Calcium Carbonate Coprecipitation: A Tool for Protein Encapsulation*. Biotechnology Progress, 2005. **21**(3): p. 918-925.
- 283.Ermakov, A.V., et al., *Influence of Heat Treatment on Loading of Polymeric Multilayer Microcapsules with Rhodamine B*. Macromolecular Rapid Communications, 2019. **40**(5): p. 1800200.
- 284.Kauscher, U., et al., *Physical stimuli-responsive vesicles in drug delivery: Beyond liposomes and polymersomes*. Advanced Drug Delivery Reviews, 2019. **138**: p. 259-275.
- 285.Radhakumary, C. and K. Sreenivasan, *Generation of pH responsive fluorescent nano capsules through simple steps for the oral delivery of low pH susceptible drugs*. Materials Research Express, 2016. **3**(11): p. 115008.
- 286.Rivera-Gil, P., et al., *Intracellular Processing of Proteins Mediated by Biodegradable Polyelectrolyte Capsules*. Nano Letters, 2009. **9**(12): p. 4398-4402.
- 287.Elbaz, N.M., et al., *Controlled synthesis of calcium carbonate nanoparticles and stimuli-responsive multi-layered nanocapsules for oral drug delivery*. International Journal of Pharmaceutics, 2020. **574**: p. 118866.

288. Blanco, E., H. Shen, and M. Ferrari, *Principles of nanoparticle design for overcoming biological barriers to drug delivery*. Nat Biotech, 2015. **33**(9): p. 941-951.
289. Hayashi, K., et al., *Red blood cell-like particles with the ability to avoid lung and spleen accumulation for the treatment of liver fibrosis*. Biomaterials, 2018. **156**: p. 45-55.
290. Bivard, A., et al., *Platelet microparticles: a biomarker for recanalization in rtPA-treated ischemic stroke patients*. Annals of Clinical and Translational Neurology, 2017. **4**(3): p. 175-179.
291. Rouch, A., et al., *Small molecules inhibitors of plasminogen activator inhibitor-1 – An overview*. European Journal of Medicinal Chemistry, 2015. **92**: p. 619-636.
292. Katzan, I.L., et al., *Utilization of intravenous tissue plasminogen activator for acute ischemic stroke*. Archives of Neurology, 2004. **61**(3): p. 346-350.
293. Yepes, M., et al., *Tissue-type plasminogen activator in the ischemic brain: more than a thrombolytic*. Trends in Neurosciences, 2009. **32**(1): p. 48-55.
294. Abebe, M., N. Hedin, and Z. Bacsik, *Spherical and Porous Particles of Calcium Carbonate Synthesized with Food Friendly Polymer Additives*. Crystal Growth & Design, 2015. **15**(8): p. 3609-3616.
295. Donnelly, F.C., et al., *Synthesis of CaCO₃ nano- and micro-particles by dry ice carbonation*. Chemical Communications, 2017. **53**(49): p. 6657-6660.
296. Cölfen, H. and M. Antonietti, *Crystal Design of Calcium Carbonate Microparticles Using Double-Hydrophilic Block Copolymers*. Langmuir, 1998. **14**(3): p. 582-589.
297. Nagaraja, A.T., S. Pradhan, and M.J. McShane, *Poly (vinylsulfonic acid) assisted synthesis of aqueous solution stable vaterite calcium carbonate nanoparticles*. Journal of Colloid and Interface Science, 2014. **418**: p. 366-372.
298. Kantner, K., et al., *Laterally and Temporally Controlled Intracellular Staining by Light-Triggered Release of Encapsulated Fluorescent Markers*. Chemistry – A European Journal, 2018. **24**(9): p. 2098-2102.
299. Luo, X., et al., *Investigation of calcium carbonate synthesized by steamed ammonia liquid waste without use of additives*. RSC Advances, 2020. **10**(13): p. 7976-7986.
300. Demichelis, R., et al., *The Multiple Structures of Vaterite*. Crystal Growth & Design, 2013. **13**(6): p. 2247-2251.
301. Correa-Paz, C., et al., *In vivo ultrasound-activated delivery of recombinant tissue plasminogen activator from the cavity of sub-micrometric capsules*. Journal of Controlled Release, 2019. **308**: p. 162-171.
302. Polowczyk, I., A. Bastrzyk, and M. Fiedot, *Protein-Mediated Precipitation of Calcium Carbonate*. Materials (Basel), 2016. **9**(11).
303. Wang, X., et al., *Role of Ovalbumin in the Stabilization of Metastable Vaterite in Calcium Carbonate Biomineralization*. The Journal of Physical Chemistry B, 2009. **113**(26): p. 8975-8982.







- 304.Chakrabarty, D. and S. Mahapatra, *Aragonite crystals with unconventional morphologies*. Journal of Materials Chemistry, 1999. **9**(11): p. 2953-2957.
- 305.Xu, B. and K. Poduska, *Linking crystal structure with temperature-sensitive vibrational modes in calcium carbonate minerals*. Physical Chemistry Chemical Physics, 2014. **16**.
- 306.The, T.H. and T.E. Feltkamp, *Conjugation of fluorescein isothiocyanate to antibodies. I. Experiments on the conditions of conjugation*. Immunology, 1970. **18**(6): p. 865-873.
- 307.Vira, S., et al., *Fluorescent-labeled antibodies: Balancing functionality and degree of labeling*. Analytical biochemistry, 2010. **402**(2): p. 146-150.
- 308.Sommerdijk, N.A.J.M. and G.d. With, *Biomimetic CaCO₃ Mineralization using Designer Molecules and Interfaces*. Chemical Reviews, 2008. **108**(11): p. 4499-4550.
- 309.Takagi, J., H. Asai, and Y. Saito, *A collagen/gelatin-binding decapeptide derived from bovine propolypeptide of von Willebrand factor*. Biochemistry, 1992. **31**(36): p. 8530-8534.
- 310.Kawata, H., et al., *A New Drug Delivery System for Intravenous Coronary Thrombolysis With Thrombus Targeting and Stealth Activity Recoverable by Ultrasound*. Journal of the American College of Cardiology, 2012. **60**(24): p. 2550-2557.
- 311.Buchtele, N., et al., *Targeting von Willebrand Factor in Ischaemic Stroke: Focus on Clinical Evidence*. Thromb Haemost, 2018. **118**(6): p. 959-978.
- 312.Jang, J.-t., et al., *Critical Enhancements of MRI Contrast and Hyperthermic Effects by Dopant-Controlled Magnetic Nanoparticles*. Angewandte Chemie International Edition, 2009. **48**(7): p. 1234-1238.
- 313.Song, W., et al., *Smart polyelectrolyte microcapsules as carriers for water-soluble small molecular drug*. Journal of Controlled Release, 2009. **139**(2): p. 160-166.
- 314.Noi, K.F., et al., *Assembly-Controlled Permeability of Layer-by-Layer Polymeric Microcapsules Using a Tapered Fluidized Bed*. ACS Applied Materials & Interfaces, 2015. **7**(50): p. 27940-27947.
- 315.Carregal-Romero, S., et al., *NIR-light triggered delivery of macromolecules into the cytosol*. Journal of Controlled Release, 2012. **159**(1): p. 120-127.
- 316.Palankar, R., et al., *Mechanical strength and intracellular uptake of CaCO₃-templated LbL capsules composed of biodegradable polyelectrolytes: the influence of the number of layers*. Journal of Materials Chemistry B, 2013. **1**(8): p. 1175-1181.
- 317.Budzynski, A.Z., *Chromogenic Substrates in Coagulation and Fibrinolytic Assays*. Laboratory Medicine, 2001. **32**(7): p. 365-368.
- 318.Gershkovich, A.A. and V.V. Kholodovych, *Fluorogenic substrates for proteases based on intramolecular fluorescence energy transfer (IFETS)*. Journal of Biochemical and Biophysical Methods, 1996. **33**(3): p. 135-162.
- 319.Ali, M.F., et al., *A hydrophobic patch surrounding Trp154 in human neuroserpin controls the helix F dynamics with implications in inhibition and aggregation*. Scientific Reports, 2017. **7**: p. 42987.

320. Choi, J.J., et al., *Noninvasive and Localized Blood–Brain Barrier Disruption using Focused Ultrasound can be Achieved at Short Pulse Lengths and Low Pulse Repetition Frequencies*. *Journal of Cerebral Blood Flow and Metabolism*, 2010. **31**(2): p. 725-737.
321. Kaczynski, J., et al., *Reproducibility of Transcranial Doppler ultrasound in the middle cerebral artery*. *Cardiovascular Ultrasound*, 2018. **16**(1): p. 15.
322. Hansen, C.E., et al., *Platelet–Microcapsule Hybrids Leverage Contractile Force for Targeted Delivery of Hemostatic Agents*. *ACS Nano*, 2017.
323. Talamini, L., et al., *Influence of Size and Shape on the Anatomical Distribution of Endotoxin-Free Gold Nanoparticles*. *ACS Nano*, 2017. **11**(6): p. 5519-5529.
324. Gustafson, H.H., et al., *Nanoparticle uptake: The phagocyte problem*. *Nano Today*, 2015. **10**(4): p. 487-510.
325. Campos, F., et al., *Fingolimod Reduces Hemorrhagic Transformation Associated With Delayed Tissue Plasminogen Activator Treatment in a Mouse Thromboembolic Model*. *Stroke*, 2013. **44**(2): p. 505-511.
326. Orset, C., et al., *Efficacy of Alteplase in a Mouse Model of Acute Ischemic Stroke*. *Stroke*, 2016. **47**(5): p. 1312-1318.





Appendix- Figures Rights & Permissions

Figures	Rights & Permissions
1.3, 4.10	<div data-bbox="437 461 609 495">  ACS Publications Most Trusted. Most Cited. Most Read. </div> <div data-bbox="627 398 1342 436"> Selected Standard Protocols for the Synthesis, Phase Transfer, and Characterization of Inorganic Colloidal Nanoparticles </div> <div data-bbox="627 443 1083 463"> Author: Jonas Hühn, Carolina Carrillo-Carrion, Mahmoud G. Soliman, et al </div> <div data-bbox="627 468 847 488"> Publication: Chemistry of Materials </div> <div data-bbox="627 490 863 510"> Publisher: American Chemical Society </div> <div data-bbox="627 512 734 530"> Date: Jan 1, 2017 </div> <div data-bbox="627 544 873 562"> <i>Copyright © 2017, American Chemical Society</i> </div> <hr/> <p>PERMISSION/LICENSE IS GRANTED FOR YOUR ORDER AT NO CHARGE</p> <p>This type of permission/license, instead of the standard Terms & Conditions, is sent to you because no fee is being charged for your order. Please note the following:</p> <ul style="list-style-type: none"> - Permission is granted for your request in both print and electronic formats, and translations. - If figures and/or tables were requested, they may be adapted or used in part. - Please print this page for your records and send a copy of it to your publisher/graduate school. - Appropriate credit for the requested material should be given as follows: "Reprinted (adapted) with permission from (COMPLETE REFERENCE CITATION). Copyright (YEAR) American Chemical Society." Insert appropriate information in place of the capitalized words. - One-time permission is granted only for the use specified in your request. No additional uses are granted (such as derivative works or other editions). For any other uses, please submit a new request. <p>If credit is given to another source for the material you requested, permission must be obtained from that source.</p>
1.4	<div data-bbox="411 873 609 952">  ACS Publications Most Trusted. Most Cited. Most Read. </div> <div data-bbox="700 922 841 940"> Search text, DOI, authors, etc. </div> <div data-bbox="991 922 1010 940">  </div> <div data-bbox="1062 922 1165 940">  My Activity </div> <div data-bbox="1193 922 1212 940">  Publications </div> <div data-bbox="1334 922 1353 940">  </div> <div data-bbox="408 972 1101 990"> COVID-19 Remote Access Support: Learn More about expanded access to ACS Publications research. </div> <h3 data-bbox="395 1008 515 1034">RightsLink</h3> <p data-bbox="395 1055 1340 1095">You have been directed to this webpage as a result of the type of license signed between the author and the American Chemical Society that provides users with some different terms of use.</p> <p data-bbox="395 1113 1316 1153">Please check to see if the article is designated as "ACS Author Choice" or "ACS Editor's Choice" (also includes CC licenses). If so, contact support@services.acs.org with your request, including the following information:</p> <ul style="list-style-type: none"> • A link to the ACS article from which you wish to reuse content • The portion of content you wish to reuse (e.g., number of figures, entire article for thesis) • A description of where the content will be reused (e.g., name of journal, book title, thesis) <p data-bbox="395 1249 778 1267">Public Domain and Crown Copyright, and Other Articles:</p> <ul style="list-style-type: none"> • For articles in the public domain: Check the copyright notice that appears with the abstract or on the first page of the article/chapter. An article is in the public domain if all of the authors of the article worked for the U.S. Government when the article was written. Requesters who want to use material that appeared in articles that are in the public domain do not need permission if the notice on the article/chapter states, "Not subject to U.S. Copyright," and credit to another source does not appear in the figure/table caption, if you are using figures/tables from the article. • For articles subject to "Crown" copyright:
1.5	<div data-bbox="443 1545 596 1565"> SPRINGER NATURE </div> <div data-bbox="622 1476 1350 1514"> Synthesis of a molecularly defined single-active site heterogeneous catalyst for selective oxidation of N-heterocycles </div> <div data-bbox="622 1525 783 1543"> Author: Yujing Zhang et al </div> <div data-bbox="622 1547 847 1565"> Publication: Nature Communications </div> <div data-bbox="622 1570 786 1588"> Publisher: Springer Nature </div> <div data-bbox="622 1592 737 1610"> Date: Apr 13, 2018 </div> <div data-bbox="622 1626 788 1641"> <i>Copyright © 2018, The Author(s)</i> </div> <hr/> <p>Creative Commons</p> <p>This is an open access article distributed under the terms of the Creative Commons CC BY license, which permits unrestricted use, distribution, and reproduction in any medium, provided the original work is properly cited.</p> <p>You are not required to obtain permission to reuse this article.</p> <p>To request permission for a type of use not listed, please contact Springer Nature</p>

1.7

Engineered Nanoparticles for Drug Delivery in Cancer Therapy
Author: Younan Xia, Miaoxin Yang, Dong Choon Hyun, et al
Publication: Angewandte Chemie International Edition
Publisher: John Wiley and Sons
Date: Oct 7, 2014
© 2014 WILEY-VCH Verlag GmbH & Co. KGaA, Weinheim

Review Order

Please review the order details and the associated terms and conditions.

No royalties will be charged for this reuse request although you are required to obtain a license and comply with the license terms and conditions. To obtain the license, click the Accept button below.

Licensed Content		Order Details	
Licensed Content Publisher	John Wiley and Sons	Type of use	Dissertation/Thesis
Licensed Content Publication	Angewandte Chemie International Edition	Requestor type	University/Academic
Licensed Content Title	Engineered Nanoparticles for Drug Delivery in Cancer Therapy	Format	Print and electronic
Licensed Content Author	Younan Xia, Miaoxin Yang, Dong Choon Hyun, et al	Portion	Figure/table
Licensed Content Date	Oct 7, 2014	Number of figures/tables	1
		Will you be translating?	No

1.8, 1.9

Colloidal bioplasmonics
Author: Ester Polo, María F. Navarro Poupard, Luca Guerrini, Pablo Taboada, Beatriz Pelaz, Ramón A. Alvarez-Puebla, Pablo del Pino
Publication: Nano Today
Publisher: Elsevier
Date: June 2018
© 2018 Elsevier Ltd. All rights reserved.

Please note that, as the author of this Elsevier article, you retain the right to include it in a thesis or dissertation, provided it is not published commercially. Permission is not required, but please ensure that you reference the journal as the original source. For more information on this and on your other retained rights, please visit: <https://www.elsevier.com/about/our-business/policies/copyright#Author-rights>

1.10






Functional Porous Coordination Polymers
Author: Shin-ichiro Noro, Ryo Kitaura, Susumu Kitagawa
Publication: Angewandte Chemie International Edition
Publisher: John Wiley and Sons
Date: Apr 22, 2004
Copyright © 2004 WILEY-VCH Verlag GmbH & Co. KGaA, Weinheim

Review Order





Please review the order details and the associated terms and conditions.

No royalties will be charged for this reuse request although you are required to obtain a license and comply with the license terms and conditions. To obtain the license, click the Accept button below.

Licensed Content		Order Details	
Licensed Content Publisher	John Wiley and Sons	Type of use	Dissertation/Thesis
Licensed Content Publication	Angewandte Chemie International Edition	Requestor type	University/Academic
Licensed Content Title	Functional Porous Coordination Polymers	Format	Print and electronic
Licensed Content Author	Shin-ichiro Noro, Ryo Kitaura, Susumu Kitagawa	Portion	Figure/table
Licensed Content Date	Apr 22, 2004	Number of figures/tables	1
		Will you be translating?	No

1.12	<div>  <p>On a Theory of the van der Waals Adsorption of Gases Author: Stephen Brunauer, Lola S. Deming, W. Edwards Deming, et al Publication: Journal of the American Chemical Society Publisher: American Chemical Society Date: Jul 1, 1940 Copyright © 1940, American Chemical Society</p> </div> <hr/> <p>PERMISSION/LICENSE IS GRANTED FOR YOUR ORDER AT NO CHARGE</p> <p>This type of permission/license, instead of the standard Terms & Conditions, is sent to you because no fee is being charged for your order. Please note the following:</p> <ul style="list-style-type: none"> - Permission is granted for your request in both print and electronic formats, and translations. - If figures and/or tables were requested, they may be adapted or used in part. - Please print this page for your records and send a copy of it to your publisher/graduate school. - Appropriate credit for the requested material should be given as follows: "Reprinted (adapted) with permission from (COMPLETE REFERENCE CITATION). Copyright (YEAR) American Chemical Society." Insert appropriate information in place of the capitalized words. - One-time permission is granted only for the use specified in your request. No additional uses are granted (such as derivative works or other editions). For any other uses, please submit a new request. <p>If credit is given to another source for the material you requested, permission must be obtained from that source.</p>
3.1	<div> <p>This service provides the legal rights to redistribute the content, it does not supply the copyrighted content itself. Price reflects the current conversion rate. ×</p> <p>1. Chemical Society reviews </p> <p>ISSN 1460-4744 Publisher ROYAL SOCIETY OF CHEMISTRY Type of Use Republish in a thesis/dissertation Portion Image/photo/illustration</p> <p> View Details 0,00 EUR  Remove</p> </div>
3.3, 3.5, 3.6, 3.7, 3.8, 3.9, 3.11, 3.12, 3.13, 3.14, 3.15, 3.16, 3.17, 3.18, 3.19, 3.20, 3.21, 3.22, 3.23	<div>  <p>Aqueous Synthesis of Copper(II)-Imidazolate Nanoparticles Author: María F. Navarro Poupard, Ester Polo, Pablo Taboada, et al Publication: Inorganic Chemistry Publisher: American Chemical Society Date: Oct 1, 2018 Copyright © 2018, American Chemical Society</p> </div> <hr/> <p>PERMISSION/LICENSE IS GRANTED FOR YOUR ORDER AT NO CHARGE</p> <p>This type of permission/license, instead of the standard Terms & Conditions, is sent to you because no fee is being charged for your order. Please note the following:</p> <ul style="list-style-type: none"> - Permission is granted for your request in both print and electronic formats, and translations. - If figures and/or tables were requested, they may be adapted or used in part. - Please print this page for your records and send a copy of it to your publisher/graduate school. - Appropriate credit for the requested material should be given as follows: "Reprinted (adapted) with permission from (COMPLETE REFERENCE CITATION). Copyright (YEAR) American Chemical Society." Insert appropriate information in place of the capitalized words. - One-time permission is granted only for the use specified in your request. No additional uses are granted (such as derivative works or other editions). For any other uses, please submit a new request. <p>If credit is given to another source for the material you requested, permission must be obtained from that source.</p>

4.1	<div> <div> </div> <div> <p>High-Throughput Synthesis of Zeolitic Imidazolate Frameworks and Application to CO₂ Capture</p> <p>Author: Rahul Banerjee, Anh Phan, Bo Wang, Carolyn Knobler, Hiroyasu Furukawa, Michael O'Keeffe, Omar M. Yaghi</p> <p>Publication: Science</p> <p>Publisher: The American Association for the Advancement of Science</p> <p>Date: Feb 15, 2008</p> <p><small>Copyright © 2008, American Association for the Advancement of Science</small></p> </div> </div> <div> <div>Review Order</div> <div>Please review the order details and the associated terms and conditions.</div> <p>No royalties will be charged for this reuse request although you are required to obtain a license and comply with the license terms and conditions. To obtain the license, click the Accept button below.</p> <div> <div> <div>Licensed Content</div> <table> <tr> <td>Licensed Content Publisher</td><td>The American Association for the Advancement of Science</td></tr> <tr> <td>Licensed Content Publication</td><td>Science</td></tr> <tr> <td>Licensed Content Title</td><td>High-Throughput Synthesis of Zeolitic Imidazolate Frameworks and Application to CO₂ Capture</td></tr> </table> </div> <div> <div>Order Details</div> <table> <tr> <td>Type of Use</td><td>Thesis / Dissertation</td></tr> <tr> <td>Requestor type</td><td>Scientist/individual at a research institution</td></tr> <tr> <td>Format</td><td>Print and electronic</td></tr> <tr> <td>Portion</td><td>Figure</td></tr> <tr> <td>Number of figures/tables</td><td>2</td></tr> </table> </div> </div> </div>	Licensed Content Publisher	The American Association for the Advancement of Science	Licensed Content Publication	Science	Licensed Content Title	High-Throughput Synthesis of Zeolitic Imidazolate Frameworks and Application to CO ₂ Capture	Type of Use	Thesis / Dissertation	Requestor type	Scientist/individual at a research institution	Format	Print and electronic	Portion	Figure	Number of figures/tables	2		
Licensed Content Publisher	The American Association for the Advancement of Science																		
Licensed Content Publication	Science																		
Licensed Content Title	High-Throughput Synthesis of Zeolitic Imidazolate Frameworks and Application to CO ₂ Capture																		
Type of Use	Thesis / Dissertation																		
Requestor type	Scientist/individual at a research institution																		
Format	Print and electronic																		
Portion	Figure																		
Number of figures/tables	2																		
4.2	<div> <div>Order Details</div> <div>1. Chemical Society reviews</div> <div> <div> <div>Order license ID</div><div>1084423-1</div> </div> <div> <div>Order detail status</div><div>Completed</div> </div> <div> <div>ISSN</div><div>1460-4744</div> </div> </div> <div> <div> <div>Type of use</div><div>Print License</div> </div> <div> <div>Publisher</div><div>ROYAL SOCIETY OF CHEMIS...</div> </div> <div> <div>Portion</div><div>Image/photo/illustration</div> </div> <div> <div>0,00 EUR</div><div>Republication Permission</div> </div> </div> <div> <div>Hide Details</div> <div>LICENSED CONTENT</div> <table> <tr> <td>Publication Title</td><td>Chemical Society reviews</td><td>Country</td><td>United Kingdom of Great Bri...</td></tr> <tr> <td>Author/Editor</td><td>Royal Society of Chemistry (...)</td><td>Rightsholder</td><td>Royal Society of Chemistry</td></tr> <tr> <td>Date</td><td>01/01/1972</td><td>Publication Type</td><td>e-journal</td></tr> <tr> <td>Language</td><td>English</td><td>URL</td><td>http://www.rsc.org/csr</td></tr> </table> </div> </div>	Publication Title	Chemical Society reviews	Country	United Kingdom of Great Bri...	Author/Editor	Royal Society of Chemistry (...)	Rightsholder	Royal Society of Chemistry	Date	01/01/1972	Publication Type	e-journal	Language	English	URL	http://www.rsc.org/csr		
Publication Title	Chemical Society reviews	Country	United Kingdom of Great Bri...																
Author/Editor	Royal Society of Chemistry (...)	Rightsholder	Royal Society of Chemistry																
Date	01/01/1972	Publication Type	e-journal																
Language	English	URL	http://www.rsc.org/csr																
4.6, 4.8, 4.9, 4.11, 4.12, 4.13, 4.15, 4.16, 4.17, 4.18, 4.19, 4.20, 4.21, 4.22, 6.1, 6.2, 6.3, 6.4, 6.5	<div> <div> </div> <div> <p>Aqueous Stable Gold Nanostar/ZIF-8 Nanocomposites for Light-Triggered Release of Active Cargo Inside Living Cells</p> <p>Author: Pablo del Pino, Ramon A. Alvarez-Puebla, Patricia Horcajada, et al</p> <p>Publication: Angewandte Chemie International Edition</p> <p>Publisher: John Wiley and Sons</p> <p>Date: Apr 12, 2019</p> <p><small>Copyright © 2019, John Wiley and Sons</small></p> </div> </div> <div> <div>Review Order</div> <div>Please review the order details and the associated terms and conditions.</div> <p>No royalties will be charged for this reuse request although you are required to obtain a license and comply with the license terms and conditions. To obtain the license, click the Accept button below.</p> <div> <div> <div>Licensed Content</div> <table> <tr> <td>Licensed Content Publisher</td><td>John Wiley and Sons</td></tr> <tr> <td>Licensed Content Publication</td><td>Angewandte Chemie International Edition</td></tr> <tr> <td>Licensed Content Title</td><td>Aqueous Stable Gold Nanostar/ZIF-8 Nanocomposites for Light-Triggered Release of Active Cargo Inside Living Cells</td></tr> </table> </div> <div> <div>Order Details</div> <table> <tr> <td>Type of use</td><td>Dissertation/Thesis</td></tr> <tr> <td>Requestor type</td><td>Author of this Wiley article</td></tr> <tr> <td>Format</td><td>Electronic</td></tr> <tr> <td>Portion</td><td>Figure/table</td></tr> <tr> <td>Number of figures/tables</td><td>26</td></tr> <tr> <td>Will you be translating?</td><td>No</td></tr> </table> </div> </div> </div>	Licensed Content Publisher	John Wiley and Sons	Licensed Content Publication	Angewandte Chemie International Edition	Licensed Content Title	Aqueous Stable Gold Nanostar/ZIF-8 Nanocomposites for Light-Triggered Release of Active Cargo Inside Living Cells	Type of use	Dissertation/Thesis	Requestor type	Author of this Wiley article	Format	Electronic	Portion	Figure/table	Number of figures/tables	26	Will you be translating?	No
Licensed Content Publisher	John Wiley and Sons																		
Licensed Content Publication	Angewandte Chemie International Edition																		
Licensed Content Title	Aqueous Stable Gold Nanostar/ZIF-8 Nanocomposites for Light-Triggered Release of Active Cargo Inside Living Cells																		
Type of use	Dissertation/Thesis																		
Requestor type	Author of this Wiley article																		
Format	Electronic																		
Portion	Figure/table																		
Number of figures/tables	26																		
Will you be translating?	No																		

5.1, 5.2	<div data-bbox="459 248 568 394">  </div> <div data-bbox="587 248 1214 271"> <p>CaCO₃ vaterite microparticles for biomedical and personal care applications</p> </div> <div data-bbox="587 277 1112 297"> <p>Author: Daria B. Trushina, Tatiana V. Bukreeva, Mikhail V. Kovalchuk, Maria N. Antipina</p> </div> <div data-bbox="587 302 893 320"> <p>Publication: Materials Science and Engineering: C</p> </div> <div data-bbox="587 324 702 340"> <p>Publisher: Elsevier</p> </div> <div data-bbox="587 344 734 362"> <p>Date: 1 December 2014</p> </div> <div data-bbox="587 378 849 394"> <p>Copyright © 2014 Elsevier B.V. All rights reserved.</p> </div> <hr/> <div data-bbox="478 450 577 468"> <p>Review Order</p> </div> <div data-bbox="491 501 911 517" style="background-color: #e0ffe0; padding: 5px;"> <p>Please review the order details and the associated terms and conditions.</p> </div> <div data-bbox="472 546 1313 580"> <p>No royalties will be charged for this reuse request although you are required to obtain a license and comply with the license terms and conditions. To obtain the license, click the Accept button below.</p> </div> <div data-bbox="472 593 619 611"> <p> Licensed Content</p> </div> <div data-bbox="472 624 911 792"> <table> <tr> <td>Licensed Content Publisher</td><td>Elsevier</td></tr> <tr> <td>Licensed Content Publication</td><td>Materials Science and Engineering: C</td></tr> <tr> <td>Licensed Content Title</td><td>CaCO₃ vaterite microparticles for biomedical and personal care applications</td></tr> <tr> <td>Licensed Content Author</td><td>Daria B. Trushina, Tatiana V. Bukreeva, Mikhail V. Kovalchuk, Maria N. Antipina</td></tr> </table> </div> <div data-bbox="927 593 1046 611"> <p> Order Details</p> </div> <div data-bbox="927 624 1342 792"> <table> <tr> <td>Type of Use</td><td>reuse in a thesis/dissertation</td></tr> <tr> <td>Portion</td><td>figures/tables/illustrations</td></tr> <tr> <td>Number of figures/tables/illustrations</td><td>3</td></tr> <tr> <td>Format</td><td>both print and electronic</td></tr> <tr> <td>Are you the author of this Elsevier article?</td><td>No</td></tr> <tr> <td>Will you be translating?</td><td>No</td></tr> </table> </div>	Licensed Content Publisher	Elsevier	Licensed Content Publication	Materials Science and Engineering: C	Licensed Content Title	CaCO ₃ vaterite microparticles for biomedical and personal care applications	Licensed Content Author	Daria B. Trushina, Tatiana V. Bukreeva, Mikhail V. Kovalchuk, Maria N. Antipina	Type of Use	reuse in a thesis/dissertation	Portion	figures/tables/illustrations	Number of figures/tables/illustrations	3	Format	both print and electronic	Are you the author of this Elsevier article?	No	Will you be translating?	No
Licensed Content Publisher	Elsevier																				
Licensed Content Publication	Materials Science and Engineering: C																				
Licensed Content Title	CaCO ₃ vaterite microparticles for biomedical and personal care applications																				
Licensed Content Author	Daria B. Trushina, Tatiana V. Bukreeva, Mikhail V. Kovalchuk, Maria N. Antipina																				
Type of Use	reuse in a thesis/dissertation																				
Portion	figures/tables/illustrations																				
Number of figures/tables/illustrations	3																				
Format	both print and electronic																				
Are you the author of this Elsevier article?	No																				
Will you be translating?	No																				
5.5, 5.7, 5.9, 5.11, 5.14, 5.15, 5.16, 5.17, 5.18, 5.19, 5.20, 5.21, 5.22, 5.23, 5.25, 5.26, 6.6, 6.7, 6.8, 6.9, 6.10	<div data-bbox="432 857 541 981">  </div> <div data-bbox="557 831 1310 871"> <p>In vivo ultrasound-activated delivery of recombinant tissue plasminogen activator from the cavity of sub-micrometric capsules</p> </div> <div data-bbox="557 880 1303 929"> <p>Author: Clara Correa-Paz, María F. Navarro Poupard, Ester Polo, Manuel Rodríguez-Pérez, Pablo Taboada, Ramón Iglesias-Rey, Pablo Hervella, Tomás Sobrino, Denis Vivien, José Castillo, Pablo del Pino, Francisco Campos, Beatriz Pelaz</p> </div> <div data-bbox="557 934 818 952"> <p>Publication: Journal of Controlled Release</p> </div> <div data-bbox="557 956 675 972"> <p>Publisher: Elsevier</p> </div> <div data-bbox="557 976 692 994"> <p>Date: 28 August 2019</p> </div> <div data-bbox="557 1010 766 1025"> <p>© 2019 Elsevier B.V. All rights reserved.</p> </div> <hr/> <div data-bbox="432 1117 1350 1167"> <p>Please note that, as the author of this Elsevier article, you retain the right to include it in a thesis or dissertation, provided it is not published commercially. Permission is not required, but please ensure that you reference the journal as the original source. For more information on this and on your other retained rights, please visit: https://www.elsevier.com/about/our-business/policies/copyright#Author-rights</p> </div>																				